DOT/FAA/TC-16/21

Federal Aviation Administration
William J. Hughes Technical Center
Aviation Research Division
Atlantic City International Airport
New Jersey 08405

Certification by Analysis—A Building Block Methodology for Composite and Metallic Aircraft Crashworthy Structures—Coupon Level

May 2017

Final Report

U.S. Department of Transportation
Federal Aviation Administration

NOTICE

Technical Report Documentation Page

1. Report No.	2. Government Accession No.	3. Recipient's Catalog No.
DOT/FAA/TC-16/21		

4. Title and Subtitle	5. Report Date
CERTIFICATION BY ANALYSIS—A BUILDING BLOCK METHODOLOGY FOR COMPOSITE AND METALLIC AIRCRAFT CRASHWORTHY STRUCTURES—COUPON LEVEL	May 2017
	6. Performing Organization Code

7. Author(s)	8. Performing Organization Report No.
J. F. Acosta, G. Olivares, and S. K. Raju	

9. Performing Organization Name and Address	10. Work Unit No. (TRAIS)
Wichita State University National Institute for Aviation Research 1845 Fairmount Street Wichita, KS 67260-0093	11. Contract or Grant No.

12. Sponsoring Agency Name and Address	13. Type of Report and Period Covered
U.S. Department of Transportation Federal Aviation Administration 245 Queens Xing Dayton, OH 45458	Final Report
	14. Sponsoring Agency Code AIR-100

15. Supplementary Notes

The Federal Aviation Administration William J. Hughes Technical Center Aviation Research Division COR was Allan Abramowitz.

16. Abstract

The incremental development of analysis and supporting tests (i.e., the building block approach [BBA]) is used to design, evaluate, and optimize the crashworthiness behavior of composite structures.

The purpose of this study was to begin the process of documenting the steps necessary in developing the BBA. This study begins with issues surrounding development of material properties and modeling considerations at the coupon level, the lowest level of the BBA pyramid.

Coupon-level test data from previous research programs were examined, material properties were extracted, and variability within test results was quantified. Limitations of dynamic material testing techniques related to the measurement of load and strain and their sources of variability were identified. The available test data were generated over a wide range of test speeds from quasi-static to 100 in/s. The data included dynamic material properties of an aluminum 7075-T6 test specimen from which a numerical model was developed using the finite element (FE) modeling code LS-DYNA. An FE model of the high-speed servo-hydraulic testing system, including a slack-inducer mechanism and the specimen-gripping attachment, was assembled. A model of the Al test specimen and test system was used to generate a baseline for high-speed test simulations of composite materials.

Numerical models of laminated composite materials (Toray T800S/3900-2B Unitape, Newport E-Glass Fabric NB321/7781, and Toray T700G-12K-PW/3900-2 Fabric) were developed. The models were used to simulate tension, compression, and in-plane shear test methods at various strain rates using LS-DYNA and verified with test results. A parametric study was conducted on mesh sizes, element formulations, element types, and integration points to provide information to define future modeling best practices and guidelines.

17. Key Words	18. Distribution Statement
Crashworthiness, Composites, Strain rate, Material models, Building block approach	This document is available to the U.S. public through the National Technical Information Service (NTIS), Springfield, Virginia 22161. This document is also available from the Federal Aviation Administration William J. Hughes Technical Center at actlibrary.tc.faa.gov.

19. Security Classif. (of this report)	20. Security Classif. (of this page)	21. No. of Pages	22. Price
Unclassified	Unclassified	252	

ACKNOWLEDGEMENTS

The authors would like to thank FAA technical monitor Allan Abramowitz for his technical guidance and input throughout this project. The authors would like to acknowledge the contributions of the Mechanical Test Lab at the National Institute for Aviation Research and its supporting staff.

TABLE OF CONTENTS

LIST OF FIGURES

LIST OF TABLES

LIST OF ACRONYMS

AGATE	Advanced General Aviation Transport Experiments
Al	Analyzed aluminum
BBA	Building block approach
CLT	Classical laminate theory
CV	Coefficient of variation
ELFORM	Element formulation
EXP	Experimental
FE	Finite element
MTS	Material Testing System
NIAR	National Institute for Aviation Research
NIP	Number of through-the-thickness integration points
SACMA	Suppliers of Advanced Composite Materials Association
SIM	Simulation
V&V	Verified & validated
vATD	Virtual Anthropomorphic Test Dummies
WP	Working package
WSU	Wichita State University

EXECUTIVE SUMMARY

Structural design for airplane safety combines varying degrees of airworthiness and crashworthiness design objectives. Airworthiness design objectives pertain to the ability of the airframe to withstand design loads or to maintain safety of flight of the airplane relative to the operational environment. Crashworthiness design objectives pertain to safety of the occupants relative to the airplane. There is, at present, no specific regulatory dynamic impact requirement for airplane-level crashworthiness. However, the FAA requires an assessment of each new model airplane to ensure that the airplane has comparable dynamic crashworthiness characteristics found in previous designs. Therefore, the introduction of composite airframes warrants an assessment to ascertain whether the crashworthiness dynamic structural response provides an equivalent or improved level of safety as compared to similar-sized conventional metallic structures. To design, evaluate, and optimize the crashworthiness behavior of composite structures, it is necessary to develop analytical methods based on the building block approach (BBA). The BBA is the incremental development of analysis and supporting tests in which, typically, there is an increase in size and complexity of the test article and a decrease in the number of corresponding tests.

The design process of aircraft structures relies to a great extent on component-level testing when validating the overall crash performance of a structure/component. However, component-level tests do not provide all of the data required to generate predictable simulation results. Designers require material properties that take into account the material response at quasi-static and higher strain rates; these material properties are generated from coupon-level testing.

The purpose of this study was to begin the process of documenting the steps necessary for developing the BBA. This study begins with issues surrounding the development of material properties and modeling considerations at the coupon level, the lowest level of the BBA pyramid.

Coupon-level test data from previous research programs were examined, material properties were extracted, and variability within test results was quantified. Limitations of dynamic material testing techniques related to the measurement of load and strain and their sources of variability were identified. The available test data were generated over a wide range of test speeds from quasi-static to 100 in/s. The data included dynamic material properties of an aluminum 7075-T6 test specimen from which a numerical model was developed using the finite element (FE) modeling code LS-DYNA. An FE model of the high-speed servo-hydraulic testing system, including a slack-inducer mechanism and the specimen-gripping attachment, was assembled. A model of the analyzed aluminum test specimen and test system was used to generate a baseline for high-speed test simulations of composite materials.

Numerical models of laminated composite materials (Toray T800S/3900-2B Unitape, Newport E-Glass Fabric NB321/7781, and Toray T700G-12K-PW/3900-2 Fabric) were developed. The models were used to simulate tension, compression, and in-plane shear test methods at various strain rates using LS-DYNA and verified with test results. A parametric study was conducted on mesh sizes, element formulations, element types, and integration points to provide information to define future modeling best practices and guidelines.

1. INTRODUCTION

Structural design for airplane safety combines airworthiness and crashworthiness design objectives. Airworthiness design objectives are the ability of the airframe to withstand design loads or to maintain safety of flight of the airplane relative to the operational environment, whereas crashworthiness design objectives are the safety of the occupants relative to the airplane. The development of current aircraft crash dynamics standards dates back to the 1970s, during which time product liability grew for small aircraft manufacturers. To address the crashworthiness characteristics of transport category aircraft, small general aviation aircraft and rotorcraft manufacturers, the FAA, and NASA initiated a wide range of research and development programs [1–3]. These programs represented a concentrated effort to analyze aircraft behavior and occupant characteristics through interrelated studies of accident data, dynamic analyses of crash events, full-scale aircraft impact tests, and aircraft seat tests. A General Aviation Safety Panel was formed in 1978 to make recommendations on crashworthiness requirements. The results of these efforts formed the basis for the development of crashworthiness design standards for civil aircraft. These requirements are defined in the Title 14 Code of Federal Regulations Parts 23, 25, and 27 for general aviation aircraft, transport aircraft, and rotorcraft, respectively. These regulations were first proposed in 1982 and became effective in 1988. Nevertheless, the crashworthiness requirements only applied to the dynamic performance of the seats and occupants; no crashworthiness requirements were defined for the structure.

Though the regulations have evolved, there is still, at present, no specific regulatory dynamic impact requirement for airplane-level crashworthiness. However, the FAA requires an assessment of each new model airplane to ensure that the airplane has comparable dynamic crashworthiness characteristics to those found in previous designs. Therefore, the introduction of composite airframes warrants an assessment of whether the crashworthiness dynamic structural response provides a comparable level of safety to similar-sized conventional metallic structures [4]. This assessment generally includes the evaluation of the survivable volume, retention of items of mass, deceleration loads experienced by the occupants, and occupant emergency egress paths.

1.1 BACKGROUND

1.1.1 National Institute of Aviation Research Crashworthiness Research Program Overview

The following section is an overview of the National Institute of Aviation Research's (NIAR) Crashworthiness Research Program. This overview forms the basis of the work found in this report and the rationale for the follow-up reports, the purpose of which is to support the development of aircraft crashworthiness guidelines and best practices. This section also describes advances that the NIAR has pursued through FAA funding.

A significant amount of test work on metallic aircraft structures has been conducted in the past in both the private and public sector. However, there is a lack of public domain data on the crashworthiness behavior of composite aircraft structures. To design, evaluate, and optimize the crashworthiness behavior of composite structures, it is necessary to develop analytical methods

and predictable computational tools. Non-Physics-Based or Physics-Based Modeling (see figure 1) are two approaches that can be used to conduct airframe crashworthiness certification by analysis:

- Non-Physics-Based Modeling: This approach has been used by the aerospace industry since the introduction of simulations. However, there are issues regarding its use due to limitations in computing power and computational tools, complexity of the problems, a limited understanding of the physics, a lack of test-to-test variability data, and limited modeling methodologies. In addition, it is necessary to conduct system-level tests and use the test results to calibrate the model, thereby limiting the predictive capabilities of the numerical model outside of the calibrated test configuration. Models are evaluated by the calibration-validation method and the validation criteria can be unreasonable (5–10%) and vague (peak, shape, subjective). This is because of the lack of test data required to develop an understanding of the test-to-test variability.
- Physics-Based Modeling: This approach proposed by the NIAR takes advantage of advances in computational power, the latest computational tools, years of research in understanding the fundamental physics of the crashworthiness event, generated test-to-test variability data, and verified & validated (V&V) modeling methodologies. This modeling methodology uses the building block approach (BBA) shown in figure 2. The BBA is the incremental development of analysis and supporting tests in which, typically, there is an increase in the size and complexity of the test article and a decrease in the number of supporting tests. To develop this method, it is necessary to have a good understanding of the physics and testing variability from the coupon to the system level. The definition of the numerical model is not driven by system level test results; rather, it is driven by a predefined, verified, and validated building block modeling methodology. Through the use of this approach, simulations should be able to predict the system-level test results within the scatter of the physical system test results. Objective validation criteria based on an understanding of the test-to-test variability are used to evaluate the numerical models, in which the correlation level between simulation and testing is defined by an understanding of the test-to-test variability of the physical system under evaluation.

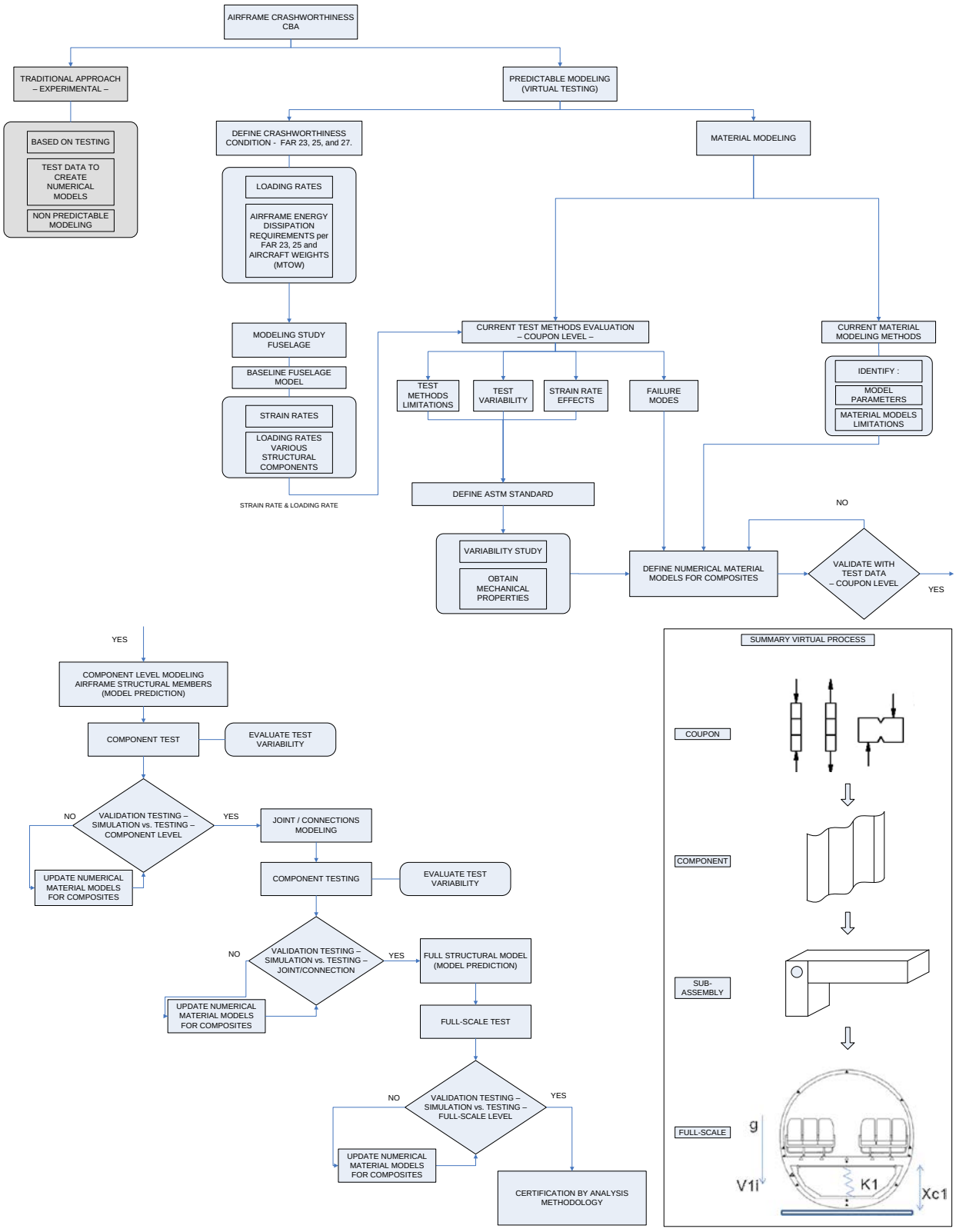

Figure 1. Airframe crashworthiness certification by analysis methodology

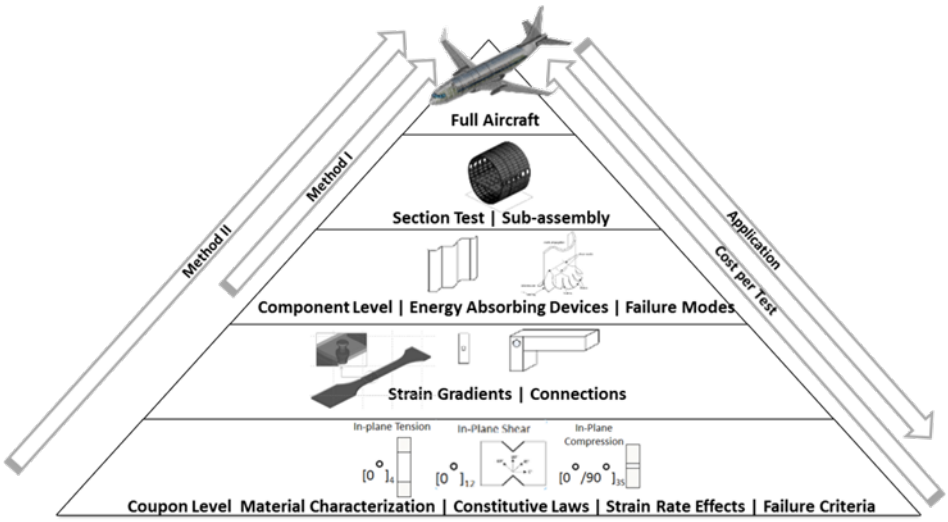

Figure 2. The NIAR building block approach for structural crashworthiness evaluations

Figure 3 shows the four research phases either planned, currently in-progress, or completed by the NIAR. Detailed descriptions of the research phases are described below:

- Phase I—Virtual Anthropomorphic Test Dummies (vATD) Development and V&V Methods: Completed. An accurate numerical vATD model could potentially be used to evaluate the level of safety to passengers and the dynamic response of the seating system in lieu of, or in conjunction with, physical testing to reduce development time and cost. A means of establishing confidence in the vATD predictive ability was needed by industry. Toward that end, the research conducted in Phase I provided the baseline test data required to define specifications for numerical occupant models of the Hybrid II and FAA Hybrid III anthropomorphic test dummies suitable for aviation impact test simulations. In addition, procedures for validation of vATD models—and modeling guidelines to assist modelers in developing efficient and accurate models—were developed. The results for this research phase are summarized in FAA Technical Report DOT/FAA/AR-11/24 [5].
- Phase II—Virtual Aerospace Seat Certification by Analysis Methodology: Completed. For aircraft seating systems, physical testing is increasingly being replaced by numerical simulation models because it provides a quicker and less expensive way to evaluate design concepts. The principal goal of this phase was to define numerical modeling techniques to accurately predict the response of the seat and vATD during emergency landing conditions.
- Phase III—Metallic and Composite Airframes Crashworthiness Section Level R&D: The following working packages (WPs) were defined to develop the NIAR BBA methodology shown in figure 3:

  – WP 1—Aerospace Crashworthiness Structural Requirements: In progress. Detailed finite element (FE) models of a metallic narrow-body transport aircraft have been developed by NIAR to study the crashworthiness behavior of typical

metallic aircraft structures during survivable impacts on hard surfaces, soft soil, and water. The intent of these models is to study the dynamic response and energy-absorbing capabilities of the individual structural members (i.e., stanchions, frames, stringers, skin), the effect on the structural response of various cargo (empty to full cargo configurations), and impact surface (rigid, soil, and water) configurations. The results of these studies will define a range of typical energy-absorbing requirements, loading, and strain rates for the various airframe structural components. The crashworthiness evaluation will also quantify the boundary condition effects on the airframe crashworthiness response, from full aircraft models to fuselage section (e.g., half and full barrel) type vertical drop test configurations.

- WP 2—Coupon Level R&D. The design process of aircraft structures relies to a great extent on component-level testing when validating the overall crash performance of a structure/component. Component-level tests do not provide the data required to generate predictable simulation results outside of the conditions defined at the component test. Designers require dynamic material properties that take into account the material response at quasi-static and higher strain rates; these material properties are generated from coupon-level testing. For this purpose, coupon-level tests were conducted over a range of strain rates for which testing techniques have not yet been standardized. Currently, obtaining accurate dynamic test data suitable for material model definitions represents a challenge; for numerical models of composite and metallic structures to be used as a predictive tool in crash event simulations, reliable testing methods to generate material properties need to be developed.

    - WP 2.1—Current study: Quasi-static and High Strain Rate Composite Material Coupon Level R&D. For this phase of the project, studies were conducted to quantify the high strain rate coupon level test variability for Toray-T800S/3900-2B Unitape, Newport-E-Glass Fabric NB321/7781, and Toray-T700G-12K-PW/3900-2 (fabric) under tension, shear, and compression. LS-DYNA MAT 54 and MAT 58 coupon-level models were evaluated with quasi-static and high strain rate data. A series of studies on mesh sizes, element formulations (ELFORM), element types, and integration points were conducted to provide the aerospace community with the data required to define future modeling best practices guidelines.
    - WP 2.2—In review: Round Robin High Strain Rate Testing Material Characterization–Tension. Because of the lack of a standard high strain rate testing protocol for composite materials at the coupon level, a round-robin exercise was conducted by the NIAR and four research partners (DLR, Oakridge National Labs, Ohio State University, and Arizona State University). The findings of this round-robin exercise can be used to define a future tensile high strain rate testing protocol.

- WP 3—Component Level R&D: In review. The component-level tests will be used to validate the coupon-level material data generated in WP2 and to study the

strain rate sensitivity of these composite material systems at the component level. The following component-level test configurations were evaluated at quasi-static and high strain rates: Pin-Bearing, C-Section Beams, and Sine Wave Beams. The results obtained will provide the data required to define future component-level testing protocols (loading rates, strain rates, energy absorbing requirements, and component-level test configurations).

- WP 4—Joints and Connections R&D: In progress.For full-scale structural models to be predictable, it is necessary to understand the numerical limitations of different modelling techniques that can be used to virtually join the various airframe structural members. A series of tests at various loading rates were conducted to evaluate single- and multiple-point load transfer mechanisms between airframe structural members. Various modeling techniques were evaluated for accuracy with the test data generated in this working package.
- WP 5—Section Level Experimental and Computational Best Practices: Future effort. The objective of this working package will be to summarize the numerical and test best practices developed in WP1 through WP4 to define a certification by analysis methodology that can be used by the aerospace industry in the future.

- Phase IV—Full-Scale Aircraft Models: In progress. The objective of this phase is to evaluate the ability of full aircraft numerical models to predict the structural deformations and passenger injuries during a real-world crash condition. To conduct this research, the Turkish Airlines Flight 1951 crash was selected. This flight was a passenger flight that crashed during landing at Amsterdam Schiphol Airport, Netherlands, on February 25, 2009, resulting in the deaths of nine passengers and crew, including all three pilots. The aircraft, a Boeing 737-800, crashed into a field approximately 1.5 kilometers (0.93 mi) north of the Polderbaan runway, 18R, prior to crossing the A9 motorway inbound, at 9:31 UTC (10:31 CET), having flown from Istanbul, Turkey. The aircraft broke into three pieces on impact. The wreckage did not catch fire. A preliminary investigation found that the crash was attributed to the aircraft's automated response to a faulty radio altimeter input. This resulted in the auto throttle decreasing the engine power to idle during approach. This was unnoticed by the crew until it was too late to increase the thrust and recover the aircraft before it stalled and crashed. The structural response of the full aircraft numerical model and crash data provided by the accident investigation team will be compared to verify and validate the model. The completed model will provide researchers with more accurate data on the behavior of the aircraft structure and passengers when subjected to a real world crash scenario.

Figure 3. The NIAR crashworthiness R&D program roadmap

1.2 SCOPE

The crash performance of a structure/component relies to a great extent on component-level tests. However, component-level tests do not provide all the data required to generate predictable simulation results. Designers require material properties that take into account the material response at quasi-static and higher strain rates; these material properties are generated from coupon-level testing. Presently, obtaining accurate dynamic material data suitable for material model definitions represents a challenge because testing techniques have not yet been standardized. For numerical models of composite and metallic structures to be used as a predictive tool in crash events simulations, reliable testing methods to generate material properties need to be developed. For this study, coupon-level tests of several different materials over a range of strain rates previously conducted by the NIAR will be used to generate the required data. In addition, the use of the Advanced General Aviation Transport Experiments (AGATE) data will be used to supplement the NIAR data when necessary.

For this phase of the overall study, several tasks were undertaken:

1. Quantified quasi-static and high strain rate coupon-level test variability for Toray-T800S/3900-2B Carbon Unitape, Newport-E-Glass Fabric NB321/7781, and Toray-T700G12K-PW/3900-2 Carbon Fabric under tension, shear, and compression from previous test data [6].
2. Analyzed Aluminum (Al) 7075-T6 test results to develop quasi-static and dynamic material properties.
3. Established an Al baseline to compare composite results and characterize the test system.
4. Evaluated LS-DYNA MAT 54 and MAT 58 coupon-level models using the quasi-static and high strain rate data.
5. Using the models, performed a series of parametric studies on mesh sizes, ELFORM, element types, and integration points to provide data to define modeling best practices guidelines.

2. TEST METHODS

The test methods described in this section reflect research conducted in previous NIAR studies. A detailed description of the methods used to generate the data is given. In this investigation, the material properties necessary for assembling a baseline material model using Al were generated from uniaxial tension testing. The in-plane mechanical properties of the laminated composites at the lamina level were obtained from tensile, compressive, and shear tests. Note that all of the material properties were generated at room-temperature conditions (70°F ±10°). The specific specimen geometry per test method is described along with the corresponding instrumentation used to measure the material response. Material properties generated at quasi-static rates, with corresponding test methods, are summarized in table 1.

Table 1. Material properties generated from testing at quasi-static rates

Material system	Test	Standard	Orientation	Properties
Baseline Aluminum 7075-T6	Uniaxial Tension	ASTM E 8	[L]	Young's modulus—E Poisson's ratio—ν Plastic strain tensile a-axis—ε_{11}^{T} Stress-strain curve—σ vs. ε
Laminated Composite Materials	Warp Tensile Strength	ASTM D 3039	$[0°]_{N}$	Young's modulus in a-direction—E_{11}^{T} Poisson's ratio—ν_{12} Strain at longitudinal tensile strength a-axis—ε_{11}^{T} Longitudinal tensile strength a-axis—F_{11}^{T}
	Warp Compressive Strength	ASTM D 695	$[0°/90°]_{NS}$	Young's modulus in a-direction—E_{11}^{C} Strain at longitudinal compressive strength a-axis—ε_{11}^{C} Longitudinal compressive strength a-axis—F_{11}^{C}
	Fill Tensile Strength	ASTM D 3039	$[0°]_{N}$	Young's modulus in b-direction—E_{22}^{T} Strain at transverse tensile strength b-axis—ε_{22}^{T} Transverse tensile strength b-axis—F_{22}^{T}
	Fill Compressive Strength	ASTM D 695	$[0°]_{N}$	Young's modulus in b-direction—E_{22}^{C} Strain at transverse compressive strength b-axis—ε_{22}^{C} Transverse compressive strength b-axis—F_{22}^{C}
	IPS Strength	ASTM D 7078	$[0°]_{N}$	Shear modulus ab—G_{12} Strain at shear strength ab plane—γ_{12} Shear strength ab plane—F_{12}^{S} Stress limit nonlinear shear stress-strain curve—F_{12}^{1} Strain limit nonlinear shear stress-strain curve—γ_{12}^{1}

2.1 MATERIAL SYSTEMS

Al 7075-T6 was used as the baseline material for the numerical simulations. In addition, there were three epoxy-based composite material systems consisting of two continuous graphite layups (a unidirectional and a plain weave fabric) and an E-glass satin weave fabric. The manufacturer's identification codes of the composite material systems were:

1. Toray Carbon Unitape T800S/3900-2B
2. Toray Carbon Fabric T700G-12K-PW/3900-2
3. Newport E-Glass Fabric NB321/7781
4. The NIAR data included three autoclave-cured laminates [6] of the composite material systems. The laminates consisted of four different stacking sequences, one along the principal material direction and three other balanced and symmetrical off-axis orientations—$[0°]N$, $[+15°/-15°]_{NS}$, $[+30°/-30°]_{NS}$, and $[+45°/-45°]_{NS}$, respectively. The quasi-static oven-cured laminate data (Newport E-Glass Fabric NB321/7781) used in the compression portion of the study was generated from the AGATE research program [7] and had a symmetric cross-ply stacking sequence—$[0°/90°]_{3S}$.

2.2 TESTING APPARATUS

Various testing systems and methodologies are used when generating dynamic material properties over a wide range of strain rates. Figure 4 shows several servo-hydraulic testing systems that are frequently used for low-to-medium strain rates (0.000167–500 s^{-1}). The speed of this type of system is a function of the distance traveled by the actuator. In addition, the ability to control the speed of the system is a function of the response capability of a servo-controlled system operating in control-loop mode [8]. Conventional servo-hydraulic systems are commonly used for quasi-static rates below 0.1 s^{-1}. High-speed servo-hydraulic systems are used to examine the strain rate regime between 0.1 and 500 s^{-1}. The higher actuator speeds are achieved with greater hydraulic power. Larger strain rates can be achieved using other test apparatus, such as a drop tower or drop weight impacts apparatus [9, 10]; a Charpy pendulum [11]; an expanding ring [12, 13]; or a Split Hopkinson Pressure Bar [14]. Different test apparatus have advantages and limitations depending on the strain rate regime (see table 2) [15].

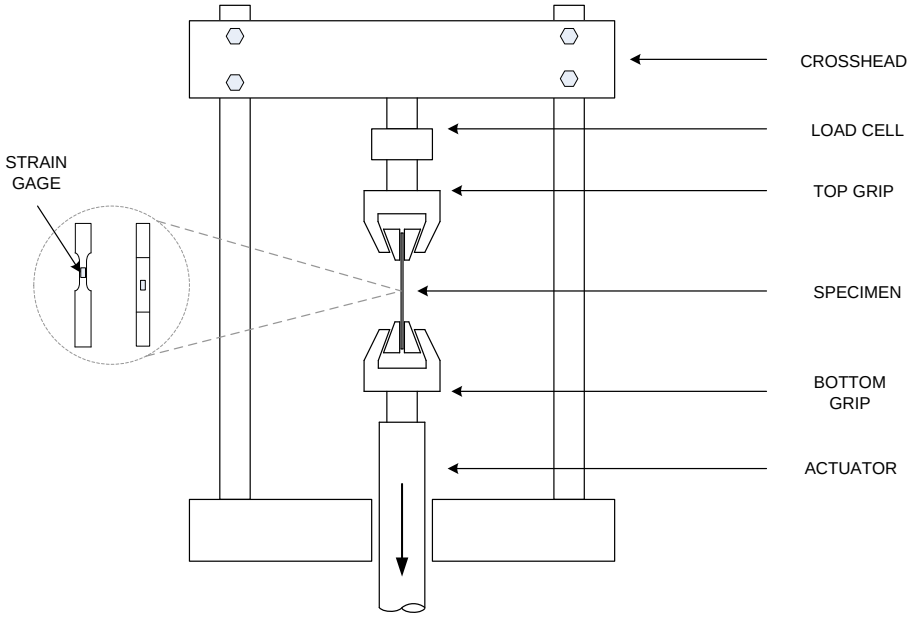

Figure 4. Schematic of servo-hydraulic testing system

Table 2. Test apparatus associated with strain rate regime

Loading Times (s)	10^{6}–10^{4}	10^{4}–10^{2}	10^{0}–10^{-1}	10^{-2}–10^{-4}	$>10^{-4}$
Strain Rate Regime (s^{-1})	$<10^{-3}$	10^{-3}–10^{-1}	10^{0}–10^{1}	10^{2}–10^{4}	$>10^{4}$
Test Apparatus	Constant load machines	Hydraulic or screw machines	Pneumatic or mechanical machines	Mechanical or explosive impact	Gas gun or explosive driven-plate impact

Two different servo-hydraulic testing machines were used to generate the NIAR data. The quasi-static composite in-plane tensile, compressive, and shear properties were generated on a standard Material Testing System (MTS) system under displacement control at a constant rate of 0.05 in/min. The high-stroke-rate system at the NIAR was used for in-plane tension testing and in-plane shear testing for speeds ranging from 0.1–75 in/s. This testing machine is rated for 5000 lbf (22,241 N) at speeds as high as 500 in/s (12.7 m/s) and 9000 lbf (40,034 N) at quasi-static rates. This system includes a slack-inducer mechanism that allows the actuator to reach the desired speed before loading the specimen. The actuator accelerates through a predefined distance before engaging a pin that pulls from a slack inducer rod attached to the bottom grip. The dynamics of the load introduction are described in figure 5, and a detailed description of the testing machine is presented in Raju and Acosta [6]. Though quasi-static testing was performed under displacement control, dynamic testing was conducted in open-loop (no feedback) control.

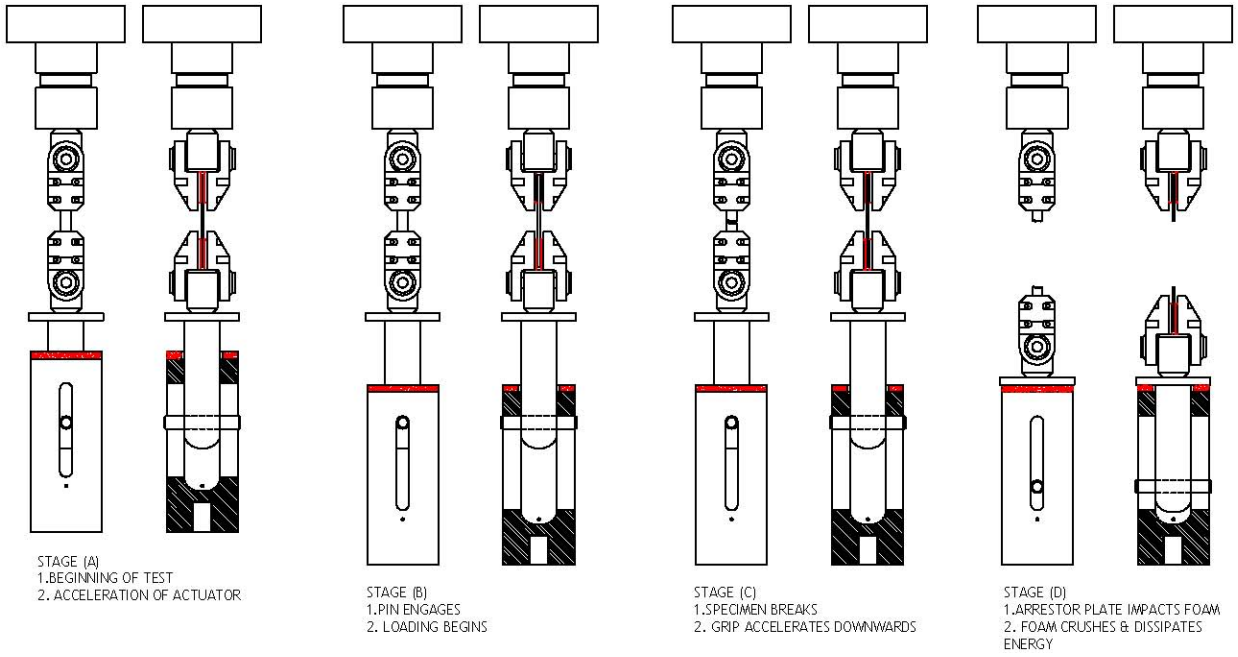

Figure 5. Slack-inducer mechanism at the NIAR/Wichita State University

2.3 TENSION TESTING

The same set of tension grips was used on the composite and Al test specimens (see figure 6). The grips were lightweight wedge-grip assemblies designed and fabricated at the NIAR/Wichita State University (WSU) [6]. The grips were manufactured from Al 7075-T6 and the wedge inserts from 17-4 PH stainless steel with a tungsten carbide surface for improved grip. The tension test specimens required two different specimen geometries: an extended-tab dog-bone specimen for Al and a straight-tabbed specimen with rectangular cross section for composite materials. Test data were available at various speeds for each material system; however, for a fixed actuator speed, the nominal strain rate varied between the two specimen geometries because their gage length differed. Al specimens were tested along the longitudinal grain

direction (L) over five different speeds. The lowest speed used to test the Al specimen is referred throughout this document as “quasi-static,” which corresponds to 0.1 in/s. The three composite material systems were tested at three speeds for each of the four stacking sequences. The lowest speed used to test the composite specimen is also referred throughout this document as “quasi-static” and corresponds to 0.00083 in/s. Each test configuration was replicated three times per speed. The test matrix in table 3 summarizes the available test data for the current investigation. Composite specimen nominal strain rates associated with each actuator speed are summarized in table 4.

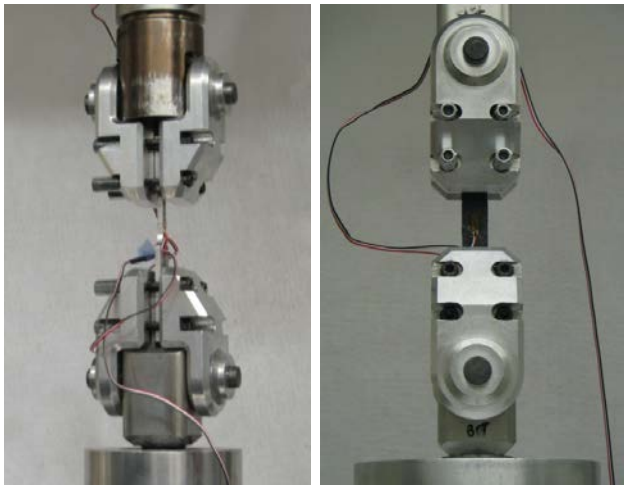

Figure 6. Tension grips at the NIAR/WSU

Table 3. Tension test matrix

Material	Stacking Sequence/ Orientation	Actuator Speed (in/s)					
		0.00083	0.1	1	10	50	75
Newport E-Glass Toray Unitape Toray Fabric	$[0°]_N$	x3	-	x3	x3	-	-
	$[+15°/-15°]_{NS}$	x3	-	x3	x3	-	-
	$[+30°/-30°]_{2S}$	x3	-	x3	x3	-	-
	$[+45°/-45°]_{2S}$	x3	-	x3	x3	-	-
Al 7075-T6	[L]	-	x3	x3	x3	x3	x3

Table 4. Nominal strain rates for composite specimens

Actuator Speed (in/s)	0.00083	1	10
Nominal Strain Rate (1/s)	0.00041	0.5	5

2.3.1 Measurement Devices

Strain gages were used for measuring strain regardless of the strain rate regime or test method. They were selected because of limitations and availability of other strain-measurement methodologies for high-strain-rate testing. Different anticipated strain levels between composite and Al materials influenced the selection of the type of gage for each material system and application. The gage section of the Al specimens was instrumented with high elongation strain gages from Vishay (EP-08-125AC-350), which are capable of measurements up to 20% strain. After proper surface preparation, gages for strain and strain-rate measurement were bonded at the mid-section gage length using Vishay M-BOND A-12 high-elongation adhesive. Bonding consisted of a curing cycle of two hours at 165°F.

Composite material specimens were instrumented with uniaxial strain gages from Vishay (CEA-06-250UN-120), which are capable of measurements up to 5% strain. Strain gages were bonded to the midsection gage length of the specimen using Vishay M-BOND 200 at room temperature.

Load measurement for the quasi-static composite material tests used a load-frame-mounted strain-gage based load cell. Tests conducted at speeds from 0.1–75 in/s were conducted using a load-frame-mounted piezoelectric load cell (PCB Piezotronics model 206M33 ICP) calibrated for loads up to 44,482 N. The load cell has a frequency limit of 40 kHz. When testing the Al specimen, two methodologies for load measurement were implemented: the piezoelectric load cell and a strain gage mounted on the extended tab of the specimen, as shown in figure 7. The strain gage mounted on the tab was a Vishay model CEA-06-250UN-102 uniaxial strain gage capable of measurements up to 5% deformation to the midsection gage length of the specimen using Vishay M-BOND 200 at room temperature.

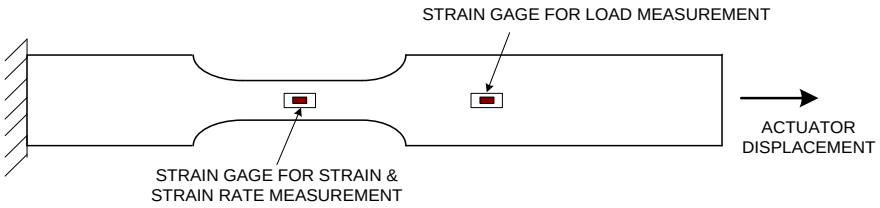

Figure 7. Location of strain gages for load and strain measurements on baseline Al specimen

2.3.2 Baseline Aluminum 7075-T6 Tension Testing

The baseline Al specimen geometry was a dog-bone shape, per the ASTM E 8 standard [16] and included an elongated tab section to accommodate an additional strain gage (see figure 8). It had a reduced cross-sectional area designed to ensure failure within the gage section. The nominal dimensions for the specimen are shown in figure 6. The specimens were machined from a single sheet of Al 7075-T6, such that the longitudinal grain direction (L) was aligned with the test direction. Al 7075-T6 was selected because it is a representative material commonly used in the aerospace industry.

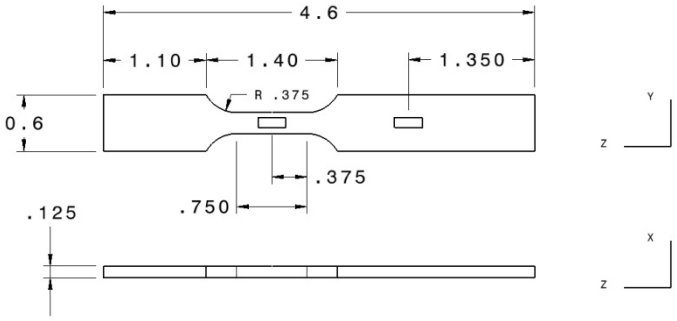

Figure 8. Geometry of baseline Al specimen (in)

2.3.3 Composite Materials Tension Testing

Laminated composite material specimens for tension testing were manufactured per ASTM D 3039 [17]; the geometry was modified to accommodate high-strain-rate testing [6]. Test specimens were machined from autoclave-cured panels. Figure 9 shows the straight-tabbed specimen with a rectangular cross section used for tension testing for rates from quasi-static to 10 in/s. Tension test data were available for the three different composite material systems listed in table 3. The stacking sequences included four different orientations: $[0°]_N$, $[+15°/-15°]_{NS}$, $[+30°/-30°]_{2S}$, and $[+45°/-45°]_{2S}$. However, the number of plies were reduced for orientations $[0°]_N$ and $[+15°/-15°]_{NS}$ to keep the applied load below the capabilities of the test apparatus.

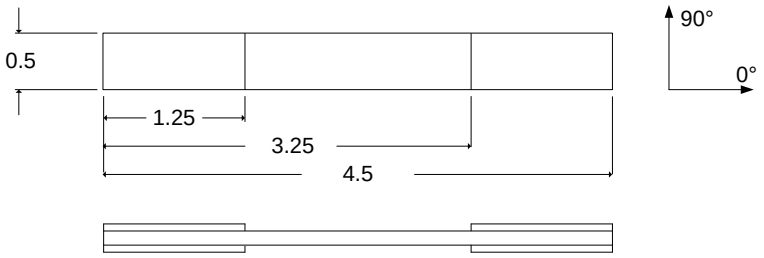

Figure 9. Geometry of tension composite specimen (in)

2.4 SHEAR TESTING

Among several available test methods to generate in-plane shear properties of composite materials, only two introduce a state of pure shear stress [18]: the Iosipescu shear test method and the V-notched rail shear test method. Previous research programs selected the latter method because of its direct implementation using a high-stroke servo-hydraulic machine. It was also selected for this investigation. In addition, test specimens, manufactured per ASTM D 7078 [19], provide a large enough test area to account for different sizes of material unit cells between material systems, as shown in figure 10. The V-notched test specimens were machined from autoclave-cured panels with a stacking sequence of $[0°]_{12}$. Shear rosette strain gages were used for measuring shear strain. Vishay model EA-06-125TH-120 gages were bonded at the

midsection of the gage length. The strain gage was mounted such that its gage elements were oriented at +45° and -45° to the loading axis. The output of each gage element was recorded individually, and the engineering shear strain in the specimen was the sum of the absolute value measured in each element. Each gage element was capable of strain measurements up to 5% normal strain/engineering shear strain. At each loading rate, the test was replicated three times. The shear test matrix for high-strain-rate testing is presented in table 5.

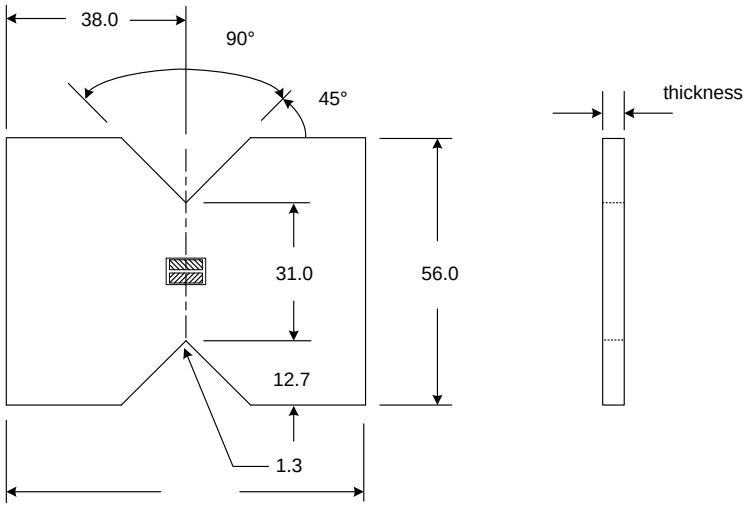

Figure 10. V-notched rail shear test specimen (in) (ASTM D 7078)

Table 5. Shear test matrix for high-strain-rate testing

Material	Stacking Sequence	Nominal Speed (in/s)		
		0.00083	1	10
Toray Unitape	$[0°]_{12}$	x3	x3	x3
Toray Fabric		x3	x3	x3
Newport E-Glass		x3	x3	x3

Quasi-static testing was conducted using a standard 22 kip MTS servo-hydraulic machine. Higher speeds up to 10 in/s were conducted in the high-speed servo-hydraulic machine used for tension testing, including the same slack-inducer mechanism. The testing system included two steel fixtures to grip the specimen, as shown in figure 11. Note that the additional weight introduced by the fixture influences the strain rate achieved during testing [6].

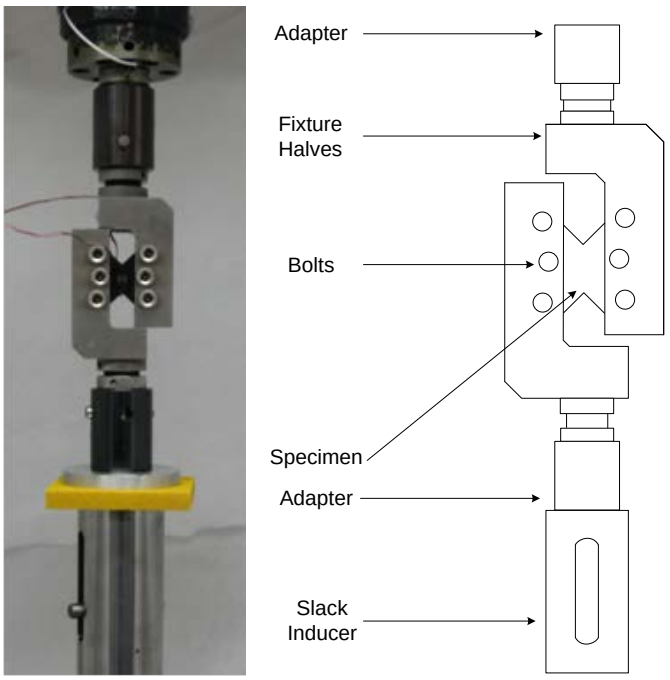

Figure 11. Shear test setup at the NIAR/WSU (ASTM D 7078)

2.5 COMPRESSION TESTING

A few acceptable methods for generating in-plane compressive material properties of laminated composite materials are commonly used [20]. Three different methods are used to introduce the loading: end loading, shear loading, or a combination of both. Test specimens may be tabbed or untabbed. Tabs are introduced to prevent end failure when the material evaluated has large compressive strength in the loading direction. When measuring the compressive modulus, untabbed specimens are recommended by the Suppliers of Advanced Composite Materials Association's (SACMA) SRM 1R-94 [21], along with a strain gage placed at the midsection of the gage length. Available compressive data from the AGATE program only includes in-plane compression data at quasi-static rates for Newport E-Glass Fabric NB321/7781. The in-plane compression tests were conducted per ASTM D 695 [22] using the end loading method on untabbed specimens. Test specimens were cut from oven-cured laminates with a stacking sequence of $[0°/90°]_{3S}$ and then instrumented with strain gages, per SACMA SRM 1R-94. The compressive modulus was estimated using a linear fit of the stress-strain data from 1000–3000 $\mu\varepsilon$. Specimen dimensions and the test fixture are shown in figure 12.

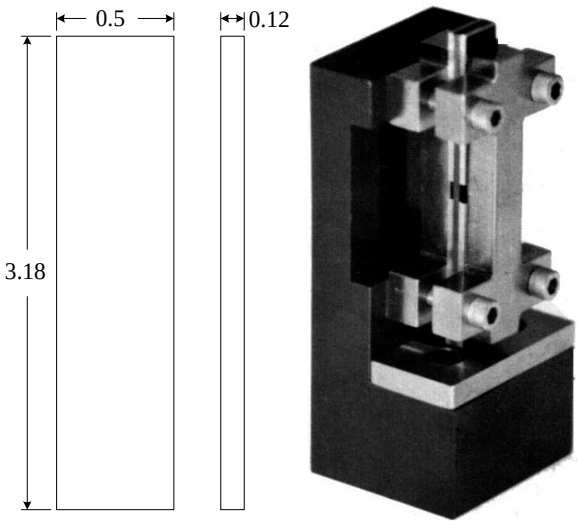

Figure 12. Compressive modulus test specimen (in) (SACMA SRM 1R-94) and test fixture (ASTM D 695)

2.6 STRAIN RATE ESTIMATION

The material response to dynamic loading is a fundamental aspect of energy-absorbing structures. Material response at high-strain-rates deviates from quasi-static response as the loading times shorten and the material inertia effects become relevant. The sudden change in particle velocity resulting from the dynamic loading propagates away from the application surface in the form of stress waves. The assumption of static equilibrium becomes invalid as the transit time of the stress waves travelling within a specimen becomes large relative to the loading time during an experiment. In coupon-level testing, average values of strain rate can be defined theoretically as:

$$\dot{\varepsilon} = \frac{\dot{\delta}}{l_o} \tag{1}$$

where $\dot{\delta}$ is the actuator speed and l_o the specimen gage length. However, average strain rate values only serve as reference values, not as the actual strain rate seen by the material. The strain rate can be estimated experimentally based on a direct strain measurement over the area of interest. Several numerical differentiation methods can be applied to the recorded data to obtain a better approximation of the strain rate over the duration of the test. However, no significant improvement has been reported after implementing numerical methods; that is, average strain rate values from raw data differ from values based on smooth rate data by less than 1% [6]. Average strain rate values from test data can be estimated by averaging the slope of the strain measurement from yield to ultimate or by applying a linear fit to the strain history between yielding and necking initiation. The average slope method of the strain measurement shows less variability than the linear fit method when applied to ductile materials. Average strain rate values shown in figure 13 for the Al specimens of this investigation are estimated using the average

slope method. Similarly, the two methodologies can be used to estimate the strain rate in composite materials testing. However, after applying the two methodologies to the available data, both were observed to yield similar results. Table 6 summarizes the average strain rates for the subject composite materials systems.

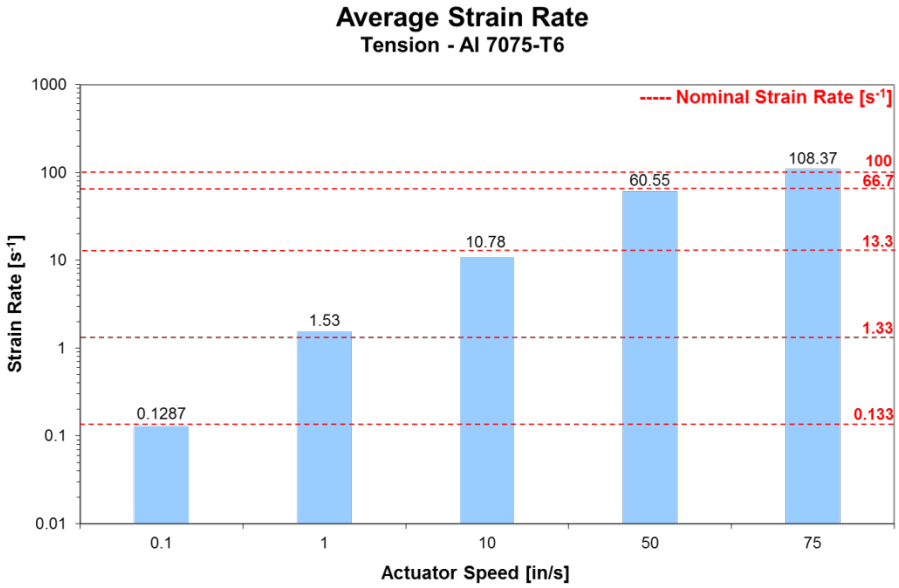

Figure 13. Actuator speed versus average strain rate for Al 7075-T6 with associated nominal strain rate

Table 6. Average strain rate of composite materials

Material	Actuator Speed (in/s)	Nominal Strain Rate (s^{-1})	Average Strain Rate (s^{-1})			
			[0°]	[+15°/-15°]	[+30°/-30°]	[+45°/-45°]
Newport E-Glass	0.00083	0.00041	0.00039	0.00032	0.00038	0.00041
	1	0.5	0.3174	0.2401	0.3188	0.5166
	10	5	1.9614	1.7612	2.6835	3.7942
Toray Unitape	0.00083	0.00041	0.00021	0.00020	0.00037	0.00046
	1	0.5	0.1963	0.1794	0.2656	0.5230
	10	5	1.0266	1.3881	1.9317	2.7974
Toray Fabric	0.00083	0.00041	0.00031	0.00025	0.00032	0.00038
	1	0.5	0.1870	0.1622	0.2285	0.3442
	10	5	0.9674	1.4761	1.8436	2.4789

It is important to note that high-strain-rate testing, conducted to address dynamic loading effects on the material response, faces the challenge of introducing a constant strain rate. It has been observed in previous investigations that the strain rate varies throughout the duration of the test and is a function of the stiffness of the test specimen and the nominal speed of the actuator [6]. Even though mechanisms, such as the slack inducer described in section 2.2, are used to accelerate the actuator, a reduction in the actuator speed is commonly observed when the mechanism engages with the test specimen. Correcting for the actuator deceleration involves proper control of the valve drive signal [23] and the system's response capability. The actuator operational principle of a servo-hydraulic system, along with the mass of each component in the load train, differentiates this test from a strain-controlled test. The direct result is that the generated stress-strain curves are non-iso-strain rate curves.

3.TEST DATA EVALUATION

In addition to the inherent variability of composite materials properties, high-strain-rate testing of composite and metallic materials faces several challenges that directly translate into variability in the test results. Because a FE model represents a numerical approximation of a real structure, variability in the material properties would simply translate into variability in the quality of the approximation. An engineering approximation of a material model requires an understanding of the interaction between the loading conditions of the part/component and the behavior of the materials involved. Additional requirements are set by the model itself; depending on the final application of the numerical model, different levels of detail can be included in the model. However, the accuracy of the simulation results is limited by the variability of the material properties regardless of the detail level in the numerical approximation. Variability in the NIAR data was evaluated and limitations in the testing methodology and sources of variability were identified. Test results are summarized in appendices A–G.

3.1 TEST DATA VARIABILITY

Variability in the material properties was quantified for the material systems listed in section 2. The material properties evaluated for Al 7075-T6 included failure strength, modulus of elasticity, and strain rate. Each property was evaluated at the respective nominal strain rate. The composite material data were evaluated for the tension and shear test results. The material properties included failure strength, modulus of elasticity, strain rate, and failure strain. Available nominal strain rates for composite materials varied from 0.00041–5 s^{-1}. The descriptive statistics used to evaluate the variability within the test data included the mean ($\bar{x}$), standard deviation (s), and coefficient of variation (CV), which are defined in equations 2–4, respectively [24]. The CV is defined as the residual variability in the data as a percentage of the mean. Variability is estimated for reference purposes only because the estimation is only based on three repetitions. A larger sample may reduce the scatter in the results:

$$\bar{x} = \frac{\sum_{i=1}^{n} x_i}{n} \tag{2}$$

$$s = \sqrt{\frac{1}{n-1}\sum_{i=1}^{n}(x_i - \bar{x})^2} \tag{3}$$

$$CV = \frac{s}{\bar{x}} \cdot 100\% \tag{4}$$

3.1.1 Baseline Al 7075-T6 Tension Data

For the baseline tension testing of the Al specimen, variability results are summarized in figures 14–16. Histograms show the average material properties along with error bars and the CV. Different levels of variability were observed in the material properties for different nominal strain rate levels. Higher CVs were observed for all evaluated properties at a nominal strain rate of 66.67s^{-1} (associated speed 50 in/s). However, there is no clear evidence if the observed variability is the result of testing practices, test equipment limitations, or material variability. Dynamic tension testing evaluations for mild steel and DP590 found in noted literature show similar levels of variability for low to medium strain rates in servo-hydraulic systems [25, 26]. However, direct comparison between the published evaluations was limited because of a lack of information in the literature. Several parameters were varied from laboratory to laboratory, including specimen geometry, the stress and strain estimation methods, and data analysis methods. In addition, it was unclear what type of servo-hydraulic testing system, either close-loop or open-loop, was used by the laboratories. Variability within the data was also omitted and only a representative stress-strain curve was reported for each strain rate level. Traditionally, complete sample data are omitted in literature, limiting the evaluation of variability within the same set of data. The repeatability of the test cannot be evaluated if only representative curves are reported. A standard for high-strain-rate testing in servo-hydraulic systems needs to be established because the results are influenced by different test methods, different specimens, and tests are conducted using different testing apparatus.

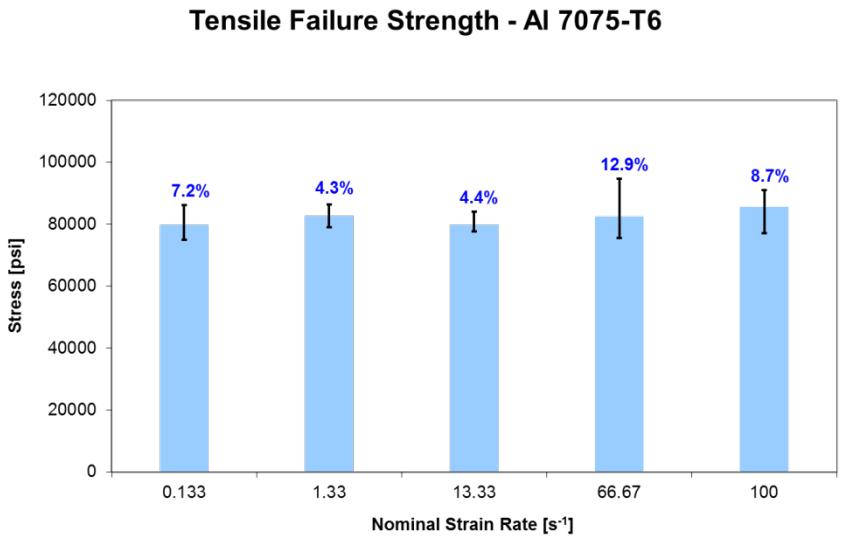

Figure 14. Variability of the tensile failure strength of Al 7075-T6 at various nominal strain rates

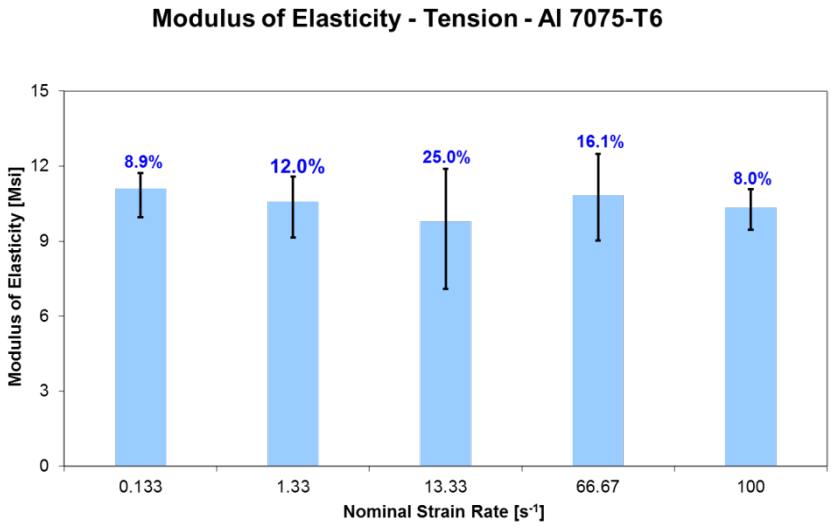

Figure 15. Variability of the tensile modulus of elasticity of Al 7075-T6 at various nominal strain rates

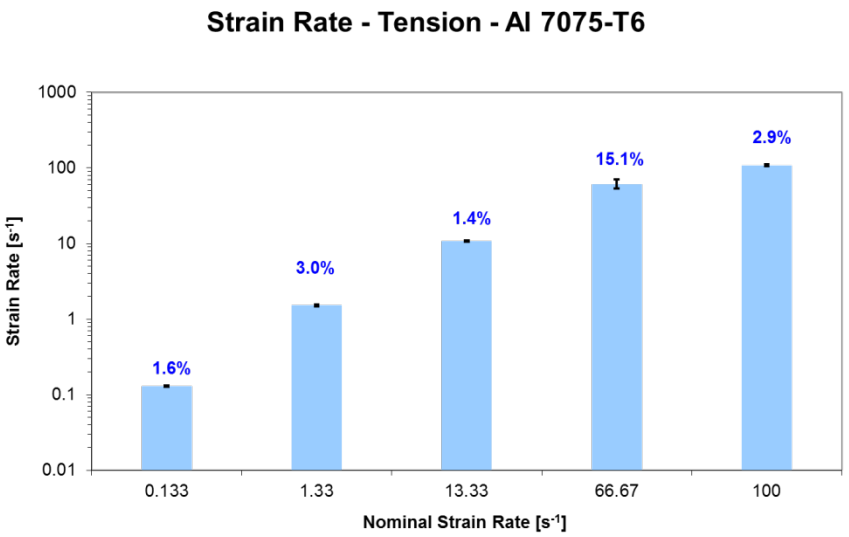

Figure 16. Variability of the strain rate of Al 7075-T6 at various nominal strain rates

3.1.2 Composite Materials Tension Data

The variability of tension material properties for three composite material systems is summarized in figures 17–28. Histograms show the average material properties, error bars, and coefficient of variation. The material system that exhibits larger levels of variability when compared to other materials is Toray Carbon Fabric, regardless of orientation. The failure strain variability is not reported for any material system oriented at $[+45°/-45°]_{NS}$, because the deformation observed by the test specimen exceeds the capability of the strain gage mounted for strain measurement.

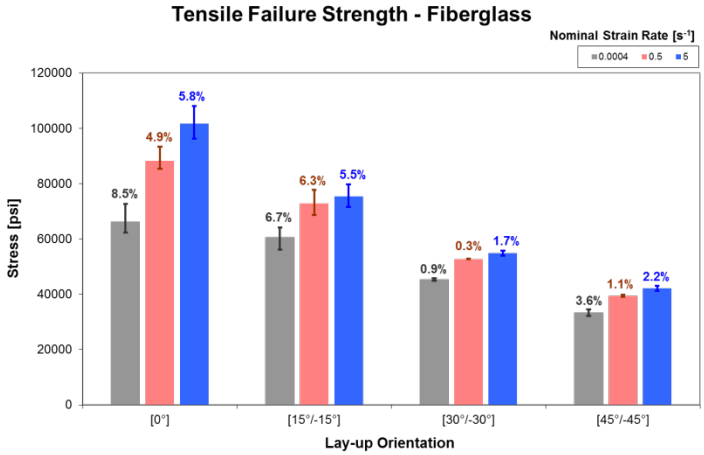

Figure 17. Variability of the tensile failure strength of various fiberglass orientations at various nominal strain rates

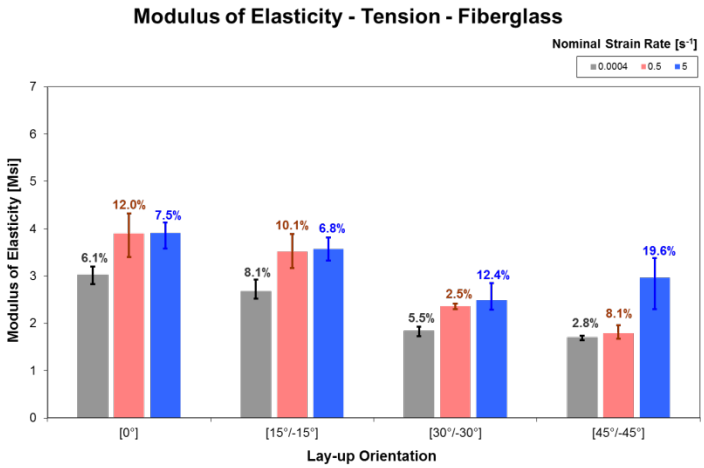

Figure 18. Variability of the tensile modulus of elasticity of various fiberglass orientations at various nominal strain rates

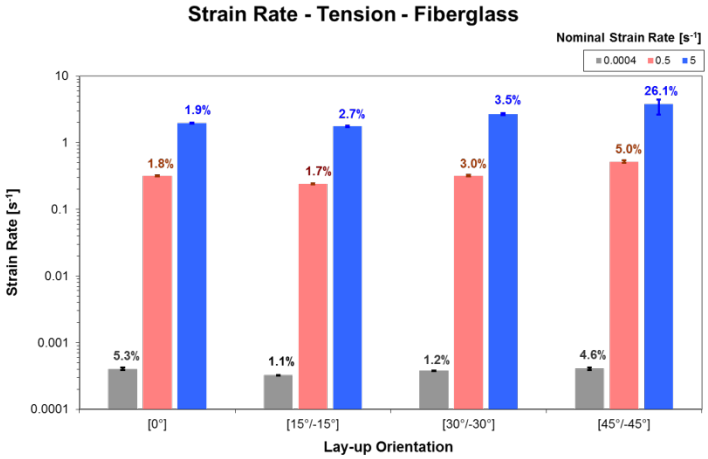

Figure 19. Variability of the strain rate of various fiberglass orientations at various nominal strain rates

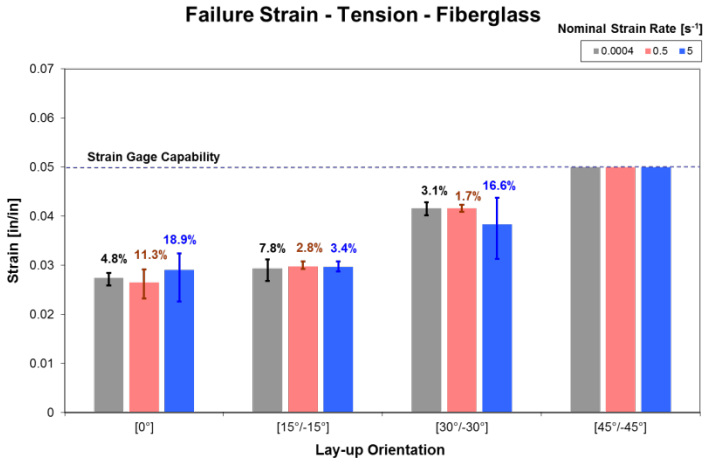

Figure 20. Variability of the tensile failure strain of various fiberglass orientations at various nominal strain rates

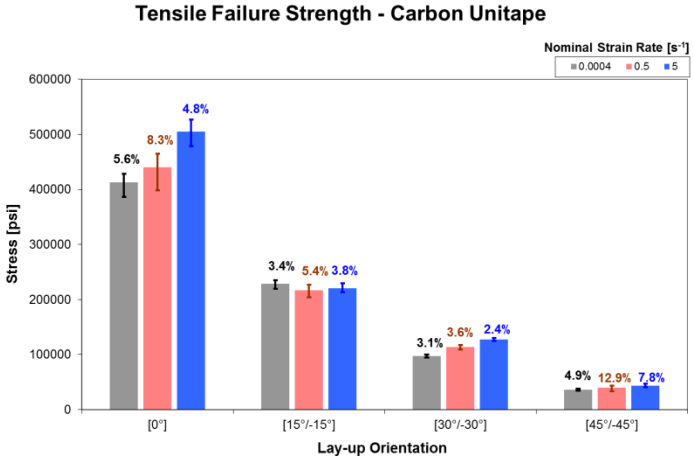

Figure 21. Variability of the tensile failure strength of various carbon Unitape orientations at various nominal strain rates

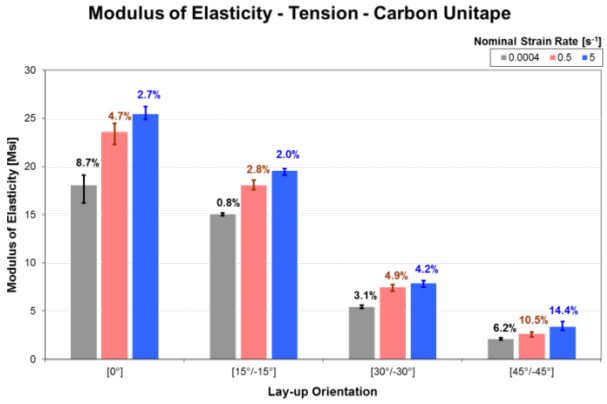

Figure 22. Variability of the tensile modulus of elasticity of various carbon Unitape orientations at various nominal strain rates

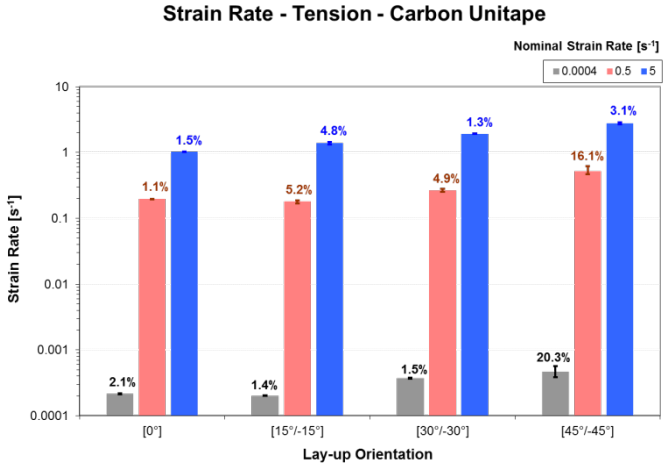

Figure 23. Variability of the strain rate of various carbon Unitape orientations at various nominal strain rates

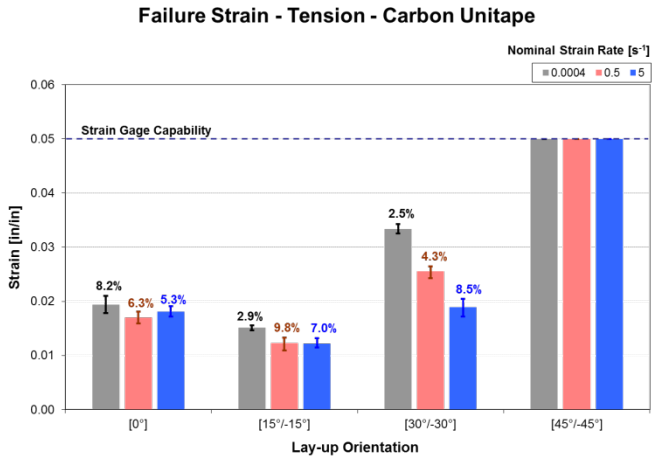

Figure 24. Variability of the tensile failure strain of various carbon Unitape orientations at various nominal strain rates

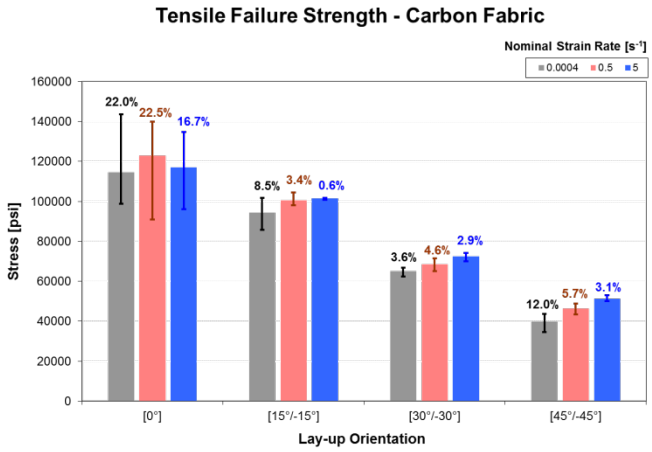

Figure 25. Variability of the tensile failure strength of various carbon fabric orientations at various nominal strain rates

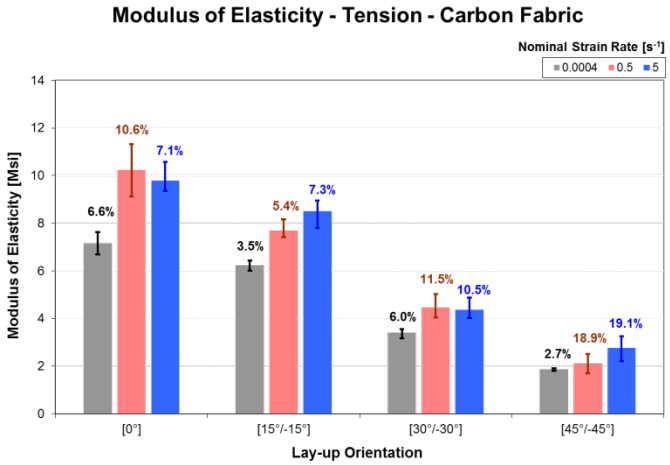

Figure 26. Variability of the tensile modulus of elasticity of various carbon fabric orientations at various nominal strain rates

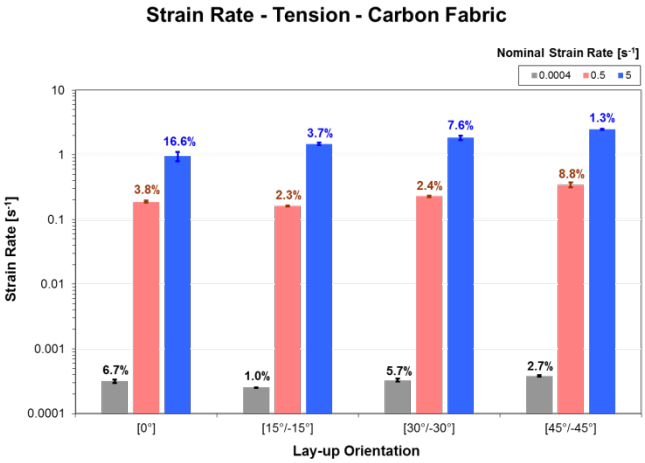

Figure 27. Variability of the strain rate of various carbon fabric orientations at various nominal strain rates

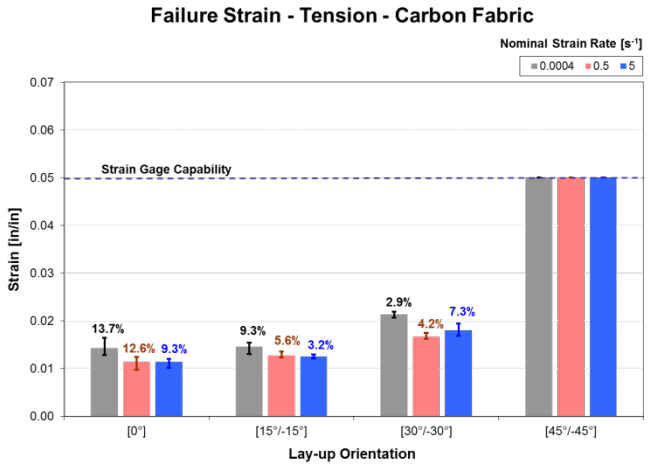

Figure 28. Variability of the tensile failure strain of various carbon fabric orientations at various nominal strain rates

3.1.3 Composite Materials Shear Data

The variability within the shear material properties for Newport E-Glass Fabric NB321/7781, Toray Unitape T800S/3900-2B, and Toray Fabric T700G-12K-PW/3900-2 is summarized in figures 29–40. Shear material properties include shear failure strength, shear modulus, strain rate, and estimated shear failure strain. Histograms show the average material properties, error bars, and the coefficient of variation. The material system that displays larger levels of variability within shear properties when compared to the other materials is Toray Unitape. Only one test result was available at the quasi-static rate for Toray Carbon Fabric, which limited an estimation of its variability.

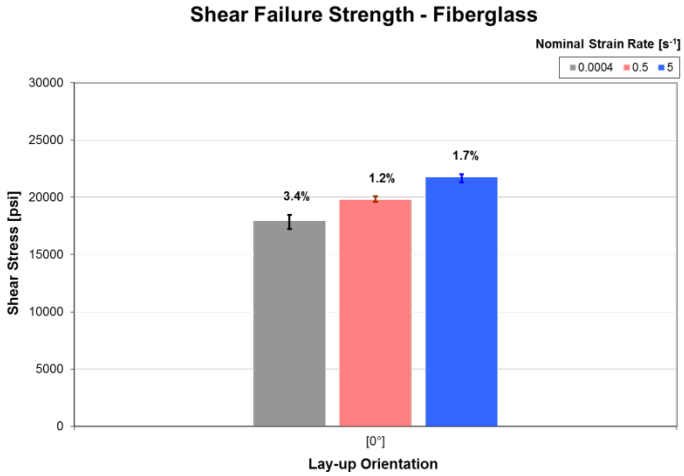

Figure 29. Variability of the shear failure strength of fiberglass at various nominal strain rates

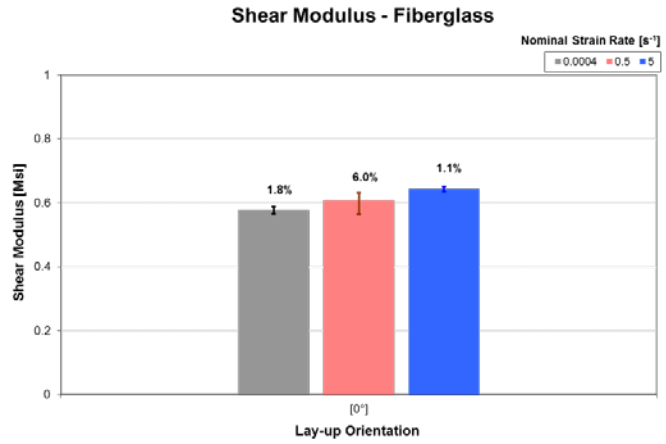

Figure 30. Variability of the shear modulus of fiberglass at various nominal strain rates

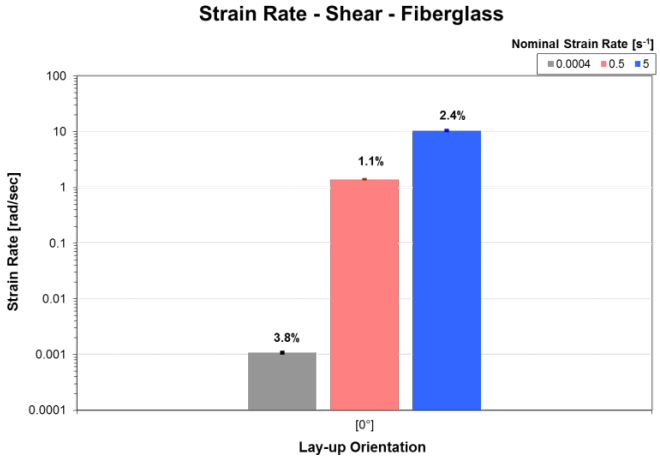

Figure 31. Variability of the strain rate of fiberglass at various nominal strain rates

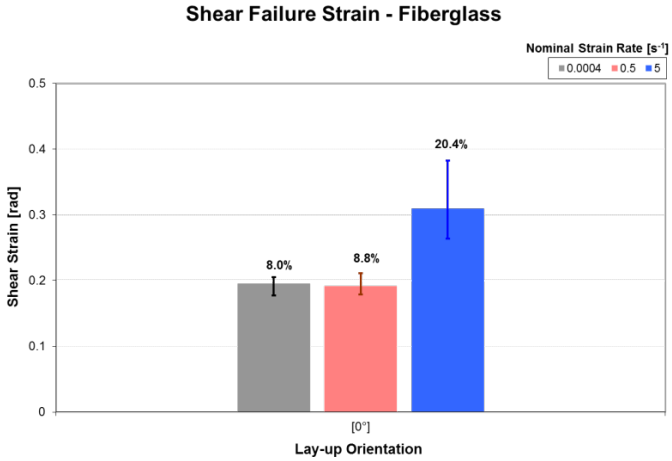

Figure 32. Variability of the shear failure strain of fiberglass at various nominal strain rates

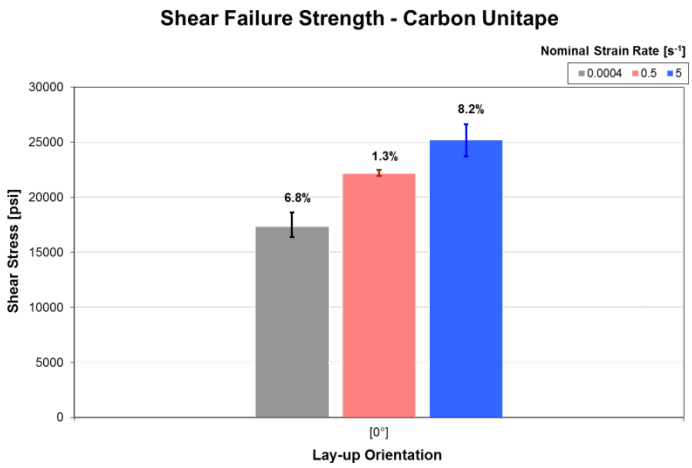

Figure 33. Variability of the shear failure strength of carbon Unitape at various nominal strain rates

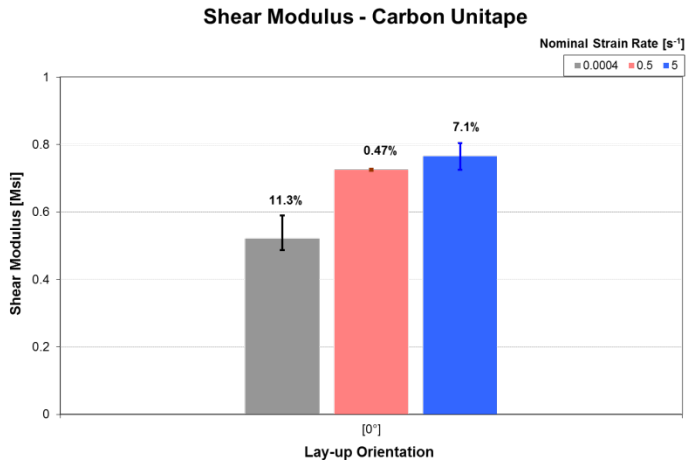

Figure 34. Variability of the shear modulus of carbon Unitape at various nominal strain rates

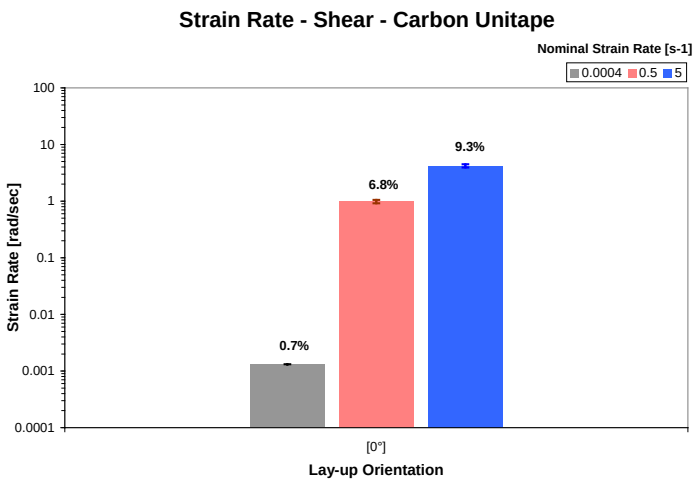

Figure 35. Variability of the strain rate of carbon Unitape at various nominal strain rates

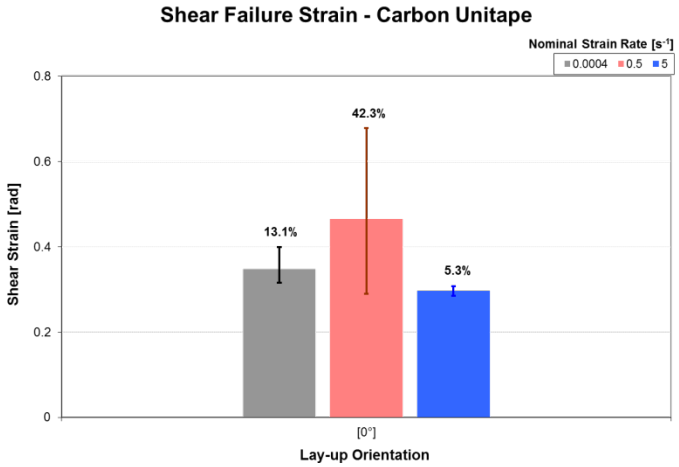

Figure 36. Variability of the shear failure strain of carbon Unitape at various nominal strain rates

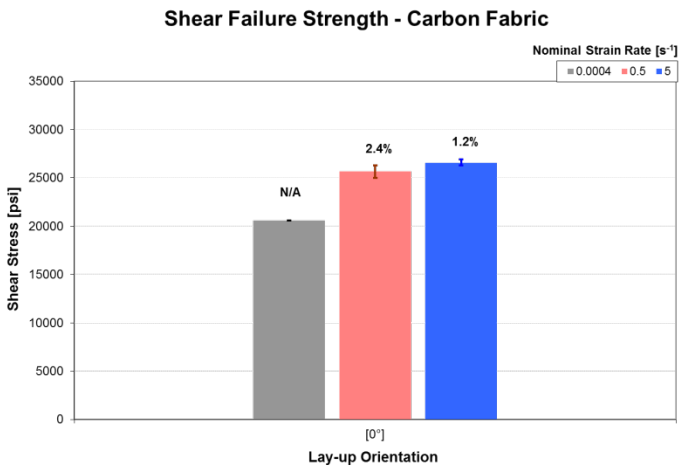

Figure 37. Variability of the shear failure strength of carbon fabric at various nominal strain rates

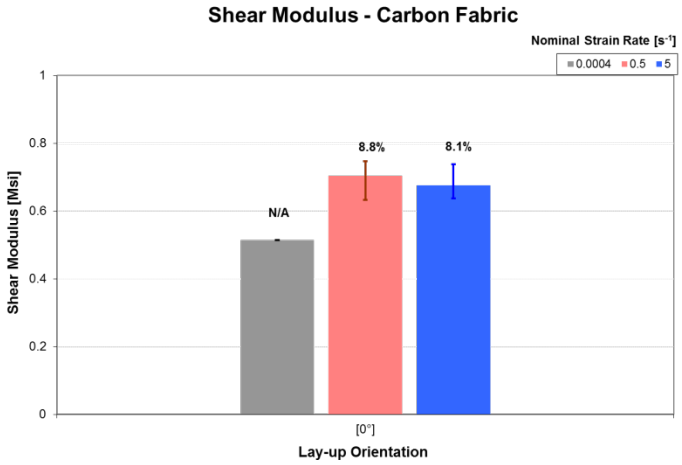

Figure 38. Variability of the shear modulus of carbon fabric at various nominal strain rates

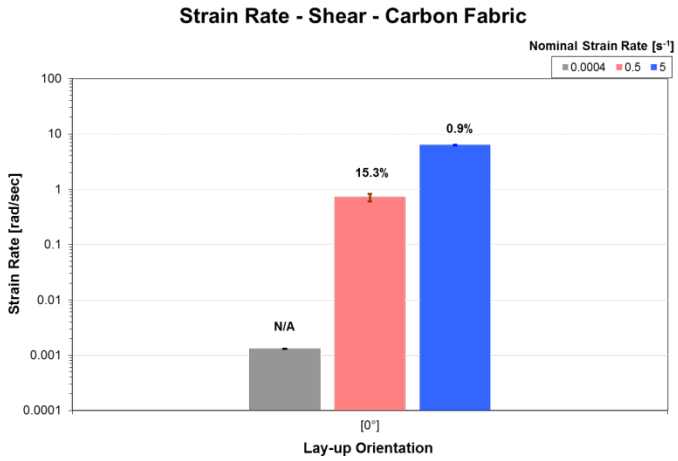

Figure 39. Variability of the strain rate of carbon fabric at various nominal strain rates

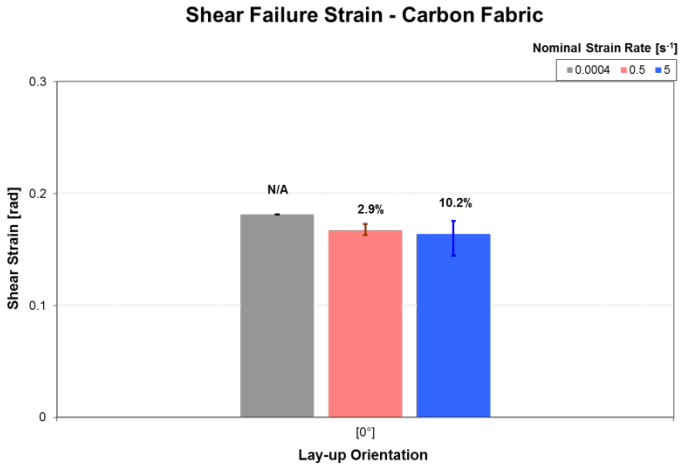

Figure 40. Variability of the shear failure strain of carbon fabric at various nominal strain rates

3.2 TEST DATA LIMITATIONS

Some of the variability observed in the material properties was introduced by the testing and measurement techniques used to collect the data. No known standard or otherwise systematic procedure for conducting high-strain-rate testing currently exists. Test devices necessary for load introduction, such as the test grips, or devices for load transfer, such as the pins and fasteners, prevent the introduction of a constant strain rate. In addition, load measurement methodologies may be affected by the low natural frequency of the load measurement system itself [27, 28]. Oscillations, also referred to as ringing, are introduced to the measured load by these low natural frequencies. Various methods such as polynomial fitting, cut-off frequency, filtering, and smoothing are used to analyze this type of data because no standard procedure currently exists. Care should be taken when using filtering and smoothing procedures because these techniques

may hide the strain-hardening behavior of metals. In addition, these data-manipulation procedures can introduce uncertainty to the actual failure strength of composites.

Previous investigations included an evaluation of a baseline metallic material, which allowed for the characterization of the high-stroke testing system, and the evaluation of piezoelectric and strain-gage-based load cells for load measurement in high-speed testing. Al 7075-T6 specimens were tested in tension over a wide range of medium loading rates, as summarized in table 3. An alternative load measurement device was introduced by mounting a strain gage on an extended tab of the specimen, as shown in figure 7. The material in the tab area was assumed to remain under elastic conditions throughout the duration of the test. Tension force histories, at a speed of 75 in/s, are plotted in figure 41 and include the tab strain gage, the load frame piezoelectric load cell, and a load frame strain-gage-based load cell. Oscillations were observed for both types of load cells following the initial rising segment. Though the piezoelectric load cell displayed smaller amplitude oscillations than the strain-gage-based load cell, the remaining oscillations in the piezoelectric load measurement prevented proper estimation of the flow stress. Conversely, load measurements taken from the extended tab were free of oscillations. However, this procedure was limited to metallic specimens with low-strain-rate sensitivity. The strain-rate sensitivity of composite materials reported in previous investigations limits the application of this methodology [5].

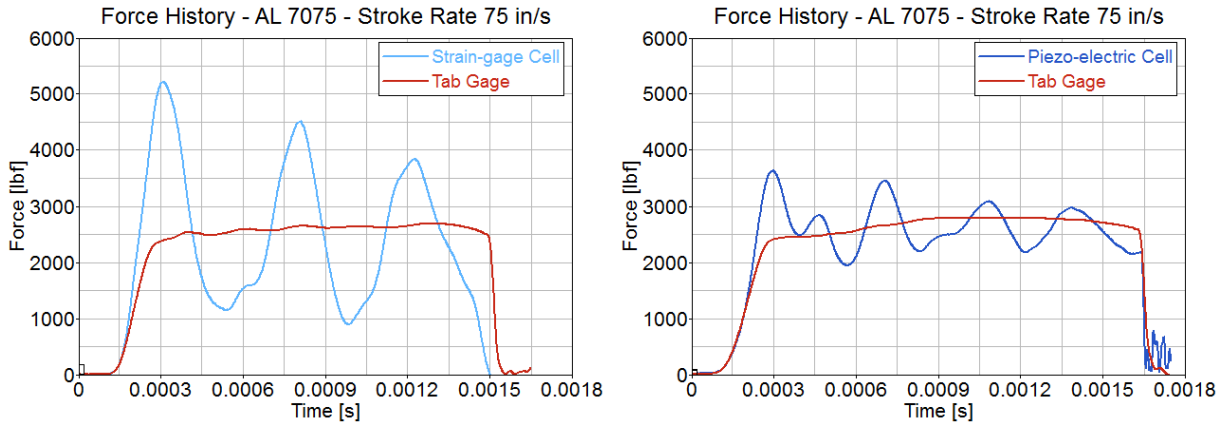

Figure 41. Comparison of load measurement of Al specimen at a speed of 75 in/s

Additional data collection limitations originate from the strain measurement technique. Various methodologies can be used to determine the strain in a specimen during quasi-static testing. Conventional extensometers, commonly used to measure strain in tension testing, are difficult to use for high-speed testing because of the inertia effects of the extensometer [25]. Alternately, strain can be estimated based on the relative displacement of the grips in a tension test or the platens in a compression test; however, precautions must be taken because such a practice would not consider the compliance of the testing system [29]. If the modulus of elasticity is to be determined and specimen dimensions are not a constraint, placing strain gages directly over the specimen surface is the best practice. However, the specific operational range of bonded strain gages may impose a practical limitation to stress-strain curves. Conventional strain gages are

limited to 5% deformation and large deformation strain gages are limited to 20% deformation. Figure 42 shows an example of this problem. The strain history plot shows a spike early in time compared to the stress history plot. The spike in the strain history may indicate either material failure, wire disconnection, or adhesive failure from the surface. Such limitations truncate the stress-strain curve, thereby preventing the extraction of the failure strength value from this curve. Conversely, other devices for strain measurement at this time, such as digital image correlation methods, are still in the developmental stage. Confidence should be built into the test method because variability levels observed in the test data will simply translate to the numerical model.

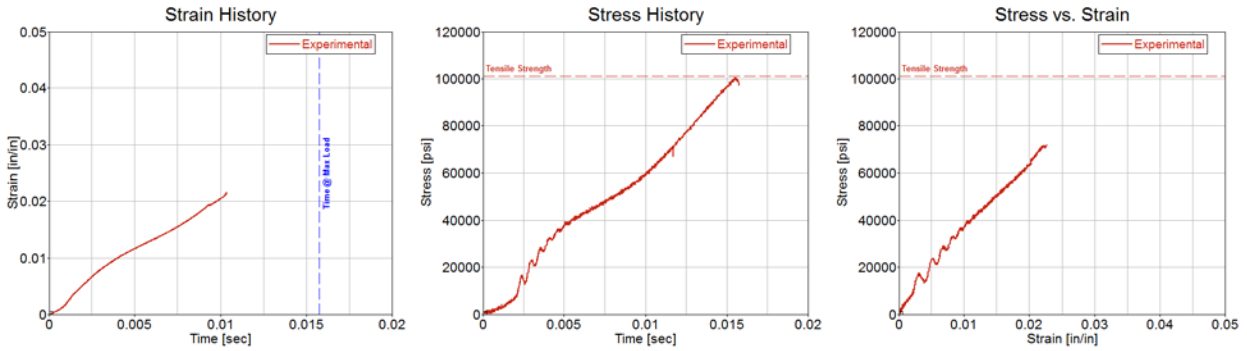

Figure 42. Stress-strain curve limited by strain gage capability in fiberglass $[0°]_4$ at a speed of 10 in/s

4. FE MODELING

Numerical material models of composite and metallic materials were developed for crash simulations using dynamic material properties. Validation of material models with test data required the development of numerical models of the coupon-level tests. The material models were integrated into the coupon-level models for specific strain rates. This approach followed the current BBA used to study rate effects on the behavior of composite airframe structures in which coupon-level testing is the foundation and rate effects are characterized at the lamina level [30]. Accordingly, the numerical material models were assembled by introducing rate-specific lamina material properties generated from test data at the coupon level.

A numerical model of the high-speed Al 7075-T6 tension test was developed to model and compare the Al material behavior and evaluate the test system response. The model included a material model of the Al specimen, described in section 2.3.2, and the test assembly including grips and adaptors. This model was used as a baseline to determine the capabilities and limitations of the current testing apparatus and measurement methodologies at the NIAR/WSU. Additional FE models were then created to simulate the high-speed tension and shear tests and the quasi-static compression tests of the composite materials. All of the numerical models were associated with a corresponding material card, which was developed with test-generated material properties.

FE models should be assembled to simulate a specific part and material and include the loading conditions the part will experience while in service. General models can be used to model the

kinematics of a part/component, but a predictive model—one used to model the mechanics of the system—requires greater levels of refinement in the domain discretization and material model. Adequate FE modeling practices require a clear understanding of the capabilities and limitations of the material law to be implemented. In addition, meshing procedures should define element quality criteria according to the purpose of the model. An example of FE quality criteria used in models for crash evaluations is presented in table 7. Element quality criteria may differ for coupon-level models.

Table 7. Example of finite element quality criteria used for crash models

Quality Parameter	Allowable MIN/MAX
Minimum side length	0.20 in (5.0 mm)
Maximum side length	1.2 in (30 mm)
Maximum aspect ratio	5
Minimum quads internal angle	45º
Maximum quads internal angle	140º
Minimum trias internal angle	30º
Maximum trias internal angle	120º
Maximum warp angle	15º
Minimum Jacobian	0.7

4.1 ALUMINUM 7075-T6 NUMERICAL MODEL

A numerical model was created for the simulation of the high-speed tension test of the Al specimen. The model included a material model that used the Al 7075-T6 test data and accounted for the strain-rate effects on the material response. A parametric study using different element types, ELFORM, and number of through-the-thickness integration points (NIP) were evaluated for computational efficiency and quality to effectively capture the mechanics of the deformation.

4.1.1 Material Card

A piecewise linear plastic material model was implemented using the LS-DYNA MAT-24 material card. This card allows for the introduction of a loading curve to model the material response after the linear region. In addition, it permits the definition of an arbitrary rate dependency. The material response was simulated by inputting effective stress vs. effective plastic strain curves into the material card. However, test stress-strain curves are commonly reported using engineering stress and engineering strain. Therefore, additional adjustments were required before the test data represented the real material behavior (i.e., engineering stress vs. engineering strain had to be converted to true stress vs. true strain). Subsequently, the effective stress vs. effective plastic strain curve could be determined.

True strain differs from engineering strain in that the latter is based on a constant initial length. The engineering strain is defined as:

$$\varepsilon_{eng} = \frac{l - l_o}{l_o} \tag{5}$$

where l_o is the original distance between gage marks and l is the distance between gage marks at any time. Conversely, the true strain, ε_T , represents the average strain between the original gage length and the gage length at any time as:

$$\varepsilon_T = \int_{l_o}^{l} \frac{dl}{l} = ln\frac{l}{l_o} \tag{6}$$

where dl is the incremental elongation. In general, the true strain can be obtained from the engineering strain by applying natural logarithm as:

$$\frac{l}{l_o} = \varepsilon_{eng} + 1 \tag{7}$$

$$\varepsilon_T = \ln\frac{l}{l_o} = \ln(\varepsilon_{eng} + 1) \tag{8}$$

Engineering stress is calculated by dividing the applied load by the original cross-sectional area of the specimen at the gage section and expressed as:

$$\sigma_{eng} = \frac{F}{A_o} \tag{9}$$

where F is the applied load and A_o is the original cross-sectional area. However, the change in cross-sectional area is disregarded in the engineering stress estimation. Instead, the true stress takes into account the variation of the cross-sectional area due to the stress-induced deformation of the material. Therefore, the true stress is equal to the load divided by the new deformed cross-sectional area:

$$\sigma_T = \frac{F}{A} \tag{10}$$

where A is the current cross-sectional area. The true stress can be obtained from the engineering stress and engineering strain [31]. If the volume of the specimen is preserved during the deformation, the material is assumed to be incompressible and, then, the cross-sectional area and the length are related during time as:

$$A_o \cdot l_o = A \cdot l \tag{11}$$

Introducing this relationship into equation 10 along with equation 7, the true stress becomes:

$$\sigma_T = \frac{F}{A} = \frac{F \cdot l}{A_o \cdot l_o} = \sigma_{eng} \cdot \frac{l}{l_o} = \sigma_{eng}(1 + \varepsilon_{eng}) \tag{12}$$

After evaluating the available data from previous research programs, it was observed that the strain was measured using strain gages mounted at the specimen gage length and at the specimen tab along the z-direction, as described in section 2.3.2. The direct measurement of strain with strain gages represents a true strain measurement and is used in this investigation. Conversely, stresses are calculated based on the original cross-sectional area, which represents engineering stress. Therefore, the true stress should be estimated. A relationship between true stress and engineering stress is found by substituting equation 8 into equation 12 to obtain:

$$\sigma_T = \sigma_{eng} \cdot e^{\varepsilon_T} \tag{13}$$

True stress vs. true strain was calculated using equation 13. Figure 43 shows the engineering stress vs. true strain and true stress vs. true strain at 0.1 in/s. Subsequently, to consider the effective plastic strain, the residual true strain after elastic unloading was estimated [32]. The elastic strain component was subtracted from the total strain as:

$$\varepsilon_T = \varepsilon_{ZZ} - \frac{\sigma_{ZZ}}{E} \tag{14}$$

where ε_{ZZ} is the current true strain, σ_{ZZ} is the current true stress, and E is the modulus of elasticity. Figure 42 shows a comparison between the true stress and true strain curves and the effective stress and effective plastic strain curves. In the case of uniaxial tension, true stress vs. true plastic strain is equivalent to effective stress versus effective plastic strain [32]. The procedure to find the loading curve for the material card, at a speed of 0.1 in/s, is shown in figures 43–45 and summarized in figure 43. Loading curves were developed for the four test speeds used in the study. Note that the raw test data are typically noisy and, therefore, it may be necessary to smooth the stress-strain curves to avoid spurious behavior in the simulation results.

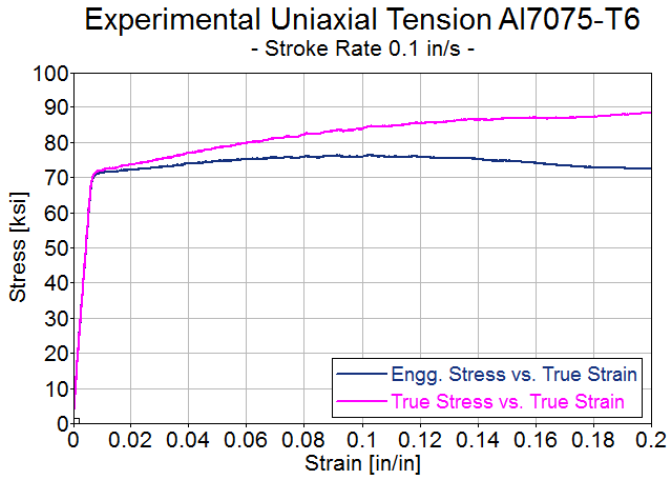

Figure 43. Uniaxial tension of Al 7075-T6 at a speed of 0.1 in/s

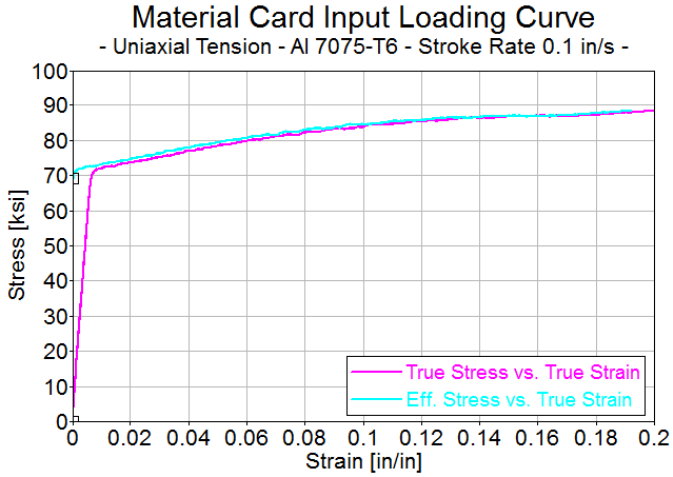

Figure 44. Comparison of true stress vs. true strain curves and effective stress vs. effective plastic strain curves

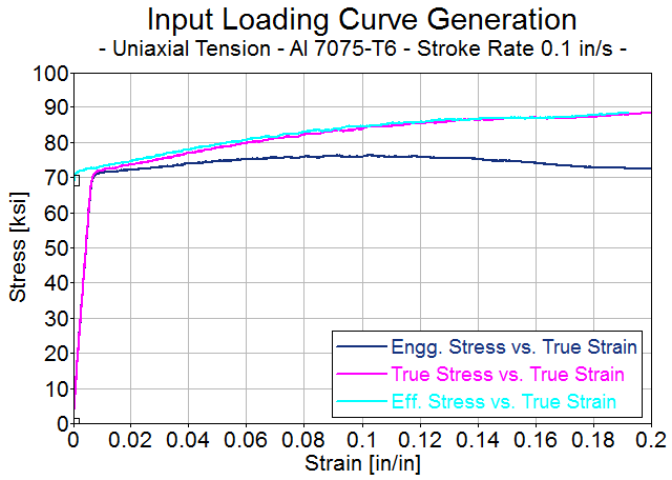

Figure 45. Generation of input loading curve of uniaxial tension of Al 7075-T6 at a speed of 0.1 in/s

4.1.2 Material Model Development

FE solvers provide different element types and formulations, thereby giving the user freedom to use the one that most closely represents the specific application. In the current study, different LS-DYNA element types, ELFORM, and NIP were evaluated for computational efficiency and quality. Shell ELFORM (selected in the Section Shell card) was first evaluated to represent sheet-type materials behavior. Then, shell elements were compared with solid elements to identify the capabilities and limitations of shell elements for crash analysis applications.

The evaluated shell ELFORM are listed in table 8.

Table 8. Evaluated LS-DYNA shell element formulations

ELFORM	Shell Type	Identifying Property
2	Belytschko-Tsay	LS-DYNA Default
10	Belytschko-Wong-Chiang	Warpage Considered
12	Plane Stress	No Perpendicular Stress
16	Fully Integrated	Very Fast
25	Fully Integrated	Element Thickness Stretching Considered

The default shell ELFORM (ELFORM 2-Belytschko-Tsay) was compared to the default solid ELFORM (ELFORM 1). Traditionally, thin-walled structures used for energy absorption are modeled using shell elements [33]. However, investigations involving simulations of Al extrusions have found that the mean crushing force was underestimated with this approach. Inherent effects for either shell or solid elements may be significant for compressive loading scenarios and, therefore, must be accounted for. The results of these simulations are presented in section 5. In general, no additional improvement over the material response correlation was

observed when solid elements were used. However, an increase in the computational cost was observed and is a factor to consider for large structural simulations.

4.1.3 Baseline Al Specimen Model for Tension Testing

An FE model of the baseline Al specimen was created using LS-DYNA. Shell elements are used to discretize the domain. The ELFORM, NIP, and shell thickness were defined within the LS-DYNA "Section_Shell" card. For the baseline model, the ELFORM 2 shell ELFORM was used, the NIP was set to five, and a shell thickness of 0.125 in. (3.175 mm) was set for all nodes.

The LS-DYNA MAT-24 material card was used for the Al specimen, where density (RO) for Al 7075-T6 is given as 0.101 lbf/in3 (2.796 tonne/mm3), Young's Modulus (E) is given as 11.1 Msi (76,560 MPa), the Poisson ratio (PR) is given as 0.33, and the plastic strain to failure (FAIL) is given as 0.1914 in/in (mm/mm). A load curve, or a table of curves, can be used to account for the strain rate effect on the material response. In the current model, the effective stress vs. effective plastic strain curve was defined from test data.

The meshed model and boundary conditions are shown in figure 46. The average element size was 0.0787 in. (2 mm). The top tab of the specimen was rigidly constrained and a test displacement history was introduced to the bottom tab along the z-direction. Appropriate material properties were entered into the material cards for each evaluated strain rate.

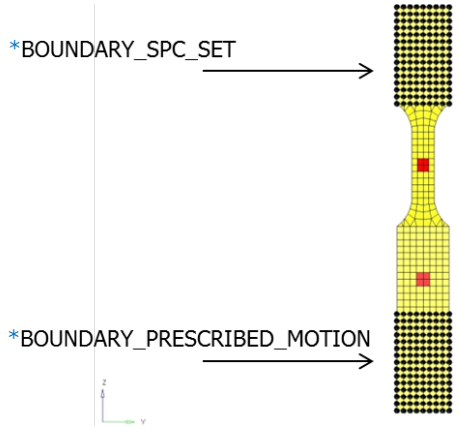

Figure 46. Boundary conditions of baseline Al specimen model for tension testing

4.2 TENSION SPECIMEN-GRIP TESTING ASSEMBLY MODEL

An FE model of the tension grip assembly—with studs, pins, and slack-inducer mechanism—was created to simulate the high-speed servo-hydraulic testing system located at the NIAR/WSU (se figures 47 and 48). The Al 7075-T6 test data were used to build a baseline FE model for the high-speed tension test simulation. This model can be extended to other material testing and load cases and further used to study the effect of the grips' mass and the system compliance, which may influence high-strain-rate test results.

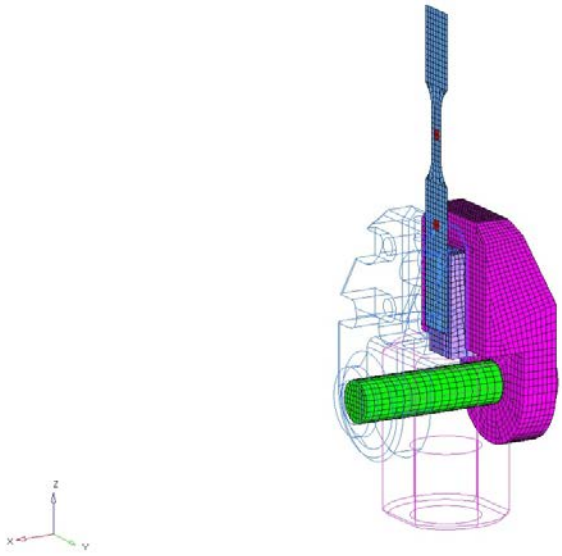

Figure 47. Mesh of tension grip assembly

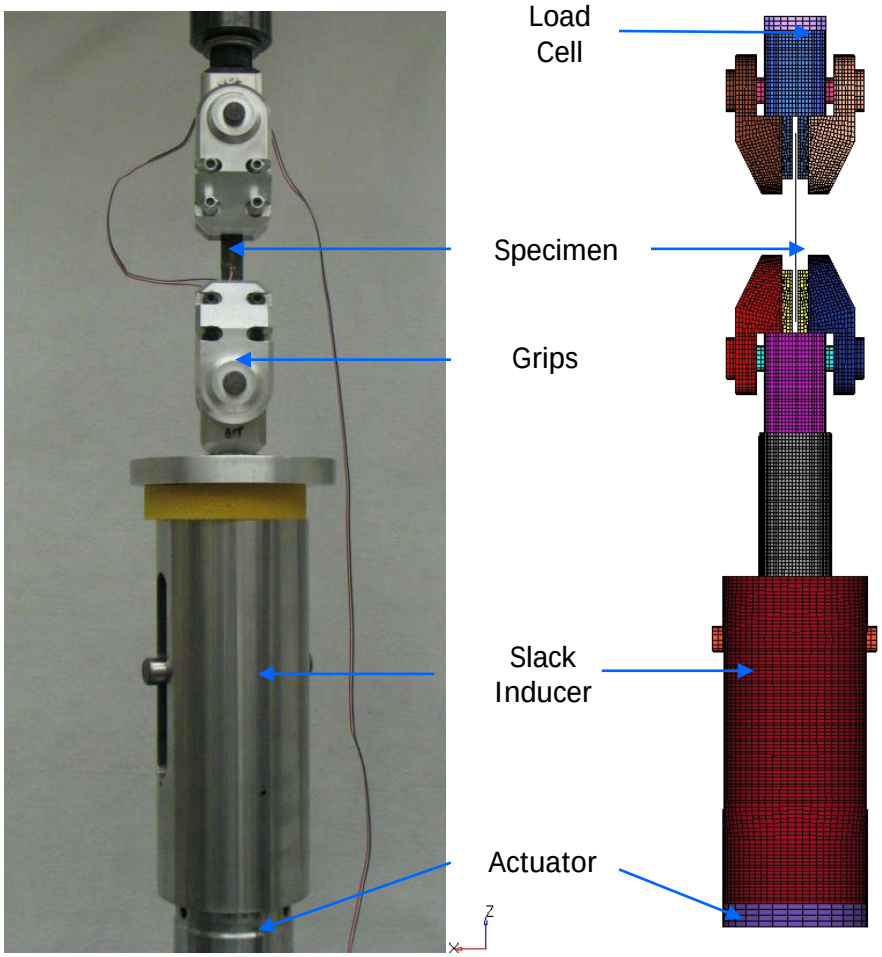

Figure 48. Model of specimen-grip assembly of high-speed servo-hydraulic testing system

The model of the test specimen for the specimen-grip assembly retains the same FE characteristics as the coupon models: dimensions, ELFORM, and number of integration points. The rest of the test fixture was modeled with under-integrated constant stress solid elements. Elastic material properties were defined for the pins and fasteners. The remaining components were defined as rigid. The meshed model and boundary conditions are shown in figure 49. The load cell at the top of the assembly was rigidly constrained and a displacement history introduced to the actuator along the z-direction. The appropriate material properties were entered into the material cards for each strain rate that was evaluated.

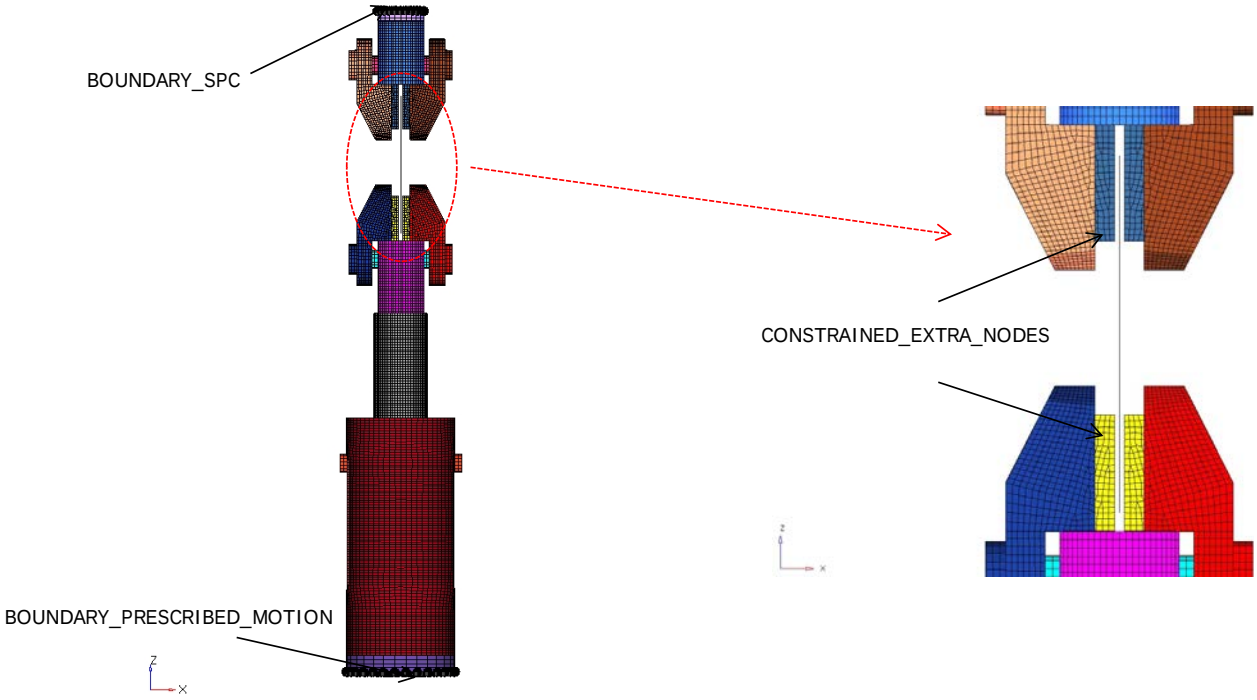

Figure 49. Boundary conditions of specimen-grip test assembly model

4.3 COMPOSITE MATERIALS MODEL

Current simulation tools provide three general approaches to simulate composite materials. Determining the appropriate approach depends on the level of detail required for the analysis [34]. First, the micromechanics approach considers the material at a constitutive level, in which fiber and matrix properties are defined along with their geometrical distribution. Second is a meso-scale-level approach, in which lamina elastic properties, layer thicknesses, and fiber orientation are defined. Third is a macro-scale-level approach, in which laminate matrices [A], [B], [D], and [H] are defined but do not consider the stacking sequence, lamina properties, or ply thickness. This investigation followed the meso-scale-level approach for which lamina properties were extracted from the available test data.

Commonly used LS-DYNA material models for crashworthiness simulations of composite shell-type structures include MAT-22, MAT-54/55, and MAT-58. MAT-54 is an enhanced version of MAT-22 and was selected along with MAT-58 for further study. The material model

structure is best described by dividing it into three main areas: material response, failure analysis, and damage evolution. Table 9 summarizes the general characteristics of these three material models.

Table 9. LS-DYNA composite materials models typically used for crashworthiness simulations

Material Card	Material Response	Pre-Failure Detection	Failure Criteria	Post-Failure Evolution
MAT-22	Linear elastic	N/A	Chang-Chang	Progressive failure
MAT-54/55	Linear elastic	N/A	Chang-Chang/Tsai-Wu	Progressive failure
MAT-58	Linear elastic	Stiffness degradation	Hashin	Damage mechanics

The material response of laminated composite materials in the evaluated material models is treated as linear elastic orthotropic behavior before failure. To capture the material response, these models require mechanical properties from material testing. Material properties include modulus of elasticity, Poisson ratio, shear modulus, etc. In addition, the models require longitudinal tensile and compressive strength, transverse tensile and compressive strength, and shear strength to detect failure at the ply level. Properties obtained from material testing are summarized in table 10. Once failure is detected, the material models initiate a damage evolution process in which material strengths are degraded progressively following a damage evolution law. However, material cards differ in the pre-damage and post-failure process. After yield, MAT-54 reduces fiber strength to account for matrix failure and implements a progressive failure model. Conversely, after yielding, MAT-58 assumes that deformation in the material introduces microcracks and cavities that cause stiffness degradation and that leads to nonlinear deformation [35].

Table 10. Lamina material properties obtained from material testing

Model Feature	Property (MAT-58)	Description
Material response	EA	Young's modulus in a-direction—E_{11}^T or E_{11}^C
	PRBA	Poisson's ratio ba—ν_{21}
	EB	Young's modulus in b-direction—E_{22}^T or E_{22}^C
	GAB	Shear modulus ab—G_{12}
Material response indirect	E11T	Strain at longitudinal tensile strength a-axis—ε_{11}^T
	E11C	Strain at longitudinal compressive strength a-axis—ε_{11}^C
	E22T	Strain at transverse tensile strength b-axis—ε_{22}^T
	E22C	Strain at transverse compressive strength b-axis—ε_{22}^C
	GMS	Strain at shear strength ab plane—γ_{12}
	TAU1	Stress limit nonlinear shear stress-strain curve—F_{12}^1
	GAMMA1	Strain limit nonlinear shear stress-strain curve—γ_{12}^1
Failure criteria	XT	Longitudinal tensile strength a-axis—F_{11}^T
	XC	Longitudinal compressive strength a-axis—F_{11}^C
	YT	Transverse tensile strength b-axis—F_{22}^T
	YC	Transverse compressive strength b-axis—F_{22}^C
	SC	Shear strength ab plane—F_{12}^S

MAT-54 provides the option of using either Chang-Chang failure criteria or Tsai-Wu failure criteria for predicting the failure in composite materials. Tsai-Wu failure criteria are included as MAT-55 within MAT-54. This is a quadratic stress-based failure criteria that was observed to be very simple. However, various failure modes observed in a composite material are not clearly considered by the Tsai-Wu criteria. Unlike the Tsai-Wu failure criteria, the Chang-Chang criteria can predict failure in both tension and compression for fiber and matrix modes separately, as in the case of Hashin failure criteria. A post-failure degradation rule is defined in MAT-54, in which the behavior of a complete laminate can be analyzed as each lamina fails. The degradation rule accounts for some nonlinearity in the material behavior post-failure, but it does not account for nonlinearities observed in the in-plane shear stress-strain response of unidirectional composites [36]. The four failure equations based on Chang-Chang failure criteria corresponding to four failure modes are presented in appendix I.

The material response in MAT-58 is linear elastic bounded by a failure surface, as described by equation 15. In this model, a basic damage evolution law is introduced to account for initial flaws in the material [37]. Figure 50 shows the effect of the pre-failure damage evolution law on a typical stress-strain curve. The damage evolution law degrades the material strength as the damage progresses. In addition, the material model allows for a special control of shear behavior of fabrics via a nonlinear shear stress-strain curve. However, shear behavior control can only be used in combination with a faceted failure surface type. Failure is detected at the lamina level based on four Hashin failure criteria. These criteria are based on the curve-fitting considerations and are quadratic in the stresses [38] (see appendix I):

$$\sigma_i = 1 - \exp\left[-\frac{\ln \beta_i}{e} \left(\frac{E_i \varepsilon_i}{\sigma_{fi}} \right)^{\frac{1}{\ln \beta_i}} \right] \cdot \varepsilon_i \cdot E_i \tag{15}$$

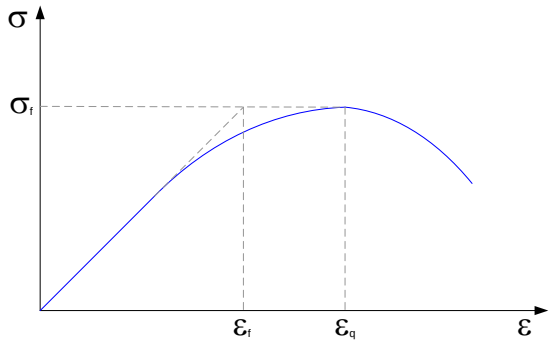

Figure 50. Typical stress-strain curve

4.3.1 Integration Rule

A user-defined integration rule is defined for each composite layer using the LS-DYNA card "PART_COMPOSITE." The card allows for the definition of ELFORM, layer thickness, and material angle per integration point. An integration point is defined per composite layer matching the composite staking sequence.

4.3.2 Development of Composite Specimen Model for Tension Testing

The composite tension specimen was modeled with ELFORM 2 shell elements, with the NIP set equal to the number of layers. The average element size was 0.0625 in. (1.58 mm). Dimensions were taken from the testing specimen described in section 2.3.3. The meshed model and associated boundary conditions are shown in figure 51. The top tab of the model was rigidly constrained to represent the test scenario. A test displacement history was introduced to the bottom tab along the negative z-direction. Lamina material properties were introduced at each integration point (layer). LS-DYNA material cards MAT-54 and MAT-58 were evaluated. MAT-58 was selected because of its superior ability to capture the failure modes, particularly of

the non-linear response of the material when there was damage. The final model implemented material card MAT-58, where a faceted failure surface was defined.

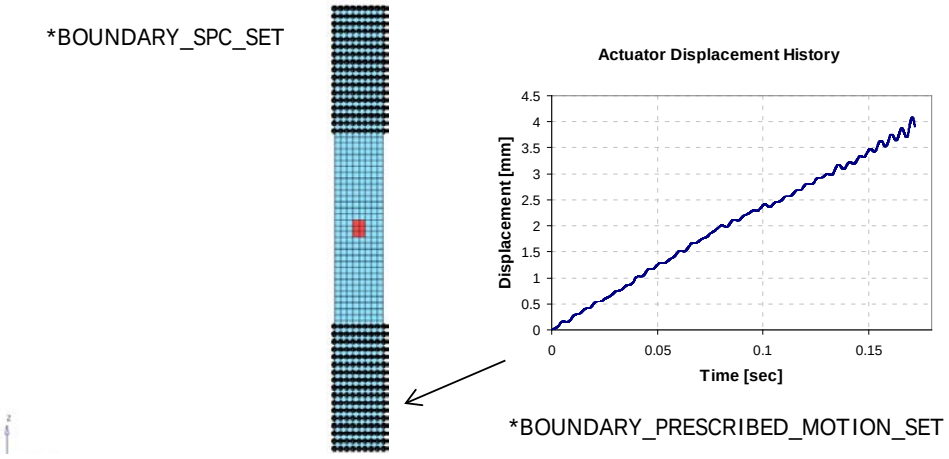

Figure 51. Boundary conditions of composite specimen model for tension testing

4.3.3 Development of Composite Specimen Model for Compression Testing

For compression testing, the only available data were for Newport E-Glass Fabric NB321/7781. The AGATE material properties [7] for specimens with a stacking sequence of $[0°/90°]_{3S}$ were used. The data were generated at quasi-static rates (0.00083 in/s) using test methods SRM 1-94 [21] and ASTM D 695 [22]. The compression testing model was created to represent the boundary conditions imposed on the specimen by the test fixture (see figure 50). The top row of nodes was rigidly constrained. End loading was introduced to the bottom row of nodes with a test displacement history in the positive z-direction. The test fixture provided lateral constraint to prevent buckling. This was modeled by constraining the out-of-plane movement of the nodes above and below the gage length of the specimen. The test fixture provided a small area not constrained for buckling. This area provided space to mount the strain gages. Accordingly, the nodes corresponding to the gage length were not constrained. The meshed model and associated boundary conditions are shown in figure 52. The composite compression specimen was modeled with ELFORM 2 shell elements with 12 NIP and an element size of 0.0625 in. (1.58 mm). Dimensions were taken for the test specimen described in section 2.5. The material model included material card MAT-58, in which a faceted failure surface was defined.

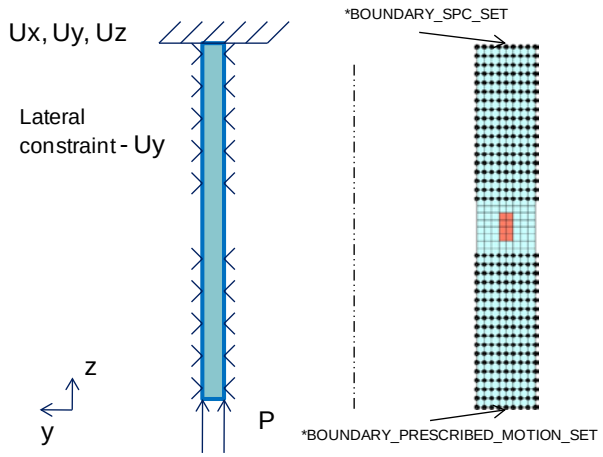

Figure 52. Boundary conditions of composite specimen model for compression testing

4.3.4 Development of Composite Specimen Model for Shear Testing

The shear specimen was modeled with ELFORM 2 shell elements and the NIP set to 12. The material axis was defined to coincide with the fiber orientation of 0°, as specified in ASTM D 7078 [19] and shown in figure 53. The 0°–90° testing plane corresponds to the material plane 1-2. An average element size of 0.1102 in. (2.8 mm) was used. A mesh size evaluation was conducted and results are summarized in section 5.4. Dimensions were taken from the testing specimen described in section 2.4. The meshed model, with associated boundary conditions, is shown in figure 54. The right tab of the specimen was rigidly constrained, similar to the physical test. A test displacement history was introduced to the left tab along the negative *z* direction. The appropriate lamina material properties were introduced at each integration point (layer). LS-DYNA material card MAT-58 was used for the material model and a faceted failure surface was defined.

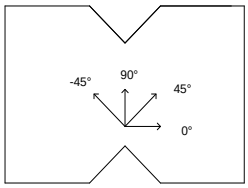

Figure 53. Fiber orientation of V-notched shear specimen

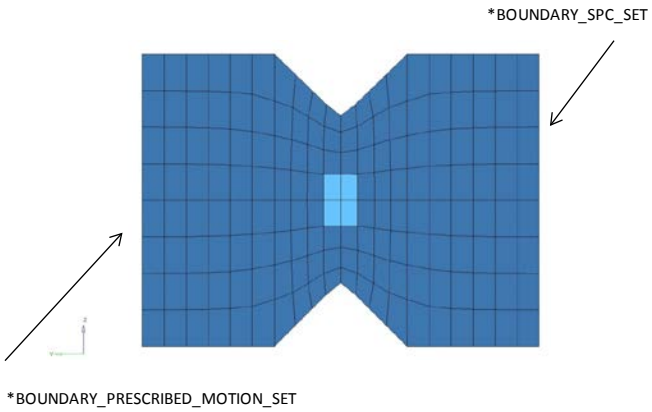

Figure 54. Boundary conditions of V-notched shear specimen model

5. ANALYSIS RESULTS

Simulation results of test methods and material systems explained in section 2 were verified using the test data. In summary, a baseline Al 7075-T6 model for high-speed tension testing was validated at the coupon level. Subsequently, a numerical model of the test assembly, including specimen-grip fixtures, was created and validated over a wide range of speeds. In addition, the baseline Al model was used to evaluate different element types and formulations and NIP.

Numerical models of tension, shear, and compression test methods for composite materials were created and validated with test data. Layered composite material models were implemented in different models and validated along with the test method model. Lamina material properties were extracted from the test data and appropriate material models were developed for each strain rate. The test data used for material property generation and model validation are summarized in appendices A–G.

5.1 BASELINE METALLIC MATERIAL MODEL

The development of the baseline dog-bone Al model for tension tests and associated material model required the evaluation of available test data and knowledge of the limitations in current test and measurement methodologies. Different levels of variability were observed in the material response at the different speeds. Therefore, an average material response for each speed was used for validation purposes.

The baseline model was evaluated using the Al 7075-T6 material model. The material card used was LS-DYNA “MAT_PIECEWISE_LINEAR_PLASTICITY” (MAT_24). Three parameters were evaluated: ELFORM, NIP, and element type. These results were then compared with the averaged test results and used to validate the model.

5.1.1 Comparison of Shell Element Formulation

Various LS-DYNA shell ELFORM were evaluated using the baseline Al specimen model and Al 7075-T6 material model. The NIP was set to 5. Five different ELFORM were considered: ELFORM 2, 10, 12, 16, and 25. A speed of 0.1 in/s was used with no differences expected at other speeds. The stress history, strain history, reaction force history, and stress vs. strain curves were compared and the results are shown in figure 55. Figure 56 shows the computational time for each ELFORM (from section shell card).

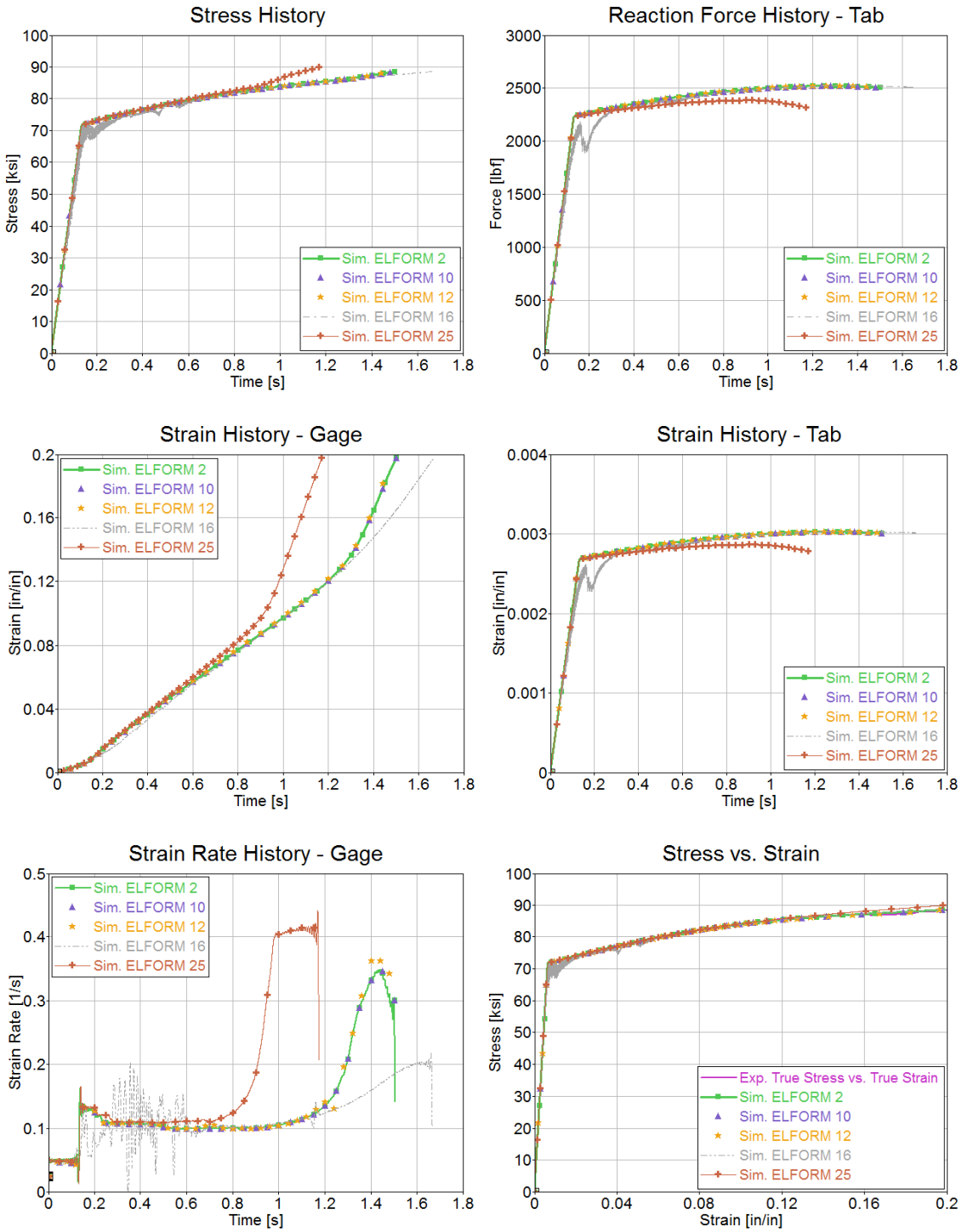

Figure 55. Comparison of shell element formulation for metallic material coupon model at a speed of 0.1 in/s, MAT-24, NIP = 5

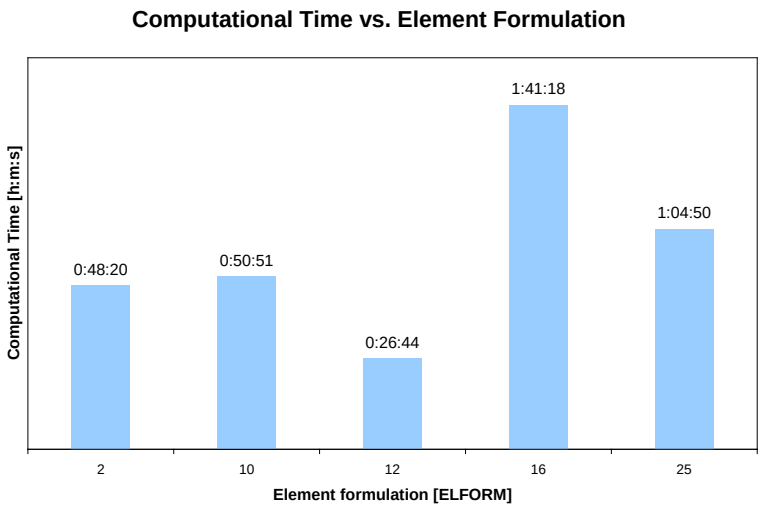

Figure 56. Computational time for various element formulations

ELFORM 2, 10, and 12 produced comparable results to the test data, whereas ELFORM 25 deviated from the test results in the plastic region. ELFORM 16 was noisy, especially in the region of transition from the elastic to the plastic regime. ELFORM 16 had the highest computational time, whereas ELFORM 12 had the lowest computational time because it only considered plane stress. Under in-plane loads within the elastic regime, the behavior of ELFORM 2, 10, and 12 should be equivalent; however, they should differ under out-of-pane loads or excessive compressive loads (ELFORM 12 is not suited for out-of-plane stresses). ELFORM 10 is designed for higher warping accuracy, with a small increment in computational time when compared with ELFORM 2. ELFORM 2 was selected as the best overall match for this application.

5.1.2 Comparison of Integration Points Through Shell Element Thickness

The effect of increasing the NIP was evaluated using ELFORM 2 (section shell card). A speed of 0.1 in/s was used with no differences expected at other speeds. The computational time along with the stress history, strain history, reaction force history, and stress-strain curves are compared for a NIP of 3, 5, and 15. The results are shown in figures 57 and 58. Figure 57 shows that as the NIP increases, so does the computational time. Figure 58 shows that under axial loads, no additional improvement was observed in the simulation results when increasing the NIP with respect to the LS-DYNA default (NIP = 3). The simulation stress vs. strain curves closely follow the material response, as exhibited in the subject input data, regardless of the NIP used. However, a higher NIP would improve the response of shell elements to out-of-plane loading, capturing the stress and strain gradient through the thickness of the element. For this study, a conservative approach was taken and the NIP was set to 5.

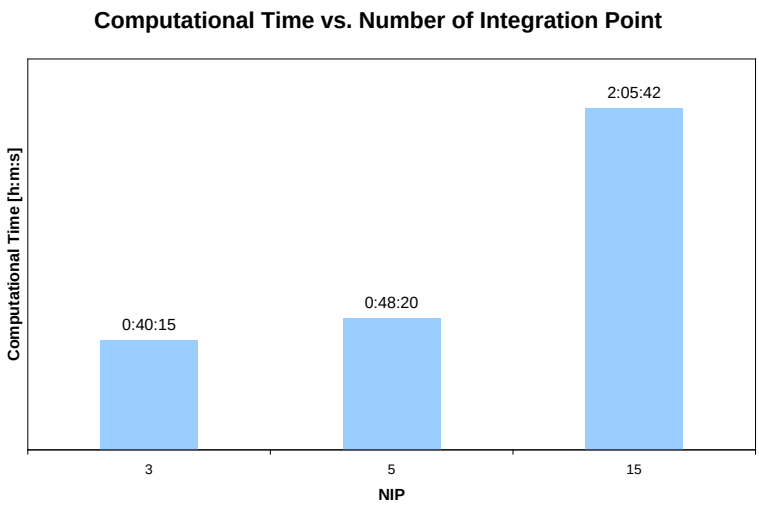

Figure 57. Estimation of computational time for several NIP in the section card

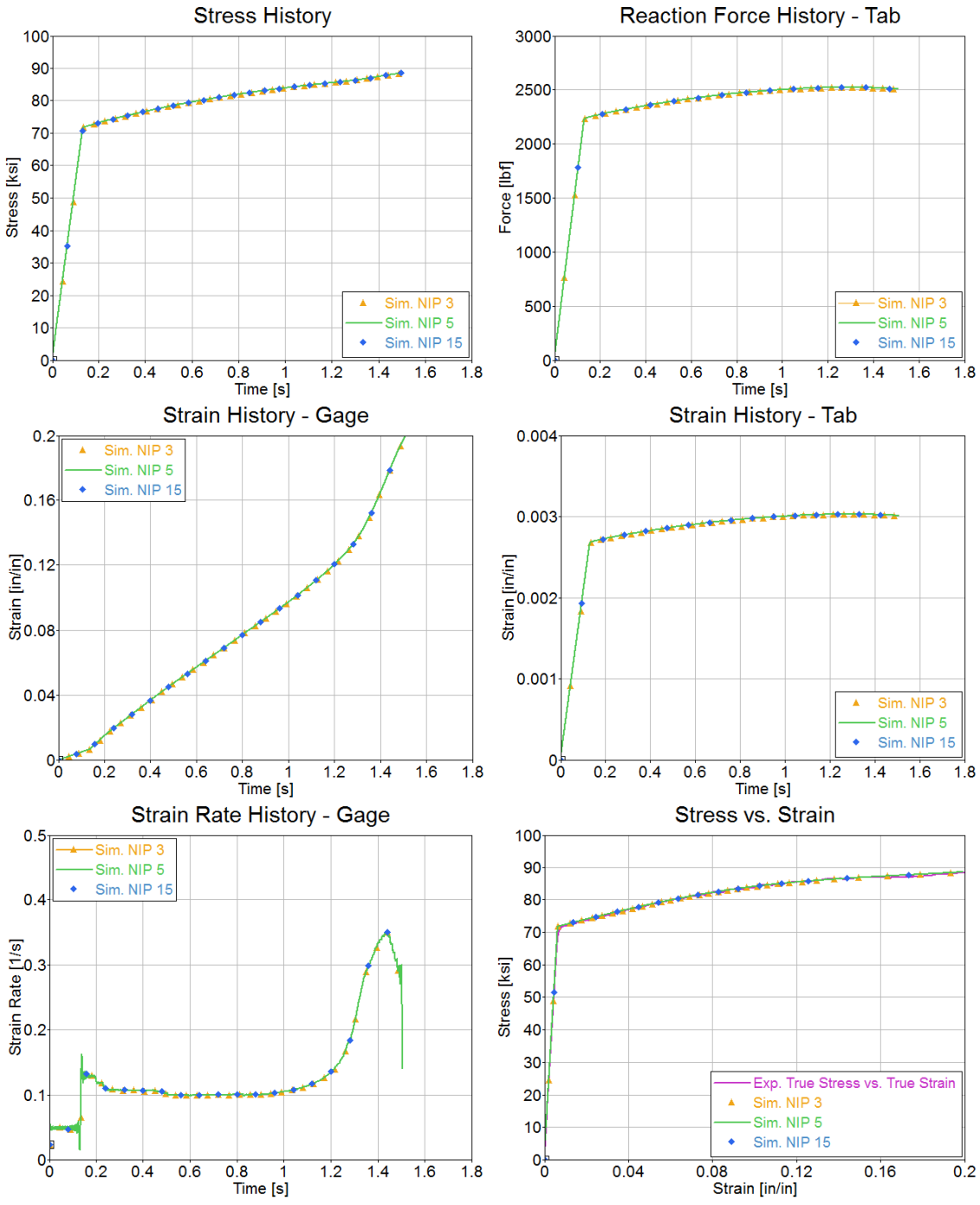

Figure 58. Comparison of NIP for the baseline Al coupon model at a speed of 0.1 in/s, MAT-24, ELFORM 2, NIP = 3, 5, 15

5.1.3 Comparison of Shell Elements Versus Solid Elements

The baseline Al model was also used to compare the results of using solid or shell elements to model the Al specimen (see figure 59). The ELFORM used for the shell elements was

ELFORM 2 with the NIP set to 5. The specimen model with solid elements includes LS-DYNA default section solid ELFORM 1, which corresponds to an under-integrated constant stress solid element. A speed of 0.1 in/s was used with no differences expected at other speeds. Figure 60 shows the stress history, strain history, reaction force history, and stress vs. strain curves. In general, no additional improvement over the material response was observed when solid elements were used. Figure 61 shows that there was approximately a 75% increase in computational time using solid elements vs. shell elements. However, because of the solid elements' inherent ability to deform out-of-plane, marginally higher stress levels are seen within the gage area as the deformation extends into the plastic regime. Shell elements are able to capture the appropriate material response while maintaining low computational times.

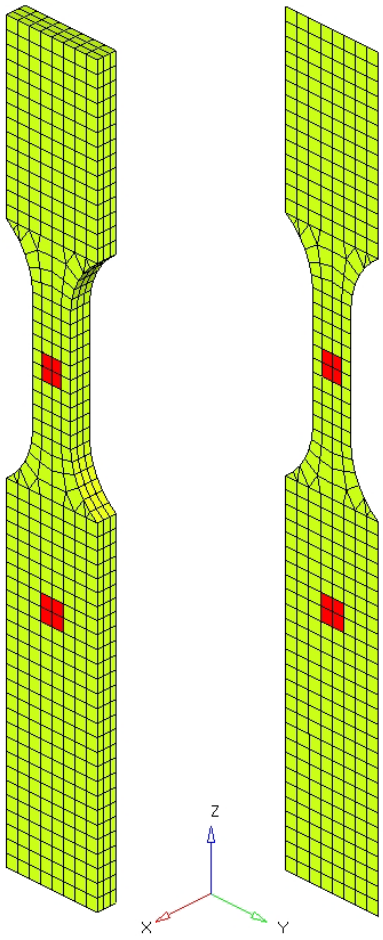

Figure 59. Baseline Al model used to compare results of solid and shell elements

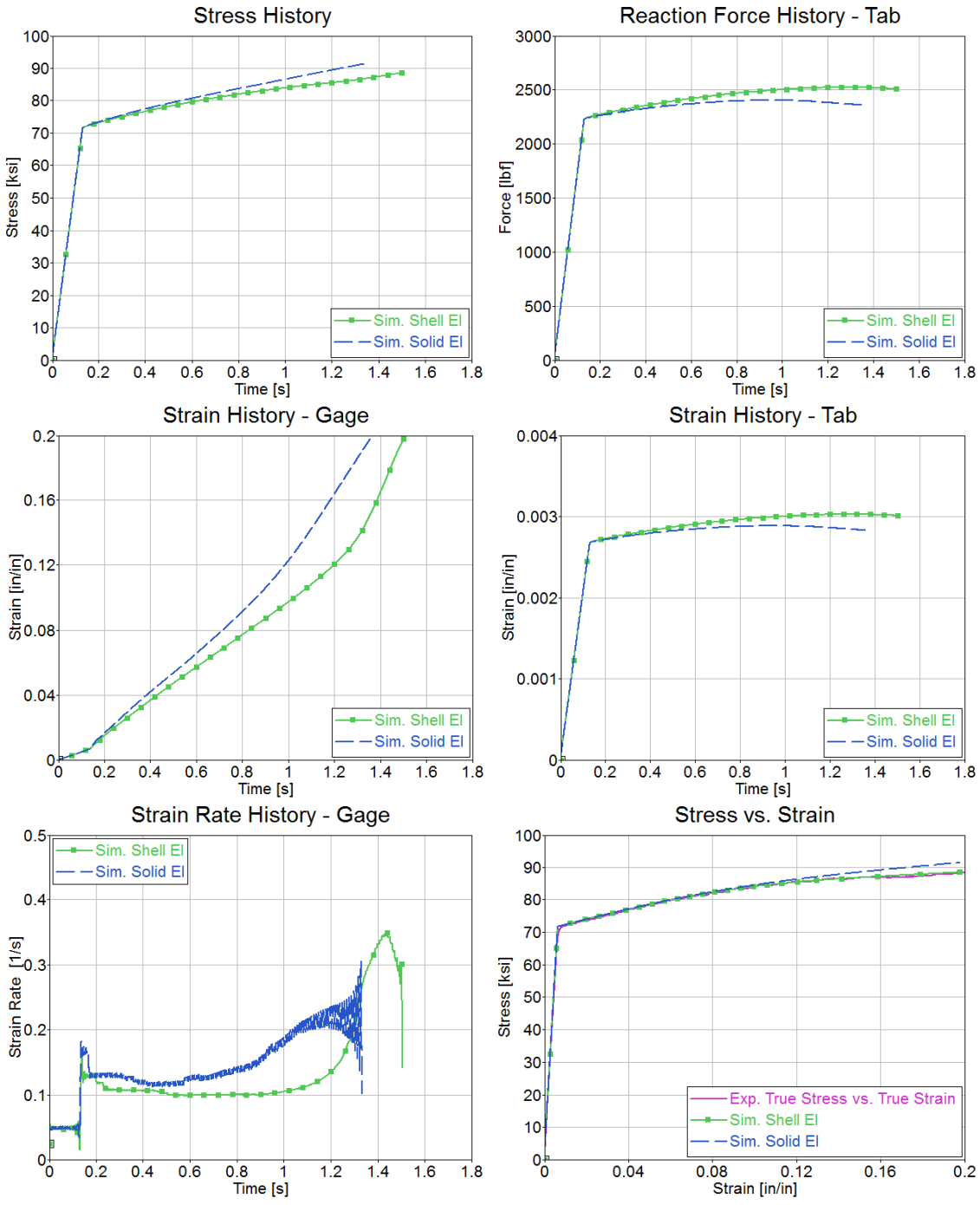

Figure 60. Comparison of element types for baseline Al model at a speed of 0.1 in/s, MAT-24, ELFORM 2, NIP = 5

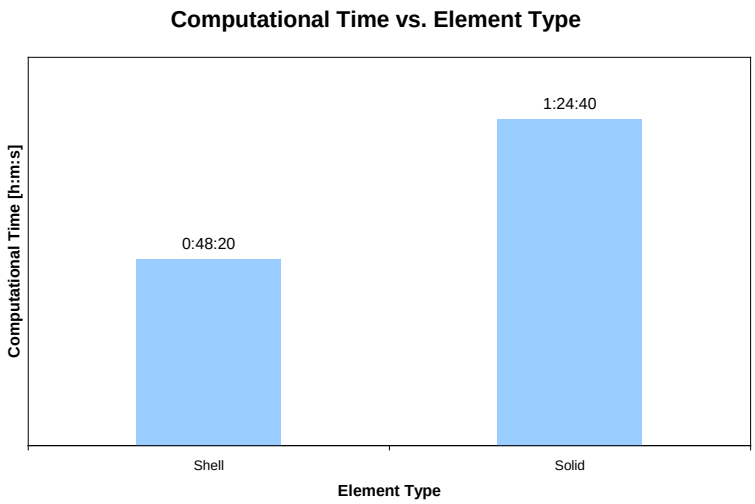

Figure 61. Estimation of computational time for shell and solid elements used in baseline Al model

5.1.4 Verification of the Aluminum 7075-T6 Coupon Model

The baseline coupon model, with the associated material model (MAT-24), was compared with the test data. The coupon model used for the comparison was assembled with ELFORM 2 shell elements and the NIP set to 5. Coupon-level simulation results were compared with the average tension test stress-strain responses for the four different speeds (see figure 62). A strong correlation was observed between the stress-strain results of the material model and the test.

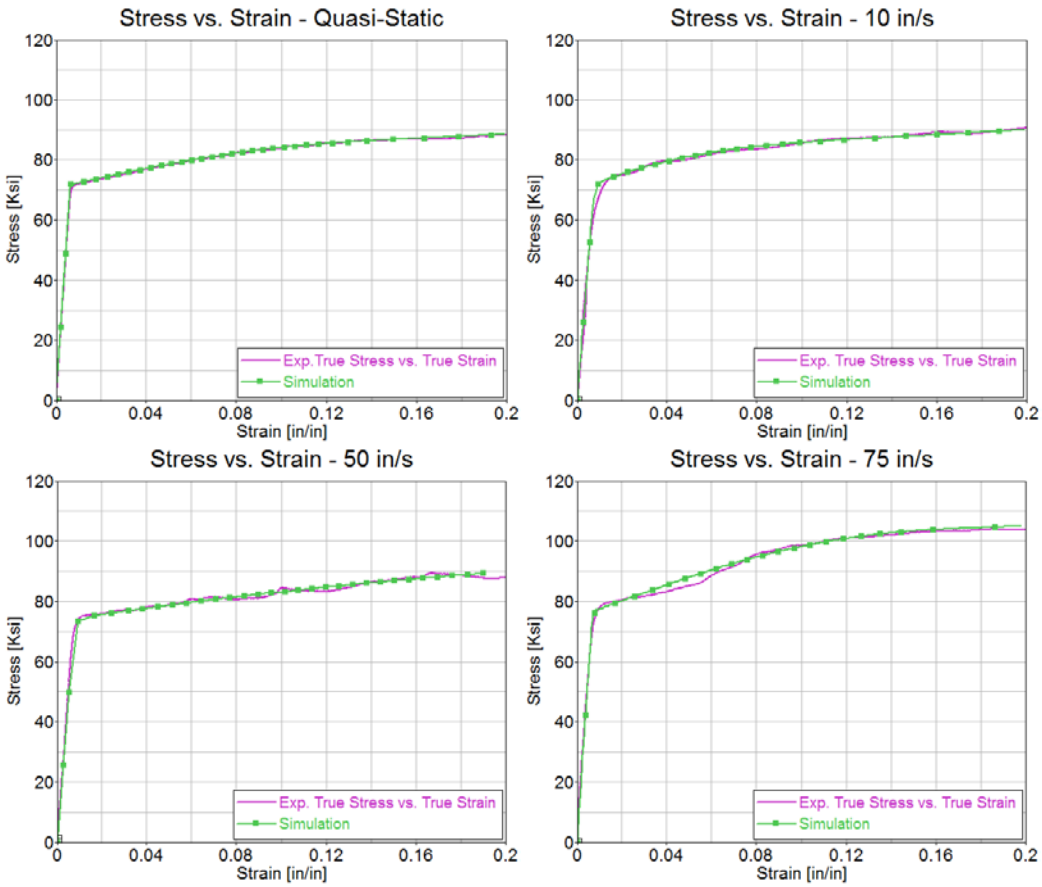

Figure 62. Verification of Al 7075-T6 specimen model at speeds of 0.1 in/s, 10 in/s, 50 in/s, and 75 in/s, shell elements, MAT-24, ELFORM 2, NIP = 5, in tension

5.2 VALIDATION OF THE TENSION SPECIMEN-GRIP ASSEMBLY MODEL

The specimen-grip assembly model was validated with test data generated over speeds ranging from quasi-static to 75 in/s. In general, simulation results show good correlation with the subject test data throughout the evaluated range of speeds (only plots for speeds of 0.1 and 75 in/s are shown). Higher levels of correlation were observed during the early stages of deformation when the material response was still in the elastic regime (the entire assembly plays an important role because of its elastic properties). At low speeds, simulation results show small deviations when compared to the test data (see figure 63) for the specimen-grip testing assembly at a speed of 0.1 in/s. Similarly, the material response at higher velocities closely follows the test data over the elastic regime and far into the plastic regime (see figure 64) for the specimen-grip test assembly at a speed of 75 in/s. Some deviation is observed in the material response far beyond the material's yield point. The strain history and the strain-rate history for the assembly model follow the trend of the test data during most of the deformation process. Reaction forces at the fixed end of the specimen are over-predicted by 6% at the peak of the load. The effective plastic strain distribution over the gage section of the specimen is shown in figure 65. Elements are deleted as the plastic strain in the necking area reaches plastic strain to failure.

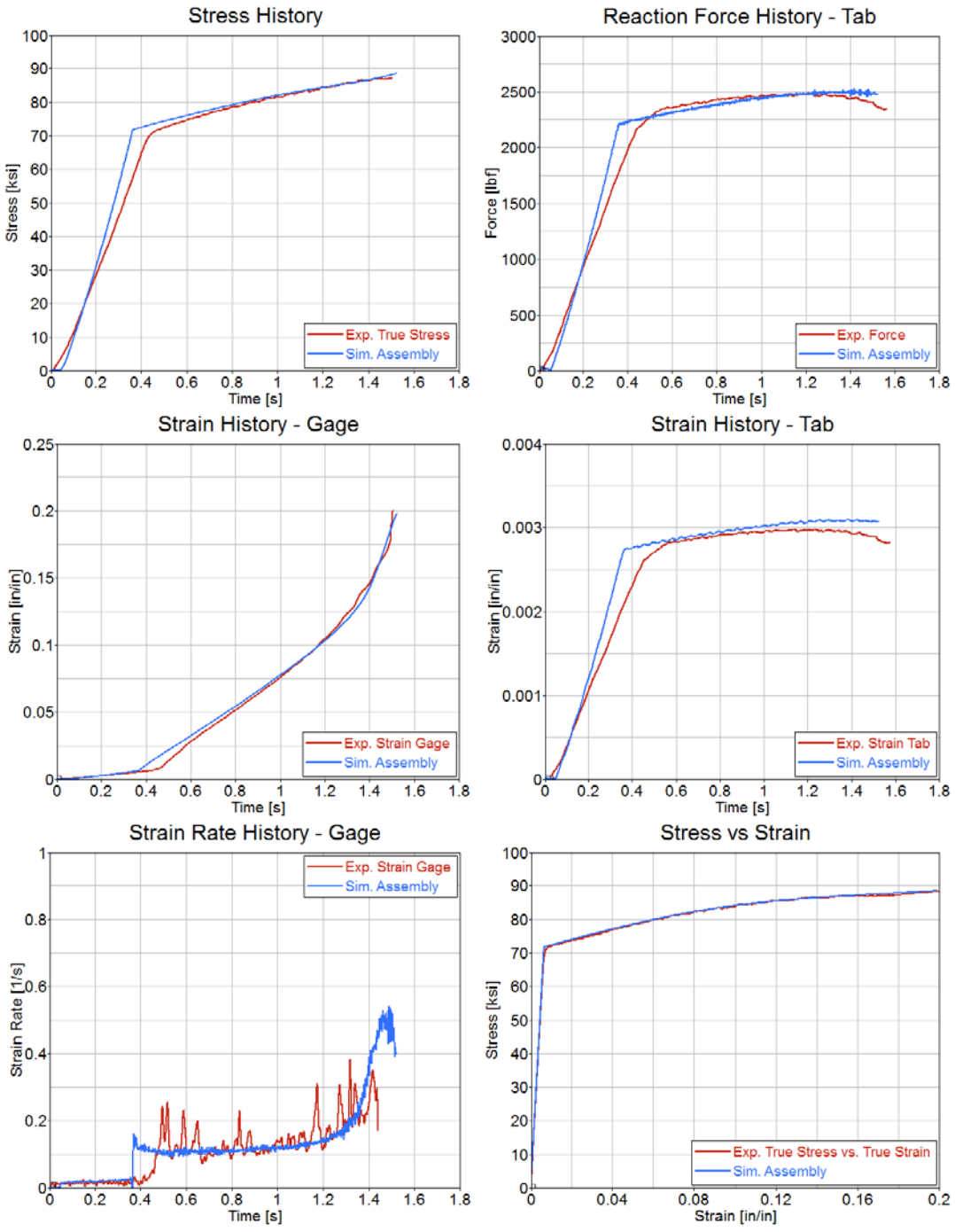

Figure 63. Validation of tension specimen-grip model at a speed of 0.1 in/s, shell elements, MAT-24, ELFORM 2, NIP = 5

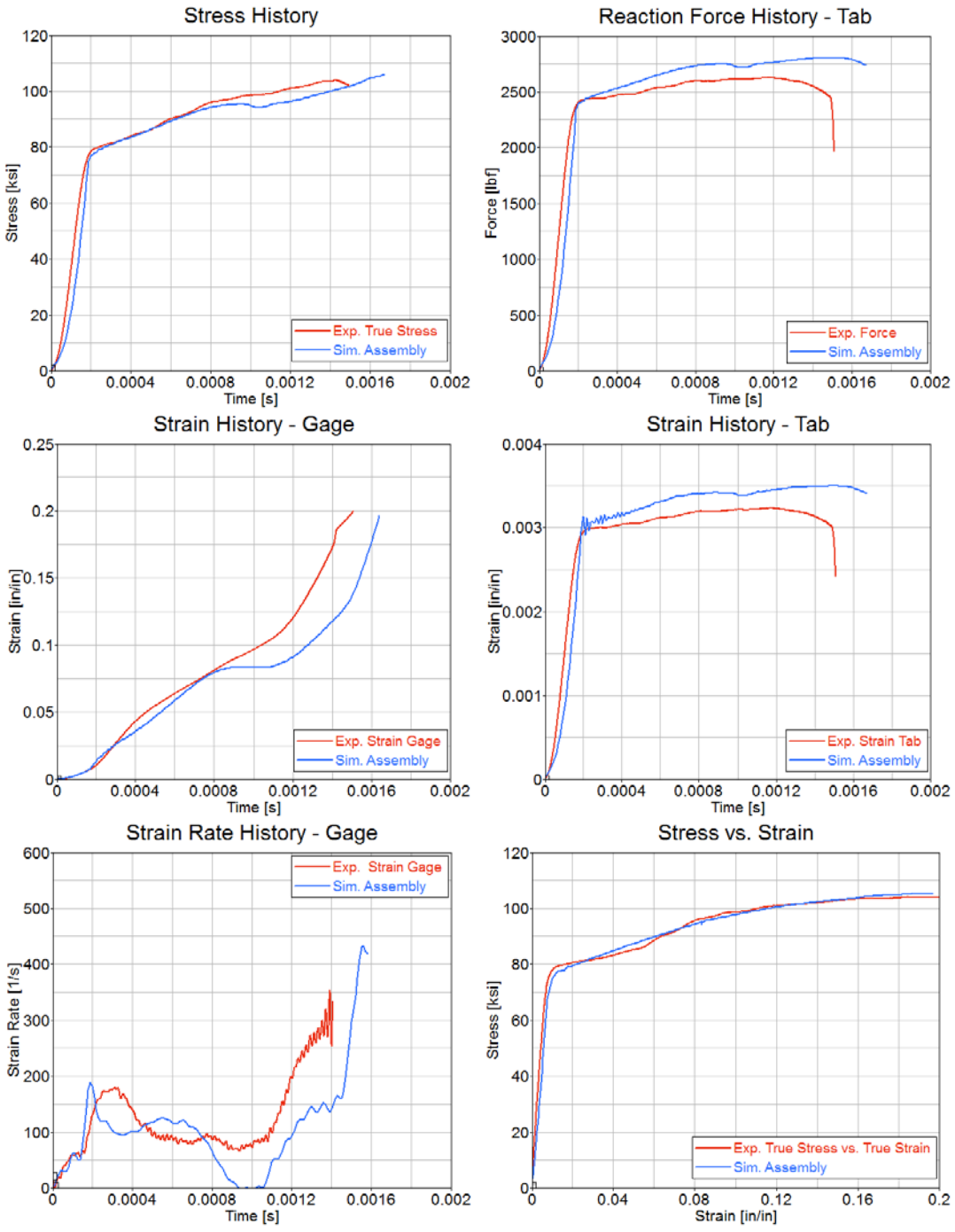

Figure 64. Validation of tension specimen-grip model at a speed of 75 in/s, shell elements, MAT-24, ELFORM 2, NIP = 5

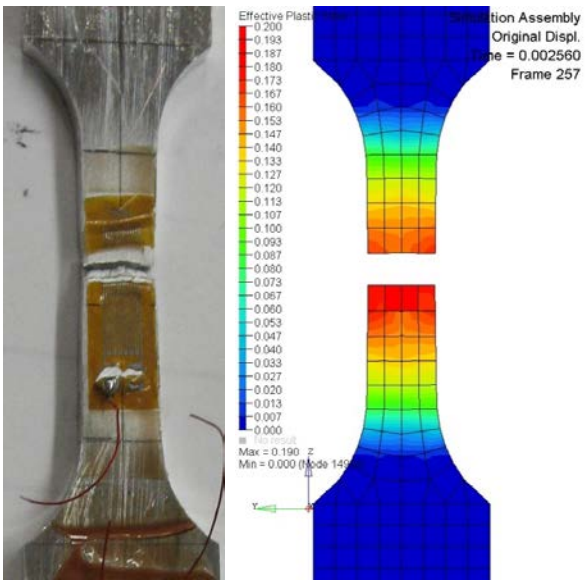

Figure 65. Effective plastic strain distribution of the Al 7075-T6 specimen at a speed of 75 in/s

When running simulations at the coupon level, the stress-strain response of the material can be captured by using a coupon model. However, if a more thorough analysis of the coupon response is required, the influence of the test equipment should be considered and the entire assembly modeled. The model of the testing assembly can be further refined to include the detailed interaction of the attachment points. The model could then be used as a tool to evaluate the testing system and it may bring the needed clarity to issues that currently limit the testing technique, such as the effect of the grip mass on the model. The model could also be used to generate corrections to test results for strain-rate-sensitive materials.

5.3 EVALUATION OF COMPOSITE MATERIAL MODEL

5.3.1 Material Model Response in Tension–MAT-54, MAT-58

The evaluation and verification of the composite material model was conducted using the Toray Unitape material and the Newport E-Glass Fabric. Similar results were expected using the Toray Carbon Fabric instead of the Newport E-Glass Fabric. Tension test data for various stacking sequences of Toray Unitape T800S/3900-2B and Newport E-Glass Fabric NB321/7781 were used. The models' responses using LS-DYNA material cards MAT-54 and MAT-58 are compared with representative test data in figures 66–73 for four different material orientations at a speed of 1 in/s. Similar results are expected at 10 in/s. MAT-54 predicts the material stiffness during early stages of deformation for material systems with fibers oriented along the loading direction (e.g., $[0°]_N$ and $[+15°/-15°]_{NS}$). However, MAT-54 fails to capture the nonlinear response of off-axis material systems (e.g., $[+30/-30]_{NS}$ and $[+45°/-45°]_{NS}$). Conversely, to some extent, MAT-58 characterized the non-linearity observed in the off-axis specimens without failure parameter manipulation.

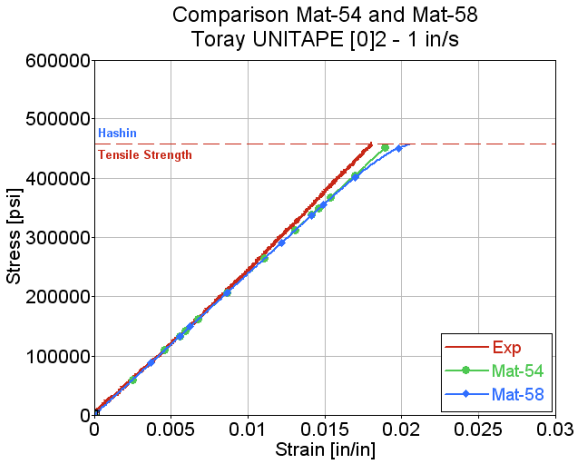

Figure 66. Comparison of MAT-54 and MAT-58: Toray carbon Unitape $[0]_2$ at a speed of 1 in/s, in tension

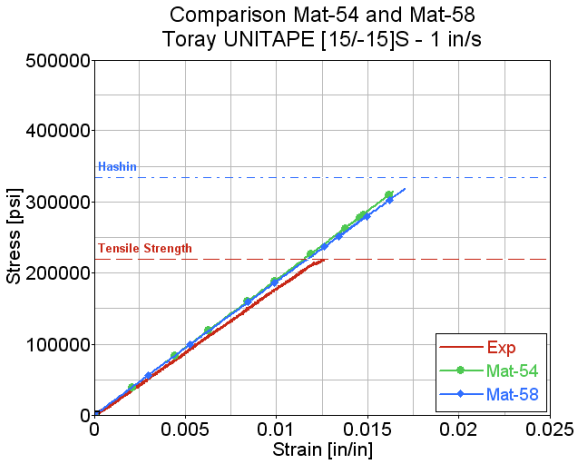

Figure 67. Comparison of MAT-54 and MAT-58: Toray carbon Unitape $[+15/-15]_S$ at a speed of 1 in/s, in tension

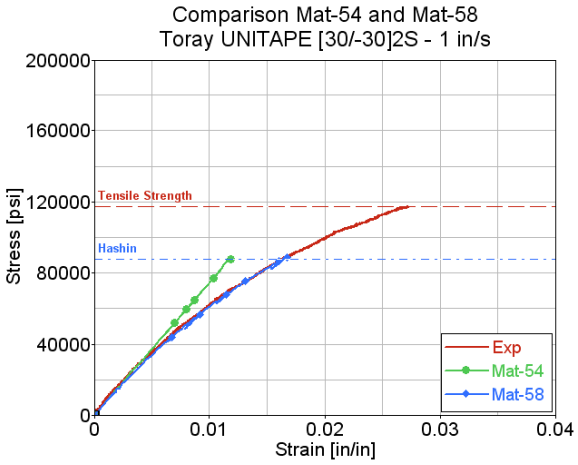

Figure 68. Comparison of MAT-54 and MAT-58: Toray carbon Unitape $[+30/-30]_{2S}$ at a speed of 1 in/s, in tension

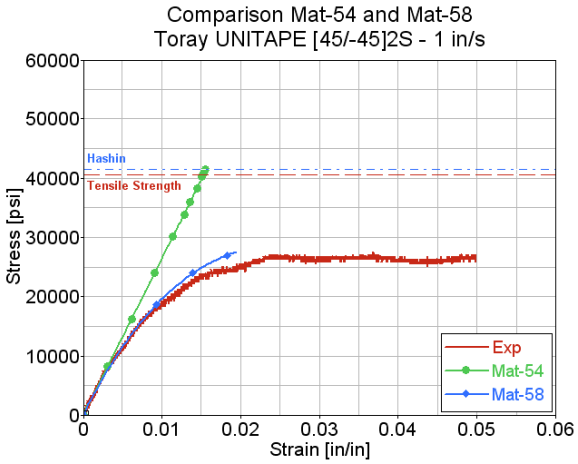

Figure 69. Comparison of MAT-54 and MAT-58: Toray carbon Unitape $[+45/-45]_{2S}$ at a speed of 1 in/s, in tension

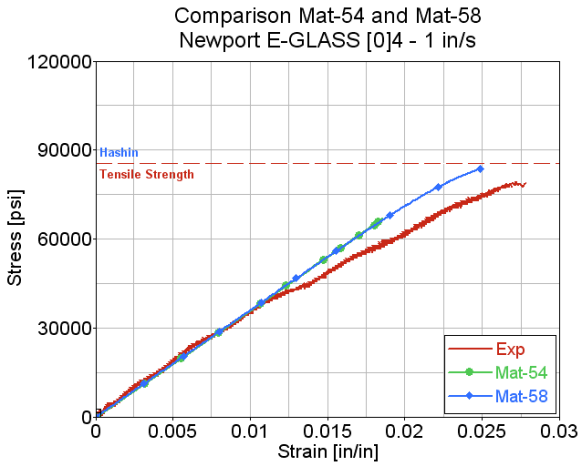

Figure 70. Comparison of MAT-54 and MAT-58: Newport E-glass fabric $[0]_4$ at a speed of 1 in/s, in tension

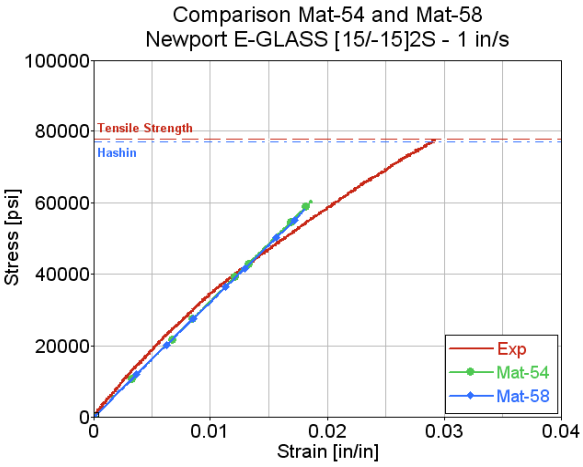

Figure 71. Comparison of MAT-54 and MAT-58: Newport E-glass fabric $[+15/-15]_{2S}$ at a speed of 1 in/s, in tension

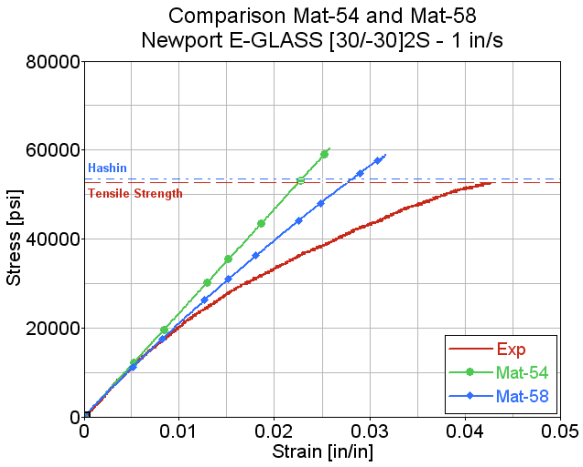

Figure 72. Comparison of MAT-54 and MAT-58: Newport E-glass fabric $[+30/-30]_{2S}$ at a speed of 1 in/s, in tension

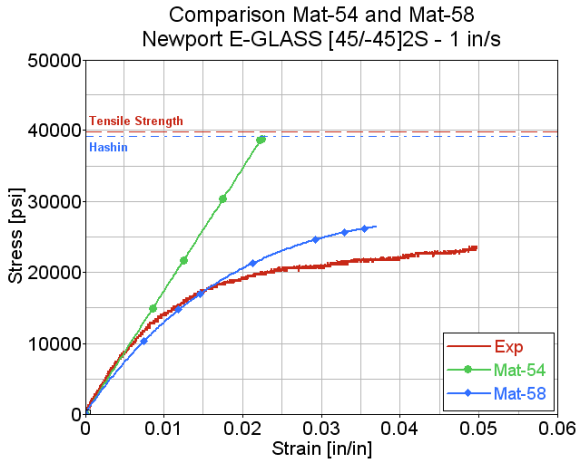

Figure 73. Comparison of MAT-54 and MAT-58: Newport E-glass fabric $[+45/-45]_{2S}$ at a speed of 1 in/s, in tension

Tensile strength is shown in each stress-strain plot as a reference to compare the simulation results. However, the stress-strain curves may not show the entire strain history of the material. Tensile strength is extracted from the load measured by a pizeo-electric load cell placed above the test. Conversely, strain is measured using a strain gage bonded to the surface of the specimen. Therefore, strain measurement faces two restraints: strain gage deformation capability and adhesive elongation capability. When testing laminates with off-axis orientation, the strain gage may reach its capability early during the material deformation; this results in a truncated stress-strain curve, as shown in figure 69. Figures 68–73 also include the tensile strength predicted by Hashin failure criteria [39] as a reference to evaluate failure in the simulation results. Refer to section 5.5 for a detailed explanation.

5.3.2 Material Model Response in Tension–Evaluation of MAT-58 Failure Surface Type

Material card MAT-58 provides three types of failure surfaces: a faceted failure surface (FS = -1), smooth failure surface with quadratic criteria for both fiber and transverse directions (FS = 1), and smooth failure surface in the transverse direction with a limiting value in the fiber direction (FS = 0) [32]. The adequacy of each failure surface when handling different fiber architectures was evaluated by fixing every parameter but the failure surface. Simulation results are summarized in figures 74–81 for two different architectures: Toray Carbon Unitape and Newport E-Glass Fabric. Analyses were carried out with four different stacking sequences at a speed of 1 in/s. Simulation results show that the faceted failure surface (FS = -1) follows the test data better than the other two failure surfaces. Similar results were expected at the three other speeds.

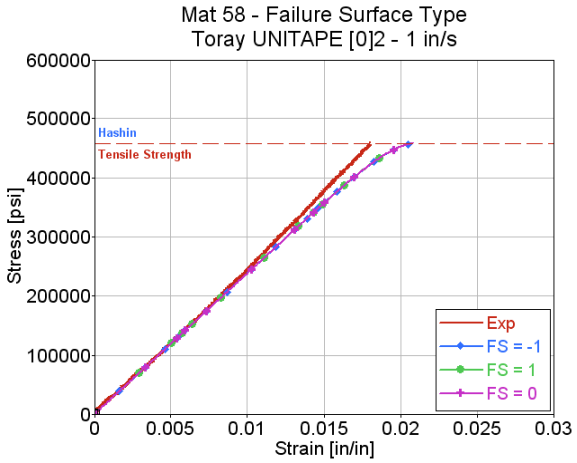

Figure 74. Comparison of failure surface using MAT-58: Toray carbon Unitape $[0]_2$ at a speed of 1 in/s, in tension

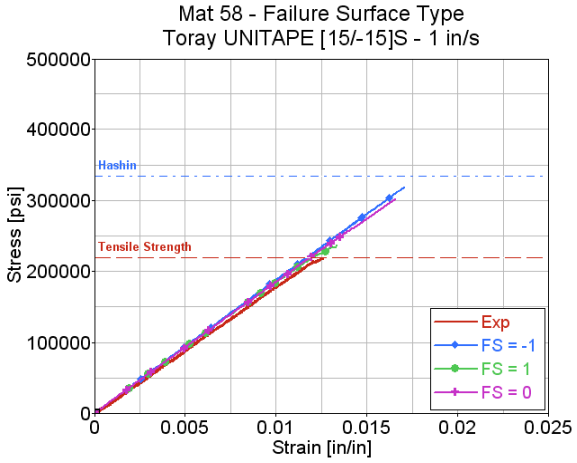

Figure 75. Comparison of failure surface using MAT-58: Toray carbon Unitape $[+15/-15]_S$ at a speed of 1 in/s, in tension

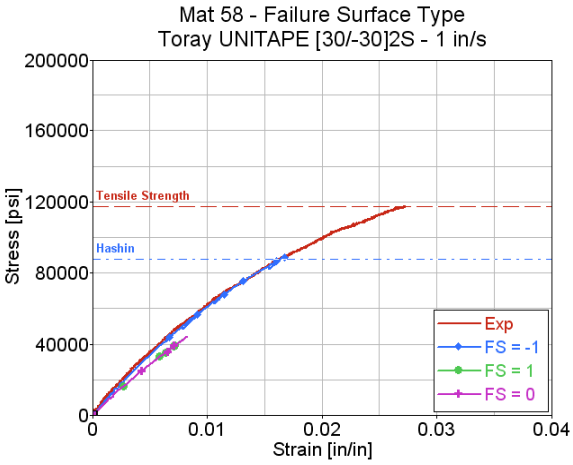

Figure 76. Comparison of failure surface using MAT-58: Toray carbon Unitape $[+30/-30]_{2S}$ at a speed of 1 in/s, in tension

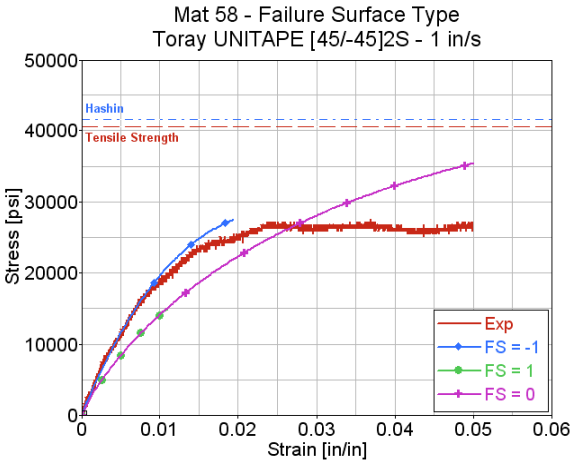

Figure 77. Comparison of failure surface using MAT-58: Toray carbon Unitape $[+45/-45]_{2S}$ at a speed of 1 in/s, in tension

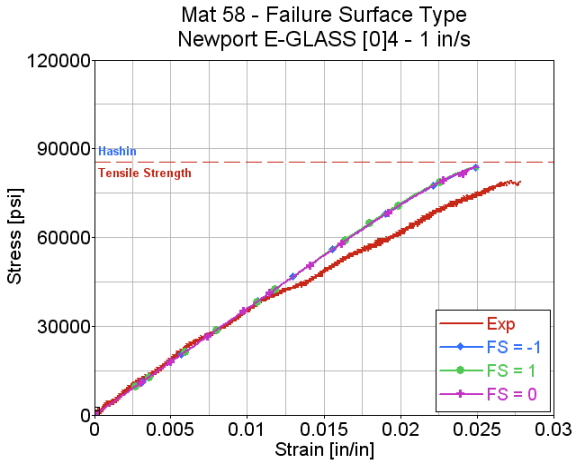

Figure 78. Comparison of failure surface using MAT-58: Newport E-glass fabric $[0]_4$ at a speed of 1 in/s, in tension

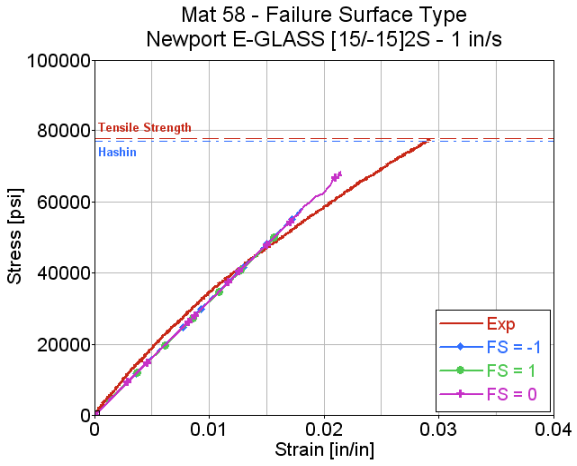

Figure 79. Comparison of failure surface using MAT-58: Newport E-glass fabric $[+15/-15]_{2S}$ at a speed of 1 in/s, in tension

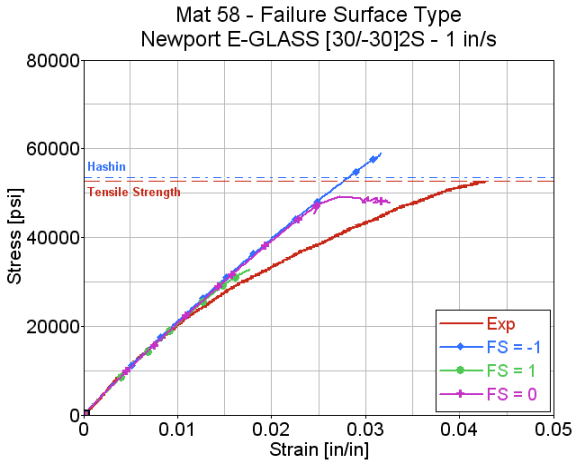

Figure 80. Comparison of failure surface using MAT-58: Newport E-glass fabric $[+30/-30]_{2S}$ at a speed of 1 in/s, in tension

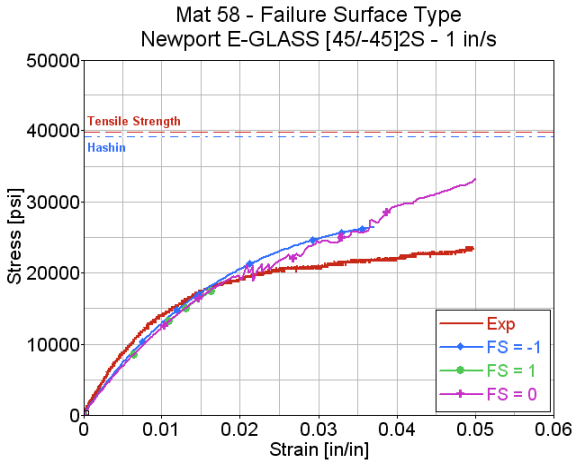

Figure 81. Comparison of failure surface using MAT-58: Newport E-glass fabric $[+45/-45]_{2S}$ at a speed of 1 in/s, in tension

5.4 EVALUATION OF MESH DENSITY

Numerical models assembled for crashworthiness evaluations may require different levels of discretization depending on the level of detail required. This translates into different regions within the structure possessing different mesh densities. However, mesh density is sometimes compromised to reduce computational time. Therefore, the effect of mesh density on the in-plane material response is evaluated at the coupon level using tension and shear numerical models. MAT-58 and material properties for Toray Carbon Unitape were used for this evaluation. The tension and shear coupon mesh with varying element densities used for the analysis is shown in figures 80–83. The brown area in figures 80–83 represents the location of the strain gages. Analyses were carried out with four different stacking sequences under tension and shear conditions at a speed of 1 in/s. Similar results were expected at the other speeds.

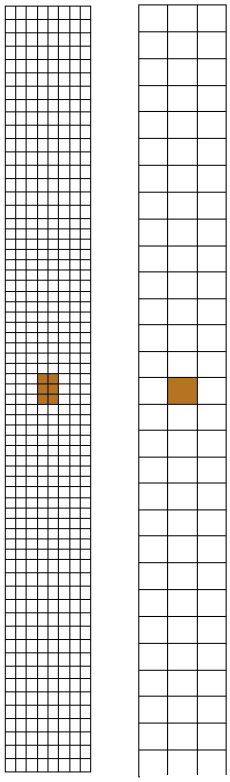

(a) (b)

Figure 80. Tension coupon: (a) fine mesh and (b) coarse mesh

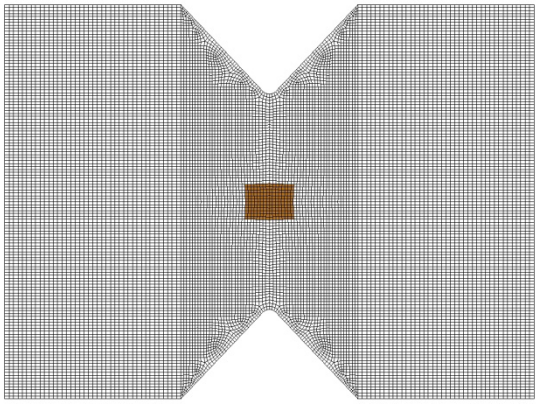

Figure 81. Shear coupon: fine mesh

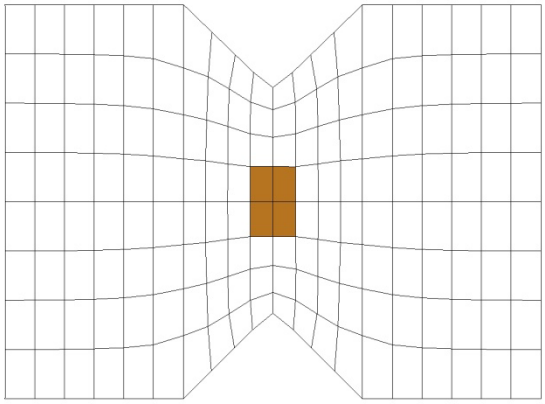

Figure 82. Shear coupon: coarse mesh-1

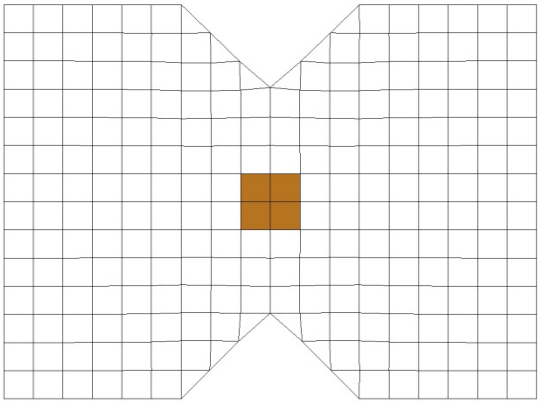

Figure 83. Shear coupon: coarse mesh-2

Two different mesh densities were evaluated for the tension test coupon: a fine mesh with an average element size of 1.5 mm and a coarse mesh density with an average element size of 3.9 mm (see figure 80). Tension results for the different mesh densities of the four different stacking sequences are shown in figures 84–87. Note that element size does not affect the in-plane tension material response of the model.

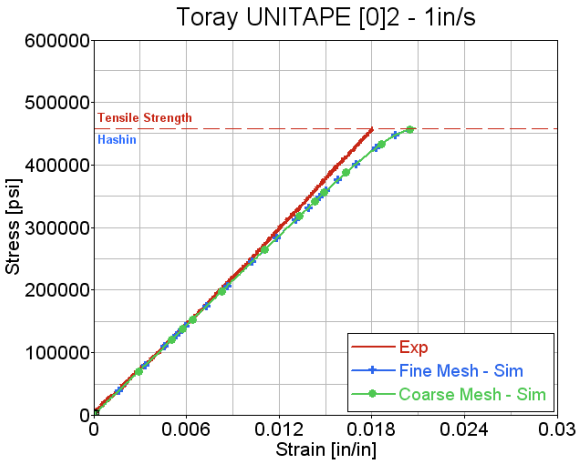

Figure 84. Comparison of mesh density using MAT-58: Toray carbon Unitape $[0]_2$ at a speed of 1 in/s, in tension

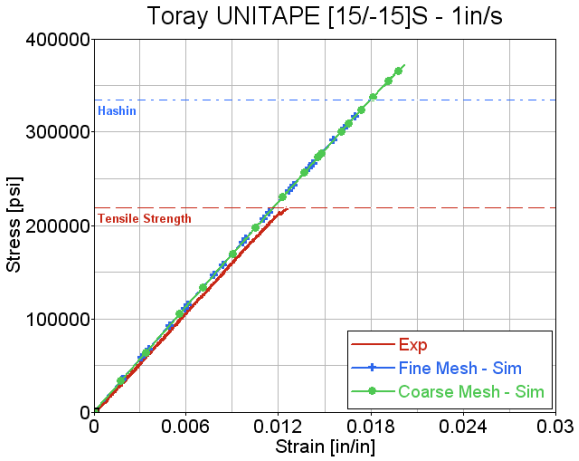

Figure 85. Comparison of mesh density using MAT-58: Toray carbon Unitape $[+15/-15]_S$ at a speed of 1 in/s, in tension

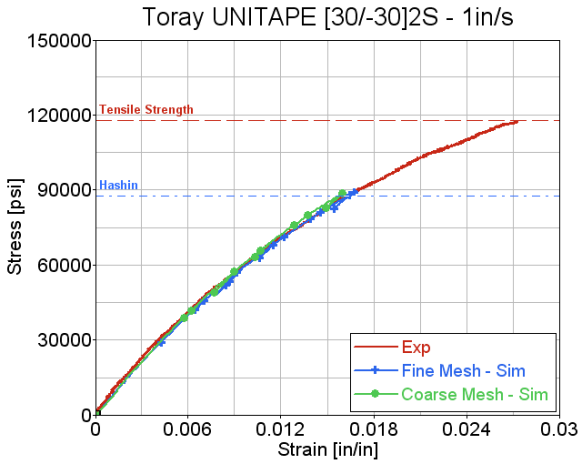

Figure 86. Comparison of mesh density using MAT-58: Toray carbon Unitape $[+30/-30]_{2S}$ at a speed of 1 in/s, in tension

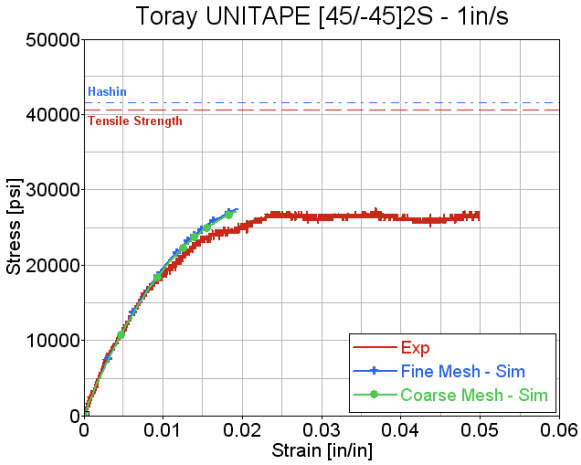

Figure 87. Comparison of mesh density using MAT-58: Toray carbon Unitape $[+45/-45]_{2S}$ at a speed of 1 in/s, in tension

Three different mesh size densities were evaluated for the shear coupon: a fine mesh with an average element size of 0.2 mm, another mesh density with an average element size of 2.8 mm, and a coarser mesh density with an average element size of 3.2 mm. In the coarser mesh, triangular elements were used in the vicinity of the specimen notch, as shown in figure 83. Shear results for the $[0°]_{12}$ stacking sequence are shown in figure 88. Note that the element size and triangular elements do not affect the in-plane shear response of the material.

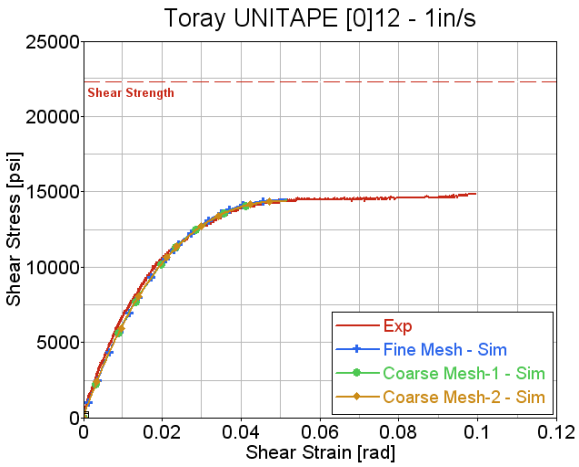

Figure 88. Comparison of mesh density using MAT-58: Toray carbon Unitape $[0]_{12}$ at a speed of 1 in/s, in shear

5.5 FAILURE ANALYSIS

Tension testing was conducted per ASTM D 3039 on three composite materials for the four stacking sequences at a speed of 1 in/s. Similar results were expected at the other speeds. Test failure strengths were compared with the values obtained from analysis using classical laminate theory (CLT) and a numerical model implementing the LS-DYNA material card MAT-58. The procedure shown in the flow chart in figure 89 was used to determine the analytical failure strengths. When determining the failure load using an iterative method, stresses in the local coordinate system (fiber), calculated using CLT, are compared to certain failure criteria, and the load is increased until the failure criteria are met.

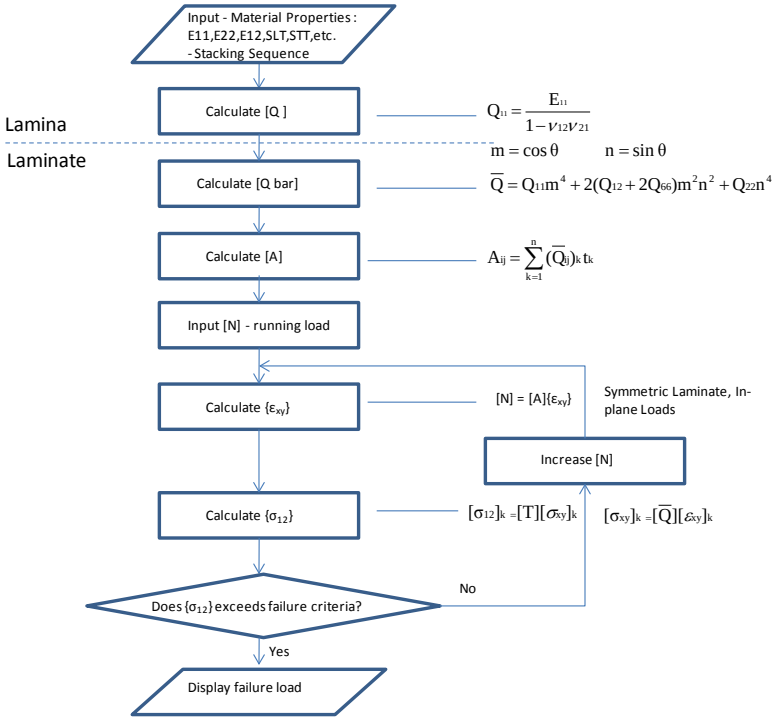

Figure 89. First-ply failure iterative process

The tensile strengths obtained from tests, simulation, and four different failure criteria for various stacking sequences were compared to evaluate how simulation failure strength values differ from test results for different stacking sequences and obtain theoretical insight for the variation. The material properties at the lamina level were obtained from testing. Then, lamina failure strengths were input into the material model for the simulation of laminates with different stacking sequences. The numerical model estimates failure strength of laminates of different stacking sequence by implementing predefined failure criteria. LS-DYNA material MAT-58 allows for the implementation of Hashin failure criteria [39]. Similarly, laminate failure strengths can be calculated using CLT, evaluating different failure criteria for failure detection. Test and simulation failure strength data at a speed of 1 in/s, along with the failure mode for Toray Unitape T800S/3900-2B, Toray Fabric T700G-12K-PW/3900-2, and Newport E-Glass Fabric NB321/7781, are compared with various lamina failure criteria in table 11 and figure 90, table 12 and figure 91, and table 13 and figure 92, respectively.

Table 11. Comparison of tensile strength of carbon Unitape at a speed of 1 in/s

Stacking Sequence	EXP		SIM	Lamina Failure Criterion						
				Maximum Strain (CLT)		Maximum Stress (CLT)		Hashin		TSAI-WU
	Tensile Strength (ksi)	Max / Min	Tensile Strength (ksi)	Tensile Strength (ksi)	Failure Mode (Direction)	Tensile Strength (ksi)	Failure Mode (Direction)	Tensile Strength (ksi)	Failure Mode	Tensile Strength (ksi)
$[0°]_2$	453	490 / 415	456	458	Tension 11	458	Tension 11	458	Tensile Fiber	458
$[+15°/-15°]_S$	219	230 / 207	318	416	Comp. 22	435	Tension 11	334	Tensile Fiber	286
$[+30°/-30°]_{2S}$	118	122 / 113	90	104	Shear	104	Shear	88	Comp. Matrix	115
$[+45°/-45°]_{2S}$	41	46 / 35	27	45	Shear	45	Shear	42	Tensile Matrix	40

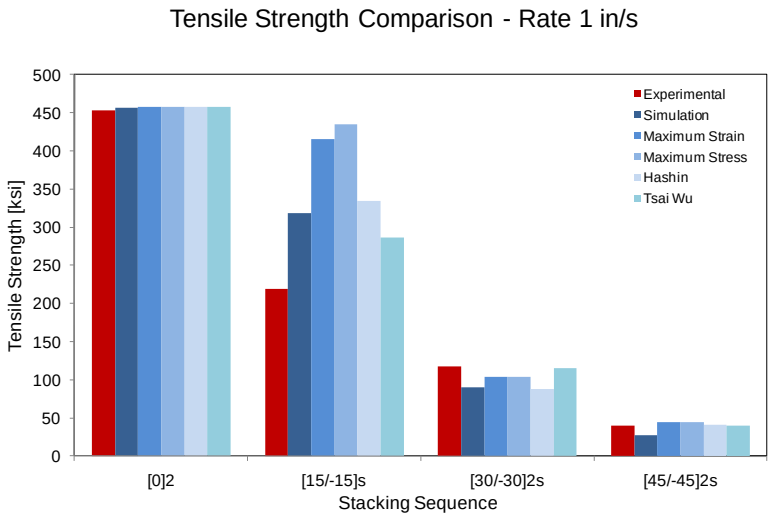

Figure 90. Comparison of tensile strength of carbon Unitape

Table 12. Comparison of tensile strength of carbon fabric at a speed of 1 in/s

Stacking Sequence	EXP		SIM	Lamina Failure Criterion						
				Maximum Strain (CLT)		Maximum Stress (CLT)		Hashin		TSAI-WU
	Tensile Strength (ksi)	Max / Min	Tensile Strength (ksi)	Tensile Strength (ksi)	Failure Mode (Direction)	Tensile Strength (ksi)	Failure Mode (Direction)	Tensile Strength (ksi)	Failure Mode	Tensile Strength (ksi)
$[0°]_4$	139	170 / 107	137	138	Tension 11	138	Tension 11	138	Tensile Fiber	138
$[+15°/-15°]_{2S}$	97	100 / 93	126	131	Tension 11	131	Tension 11	128	Tensile Fiber	124
$[+30°/-30°]_{2S}$	71	74 / 67	88	113	Tension 11	114	Tension 11	91	Tensile Fiber	85
$[+45°/-45°]_{2S}$	43	45 / 40	39	50	Shear	50	Shear	49	Tensile Matrix	51

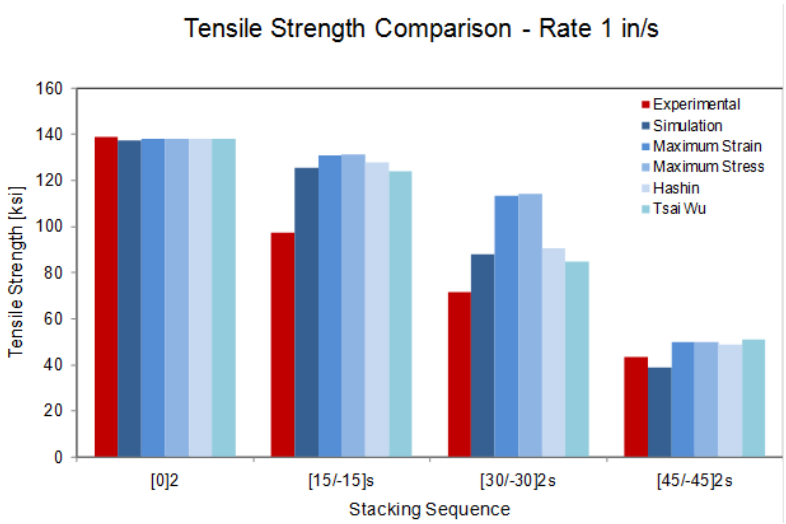

Figure 91. Comparison of tensile strength of carbon fabric

Table 13. Comparison of tensile strength of fiberglass at a speed of 1 in/s

Stacking Sequence	EXP		SIM	Lamina Failure Criterion						
				Maximum Strain (CLT)		Maximum Stress (CLT)		Hashin		TSAI-WU
	Tensile Strength (ksi)	Max / Min	Tensile Strength (ksi)	Tensile Strength (ksi)	Failure Mode (Direction)	Tensile Strength (ksi)	Failure Mode (Direction)	Tensile Strength (ksi)	Failure Mode	Tensile Strength (ksi)
$[0°]_4$	85	89 / 80	84	85	Tension 11	85	Tension 11	85	Tensile Fiber	85
$[+15°/-15°]_{2S}$	78	82 / 73	58	84	Tension 11	84	Tension 11	77	Tensile Fiber	77
$[+30°/-30°]_{2S}$	53	53.1 / 52.8	59	68	Shear	68	Shear	53	Tensile Fiber	54
$[+45°/-45°]_{2S}$	39	39.4 / 35.5	26	40	Shear	40	Shear	39	Tensile Matrix	40

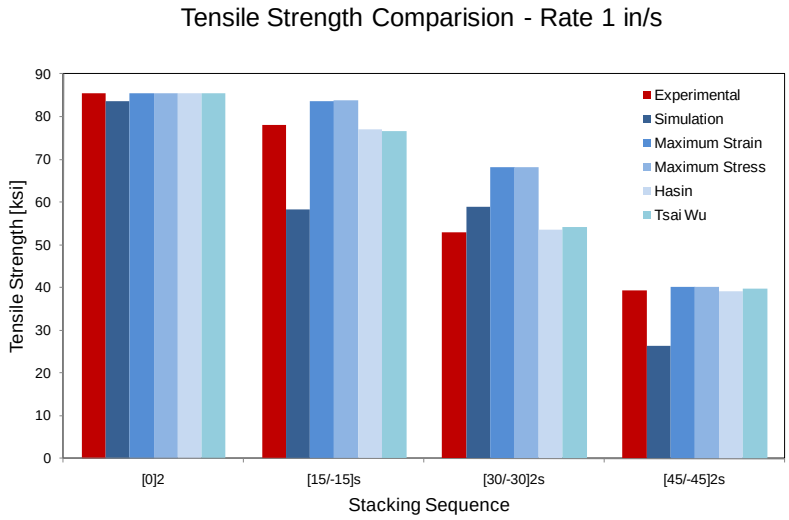

Figure 92. Comparison of tensile strength of fiberglass

Simulation, CLT, and test results provided equivalent tensile strengths for tensile failure modes of [0°] specimens, which is characteristic of laminates with fibers along the loading direction. However, results show great variation when off-axis laminates are evaluated. Failure modes can be predicted using maximum strain, maximum stress, or Hashin failure criteria. When the stacking sequence is $[0°]_2$, shear stress is not present and the different failure criteria estimate the same failure strength. In other stacking sequences, tension load introduces in-plane shear stresses, and the different failure criteria give different failure strengths. Maximum stress criteria

compare stresses in different directions with their corresponding ultimate strengths and do not account for stress interactions. Maximum strain criteria compare strains in different directions with their corresponding ultimate strain. Hashin criteria account for the presence of shear stress, and Tsai-Wu criteria consider the interaction of different stress components. Therefore, because different failure criteria use different methods, the values of failure strengths differ in the presence of multiple stresses.

5.6 VALIDATION OF NEWPORT E-GLASS FABRIC NB321/7781 MATERIAL MODEL

Simulation results are presented for the three different test methods: tension, compression, and shear. Numerical models represent the in-plane testing of laminated composite materials described in section 2. The material models were developed at the lamina level using the NIAR test data for Newport E-Glass Fabric NB321/7781. The tensile material properties and test results are summarized in appendix B. The shear material properties and test results are summarized in appendix E. Each speed corresponds to a specific set of properties. The associated material card for the material model corresponds to LS-DYNA MAT-58, in which a faceted failure surface was defined. The input decks for the material models for each speed are listed in appendix H.

5.6.1 Newport E-Glass Fabric Tension Test Model

This section summarizes the simulation results for the tension testing of Newport E-Glass Fabric NB321/7781 over three speeds: quasi-static 0.0008 in/s, 1 in/s, and 10 in/s. The available test data included laminates with four different stacking sequences: $[0°]_4$, $[+15°/-15°]_{2S}$, $[+30°/-30°]_{2S}$, and $[+45°/-45°]_{2S}$. All laminates are balanced and symmetric. One numerical model was assembled for each stacking sequence and then simulated at each speed, with a specific material model associated per speed. The simulation results for orientation $[0°]_4$ are summarized in figures 93–95 for each speed. The numerical model closely follows the material response during the early stages of deformation. However, it deviates from the test response as additional damage is introduced to the material by the deformation process. The simulation axial strain distribution is uniform across the gage section of the testing specimen at the evaluated speeds. Figure 96 shows an example for 1 in/s. The random failure locations (see appendix B) observed in the test specimens verify this observation.

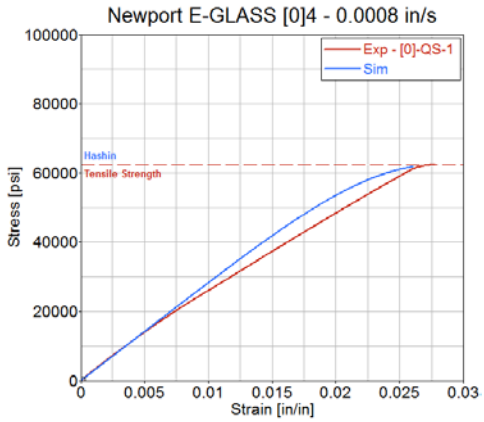

Figure 93. Comparison of MAT-58 simulated and test stress strain data: Newport E-Glass Fabric $[0]_4$ at a speed of 0.0008 in/s, in tension

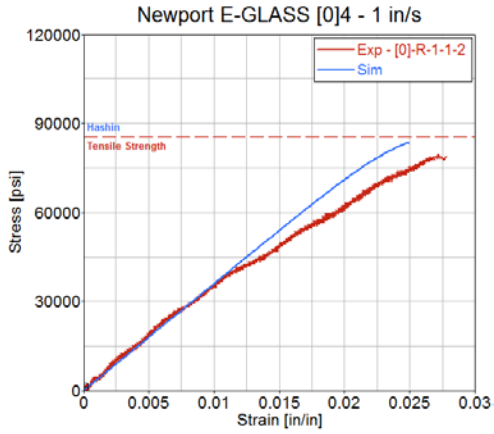

Figure 94. Comparison of MAT-58 simulated and test stress strain data: Newport E-Glass Fabric $[0]_4$ at a speed of 1 in/s, in tension

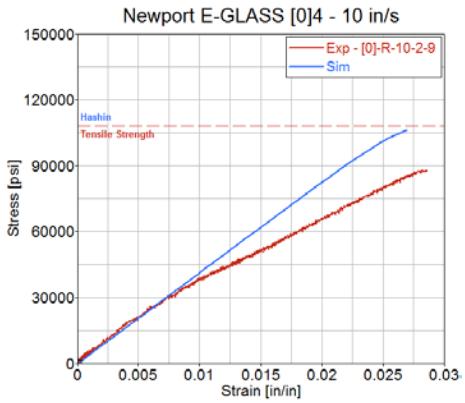

Figure 95. Comparison of MAT-58 simulated and test stress strain data: Newport E-Glass Fabric $[0]_4$ at a speed of 10 in/s, in tension

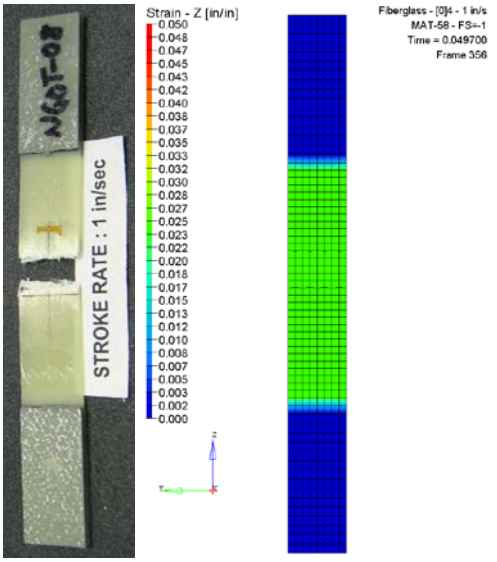

Figure 96. Axial strain distribution in Newport E-Glass Fabric $[0]_4$ at a speed of 1 in/s, in tension

The simulation results for orientation $[+15°/-15°]_{2S}$ are summarized in figures 97–99 for each speed. The numerical model deviates from the test material response at the early stages of deformation. This deviation increases with increased speed. The material model does not appear to adequately capture the combined state of stress resulting from the off-axis fiber orientation. Therefore, the fabric materials' shear control introduced in the material model does not necessarily capture the nonlinear effect in the fabrics' behavior under off-axis loading. However, the material model does capture strain concentrations within the gage section of the specimen resulting from off-axis fiber orientations. The strain distribution in figure 100 shows areas in the mid-section that exhibit slightly higher strain levels, which may lead to damage initiation and subsequent failure. The failure locations (see appendix B) observed in the test specimens verify this observation.

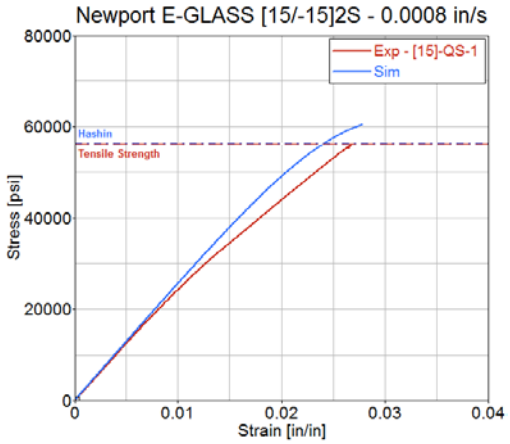

Figure 97. Comparison of MAT-58 simulated and test stress strain data: Newport E-Glass Fabric $[+15°/-15°]_{2S}$ at a speed of 0.0008 in/s, in tension

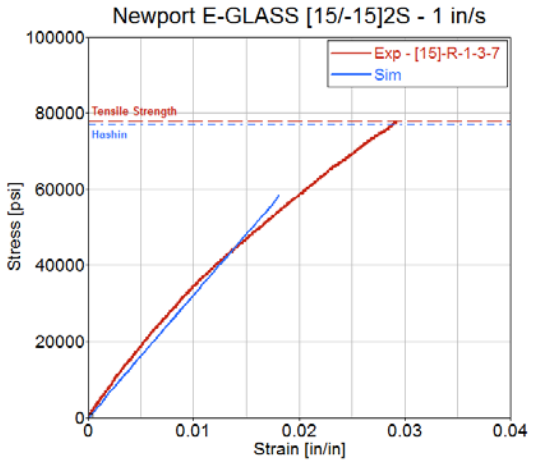

Figure 98. Comparison of MAT-58 simulated and test stress strain data: Newport E-Glass Fabric $[+15°/-15°]_{2S}$ at a speed of 1 in/s, in tension

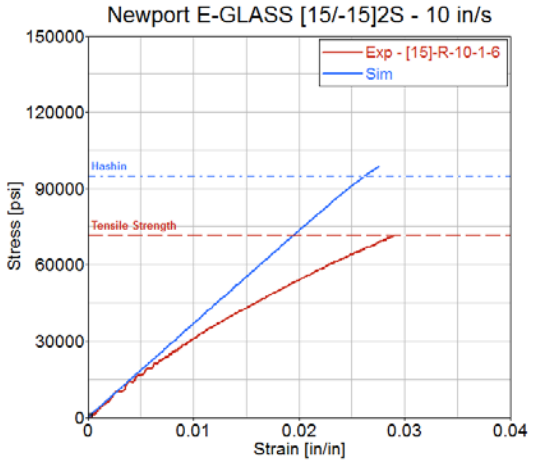

Figure 99. Comparison of MAT-58 simulated and test stress strain data: Newport E-Glass Fabric $[+15°/-15°]_{2S}$ at a speed of 10 in/s, in tension

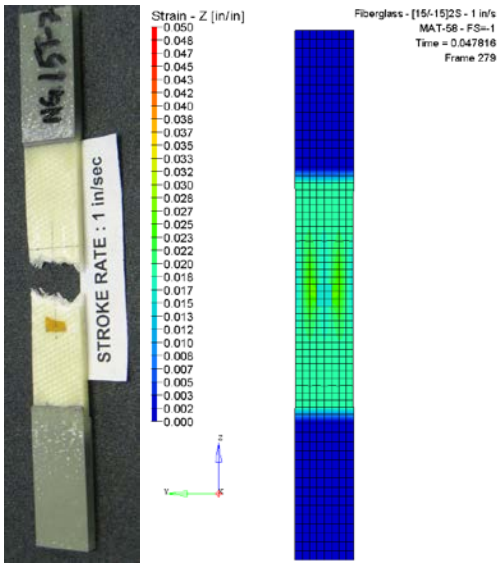

Figure 100. Axial strain distribution in Newport E-Glass Fabric $[+15°/-15°]_{2S}$ at a speed of 1 in/s, in tension

The simulation results for orientation $[30°/-30°]_{2S}$ are summarized in figures 101–103 for each speed. The numerical model deviates from the material response during the early stages of deformation. This deviation increases with increased speed. The material model does not appear to adequately capture the combined state of stress resulting from the off-axis material orientation. However, the strain distribution captured by the material model in figure 104 shows areas close to the specimen tab where deformation may result in failure modes similar to those in the actual test specimens (i.e., as the material becomes more compliant with larger material fiber orientations, the tab area constrains such deformation).

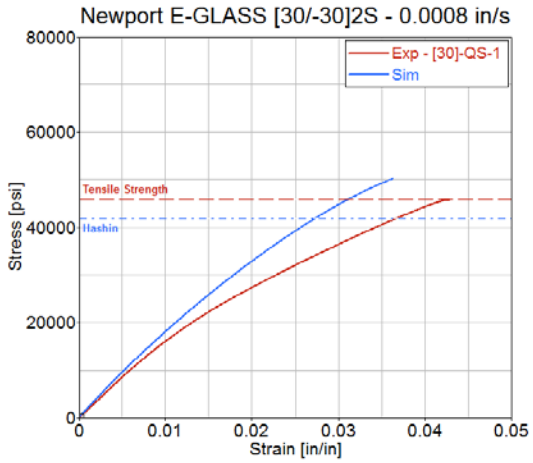

Figure 101. Comparison of MAT-58 simulated and test stress strain data: Newport E-Glass Fabric $[+30°/-30°]_{2S}$ at a speed of 0.0008 in/s, in tension

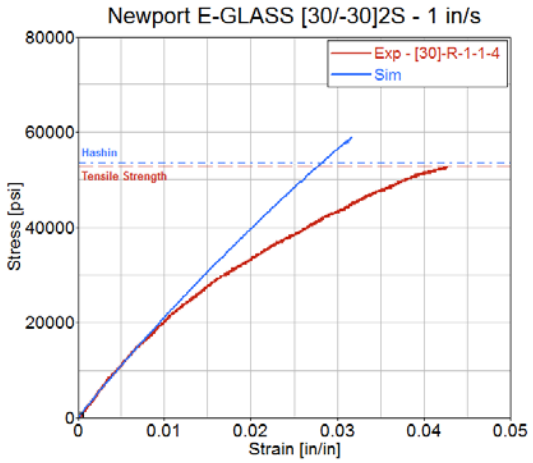

Figure 102. Comparison of MAT-58 simulated and test stress strain data: Newport E-Glass Fabric $[+30°/-30°]_{2S}$ at a speed of 1 in/s, in tension

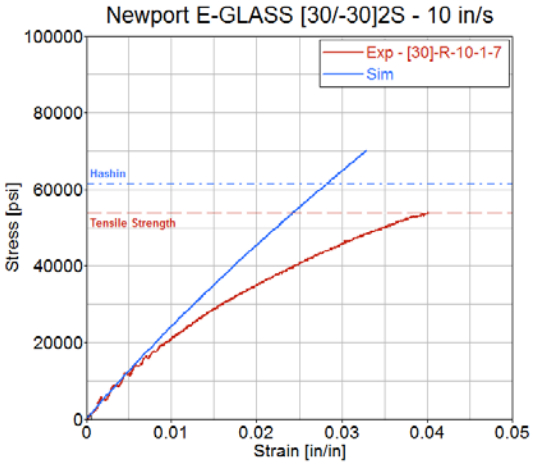

Figure 103. Comparison of MAT-58 simulated and test stress strain data: Newport E-Glass Fabric $[+30°/-30°]_{2S}$ at a speed of 10 in/s, in tension

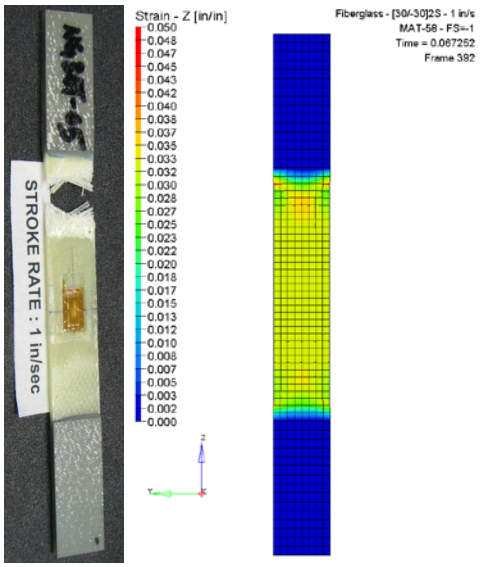

Figure 104. Axial strain distribution in Newport E-Glass Fabric $[+30°/-30°]_{2S}$ at a speed of 1 in/s, in tension

The simulation results for orientation $[45°/-45°]_{2S}$ are summarized in figures 105–107 for each speed. The numerical model follows the nonlinear trend of the material response during the early stages of deformation. However, it deviates from the test response as deformation progresses for the evaluated speeds. The strain distribution in figure 108 shows areas with larger strain values where failure could develop.

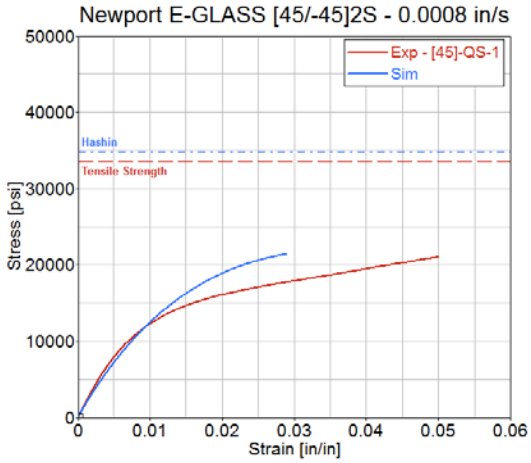

Figure 105. Comparison of MAT-58 simulated and test stress strain data: Newport E-Glass Fabric $[+45°/-45°]_{2S}$ at a speed of 0.0008 in/s, in tension

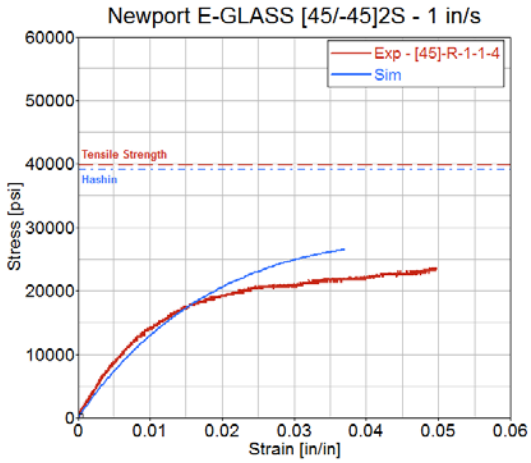

Figure 106. Comparison of MAT-58 simulated and test stress strain data: Newport E-Glass Fabric $[+45°/-45°]_{2S}$ at a speed of 1 in/s, in tension

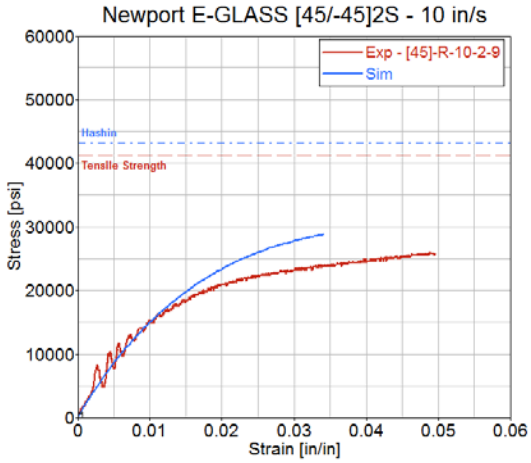

Figure 107. Comparison of MAT-58 simulated and test stress strain data: Newport E-Glass Fabric $[+45°/-45°]_{2S}$ at a speed of 10 in/s, in tension

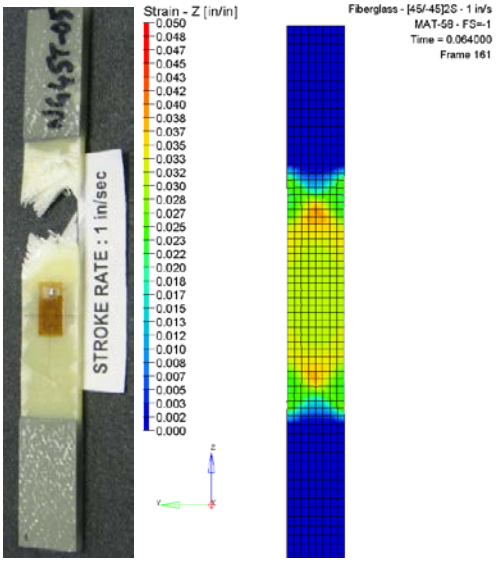

Figure 108. Axial strain distribution in Newport E-Glass Fabric $[+45°/-45°]_{2S}$ at a speed of 1 in/s, in tension

5.6.2 Newport E-Glass Compression Testing Model

The model for compression testing was validated with AGATE compression data for Newport E-Glass Fabric NB321/7781, with a stacking sequence of $[0°/90°]_{3S}$, and tested at quasi-static rates [37]. This material model implements LS-DYNA material card MAT-58 and includes a faceted failure surface. Figure 109 shows good correlation of the material model response when compared to the experimental data for most of the stress-strain response. The strain distribution plot in figure 110 exhibits uniform deformation throughout the length of the specimen, except near the bottom where the loading is introduced.

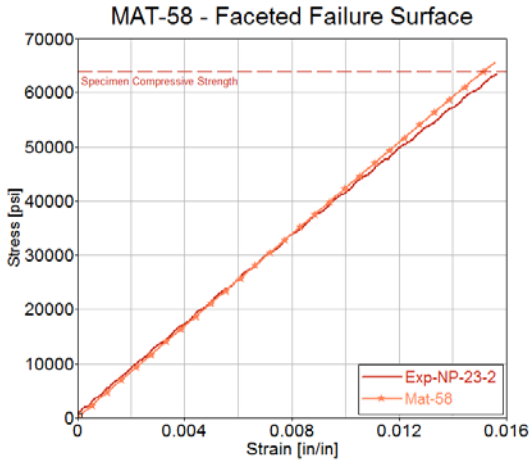

Figure 109. Comparison of MAT-58 simulated and test stress strain data: Newport E-Glass Fabric $[0/90]_{3S}$ at a speed of 0.0008 in/s, faceted failure surface, in compression

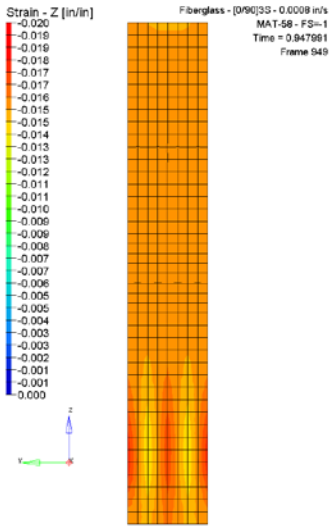

Figure 110. Axial strain distribution in Newport E-Glass Fabric $[0/90]_{3S}$ at a speed of 0.0008 in/s, in compression

5.6.3 Newport E-Glass Shear Testing Model

This section summarizes the simulation results for the shear testing of Newport E-Glass Fabric NB321/7781 for two speeds: 1 in/s and 10 in/s. The available test data included specimens with a single stacking sequence of $[0°]_{12}$. For each speed, an appropriate material model was associated to the numerical model. The simulation results are shown in figures 111 and 112 for each speed. The numerical model closely follows the test shear material response until reliable shear strain data were recorded at approximately 0.09 rad shear strain. The shear test data exhibit two characteristic segments: a nonlinear segment followed by a linear segment. The simulation results capture the response up until the initiation of the linear segment. The shear strain distribution observed in figure 113 is fairly uniform across the gage section of the testing specimen. The damage process was observed to initiate at the notch root, similar to the test specimen (appendix E).

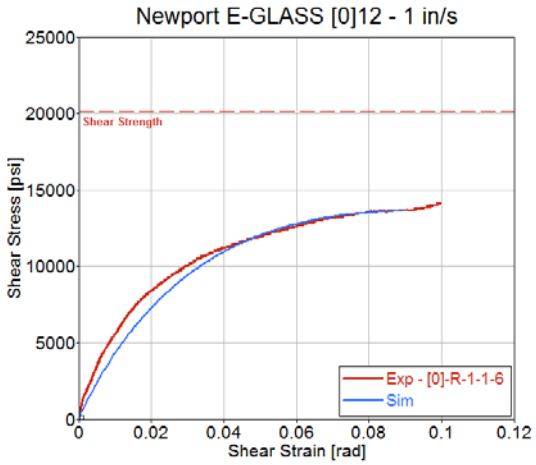

Figure 111. Comparison of MAT-58 simulated and test stress strain data: validation of shear Newport E-Glass Fabric $[0]_{12}$ at a speed of 1 in/s, in shear

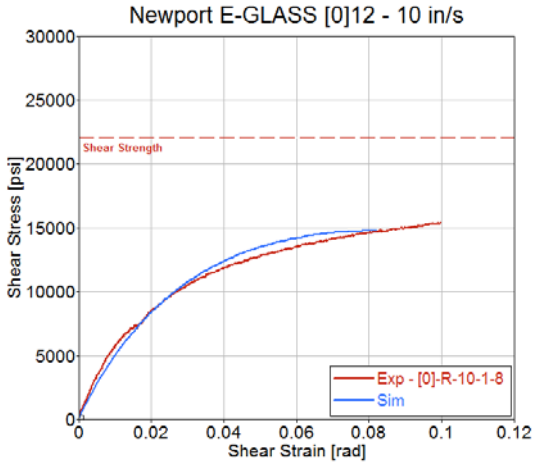

Figure 112. Comparison of MAT-58 simulated and test stress strain data: Newport E-Glass Fabric $[0]_{12}$ at a speed of 10 in/s, in shear

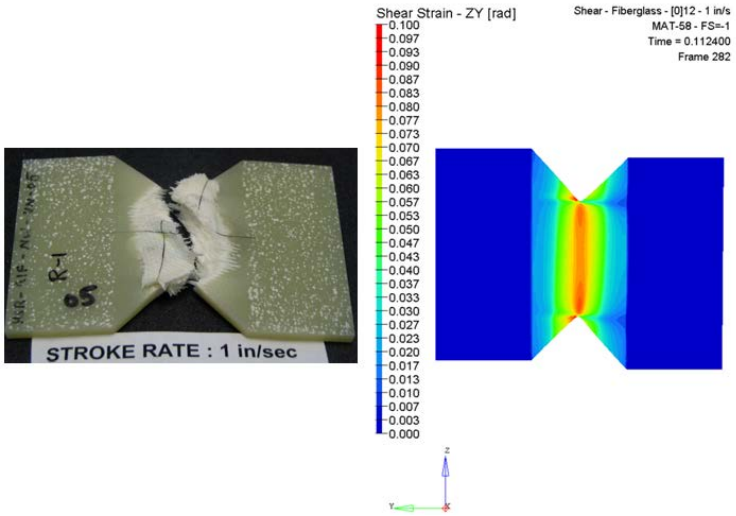

Figure 113. Distribution of shear strain in Newport E-Glass Fabric $[0]_{12}$ at a speed of 1 in/s, in shear

5.7 VALIDATION OF TORAY UNITAPE T800S/3900-2B MATERIAL MODEL

In this section, simulation results are presented for the in-plane tension and shear test methods. The material models were developed at the lamina level using the NIAR test data for Toray Unitape T800S/3900-2B. The material properties and test results are summarized in appendix C for tension testing and appendix F for shear testing. The model has a specific set of properties for each speed. The associated material card for the material model corresponds to LS-DYNA MAT-58, in which a faceted failure surface is defined. The input decks for the material models per speed are listed in appendix H.

5.7.1 Toray Unitape Tension Test Model

This section summarizes the simulation results for the tension testing of Toray Unitape T800S/3900-2B over three speeds: quasi-static 0.0008 in/s, 1 in/s, and 10 in/s. The available test data included laminates with four different stacking sequences: $[0°]_2$, $[+15°/-15°]_S$, $[+30°/-30°]_{2S}$, and $[+45°/-45°]_{2S}$. All laminates are balanced and symmetric. One numerical model was assembled for each stacking sequence, with a specific material model associated per speed.

Simulation results for orientation $[0°]_2$ are shown in figures 114–116 for each speed. The numerical model follows the material response during the early stages of deformation. However, it deviates from the test response before reaching failure. The material model response softens as the deformation progresses when compared with the experimental response. The strain distribution observed in figure 117 shows a uniform distribution across the gage section of the testing specimen, which results in longitudinal splitting as observed in the test specimens (see appendix C).

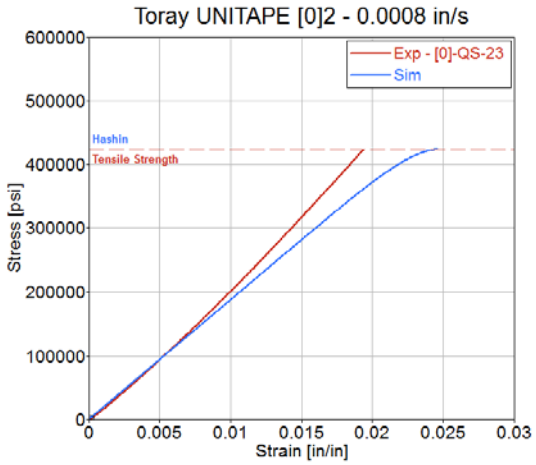

Figure 114. Comparison of MAT-58 simulated and test stress strain data: Toray Carbon Unitape $[0°]_2$ at a speed of 0.0008 in/s, in tension

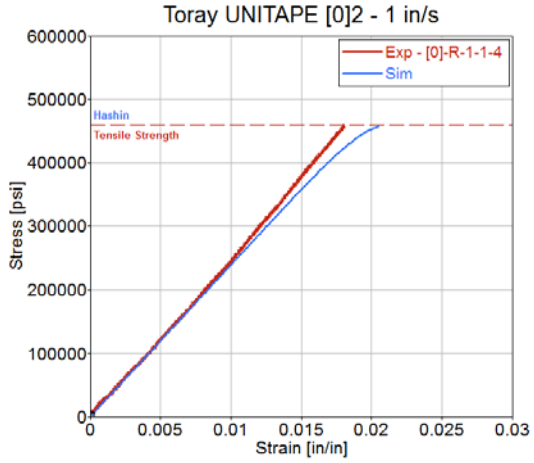

Figure 115. Comparison of MAT-58 simulated and test stress strain data: Toray Carbon Unitape $[0°]_2$ at a speed of 1 in/s, in tension

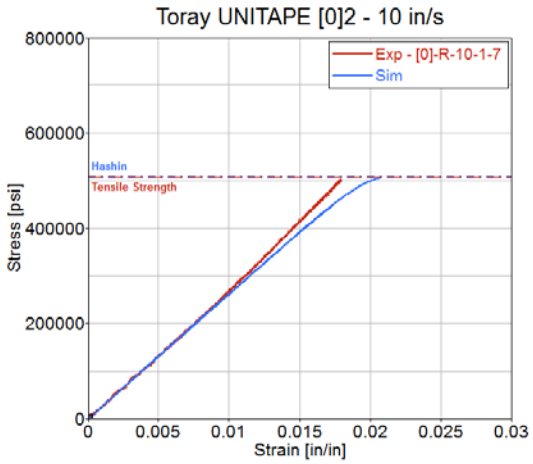

Figure 116. Comparison of MAT-58 simulated and test stress strain data: Toray Carbon Unitape $[0°]_2$ at a speed of 10 in/s, in tension

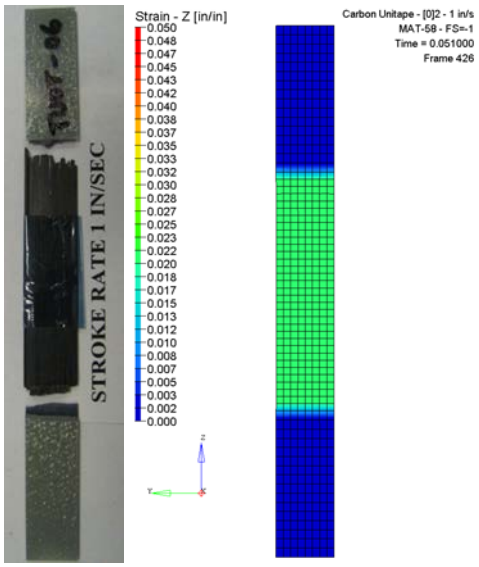

Figure 117. Axial strain distribution in Toray Carbon Unitape $[0°]_2$ at a speed of 1 in/s, in tension

The simulation results for orientation $[+15°/-15°]_S$ are shown in figures 118–120 for each speed. The numerical model closely follows the material response. However, it overestimates failure for larger values of strength and strain. The failure criteria used by the material model suggest a fiber dominant behavior for this particular material orientation, allowing for a larger tensile strength. The strain distribution observed in figure 121 shows a fairly uniform distribution across the gage section of the testing specimen, but some small areas show higher strains that result from the off-axis material orientations. The failure locations (appendix C) observed in the test specimens verify this observation.

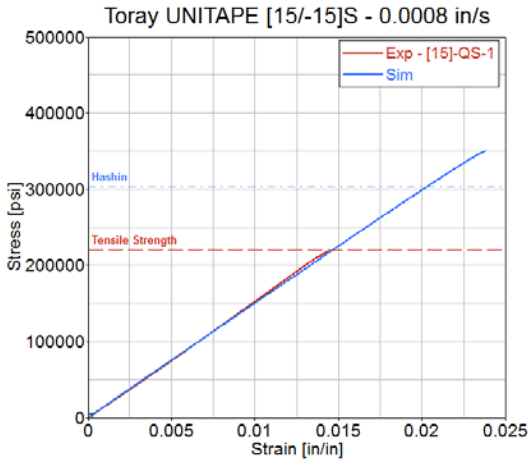

Figure 118. Comparison of MAT-58 simulated and test stress strain data: Toray Carbon Unitape $[+15°/-15°]_S$ at a speed of 0.0008 in/s, in tension

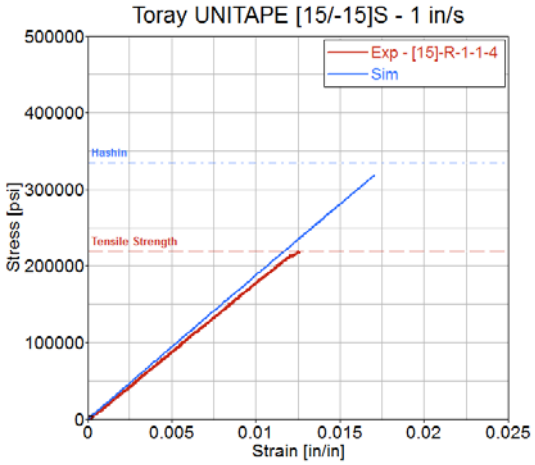

Figure 119. Comparison of MAT-58 simulated and test stress strain data: Toray Carbon Unitape $[+15°/-15°]_S$ at a speed of 1 in/s, in tension

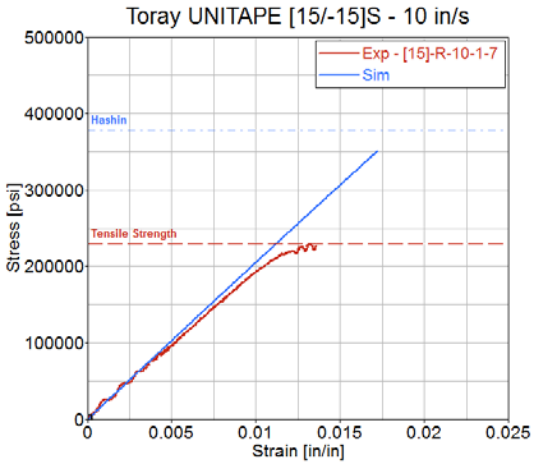

Figure 120. Comparison of MAT-58 simulated and test stress strain data: Toray Carbon Unitape $[+15°/-15°]_S$ at a speed of 10 in/s, in tension

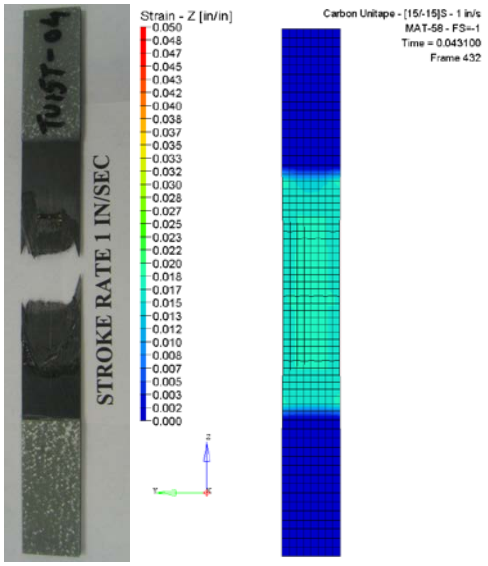

Figure 121. Axial strain distribution in Toray Carbon Unitape $[+15°/-15°]_S$ at a speed of 1 in/s, in tension

The simulation results for orientation $[+30°/-30°]_{2S}$ are shown in figures 122–124 for each speed. The numerical model follows the general trend of the material response, but it underestimates the failure strength and failure strain for the evaluated loading rates. The failure criteria for this particular material orientation suggest a somewhat matrix-dominant behavior limiting the tensile strength of the material. The strain distribution observed in figure 125 suggests that the model is capable of capturing the combined state of stress resulting from the off-axis material orientation. The failure locations (see appendix C) observed in the test specimens verify this observation.

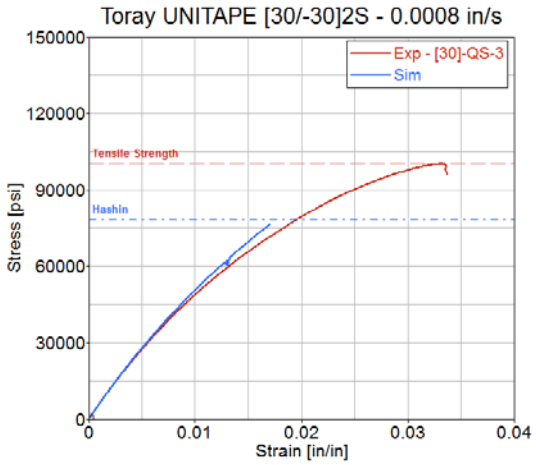

Figure 122. Comparison of MAT-58 simulated and test stress strain data: Toray Carbon Unitape $[+30°/-30°]_{2S}$ at a speed of 0.0008 in/s, in tension

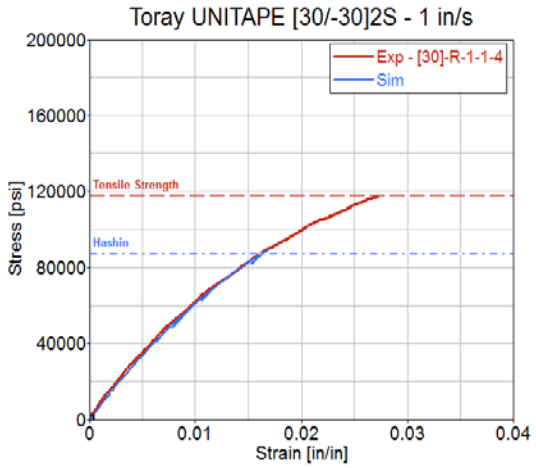

Figure 123. Comparison of MAT-58 simulated and test stress strain data: Toray Carbon Unitape $[+30°/-30°]_{2S}$ at a speed of 1 in/s, in tension

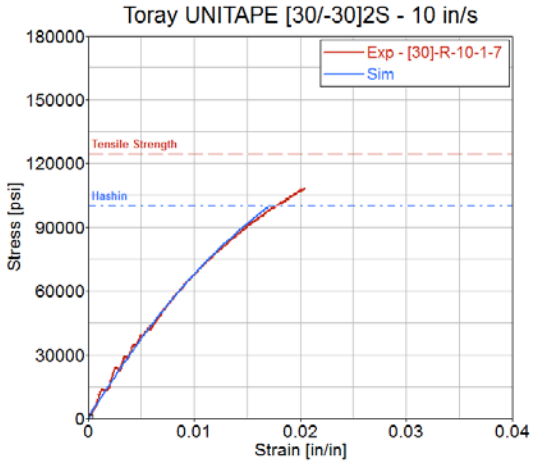

Figure 124. Comparison of MAT-58 simulated and test stress strain data: Toray Carbon Unitape $[+30°/-30°]_{2S}$ at a speed of 10 in/s, in tension

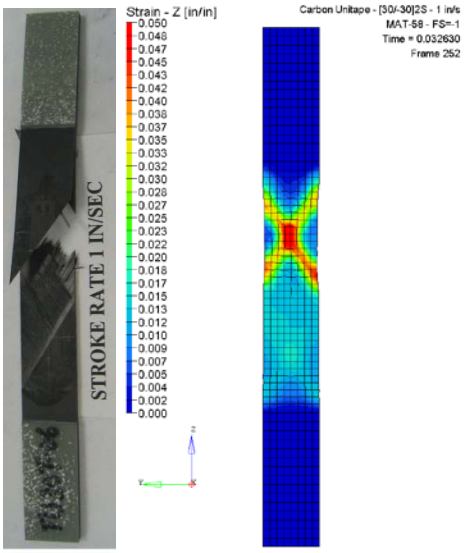

Figure 125. Axial strain distribution in Toray Carbon Unitape $[+30°/-30°]_{2S}$ at a speed of 1 in/s, in tension

The simulation results for orientation $[+45°/-45°]_{2S}$ are shown in figures 126–128 for each speed. The numerical model follows the nonlinear trend of the material response. The strain distribution observed in figure 129 shows areas where larger strain value suggests possible failure locations when compared with the physical testing specimen.

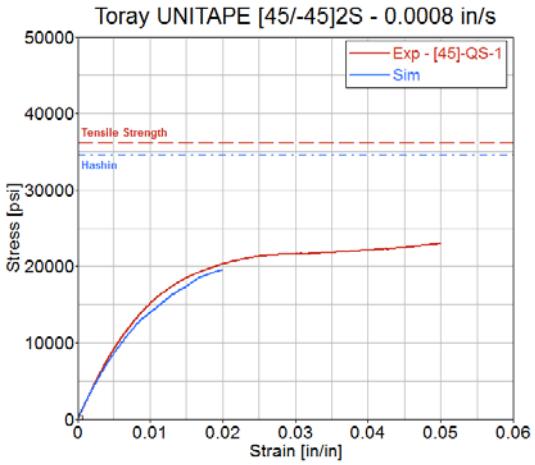

Figure 126. Comparison of MAT-58 simulated and test stress strain data: Toray Carbon Unitape $[+45°/-45°]_{2S}$ at a speed of 0.0008 in/s in tension

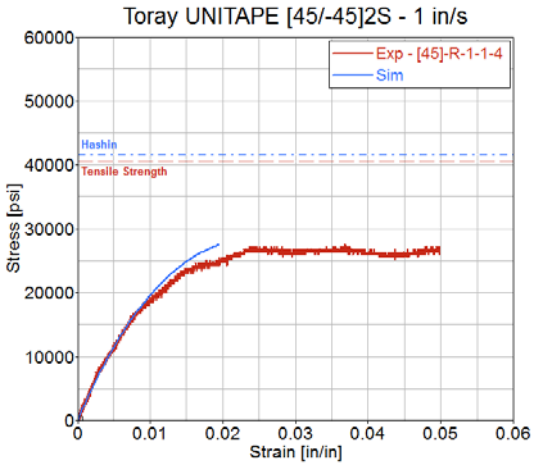

Figure 127. Comparison of MAT-58 simulated and test stress strain data: Toray Carbon Unitape $[+45°/-45°]_{2S}$ at a speed of 1 in/s in tension

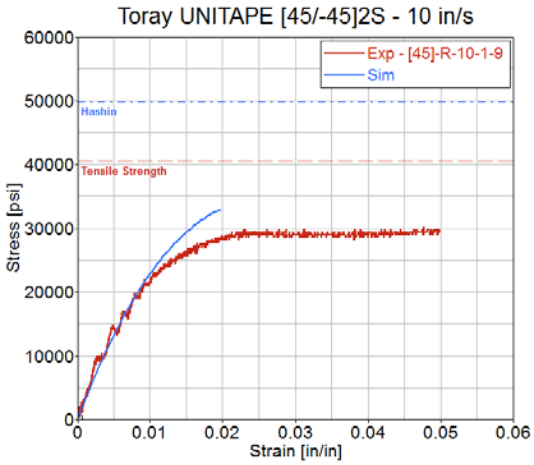

Figure 128. Comparison of MAT-58 simulated and test stress strain data: Toray Carbon Unitape $[+45°/-45°]_{2S}$ at a speed of 10 in/s, in tension

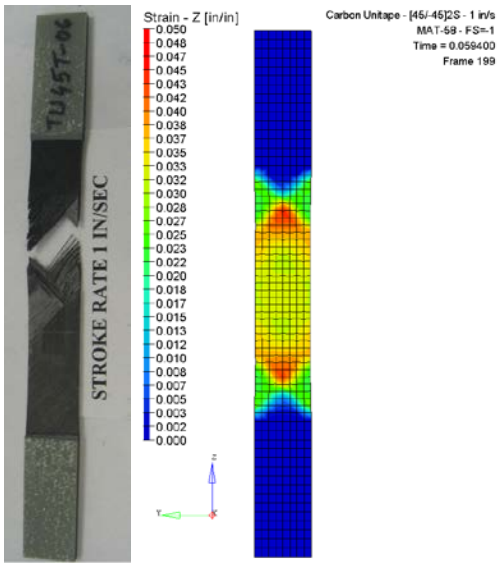

Figure 129. Axial strain distribution in Toray Carbon Unitape $[+45°/-45°]_{2S}$ at a speed of 1 in/s, in tension

5.7.2 Toray Unitape Shear Testing Model

This section summarizes the simulation results for the shear testing of Toray Unitape T800S/3900-2B for three speeds: 0.0008 in/s, 1 in/s, and 10 in/s. The available test data included specimens with a single stacking sequence of $[0°]_{12}$. One material model was assembled for each speed. The simulation results are shown in figures 130–132 for each speed. The numerical model closely follows the nonlinear segment of the shear test material response up to 0.03 rad strain, where the damage process at the notch root is initiated. The experiment showed that, at that point, a crack develops at the notch root causing a drop in the applied load. The simulation did

not capture such damage process. This phenomenon is reported in the test method standard to introduce error into the test results [19]. In addition, the test method does not recommend the use of unidirectional specimen $[0°]_N$ for this test. The shear strain distribution shown in figure 133 is uniform in the center of the gage section. The transverse strain distribution in figure 134 shows the damage process initiating at the notch root, similar to the test specimen (see appendix F).

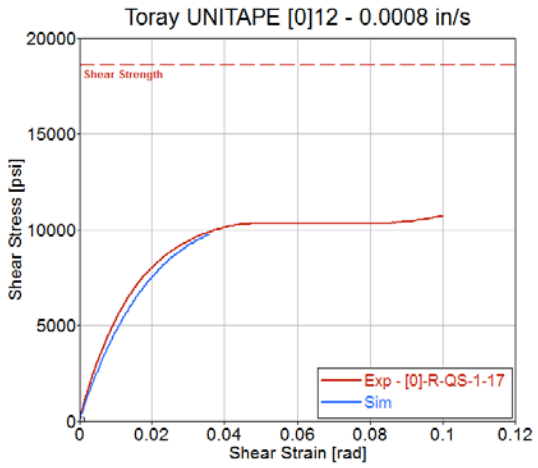

Figure 130. Comparison of MAT-58 simulated and test stress strain data: Toray Carbon Unitape $[0°]_{12}$ at a speed of 0.0008 in/s, in shear

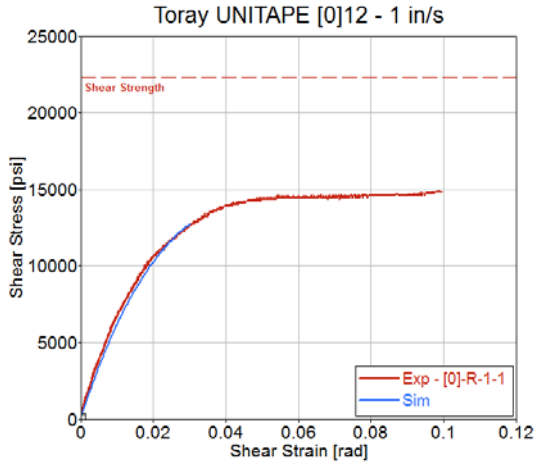

Figure 131. Comparison of MAT-58 simulated and test stress strain data: Toray Carbon Unitape $[0°]_{12}$ at a speed of 1 in/s, in shear

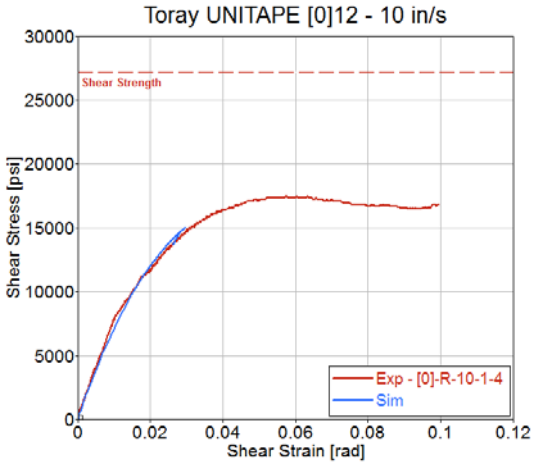

Figure 132. Comparison of MAT-58 simulated and test stress strain data: Toray Carbon Unitape $[0°]_{12}$ at a speed of 10 in/s, in shear

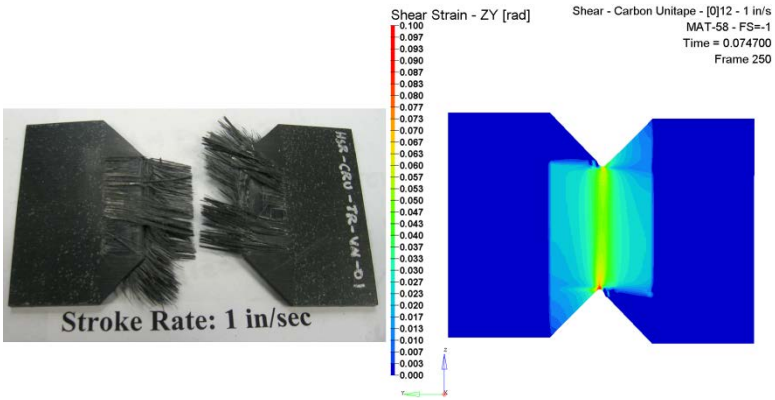

Figure 133. Shear strain distribution in Toray Carbon Unitape $[0°]_{12}$ at a speed of 1 in/s, in shear

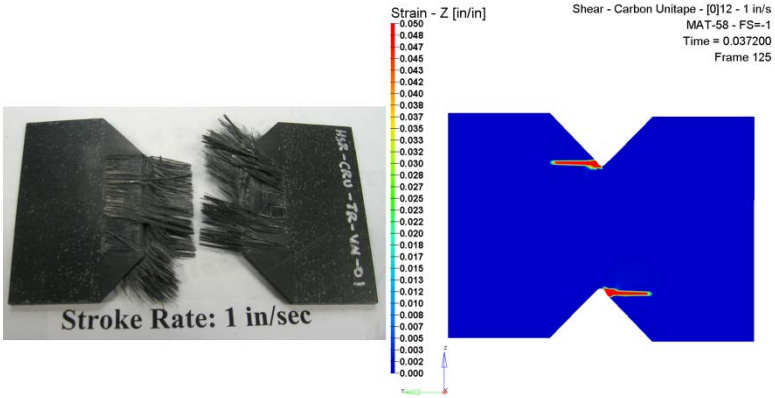

Figure 134. Transverse strain distribution in Toray Carbon Unitape $[0°]_{12}$ at a speed of 1 in/s

5.8 VALIDATION OF TORAY CARBON FABRIC T700G-12K-PW/3900-2 MATERIAL MODEL

In this section, the simulation results are presented for in-plane tension and shear tests. The material models were developed at the lamina level using the NIAR test data for Toray Fabric T700G-12K-PW/3900-2. The material properties and test results are summarized in appendices D and G. The material card used corresponds to LS-DYNA MAT-58, which includes a faceted failure surface. The input decks for the material models are listed in appendix H for each speed.

5.8.1 Toray Carbon Fabric Tension Testing Model

This section summarizes the simulation results for the tension testing of Toray Carbon Fabric T700G-12K-PW/3900-2 over three speeds: quasi-static 0.0008 in/s, 1 in/s, and 10 in/s. The available test data included laminates with four different stacking sequences: $[0°]_4$, $[+15°/-15°]_{2S}$, $[+30°/-30°]_{2S}$, and $[+45°/-45°]_{2S}$. All laminates are balanced and symmetric. One numerical model was assembled for each stacking sequence and a specific material model was associated per speed.

The simulation results for orientation $[0°]_4$ are shown in figures 135–137 for each speed. The numerical model, until failure, closely follows the material response. The strain distribution observed in figure 138 shows a uniform distribution across the gage section of the test specimen. This suggests that failure can occur anywhere within the gage section, as can be seen in the failure mode observed in the test specimen. However, failure locations (see appendix D) observed in the test specimens tend to focus toward the tabs.

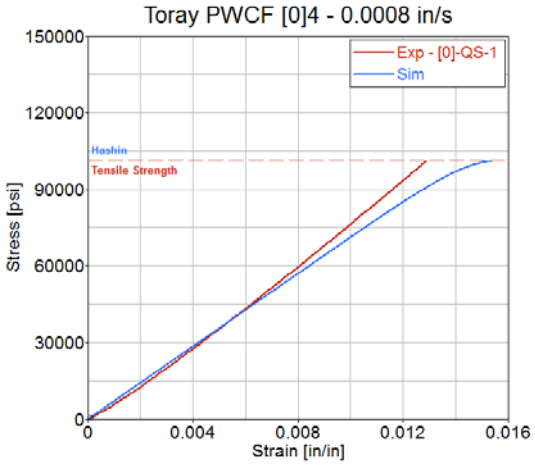

Figure 135. Comparison of MAT-58 simulated and test stress strain data: Toray PW Carbon Fabric $[0°]_4$ at a speed of 0.0008 in/s, in tension

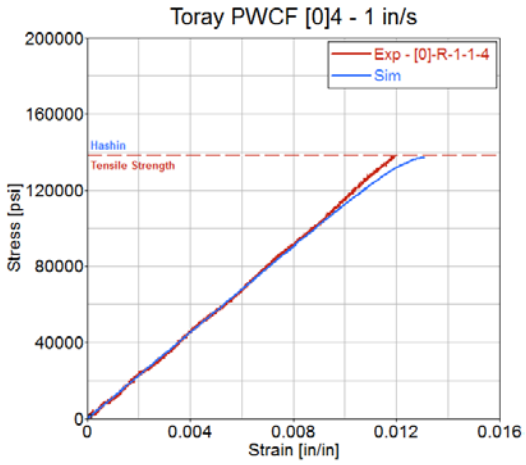

Figure 136. Comparison of MAT-58 simulated and test stress strain data: Toray PW Carbon Fabric $[0°]_4$ at a speed of 1 in/s, in tension

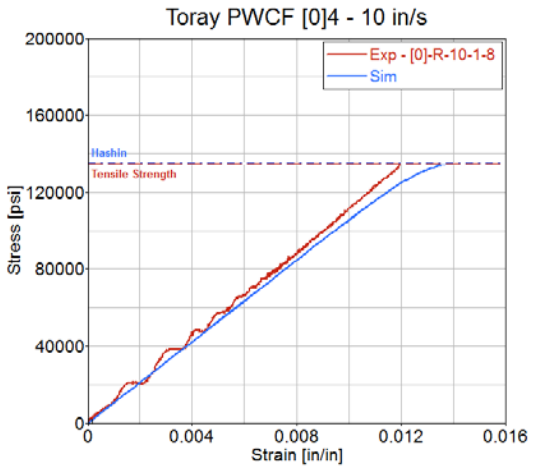

Figure 137. Comparison of MAT-58 simulated and test stress strain data: Toray PW Carbon Fabric $[0°]_4$ at a speed of 10 in/s, in tension

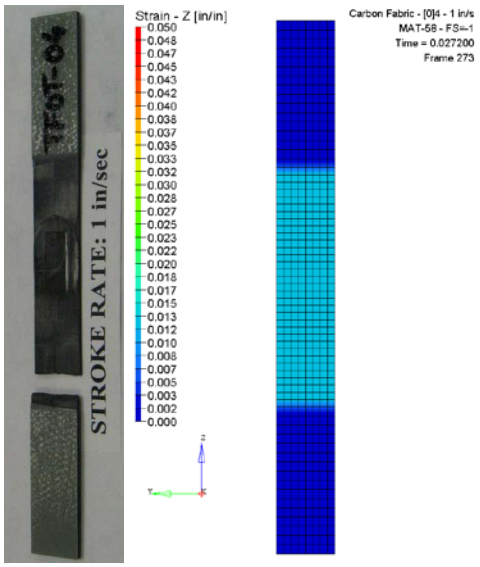

Figure 138. Axial strain distribution in Toray PW Carbon Fabric $[0°]_4$ at a speed of 1 in/s, in tension

The simulation results for orientation $[+15°/-15°]_{2S}$ are shown in figures 139–141 for each speed. The numerical model deviates from the material response during the early stages of deformation. The material model does not adequately capture the combined state of stress resulting from the off-axis material orientation. However, the strain distribution in figure 142 shows a uniform strain distribution over the gage length of the specimen. The random failure locations (see appendix D) observed in the test specimens verify this observation.

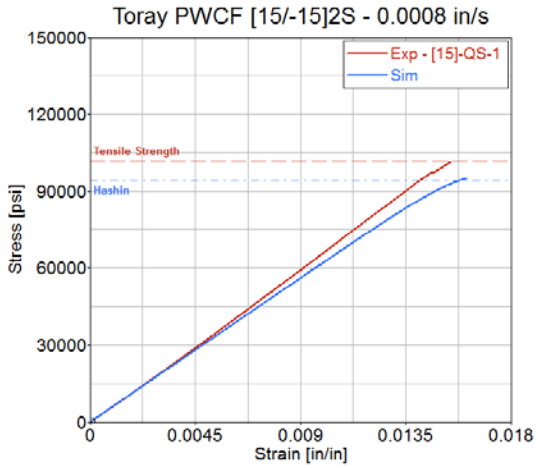

Figure 139. Comparison of MAT-58 simulated and test stress strain data: Toray PW Carbon Fabric $[+15°/-15°]_{2S}$ at a speed of 0.0008 in/s, in tension

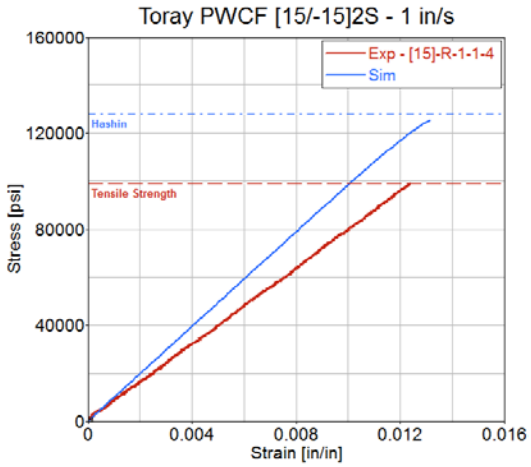

Figure 140. Comparison of MAT-58 simulated and test stress strain data: Toray PW Carbon Fabric $[+15°/-15°]_{2S}$ at a speed of 1 in/s, in tension

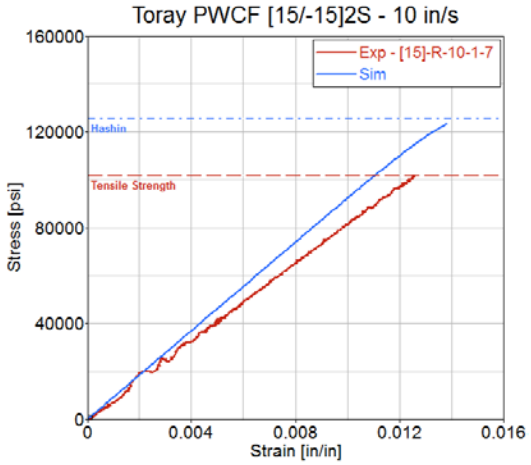

Figure 141. Comparison of MAT-58 simulated and test stress strain data: Toray PW Carbon Fabric $[+15°/-15°]_{2S}$ at a speed of 10 in/s, in tension

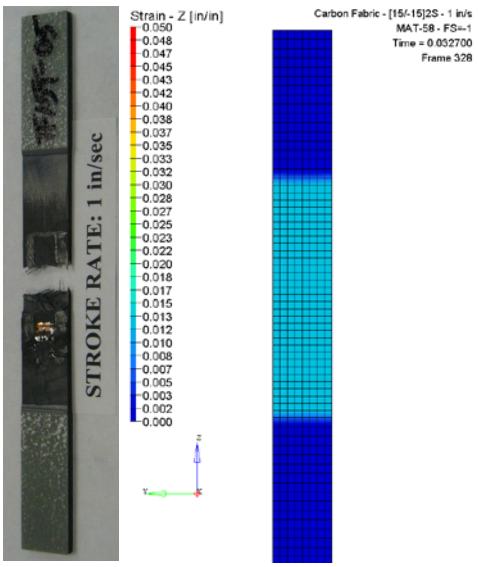

Figure 142. Axial strain distribution in Toray PW Carbon Fabric $[+15°/-15°]_{2S}$ at a speed of 1 in/s, in tension

The simulation results for orientation $[+30°/-30°]_{2S}$ are shown in figures 143–146 for each speed. The numerical model deviates from the test material response during the early stages of deformation; as deformation progresses, the slope differs between the simulation and the test response. To verify such observation, the modulus of elasticity for orientations $[+15°/-15°]_{2S}$ and $[+30°/-30°]_{2S}$ were estimated using CLT and the material properties at the lamina level: the slope of simulation curves correspond to moduli estimated using CLT. Therefore, simulation results follow an ideal trend and only capture the progressive degradation of material properties to some extent. In addition, simulation results show higher failure strengths when compared to the test results. The material model does not adequately capture the combined state of stress resulting from the off-axis material orientation. However, the strain distribution in figure 146 shows areas close to the specimen tab where the deformation is constrained, which may result in failure types similar to those observed in the physical specimen. The random failure locations (see appendix D) observed in the test specimens verify this observation.

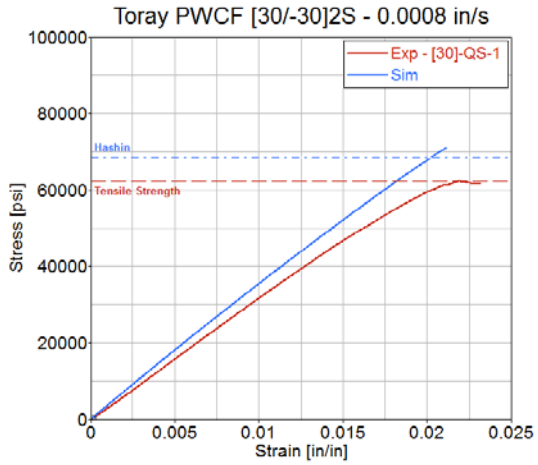

Figure 143. Comparison of MAT-58 simulated and test stress strain data: Toray PW Carbon Fabric $[+30°/-30°]_{2S}$ at a speed of 0.0008 in/s, in tension

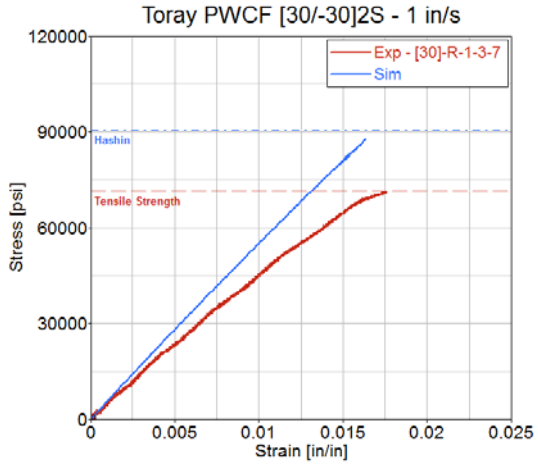

Figure 144. Comparison of MAT-58 simulated and test stress strain data: Toray PW Carbon Fabric $[+30°/-30°]_{2S}$ at a speed of 1 in/s, in tension

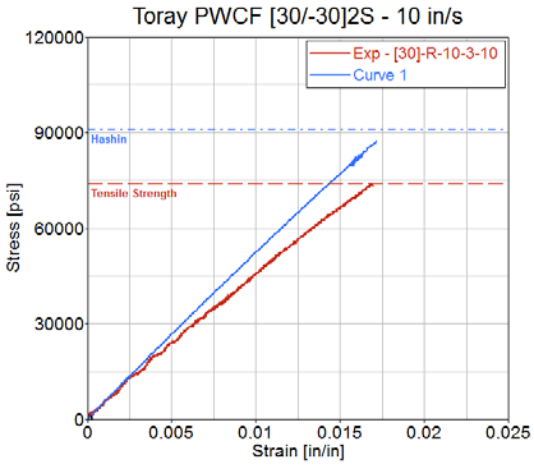

Figure 145. Comparison of MAT-58 simulated and test stress strain data: Toray PW Carbon Fabric $[+30°/-30°]_{2S}$ at a speed of 10 in/s, in tension

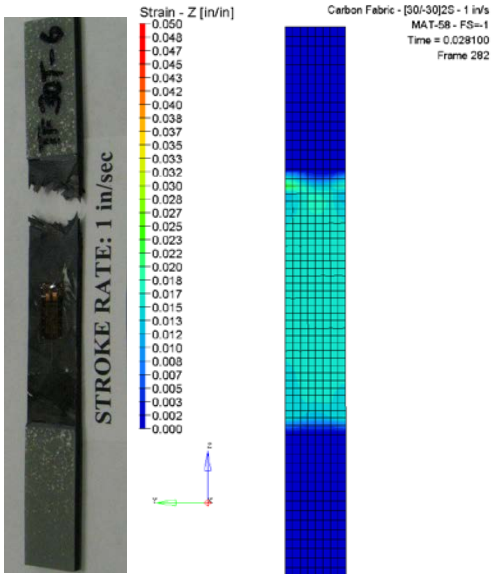

Figure 146. Axial strain distribution in Toray PW Carbon Fabric $[+30°/-30°]_{2S}$ at a speed of 1 in/s, in tension

The simulation results for orientation $[+45°/-45°]_{2S}$ are shown in figures 147–149 for each speed. The numerical model follows the nonlinear trend of the material response. Notice that the test curve only extends to approximately 2.1% strain for speed of 1 in/s and 3.5% for 10 in/s. This corresponds to the strain gage peeling from the specimen early in the test, limiting any further data collection. The strain distribution in figure 150 shows areas where larger strain values could imply failure locations when compared with the actual test specimen (see appendix D).

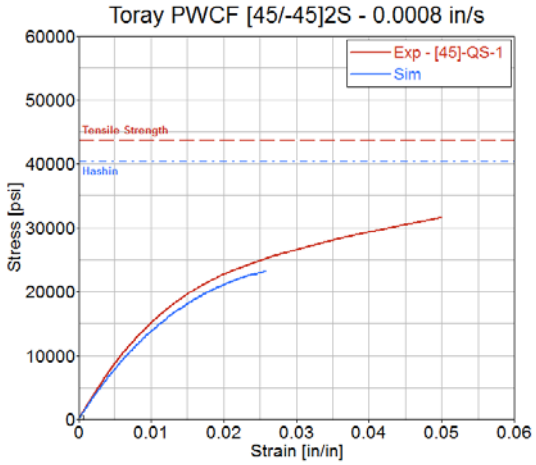

Figure 147. Comparison of MAT-58 simulated and test stress strain data: Toray PW Carbon Fabric $[+45°/-45°]_{2S}$ at a speed of 0.0008 in/s, in tension

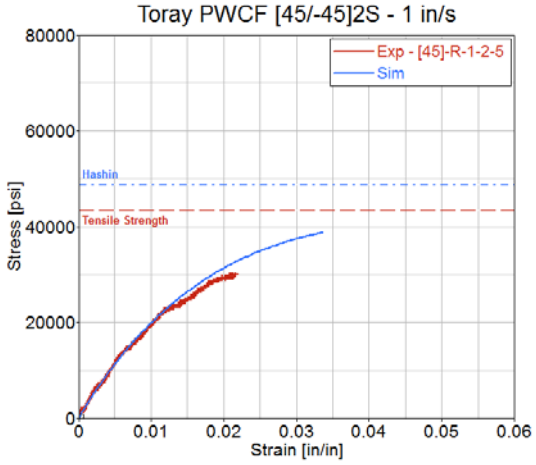

Figure 148. Comparison of MAT-58 simulated and test stress strain data: Toray PW Carbon Fabric $[+45°/-45°]_{2S}$ at a speed of 1 in/s, in tension

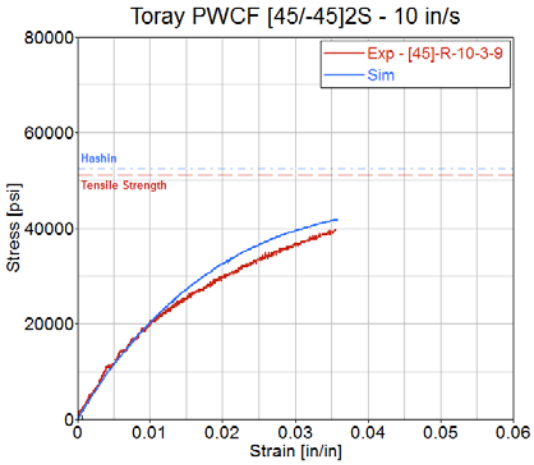

Figure 149. Comparison of MAT-58 simulated and test stress strain data: Toray PW Carbon Fabric $[+45°/-45°]_{2S}$ at a speed of 10 in/s, in tension

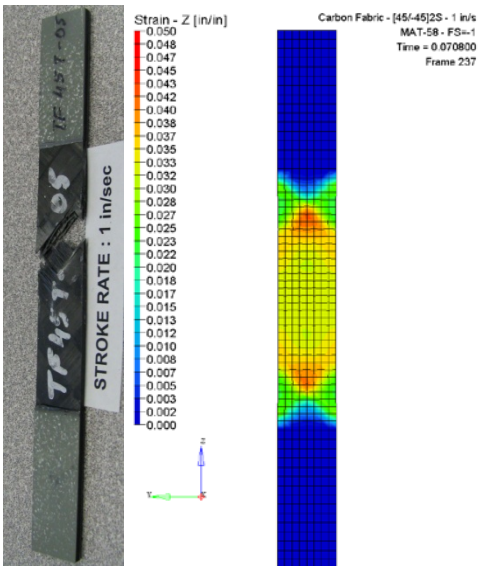

Figure 150. Axial strain distribution in Toray PW Carbon Fabric $[+45°/-45°]_{2S}$ at a speed of 1 in/s, in tension

5.8.2 Toray Carbon Fabric Shear Testing Model

This section summarizes the simulation results for the shear testing of Toray Carbon Fabric T700G-12K-PW/3900-2 for two speeds: 1 in/s and 10 in/s. The available test data included specimens with a single stacking sequence of $[0°]_{12}$.

Simulation results are summarized in figures 151 and figure 152 for each speed. The numerical model closely follows the initial nonlinear segment of the shear test material response, up until the initiation of the linear segment. The shear strain distribution observed in figure 153 shows

some discontinuities in the shear strain distribution across the gage section of the test specimen. The damage process was observed to initiate at the notch root, similar to the test specimen (see appendix G).

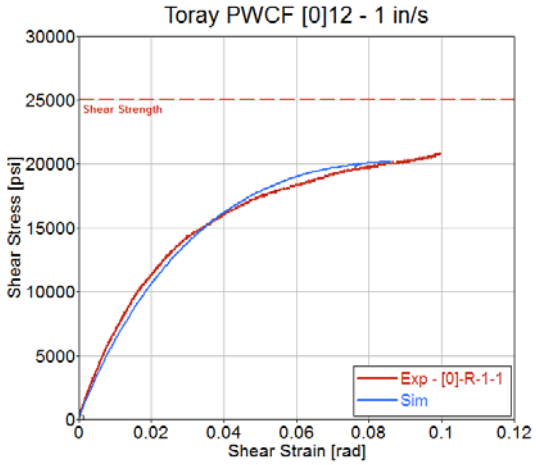

Figure 151. Comparison of MAT-58 simulated and test stress strain data: Toray PW Carbon Fabric $[0°]_{12}$ at a speed of 1 in/s, in shear

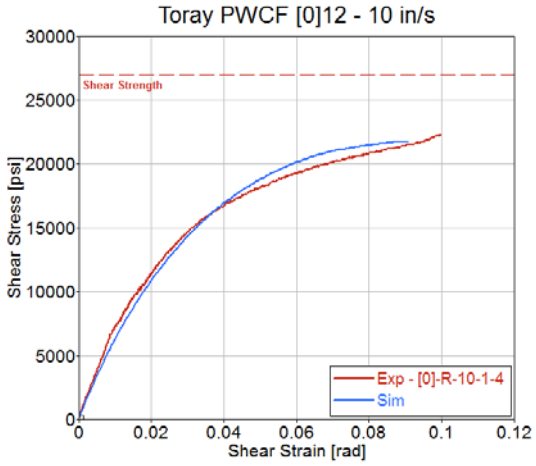

Figure 152. Comparison of MAT-58 simulated and test stress strain data: Toray PW Carbon Fabric $[0°]_{12}$ at a speed of 10 in/s, in shear

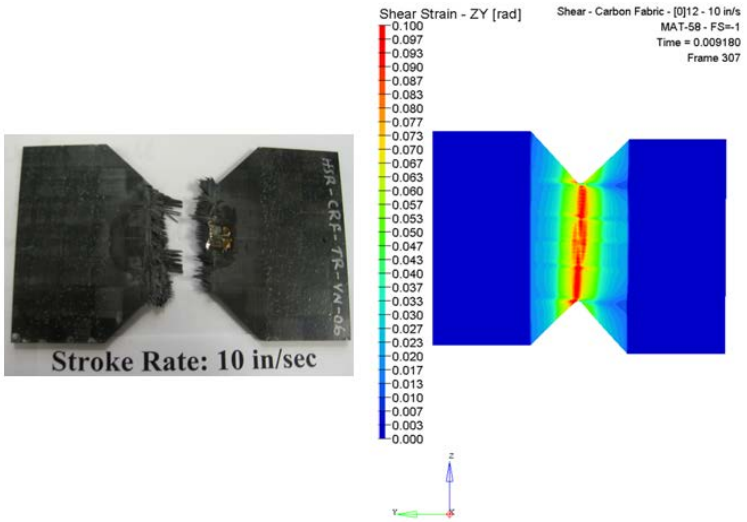

Figure 153. Distribution of strain in Toray PW Carbon Fabric $[0°]_{12}$ at a speed of 10 in/s, in shear

6. CONCLUSIONS AND FUTURE WORK

The process of developing composite and metallic numerical models that can be used to support the building block approach of designing crashworthy composite and metallic structures to meet crashworthiness requirements using numerical simulations is outlined in this report. Metallic and composite coupon-level test data from previous research programs were examined. Subsequently, material properties were extracted and variability within test results was quantified. Because the available test data were generated over a wide range of test speeds, from quasi-static to 100 in/s, the limitations of the dynamic material testing techniques and their sources of variability were identified. First, a numerical model of Aluminum 7075-T6 was developed using LS-DYNA material cards. Second, a finite element model of a high-speed servo-hydraulic testing system, including a slack-inducer mechanism and the associated specimen-gripping attachment, was assembled. The Al 7075-T6 material model was used as a benchmark for high-speed tension testing simulations of composite materials. Finally, numerical models of laminated composite materials were developed to simulate tension, compression, and in-plane shear test methods at various strain rates using LS-DYNA material cards and verified with test results.

Dynamic material properties exhibited different levels of variability in the test results. The repeatability among different laboratories could be questioned based on that observation. This is a consequence of the limited guidelines that are available for dynamic material property generation. The reliability and repeatability of the various in-house methodologies could be evaluated by generating a set of results that could then be compared directly with published data. In the absence of published data, comparable data between laboratories should be generated in which several parameters, such as specimen geometry, load and strain measurement techniques, data analysis, and test equipment, are standardized. Confidence should be built into the test method because variability levels observed in the test data will simply translate to the numerical model.

The material model developed for Aluminum 7075-T6 captured the material stress-strain response seen in the test results. A numerical model of the test specimen (only) was adequate to evaluate the material model. When evaluating the time history of individual measurements such as force, strain, or displacement, it was required to model the test assembly constituents involved in the load train. Simulation results for the specimen-gripping assembly exhibited high levels of correlation when compared to test data, especially during the early stages of elastic deformation. The test assembly was observed to play an important role in measuring physical quantities because of the elastic properties of the different components. The model can be further used as a tool to evaluate the testing system and may bring needed clarity to issues that currently limit the high-speed testing technique, such as the effect of the grip mass on the test.

Simulation results for laminated composite materials exhibited high levels of correlation with test data, regardless of the material, when simulating the response along the principal material direction, $[0°]_N$. This was anticipated, because material properties at the lamina level are generated from testing laminates along the principal material direction. Conversely, simulation results for the balanced and symmetric off-axis orientations exhibited different levels of correlation depending on the material architecture. The simulation results for Toray PW Carbon Fabric and Newport E-Glass Fabric for orientations $[+15°/-15°]_{2S}$ and $[+30°/-30°]_{2S}$ showed evidence of deviations from the test results. The numerical model deviated from the material response during the early stages of deformation and did not adequately capture the combined state of stress resulting from the off-axis material orientation. However, simulation results for Toray Carbon Unitape exhibited good correlation with the material response for orientations $[+15°/-15°]_S$, $[+30°/-30°]_{2S}$, and $[+45°/-45°]_{2S}$. This was expected, because the constitutive model implemented in the LS-DYNA material card MAT-58 assumes each lamina to be unidirectional.

The LS-DYNA material card MAT-58 was observed to capture part of the non-linearity observed in the test specimens with off-axis orientations. In contrast to MAT-54, MAT-58 damage evolution pre-failure detection introduces a smooth change in material behavior by using failure strain data. Therefore, the model response is calibrated with experimental strain data without manipulation of non-physical parameters. The material model response was observed to be highly sensitive to the definition of a failure strain; therefore, caution is required when extracting failure strain from test data. Variability in the test measurement will simply translate to the simulation results.

The in-plane material response was simulated with shell elements in an efficient manner. The MAT-58 implementation of Hashin failure criteria was observed to overestimate the failure strength for tensile failure modes and underestimate the failure strength for matrix failure modes. The observed material model limitations depend in part on the complexity of the various failure modes observed in the test specimen. Higher levels of detail when dealing with other failure modes may require the implementation of more computationally expensive elements, such as solid or cohesive elements, to simulate delamination in composite materials.
The simulation results for the in-plane shear testing of fabric architectures, such as carbon plain weave or fiber satin weave, showed good correlation of the material response over the first

nonlinear segment until reliable shear strain data were recorded close to 0.09 rad shear strain. Toray Carbon Unitape was a special case: simulation results exhibited good correlation with the test material response over the nonlinear segment of the stress-strain curve up to 0.03 rad shear strain, at which point a crack developed at the notch root of the unidirectional material, causing a drop in the applied load. The simulation did not capture this phenomenon or the subsequent damage process that is reported to introduce error into the test results.

7. REFERENCES

1. Abramowitz, A., Smith, T.G., Vu, T., and Zvanya, J.R., "Vertical Drop Test of a Narrow-Body Transport Fuselage Section With Overhead Stowage Bins," FAA report DOT/FAA/AR-01/100, September 2002.

2. Jackson, K.E. and Fasanella, E.L., "Crash Simulation of a Vertical Drop Test of B737 Fuselage Section with Overhead Bins and Luggage," Proceedings of the Third Triennial Aircraft Fire and Cabin Safety Conference, Atlantic City, NJ, October 2001.

3. Jackson, K.E., Fuchs, Y., and Kellas, S., "Overview of the NASA Subsonic Rotary Wing Aeronautics Research Program in Rotorcraft Crashworthiness," *Journal of Aerospace Engineering*, Vol. 22, No. 3, 2009, pp. 229–239.

4. Federal Register E7-11153, "Special Conditions: Boeing Model 787-8 Airplane; Crashworthiness," Federal Aviation Administration, Vol. 72, No. 111, September 2007, pp. 32021–32023.

5. Olivares, G., "Hybrid II and Federal Aviation Administration Hybrid III Anthropomorphic Test Dummy Dynamic Evaluation Test Series," FAA report DOT/FAA/AR-11/24, June 2013.

6. Raju, K.S. and Acosta, J.F., "Crashworthiness of Composite Fuselage Structures – Material Dynamic Properties (Phase-I)," FAA report DOT/FAA/AR-09/8, November 2010.

7. Tomblin, J., McKenna, J., Ng, Y., and Raju, K.S., "B-Basis Design Allowables for Epoxy-Based Prepreg Newport E-Glass Fabric NB321/7781," available at http://www.niar.wichita.edu/agate/Documents/Materials/WP3.3-033051-097.pdf (accessed on 03/01/2016).

8. Davis, J.R., "Tensile Testing," *ASM International*, 2nd ed., Materials Park, OH, 2004, pp. 215–260.

9. Kleiner, M., Tekkaya, A.E., Demir, O.K., Risch, D., and Psyk, V., "A Drop-weight High-speed Tensile Testing Instrument," *Computer Aided Engineering*, Vol. 3, No. 2, June 2009, pp. 175–180.

10. Barre, S., Chotard, T., and Benzeggagh, M.L., "Comparative Study of Strain Rate Effects on Mechanical Properties of Glass Fibre-Reinforced Thermoset Matrix Composites," *Composites Part A: Applied Science and Manufacturing*, Vol. 27, No. 12, 1996, pp. 1169–1181.

11. Harris, B., Beaumont, P.W.R., and de Ferran, E.M., "Strength and Fracture Toughness of Carbon Fibre Polyester Composites," *Journal of Materials Science*, Vol. 6, Issue 3, March 1971, pp. 238–251.

12. Hoggatt, C.R. and Recht, R.F., "Stress-Strain Data Obtained at High Rates Using an Expanding Ring," *Experimental Mechanics*, Vol. 9, No. 10, October 1969, pp. 441–448.

13. Niordson, F., "A Unit for Testing Materials at High Strain Rates," *Experimental Mechanics*, Vol. 5, No. 1, January 1965, pp. 29–32.

14. Hsiao, H.M., Daniel, I.M., and Cordes, R.D., "Strain Rate Effects on the Transverse Compressive and Shear Behavior of Unidirectional Composites," *Journal of Composite Materials*, Vol. 33, No. 17, September 1999, pp. 1620–1642.

15. Sierakowski, R.L. and Chaturvedi, S.K., *Dynamic Loading and Characterization of Fiber-Reinforced Composites*, Wiley, 1997, Chapter 2, "Dynamic Properties," pp. 15–98.

16. ASTM E8, "Standard Test Method for Tension Testing of Metallic Materials," *ASTM International*, West Conshohocken, PA, 2012.

17. ASTM D3039, "Standard Test Method for Tensile Properties of Polymer Matrix Composite Materials," *ASTM International*, West Conshohocken, PA, 2014.

18. Adams, D., "A Comparison of Shear Test Methods," *High-Performance Composites*, Vol. 13, No. 5, September 2005.

19. ASTM D7078, "Standard Test Method for Shear Properties of Composite Materials by V-Notched Rail Shear Method," *ASTM International*, West Conshohocken, PA, 2012.

20. Wegner, P. and Adams, D., "Verification of the Combined Load Compression (CLC) Test Method," FAA report DOT/FAA/AR-00/26, 2000.

21. SACMA SRM 1-94, "SACMA Recommended Test Method for Compressive Properties of Oriented Fiber-Resin Composites," Suppliers of Advance Composites Materials Association, 1994.

22. ASTM D695, "Standard Test Method for Compressive Properties of Rigid Plastics," *ASTM International*, West Conshohocken, PA, 2010.

23. Bardenheier, R. and Rogers, G., "Dynamic Impact Testing," available at http://www.gef.es/Congresos/21/pdf/2-07.pdf (accessed on 02/01/16).

24. Montgomery, D., *Design and Analysis of Experiments*, Wiley, Hoboken, NJ, 2000.

25. Borsutzki, M., Cornette, D., Kuriyama, Y., et al., "Recommendations for Dynamic Tensile Testing of Sheet Steels," available at http://www.worldautosteel.org/download_files/High%20Strain%20Rate/HighStrainRate_Recommended_Procedure.pdf (accessed on 03/01/16).

26. Wong, C. "IISI AutoCo Round-Robin Dynamic Tensile Testing Project," available at http://www.worldautosteel.org/download_files/High%20Strain%20Rate/HighStrainRate_RptRndRobResults.pdf (accessed on 03/01/16).

27. Hove, I.H., Andersson, B., and Johnsen, T.E., "High Speed Tensile Testing," *Journal de Physique IV*, Vol. 7, 1997, pp. 229–234.

28. Rusinek, A., Cheriguene, R., Baumer, A., Klepaczko, J.R., and Larour, P., "Dynamic Behavior of High-Strength Sheet Steel in Dynamic Tension: Experimental and Numerical Analysis," *The Journal Strain Analysis for Engineering Design*, Vol. 43, No. 1, January 2008, pp. 37–53.

29. Acosta, J.F. and Raju, K.S., "Evaluation of Cubic Specimens for Compression Testing at Different Strain Rates," 41st SAMPE Fall Technical Conference, Wichita, KS, 2009.

30. Keshavanarayana, S., Tan, K.Y., Siddique, M., and Elyas, S.F., "Crashworthiness of Composites—Material Dynamic Properties," available at https://www.niar.wichita.edu/niarworkshops/Portals/0/Crashworthiness%20Raju%20JAMS%202011_Rev1.pdf (accessed on 03/01/16).

31. Mendelson, A., *Plasticity: Theory and Application*, Krieger Publishing Co., Malabar, Florida, 1983.

32. "LS-DYNA Keyword User's Manual: Volume 1 Version 971," available at http://www.lstc.com/pdf/ls-dyna_971_manual_k.pdf (accessed on 03/01/16).

33. Fyllingen, Ø., Hopperstad, O.S., Hanssen, A.G., and Langseth, M., "Brick Versus Shell Elements in Simulations of Aluminum Extrusions Subjected to Axial Crushing," available at http://www.dynalook.com/european-conf-2009/G-I-01.pdf (accessed on 03/01/16).

34. Barbero, E., *Finite Element Analysis of Composite Materials Using ANSYS*, Second Edition, CRC Press, Boca Raton, FL, 2008.

35. Zheng, X., *Nonlinear Strain Rate Dependent Composite Model for Explicit Finite Element Analysis* (Doctoral Dissertation), The University of Akron, Ohio, retrieved from OhioLINK Electronic Theses and Dissertations Center, 2006.

36. Hamidreza, Z., *Experimental and Numerical Investigation of Crash Structures Using Aluminum Alloys*, Cuvillier Verlag, Gottingen, 2008.

37. Schweizerhof, K., "Crashworthiness Analysis with Enhanced Composite Material Models in LS-DYNA—Merits and Limits," LS-DYNA World Conference, Detroit, 1998.

38. Richard, M.C., "Failure Theory for Materials Science and Engineering," available at www.failurecriteria.com (accessed on 03/01/16).

39. Hashin, Z., "Failure Criteria for Unidirectional Fiber Composites," *Journal of Applied Mechanics*, Vol. 47, No. 2, 1980, pp. 329–334.

APPENDIX A—ALUMINUM 7075-T6 TENSION TESTING RESULTS

Table A-1. Summary of test results for aluminum 7075-T6 at a speed of 0.1 in/s

Actuator Speed [in/s]	Specimen ID	Tensile Strength [ksi]	Strain at Ultimate [in/in]	Young's Modulus [ksi]	Yield Stress [ksi]	Average Strain Rate [s-1]
0.1	R-0.1-1-04	74.94	0.08007	11,616	70.8	0.217
	R-0.1-2-09	86.14	0.1325	11,736	74.4	0.131
	R-0.1-3-36	78.18	0.1019	9,962	72.9	0.128
Average		79.75	0.1048	11,101	72.7	0.128
Standard Deviation		5.7	0.0263	992	1.81	0.002
Coefficient of Variation [%]		7.2	25.1	8.93	2.49	1.62

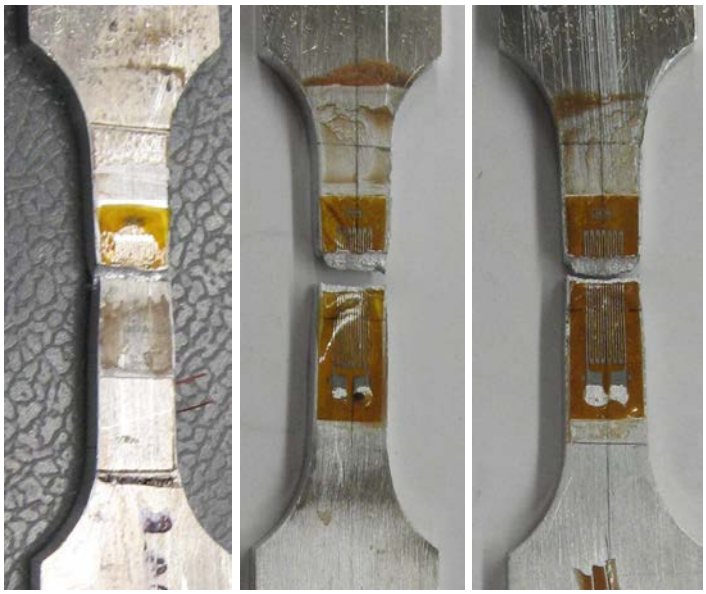

Figure A-1. Failure modes for aluminum 7075-T6 at a speed of 0.1 in/s

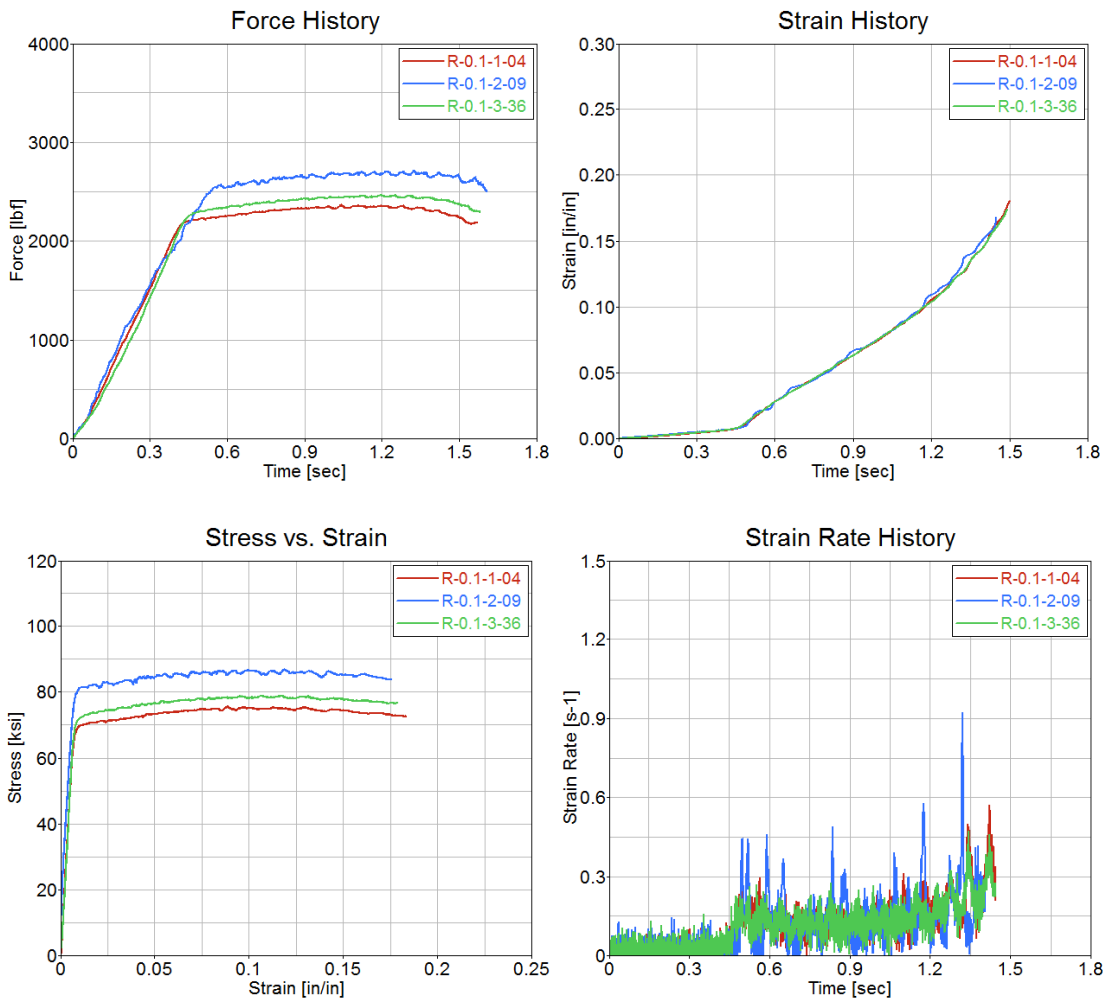

Figure A-2. Test results for aluminum 7075-T6 at a speed of 0.1 in/s

Table A-2. Summary of test results for aluminum 7075-T6 at a speed of 1 in/s

Actuator Speed [in/s]	Specimen ID	Tensile Strength [ksi]	Strain at Ultimate [in/in]	Young's Modulus [ksi]	Yield Stress [ksi]	Average Strain Rate [s^{-1}]
1	R-1-1-11	86.26	0.1171	10,989	80.4	1.56
	R-1-2-17	79.01	0.0936	11,571	80.3	1.48
	R-1-3-42	82.64	0.0902	9,139	75.3	1.56
Average		82.6	0.1003	10,566	78.67	1.53
Standard Deviation		3.6	0.0146	1,270	2.9	0.046
Coefficient of Variation [%]		4.39	14.6	12.02	3.71	3.01

Figure A-3. Failure modes for aluminum 7075-T6 at a speed of 1 in/s

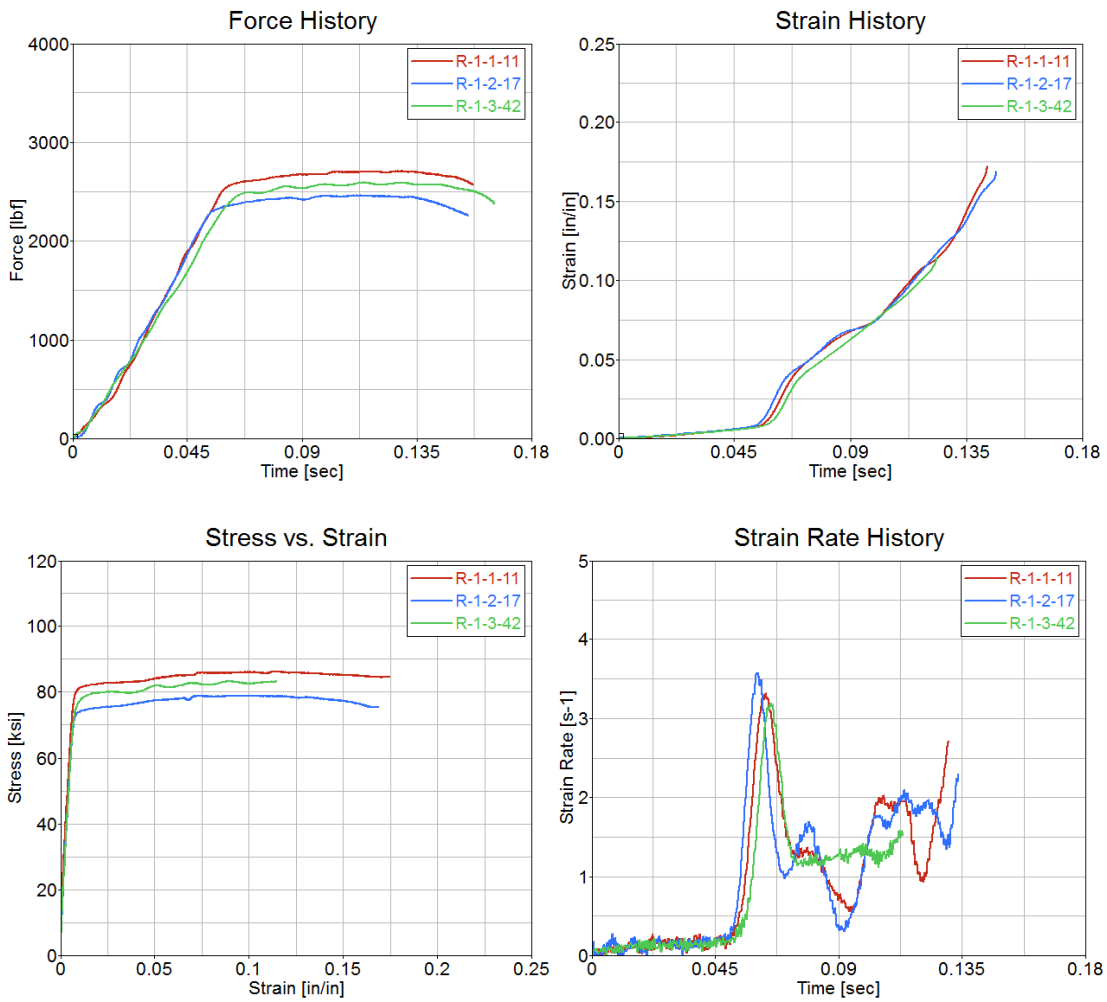

Figure A-4. Test results for aluminum 7075-T6 at a speed of 1 in/s

Table A-3. Summary of test results for aluminum 7075-T6 at a speed of 10 in/s

Actuator Speed [in/s]	Specimen ID	Tensile Strength [ksi]	Strain at Ultimate [in/in]	Young's Modulus [ksi]	Yield Stress [ksi]	Average Strain Rate [s^{-1}]
10	R-10-1-03	83.95	0.1164	11,889	76.2	10.95
	R-10-2-21	78.02	0.0925	7,103	71.6	10.76
	R-10-3-30	77.58	0.0818	10,416	68.2	10.64
Average		79.85	0.0969	9,803	72.0	10.78
Standard Deviation		3.55	0.0177	2,452	4.01	0.15
Coefficient of Variation [%]		4.45	18.25	25.01	5.58	1.45

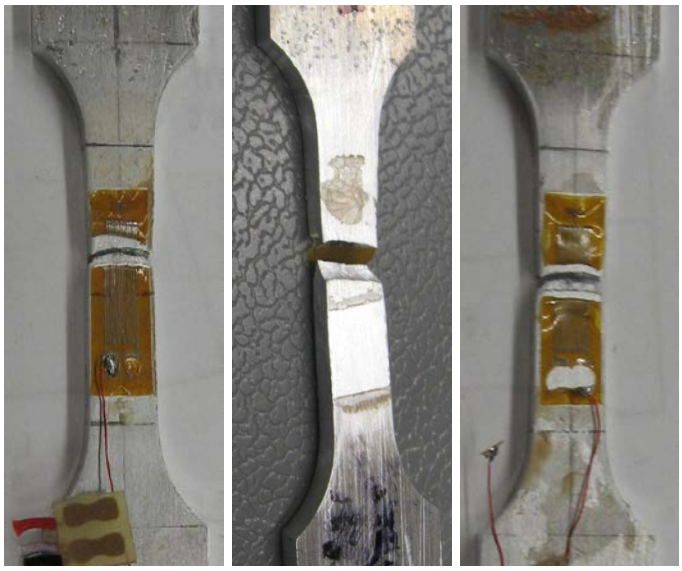

Figure A-5. Failure modes for aluminum 7075-T6 at a speed of 10 in/s

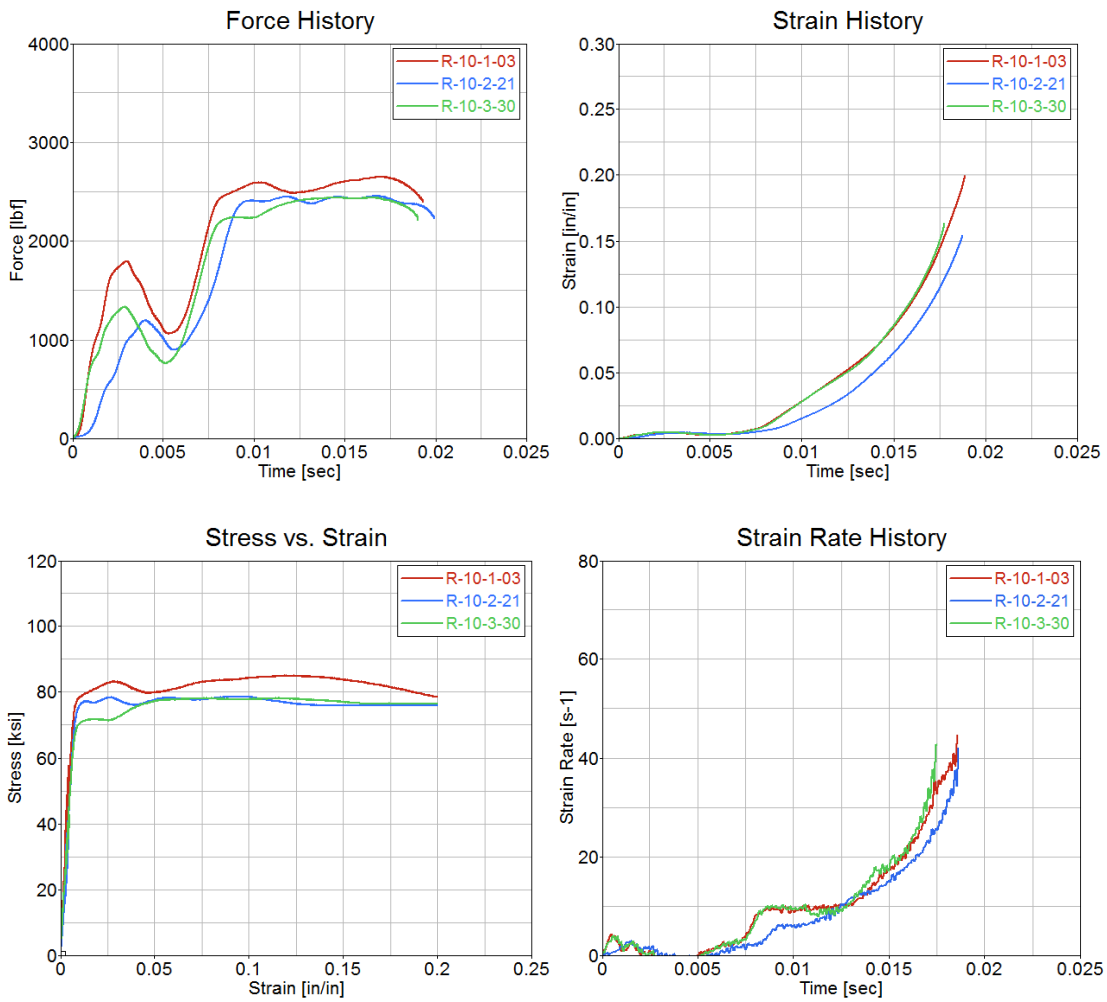

Figure A-6. Test results for aluminum 7075-T6 at a speed of 10 in/s

Table A-4. Summary of test results for aluminum 7075-T6 at a speed of 50 in/s

Actuator Speed [in/s]	Specimen ID	Tensile Strength [ksi]	Strain at Ultimate [in/in]	Young's Modulus [ksi]	Yield Stress [ksi]	Average Strain Rate [s^{-1}]
50	R-50-1-16	75.51	0.1001	9019	73.2	53.93
	R-50-2-18	94.74	0.1109	12,492	79.5	56.69
	R-50-3-35	77.04	0.0106	11,005	77.8	71.02
Average		82.43	0.0749	10,839	76.83	60.55
Standard Deviation		10.68	0.0561	1,743	3.26	9.17
Coefficient of Variation [%]		12.96	74.93	16.09	4.24	15.15

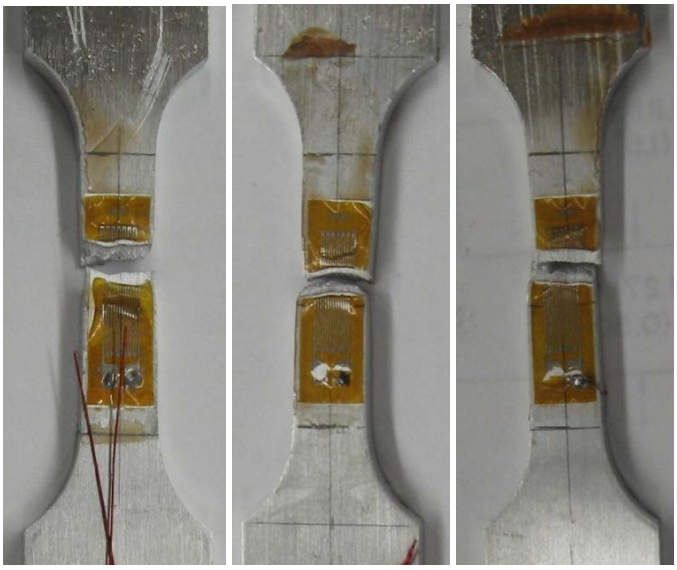

Figure A-7. Failure modes for aluminum 7075-T6 at a speed of 50 in/s

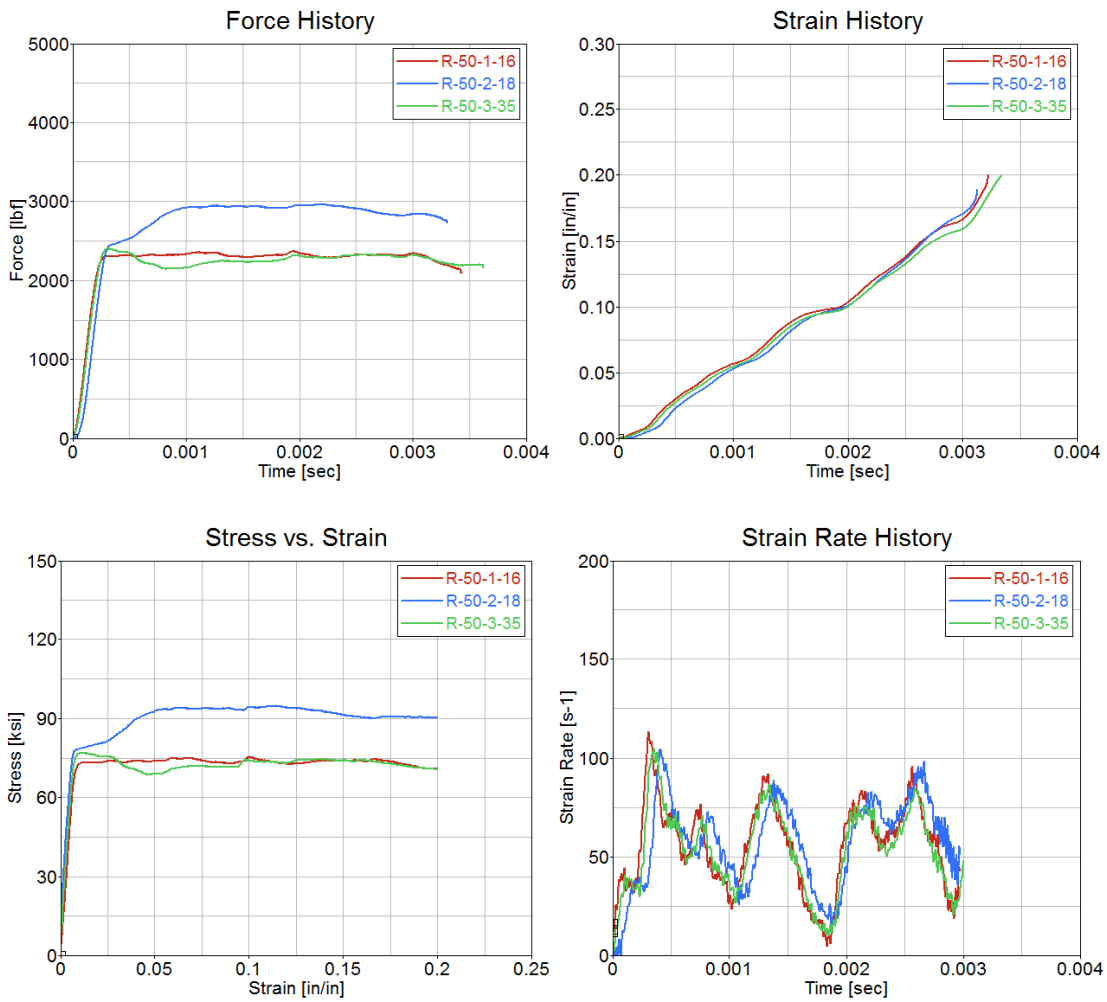

Figure A-8. Test results for aluminum 7075-T6 at a speed of 50 in/s

Table A-5. Summary of test results for aluminum 7075-T6 at a speed of 75 in/s

Actuator Speed [in/s]	Specimen ID	Tensile Strength [ksi]	Strain at Ultimate [in/in]	Young's Modulus [ksi]	Yield Stress [ksi]	Average Strain Rate [s^{-1}]
75	R-75-1-25	88.63	0.0914	9,445	75.2	105.2
	R-75-2-32	90.95	0.1186	10,465	76.9	111.5
	R-75-3-39	77.02	0.048	11,085	79.7	108.3
Average		85.5	0.086	10,332	77.27	108.37
Standard Deviation		7.4	0.0356	828	2.27	3.18
Coefficient of Variation [%]		8.7	41.39	8.01	2.94	2.93

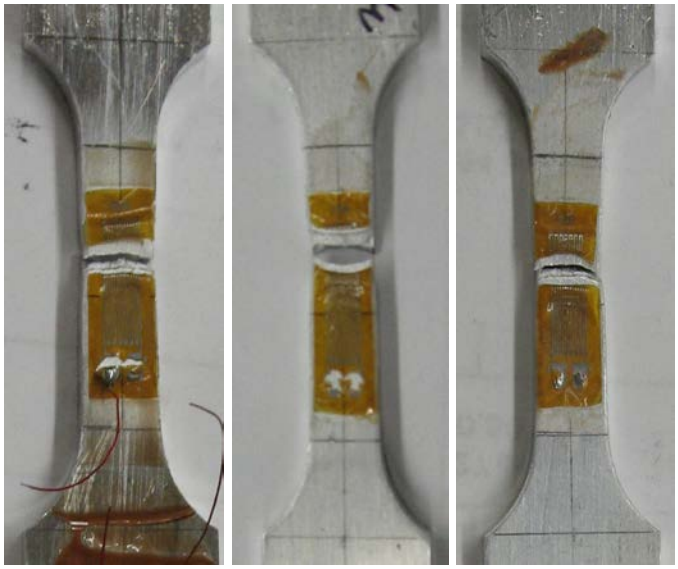

Figure A-9. Failure modes for aluminum 7075-T6 at a speed of 75 in/s

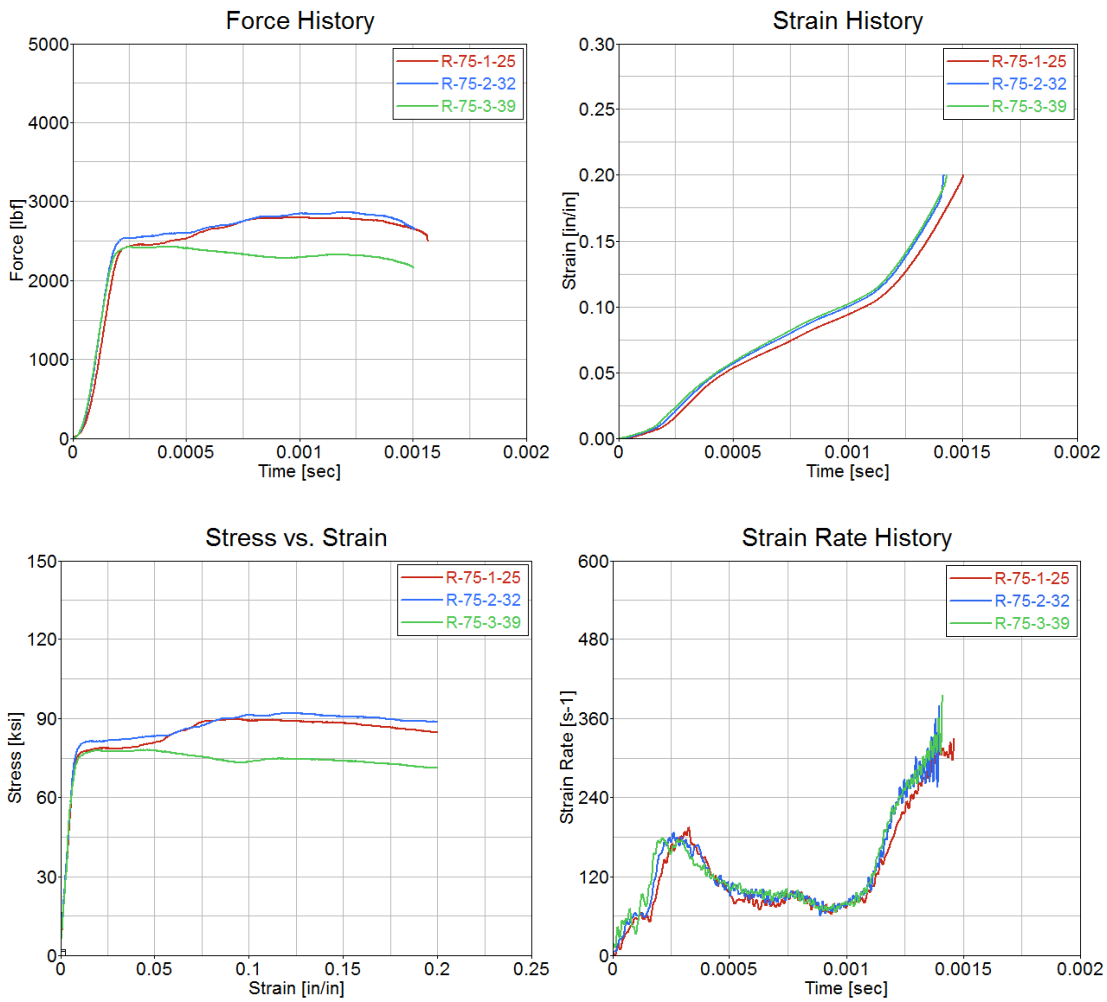

Figure A-10. Test results for aluminum 7075-T6 at a speed of 75 in/s

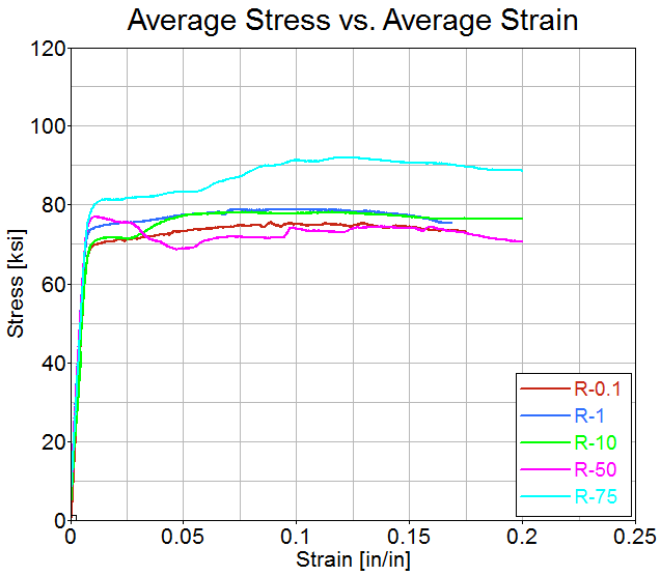

Figure A-11. Test results for aluminum 7075-T6: summary of all speeds

APPENDIX B—NEWPORT E-GLASS FABRIC TENSION TESTING RESULTS

B.1 FIBERGLASS $[0^{\circ}]_4$

Table B-1. Summary of test results for fiberglass $[0^{\circ}]_4$ at a speed of 0.0008 in/s

Actuator Speed [in/s]	Specimen ID	Tensile Strength [psi]	Maximum Recorded Strain [in/in]	Young's Modulus [Msi]	Average Strain Rate [s^{-1}]
0.00083	[0]-R-QS-1	62,287	0.0278	2.83	0.000424
	[0]-R-QS-2	63,414	0.0259	3.05	0.000389
	[0]-R-QS-3	72,580	0.0285	3.20	0.000385
Average		66,094	0.0274	3.03	0.000399
Standard Deviation		5645	0.0013	0.19	0.000021
Coefficient of Variation [%]		8.54	4.88	6.15	5.37

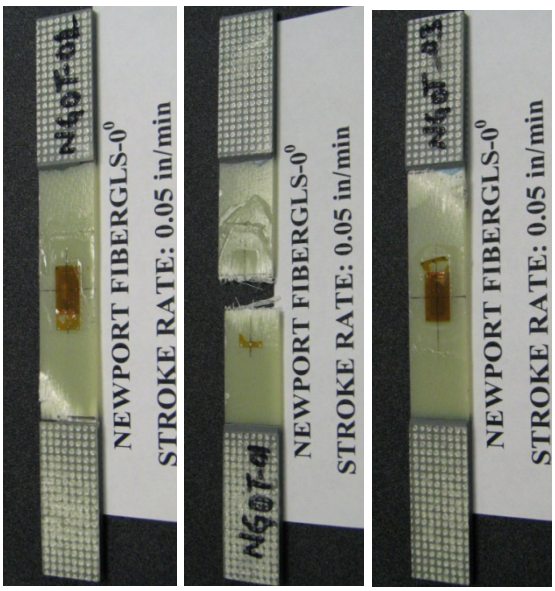

Figure B-1. Failure modes for fiberglass $[0^{\circ}]_4$ at a speed of 0.0008 in/s

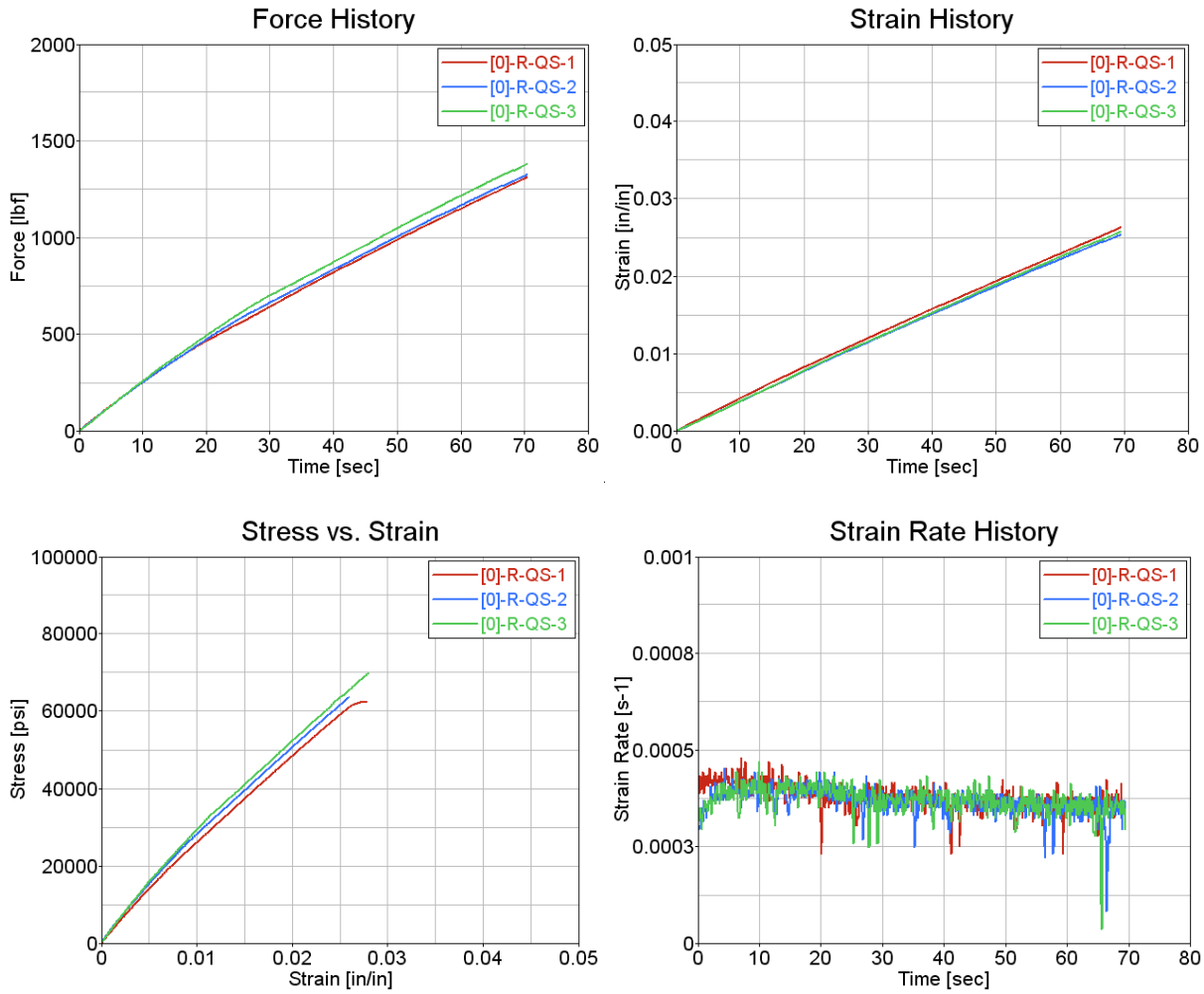

Figure B-2. Test results for fiberglass $[0^{\circ}]_4$ at a speed of 0.0008 in/s

Table B-2. Summary of test results for fiberglass $[0^{\circ}]_4$ at a speed of 1 in/s

Actuator Speed [in/s]	Specimen ID	Tensile Strength [psi]	Maximum Recorded Strain [in/in]	Young's Modulus [Msi]	Average Strain Rate [s^{-1}]
1	[0]-R-1-1-6	85,366	0.0271	4.33	0.3183
	[0]-R-1-2-7	93,285	0.0291	3.97	0.3226
	[0]-R-1-3-8	86,062	0.0232	3.40	0.3112
Average		88,238	0.0265	3.90	0.3174
Standard Deviation		4,385	0.0030	0.47	0.0058
Coefficient of Variation [%]		4.97	11.34	12.04	1.81

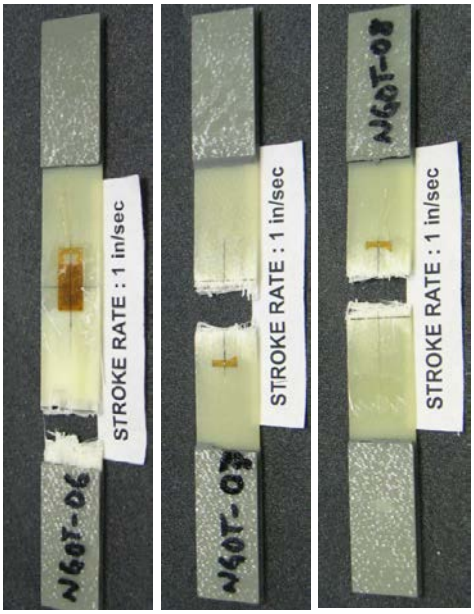

Figure B-3. Failure modes for fiberglass $[0^{\circ}]_4$ at a speed of 1 in/s

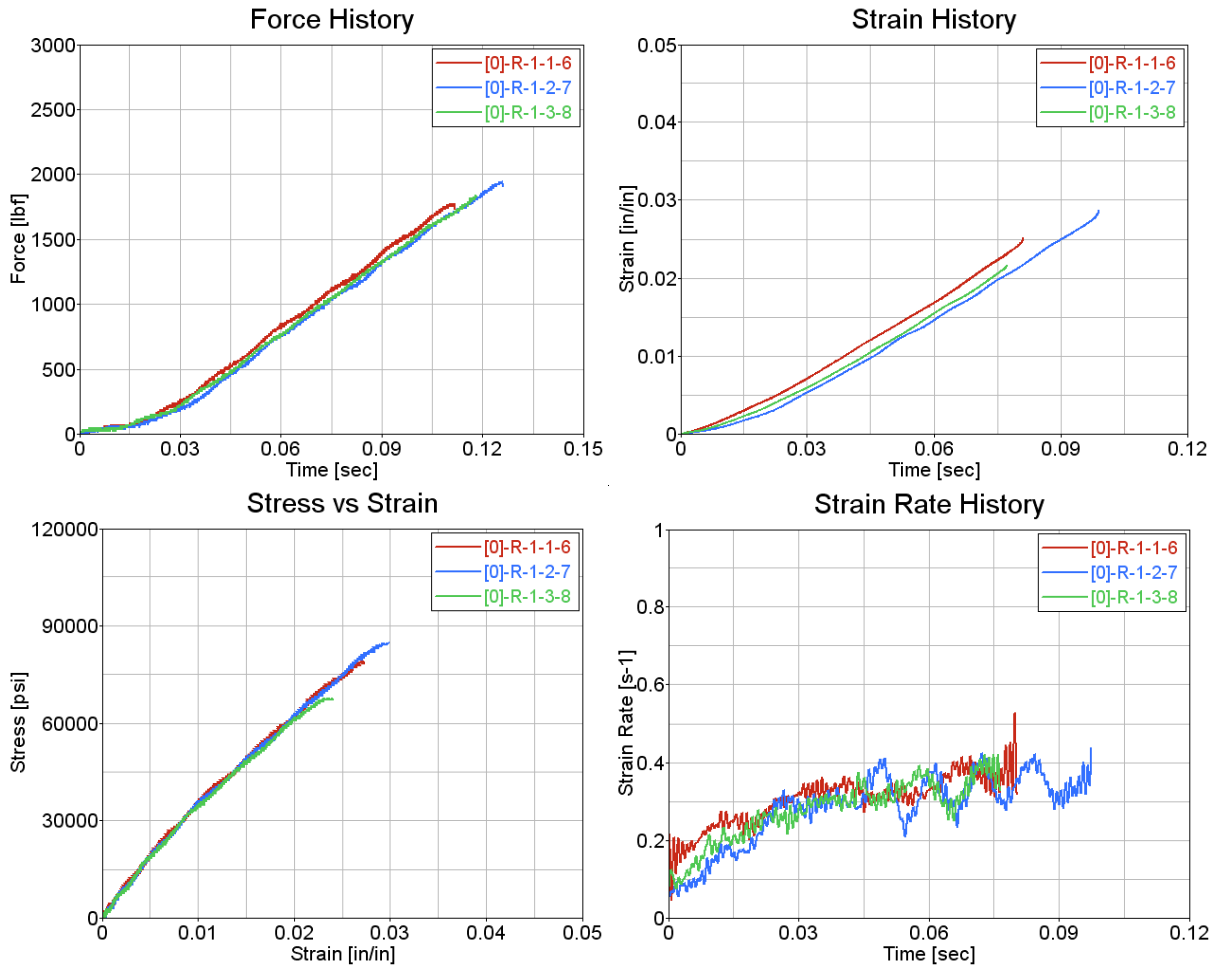

Figure B-4. Test results for fiberglass [0°]$_4$ at a speed of 1 in/s

Table B-3. Summary test results for fiberglass $[0^{\circ}]_4$ at a speed of 10 in/s

Actuator Speed [in/s]	Specimen ID	Tensile Strength [psi]	Maximum Recorded Strain [in/in]	Young's Modulus [Msi]	Average Strain Rate [s^{-1}]
10	[0]-R-10-1-5	100,937	0.0227	4.03	1.9185
	[0]-R-10-2-9	108,017	0.0320	4.13	1.9939
	[0]-R-10-3-10	96,158	0.0324	3.58	1.9718
Average		101,704	0.0290	3.91	1.9614
Standard Deviation		5,967	0.0055	0.30	0.0388
Coefficient of Variation [%]		5.87	18.97	7.57	1.98

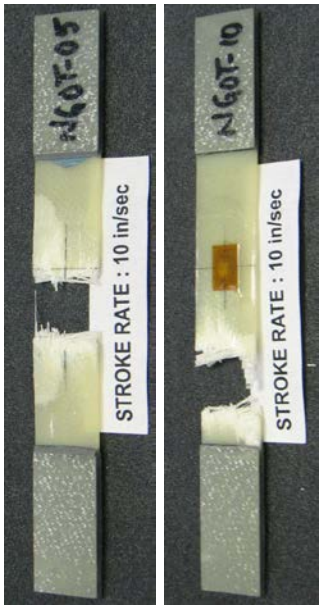

Figure B-5. Failure modes for fiberglass $[0^{\circ}]_4$ at a speed of 10 in/s

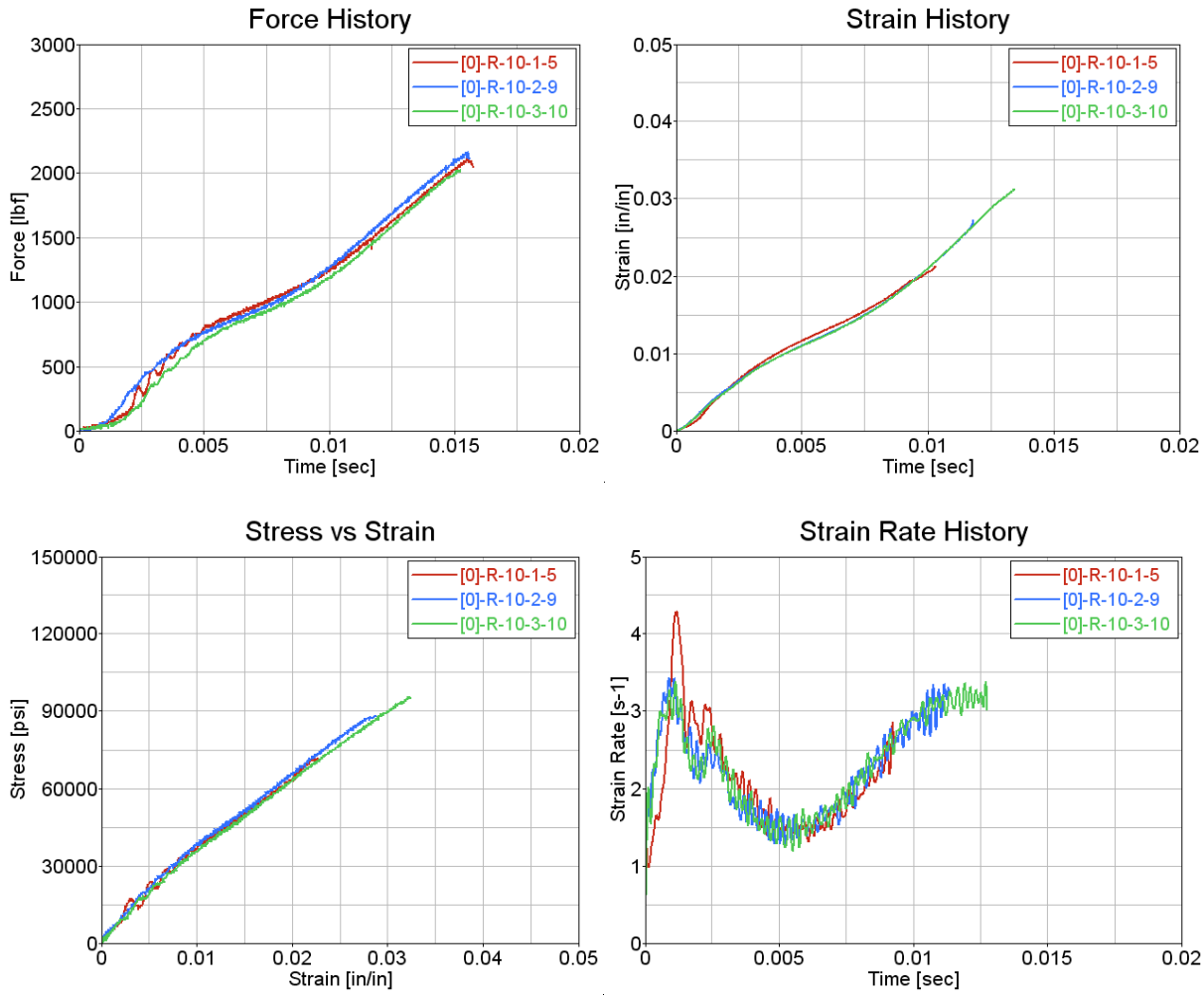

Figure B-6. Test results for fiberglass $[0^{\circ}]_4$ at a speed of 10 in/s

Figure B-7. Failure modes for fiberglass $[0^{\circ}]_4$: summary of all speeds

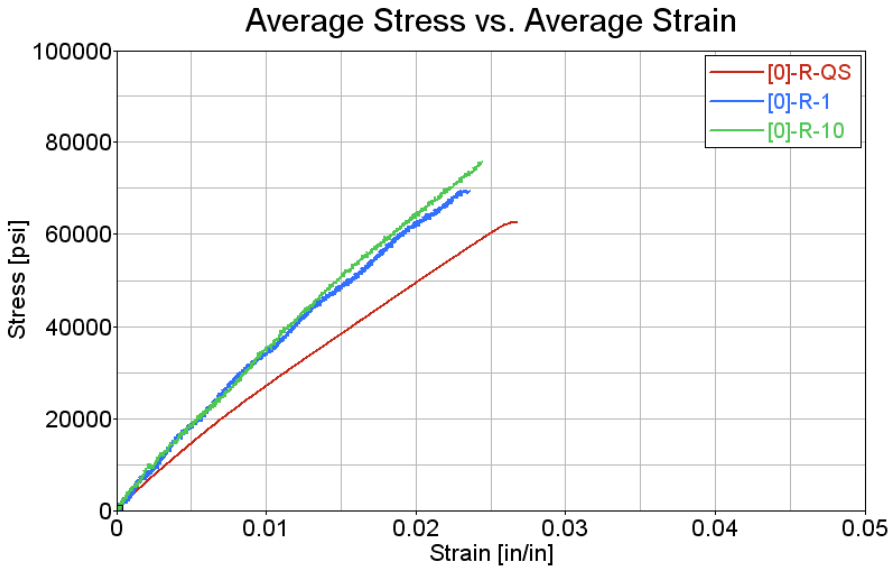

Figure B-8. Test results for fiberglass $[0^{\circ}]_4$: summary of all speeds

B.2 **FIBERGLASS [15°/-15°]$_{2S}$**

Table B-4. Summary of test results for fiberglass [15°/-15°]$_{2S}$ at a speed of 0.0008 in/s

Actuator Speed [in/s]	Specimen ID	Tensile Strength [psi]	Maximum Recorded Strain [in/in]	Young's Modulus [Msi]	Average Strain Rate [s^{-1}]
0.00083	[15]-R-QS-1	56,118	0.0268	2.52	0.000327
	[15]-R-QS-2	64,027	0.0312	2.92	0.000320
	[15]-R-QS-3	61,678	0.0300	2.58	0.000326
Average		60,608	0.0293	2.67	0.000324
Standard Deviation		4,062	0.0023	0.22	0.000004
Coefficient of Variation [%]		6.70	7.80	8.07	1.15

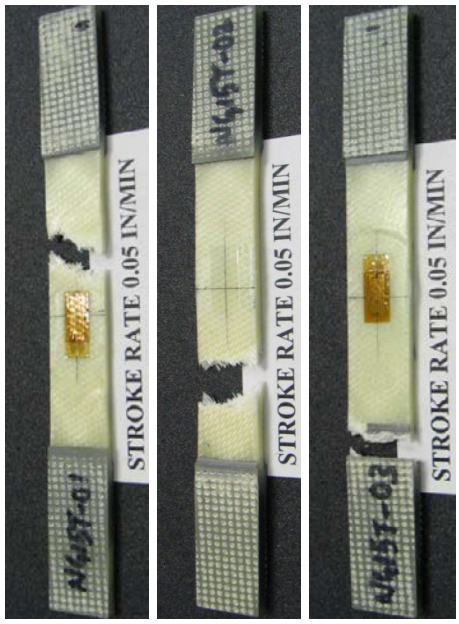

Figure B-9. Failure modes for fiberglass [15°/-15°]$_{2S}$ at a speed of 0.0008 in/s

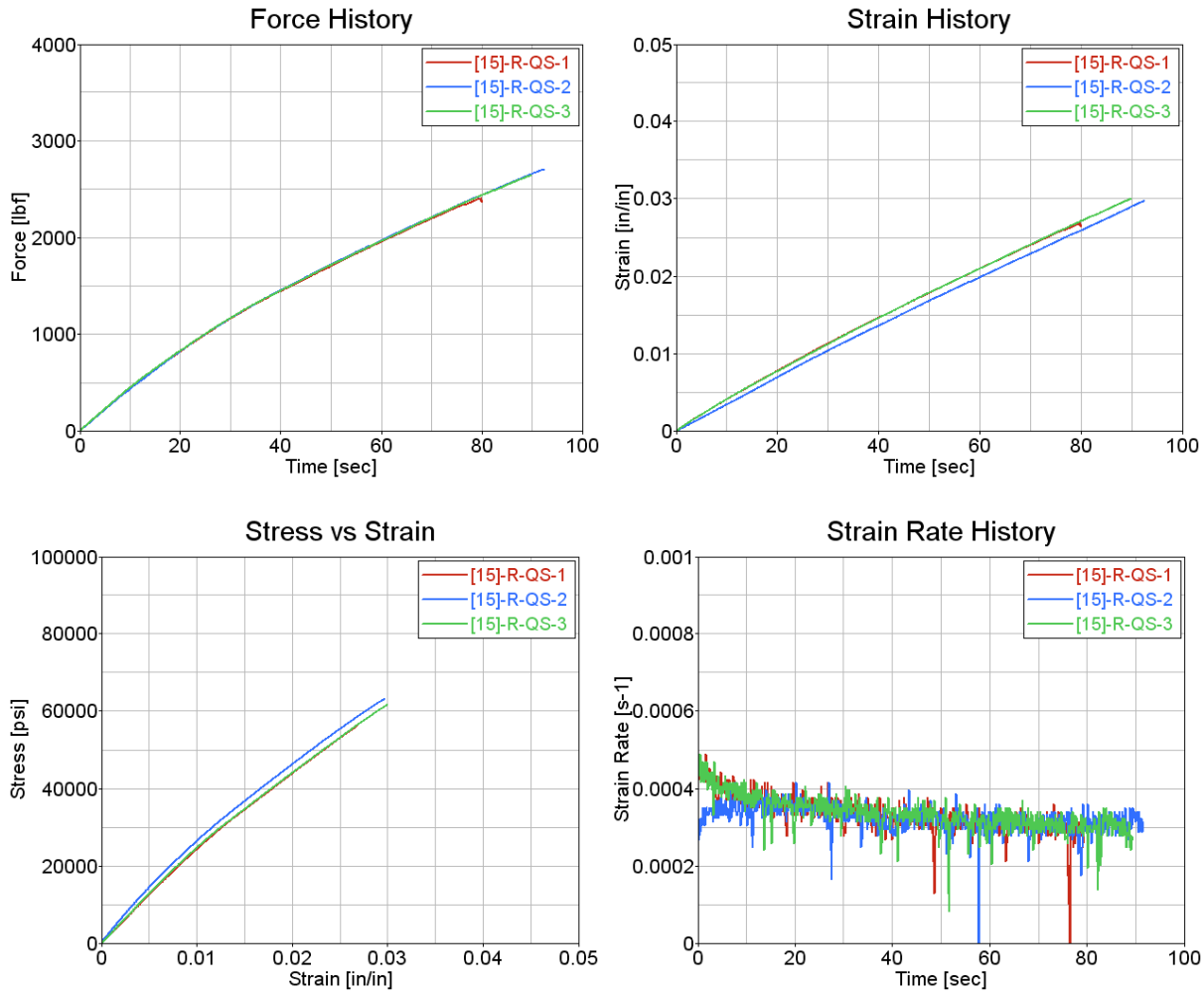

Figure B-10. Test results for fiberglass [15°/-15°]$_{2S}$ at a speed of 0.0008 in/s

Table B-5. Summary of test results for fiberglass $[15^{\circ}/-15^{\circ}]_{2S}$ at a speed of 1 in/s

Actuator Speed [in/s]	Specimen ID	Tensile Strength [psi]	Maximum Recorded Strain [in/in]	Young's Modulus [Msi]	Average Strain Rate [s^{-1}]
1	[15]-R-1-1-4	71,969	0.0307	3.49	0.2449
	[15]-R-1-2-5	68,714	0.0293	3.17	0.2373
	[15]-R-1-3-7	77,798	0.0292	3.88	0.2380
Average		72,827	0.0298	3.51	0.2401
Standard Deviation		4,603	0.0008	0.36	0.0042
Coefficient of Variation [%]		6.32	2.85	10.16	1.75

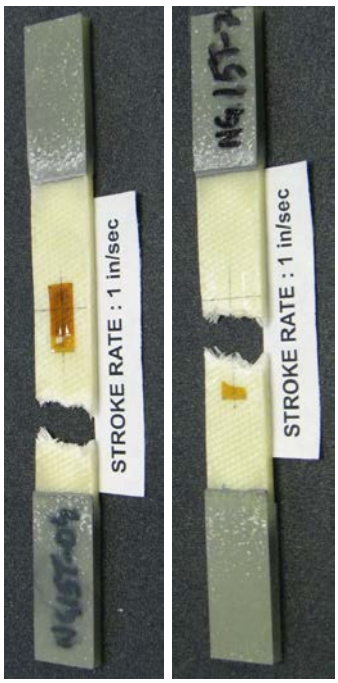

Figure B-11. Failure modes for fiberglass $[15^{\circ}/-15^{\circ}]_{2S}$ at a speed of 1 in/s

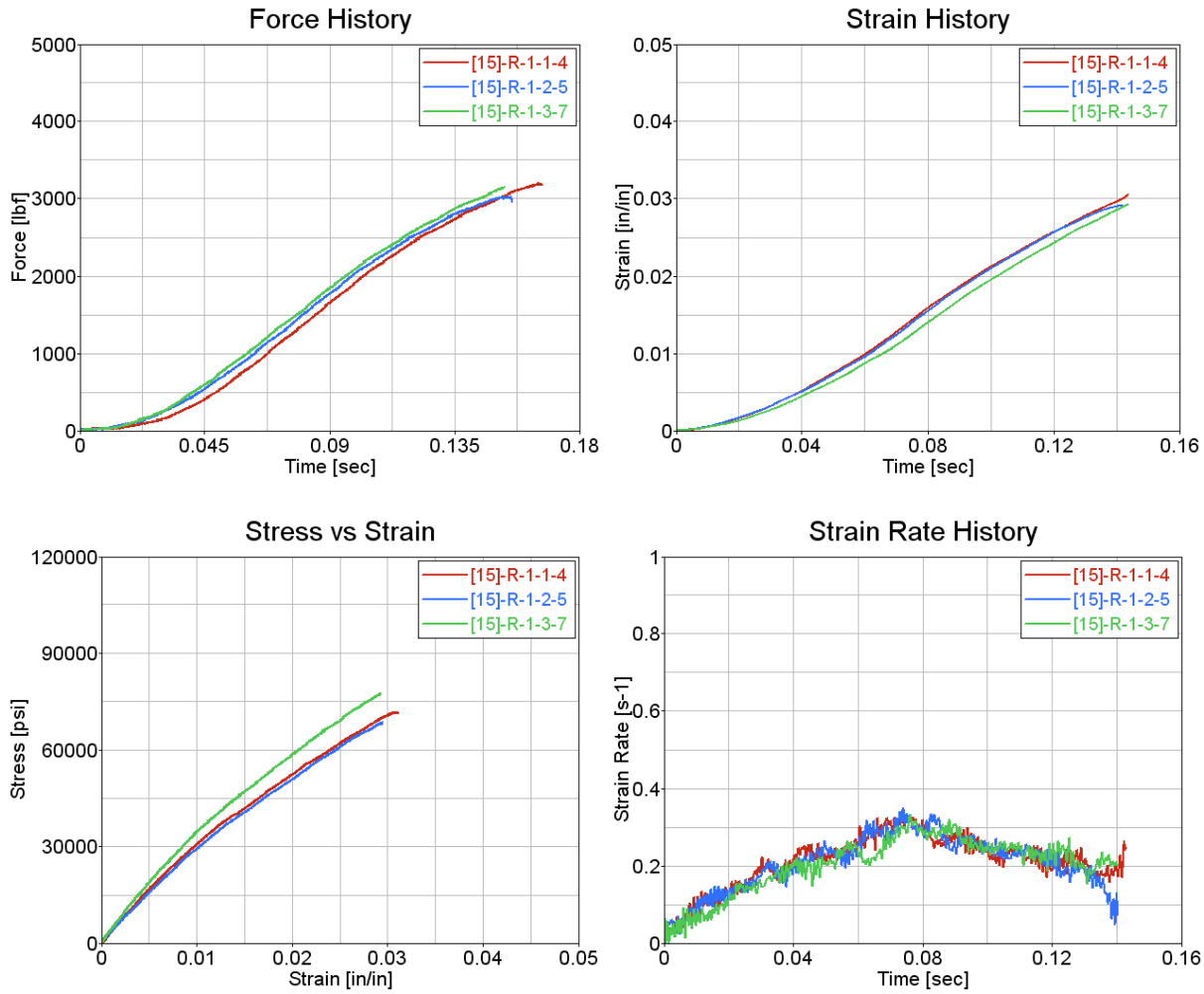

Figure B-12. Test results for fiberglass [15°/-15°]$_{2S}$ at a speed of 1 in/s

Table B-6. Summary test results for fiberglass $[15^{\circ}/-15^{\circ}]_{2S}$ at a speed of 10 in/s

Actuator Speed [in/s]	Specimen ID	Tensile Strength [psi]	Maximum Recorded Strain [in/in]	Young's Modulus [Msi]	Average Strain Rate [s^{-1}]
10	[15]-R-10-1-6	71,459	0.0287	3.81	1.7887
	[15]-R-10-2-8	79,762	0.0307	3.32	1.7895
	[15]-R-10-3-9	74,628	0.0294	3.56	1.7053
Average		75,283	0.0296	3.56	1.7612
Standard Deviation		4,190	0.0010	0.25	0.0484
Coefficient of Variation [%]		5.57	3.47	6.88	2.75

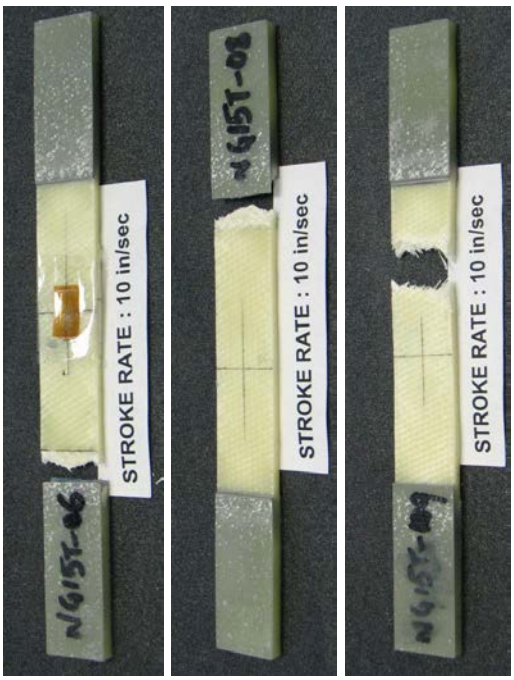

Figure B-13. Failure modes for fiberglass $[15^{\circ}/-15^{\circ}]_{2S}$ at a speed of 10 in/s

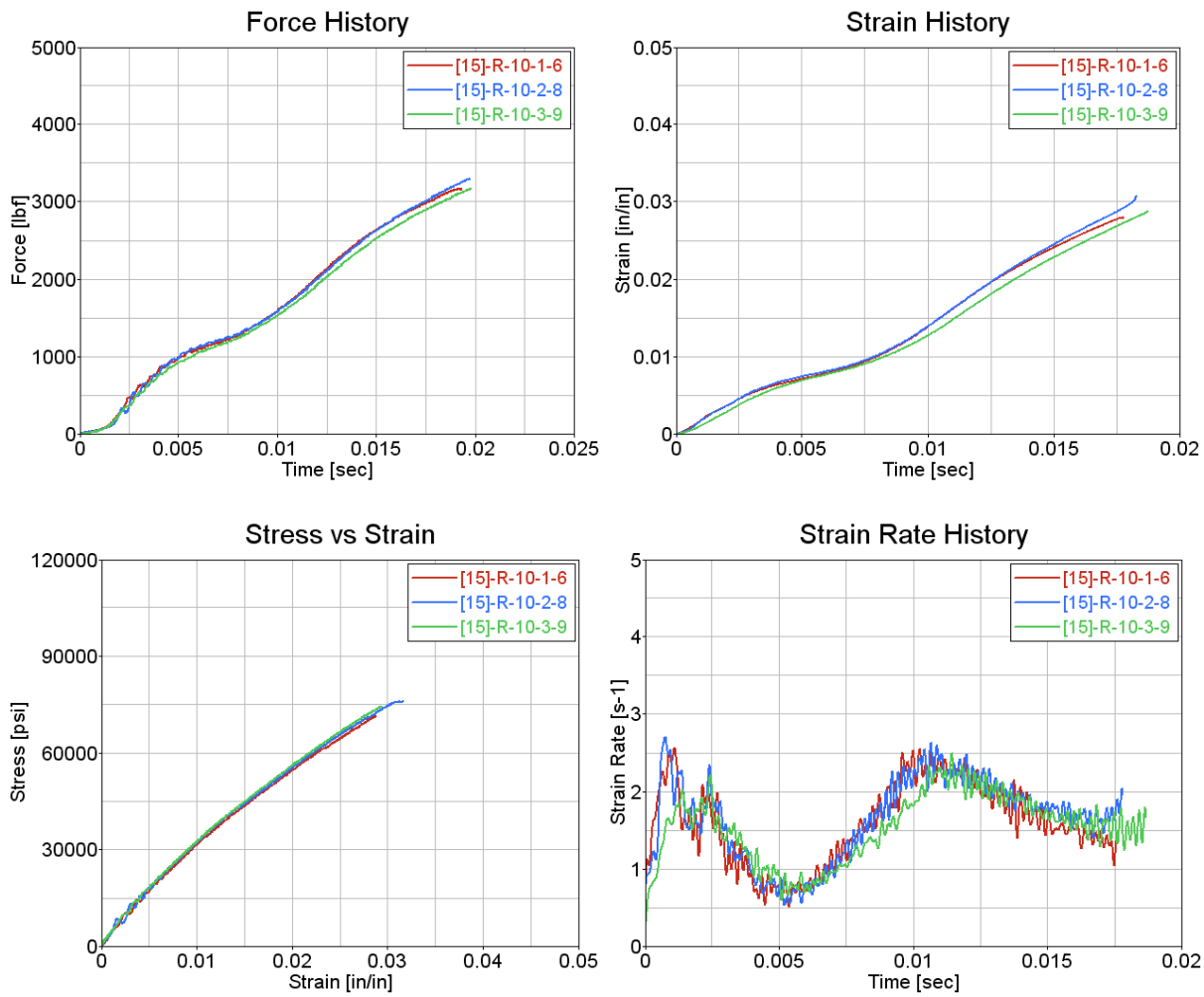

Figure B-14. Test results for fiberglass [15°/-15°]$_{2S}$ at a speed of 10 in/s

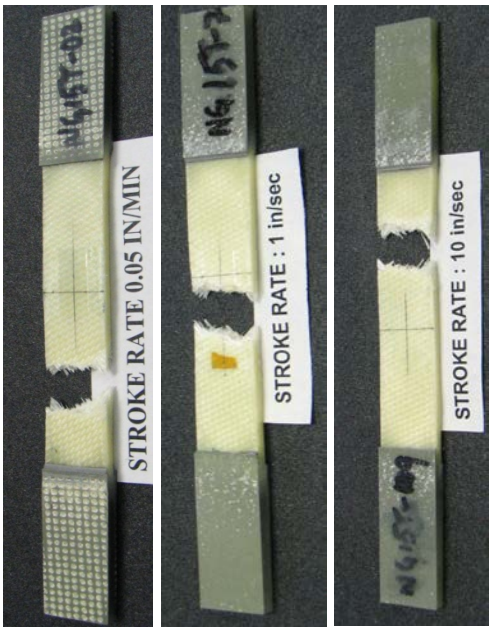

Figure B-15. Failure modes for fiberglass [15°/-15°]$_{2S}$: summary of all speeds

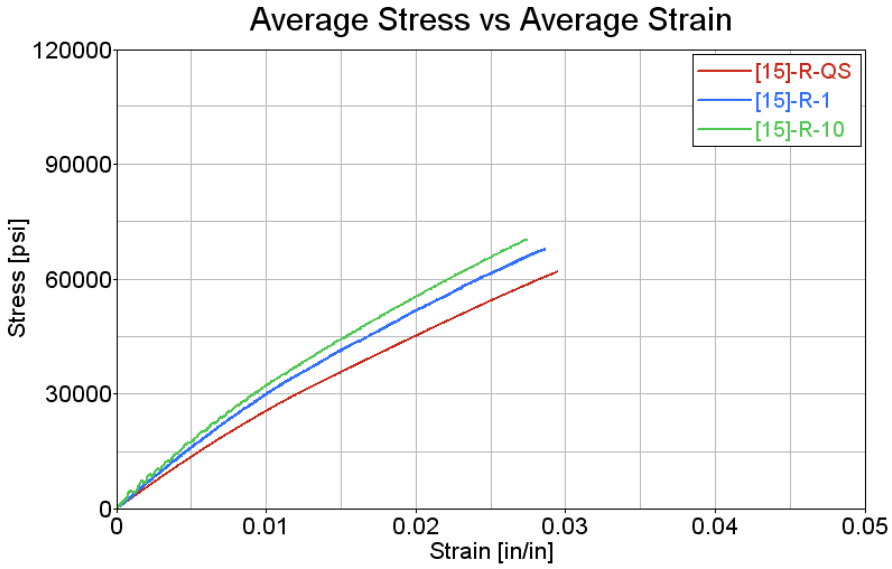

Figure B-16. Test results for fiberglass [15°/-15°]$_{2S}$: summary of all speeds

B.3 **FIBERGLASS [30°/-30°]$_{2S}$**

Table B-7. Summary of test results for fiberglass [30°/-30°]$_{2S}$ at a speed of 0.0008 in/s

Actuator Speed [in/s]	Specimen ID	Tensile Strength [psi]	Maximum Recorded Strain [in/in]	Young's Modulus [Msi]	Average Strain Rate [s^{-1}]
0.00083	[30]-R-QS-1	45,753	0.0428	1.73	0.000383
	[30]-R-QS-2	45,242	0.0418	1.86	0.000380
	[30]-R-QS-3	44,863	0.0402	1.93	0.000374
Average		45,286	0.0416	1.84	0.000379
Standard Deviation		447	0.0013	0.10	0.000005
Coefficient of Variation [%]		0.99	3.17	5.52	1.21

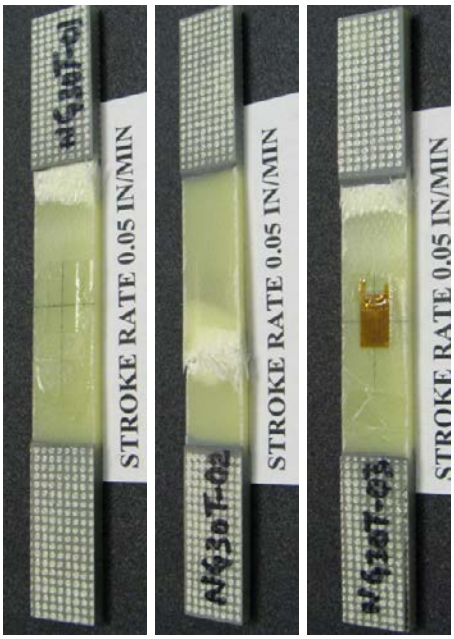

Figure B-17. Failure modes for fiberglass [30°/-30°]$_{2S}$ at a speed of 0.0008 in/s

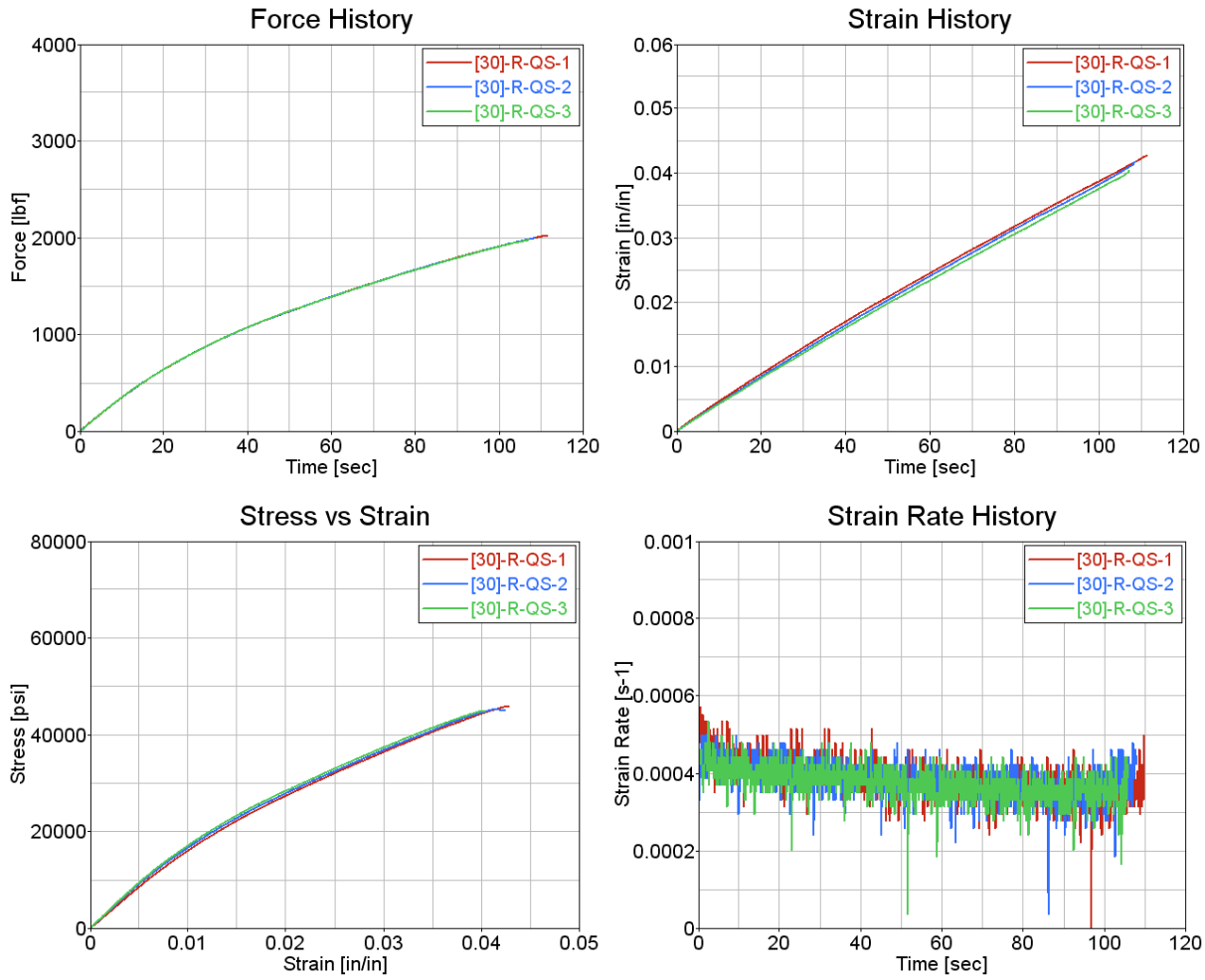

Figure B-18. Test results for fiberglass [30°/-30°]$_{2S}$ at a speed of 0.0008 in/s

Table B-8. Summary test results for fiberglass $[30^{\circ}/-30^{\circ}]_{2S}$ at a speed of 1 in/s

Actuator Speed [in/s]	Specimen ID	Tensile Strength [psi]	Maximum Recorded Strain [in/in]	Young's Modulus [Msi]	Average Strain Rate [s^{-1}]
1	[30]-R-1-1-4	52,742	0.0423	2.41	0.3161
	[30]-R-1-2-5	52,579	0.0417	2.30	0.3107
	[30]-R-1-3-6	52,901	0.0409	2.38	0.3296
Average		52,741	0.0416	2.36	0.3188
Standard Deviation		161	0.0007	0.06	0.0097
Coefficient of Variation [%]		0.30	1.76	2.53	3.05

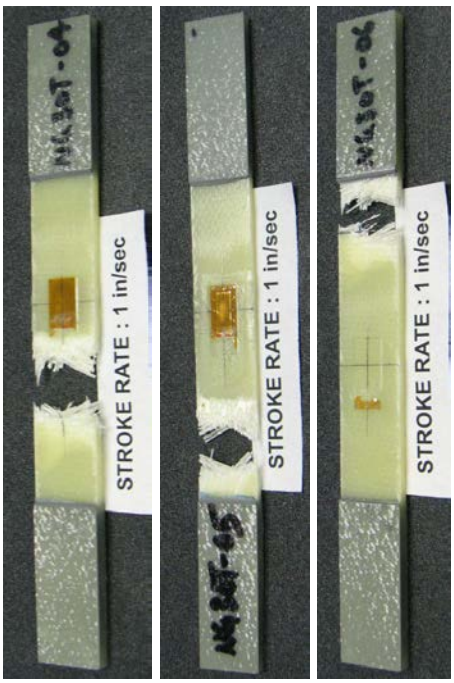

Figure B-19. Failure modes for fiberglass $[30^{\circ}/-30^{\circ}]_{2S}$ at a speed of 1 in/s

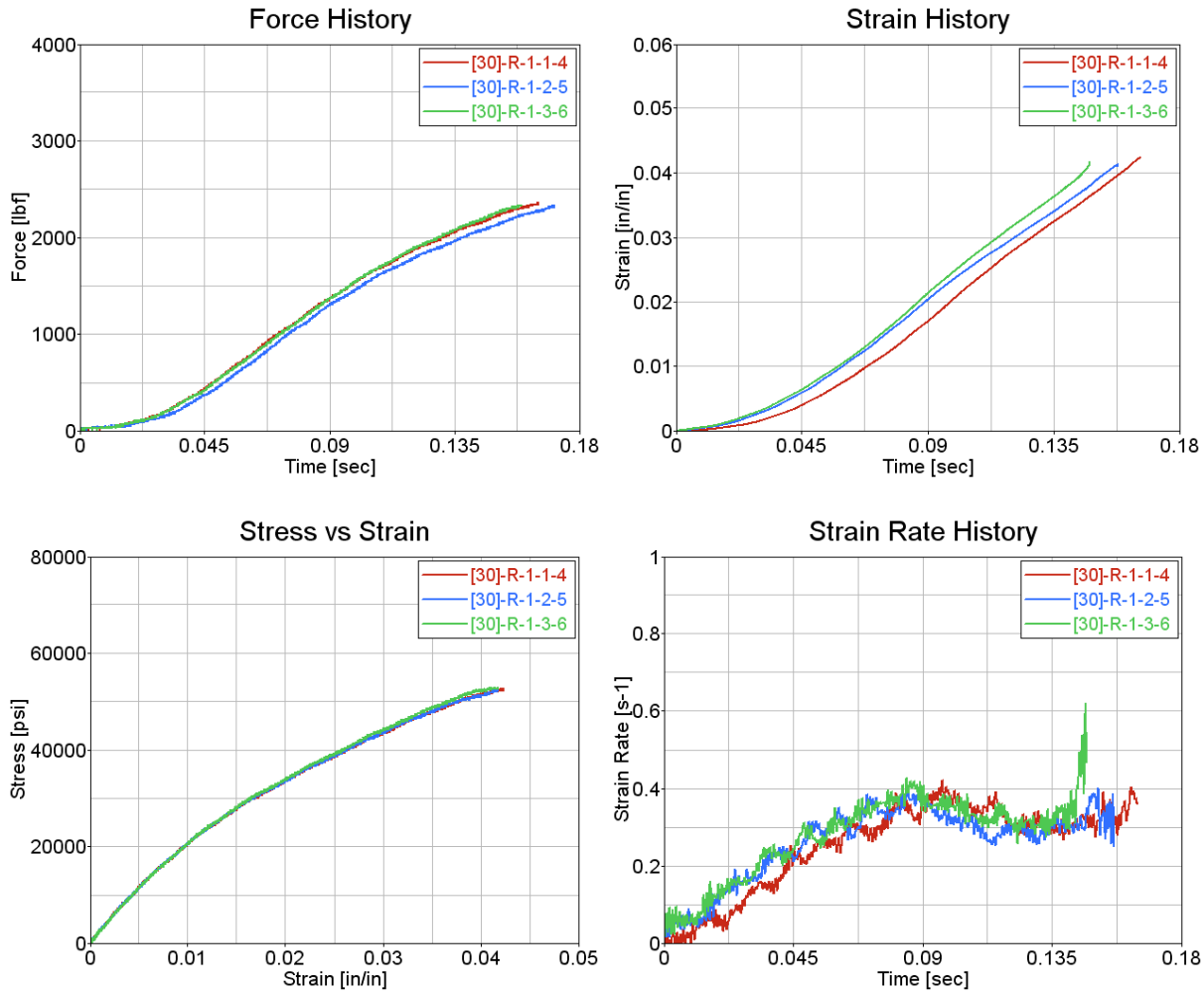

Figure B-20. Test results for fiberglass $[30^{\circ}/-30^{\circ}]_{2S}$ at a speed of 1 in/s

Table B-9. Summary of test results for fiberglass [30°/-30°]$_{2S}$ at a speed of 10 in/s

Actuator Speed [in/s]	Specimen ID	Tensile Strength [psi]	Maximum Recorded Strain [in/in]	Young's Modulus [Msi]	Average Strain Rate [s^{-1}]
10	[30]-R-10-1-7	53,860	0.0398	2.28	2.6755
	[30]-R-10-2-8	55,819	0.0438	2.85	2.7815
	[30]-R-10-3-9	54,925	0.0313	2.34	2.5936
Average		54,868	0.0383	2.49	2.6835
Standard Deviation		981	0.0064	0.31	0.0942
Coefficient of Variation [%]		1.79	16.67	12.40	3.51

Figure B-21. Failure modes for fiberglass [30°/-30°]$_{2S}$ at a speed of 10 in/s

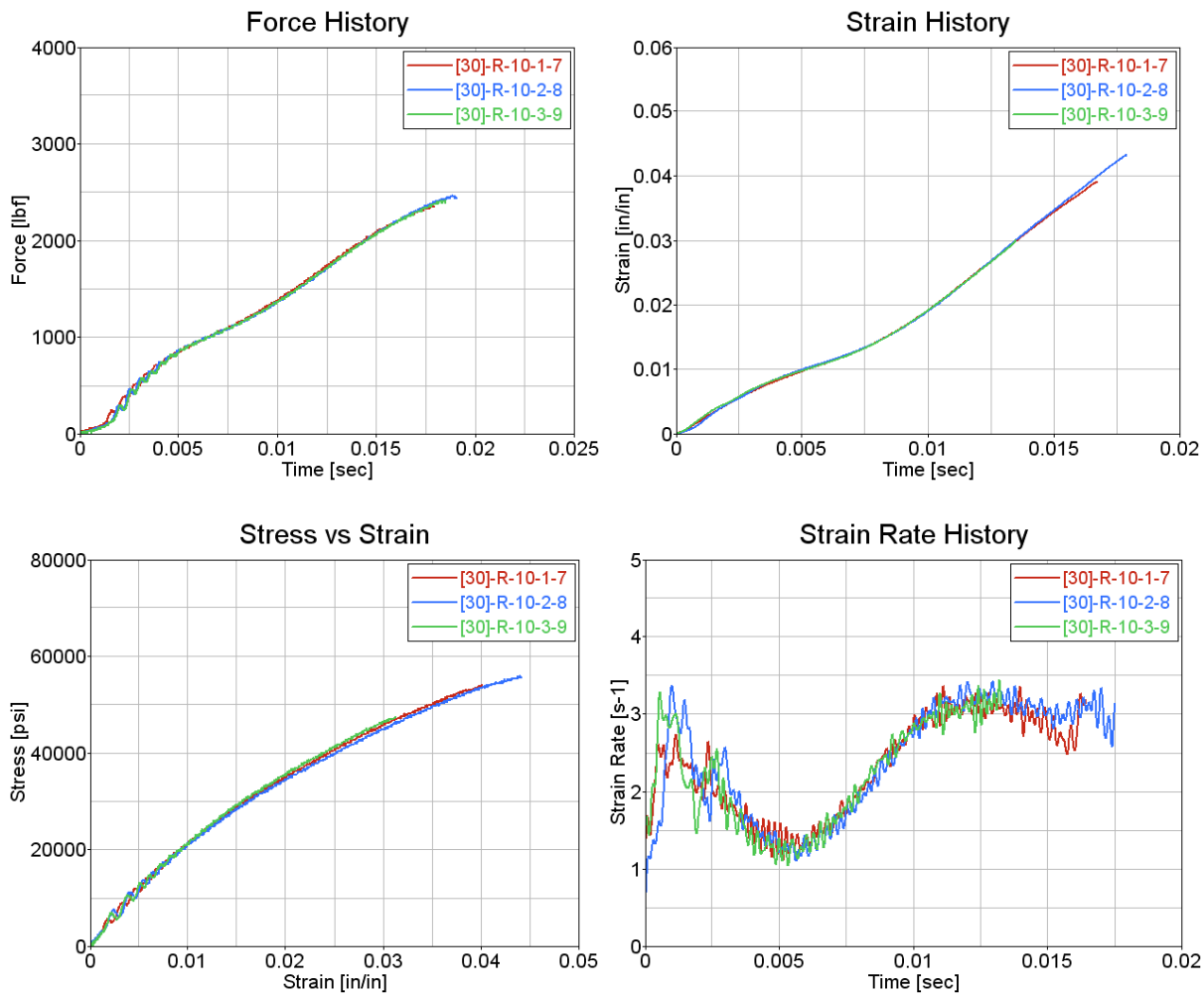

Figure B-22. Test results for fiberglass [30°/-30°]$_{2S}$ at a speed of 10 in/s

Figure B-23. Failure modes for fiberglass [30°/-30°]$_{2S}$: summary of all speeds

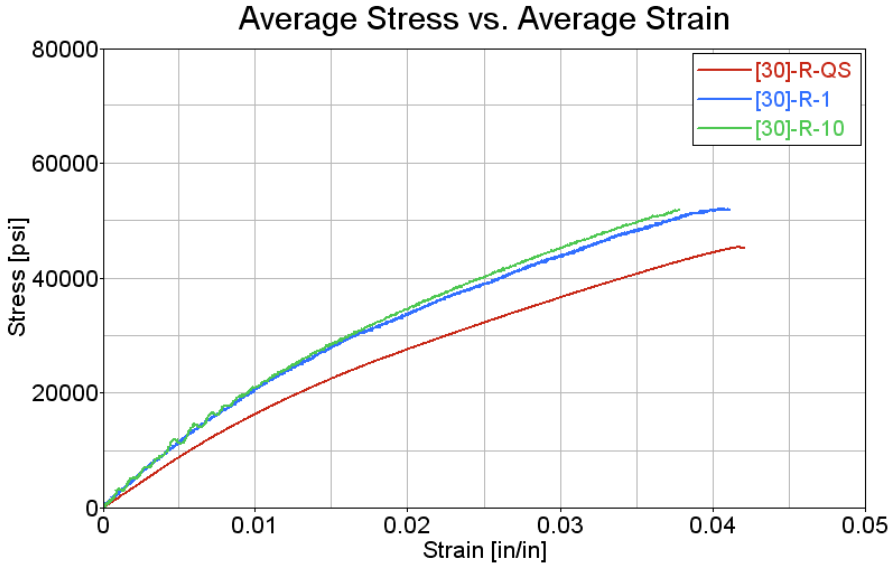

Figure B-24. Test results for fiberglass [30°/-30°]$_{2S}$: summary of all speeds

B.4 **FIBERGLASS [45°/-45°]$_{2S}$**

Table B-10. Summary test results fiberglass [45°/-45°]$_{2S}$ at a speed of 0.0008 in/s

Actuator Speed [in/s]	Specimen ID	Tensile Strength [psi]	Maximum Recorded Strain [in/in]	Young's Modulus [Msi]	Average Strain Rate [s^{-1}]
0.00083	[45]-R-QS-1	33,550	*	1.70	0.000386
	[45]-R-QS-2	34,531	*	1.64	0.000419
	[45]-R-QS-3	32,097	*	1.73	0.000418
Average		33,393	-	1.69	0.000408
Standard Deviation		1,225	-	0.04	0.000019
Coefficient of Variation [%]		3.67	-	2.82	4.60

*Exceeded strain gage capability of 0.05 in/in

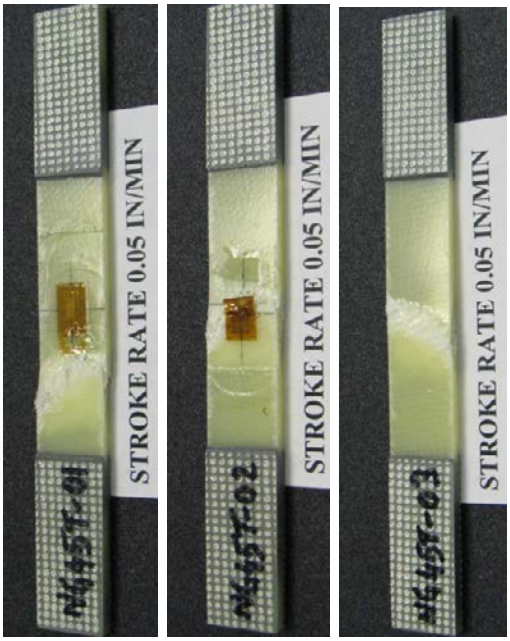

Figure B-25. Failure modes for fiberglass [45°/-45°]$_{2S}$ at a speed of 0.0008 in/s

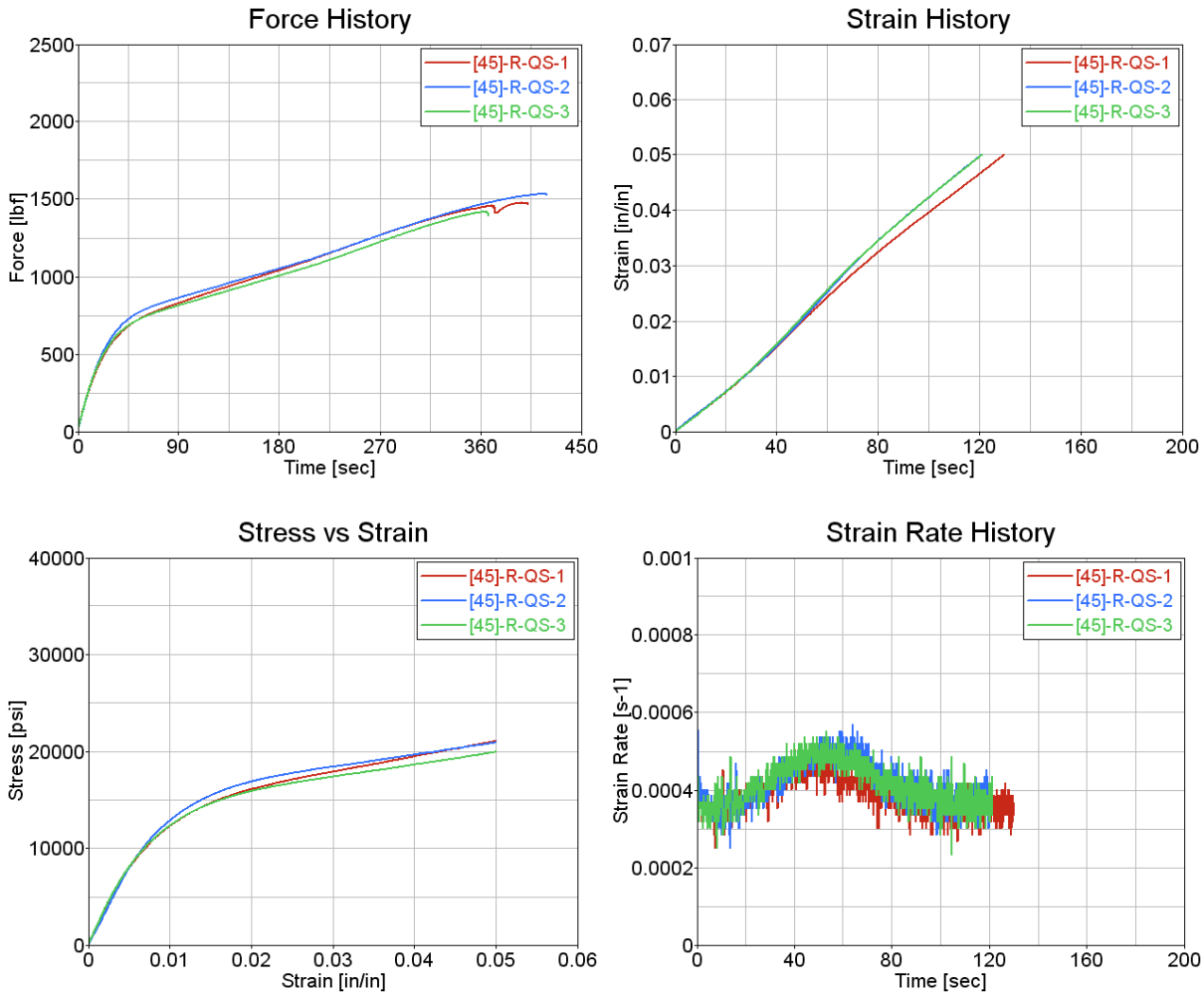

Figure B-26. Test results for fiberglass [45°/-45°]$_{2S}$ at a speed of 0.0008 in/s

Table B-11. Summary test results for fiberglass $[45^{\circ}/-45^{\circ}]_{2S}$ at a speed of 1 in/s

Actuator Speed [in/s]	Specimen ID	Tensile Strength [psi]	Maximum Recorded Strain [in/in]	Young's Modulus [Msi]	Average Strain Rate [s^{-1}]
1	[45]-R-1-1-4	39,847	*	1.75	0.5010
	[45]-R-1-2-5	38,946	**	1.96	0.5469
	[45]-R-1-3-6	39,361	*	1.67	0.5019
Average		39,385	-	1.79	0.5166
Standard Deviation		451	-	0.14	0.0262
Coefficient of Variation [%]		1.15	-	8.16	5.08

*Exceeded strain gage capability of 0.05 in/in
**Strain gage detached from test specimen

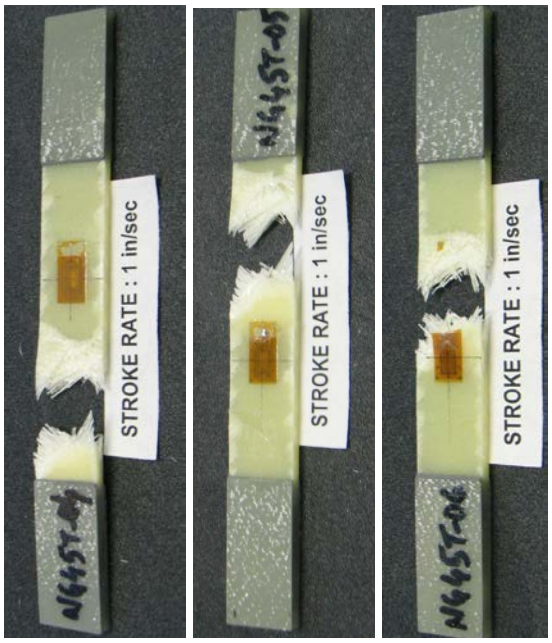

Figure B-27. Failure modes for fiberglass $[45^{\circ}/-45^{\circ}]_{2S}$ at a speed of 1 in/s

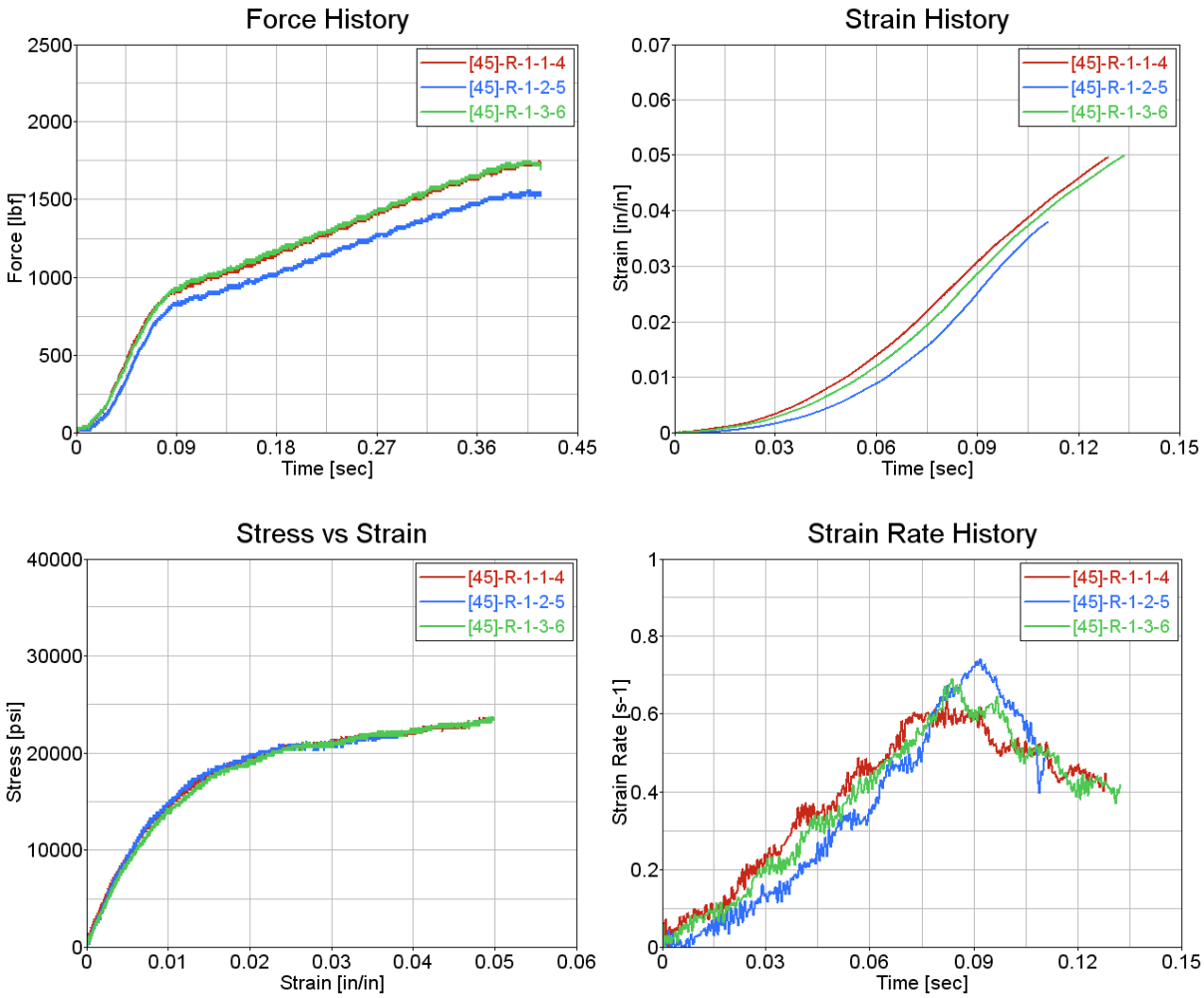

Figure B-28. Test results for fiberglass [45°/-45°]$_{2S}$ at a speed of 1 in/s

Table B-12. Summary test results for fiberglass [45°/-45°]$_{2S}$ at a speed of 10 in/s

Actuator Speed [in/s]	Specimen ID	Tensile Strength [psi]	Maximum Recorded Strain [in/in]	Young's Modulus [Msi]	Average Strain Rate [s^{-1}]
10	[45]-R-10-1-7	43,100	**	2.30	2.6480
	[45]-R-10-2-9	41,223	*	3.38	4.3330
	[45]-R-10-3-10	42,177	*	3.21	4.4017
Average		42,167	-	2.96	3.7942
Standard Deviation		939	-	0.58	0.9933
Coefficient of Variation [%]		2.23	-	19.59	26.18

*Exceeded strain gage capability of 0.05 in/in
**Strain gage detached from test specimen

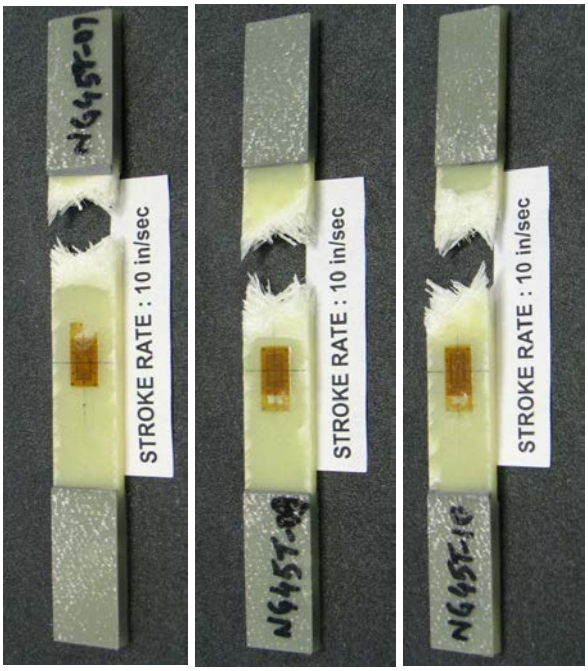

Figure B-29. Failure modes for fiberglass [45°/-45°]$_{2S}$ at a speed of 10 in/s

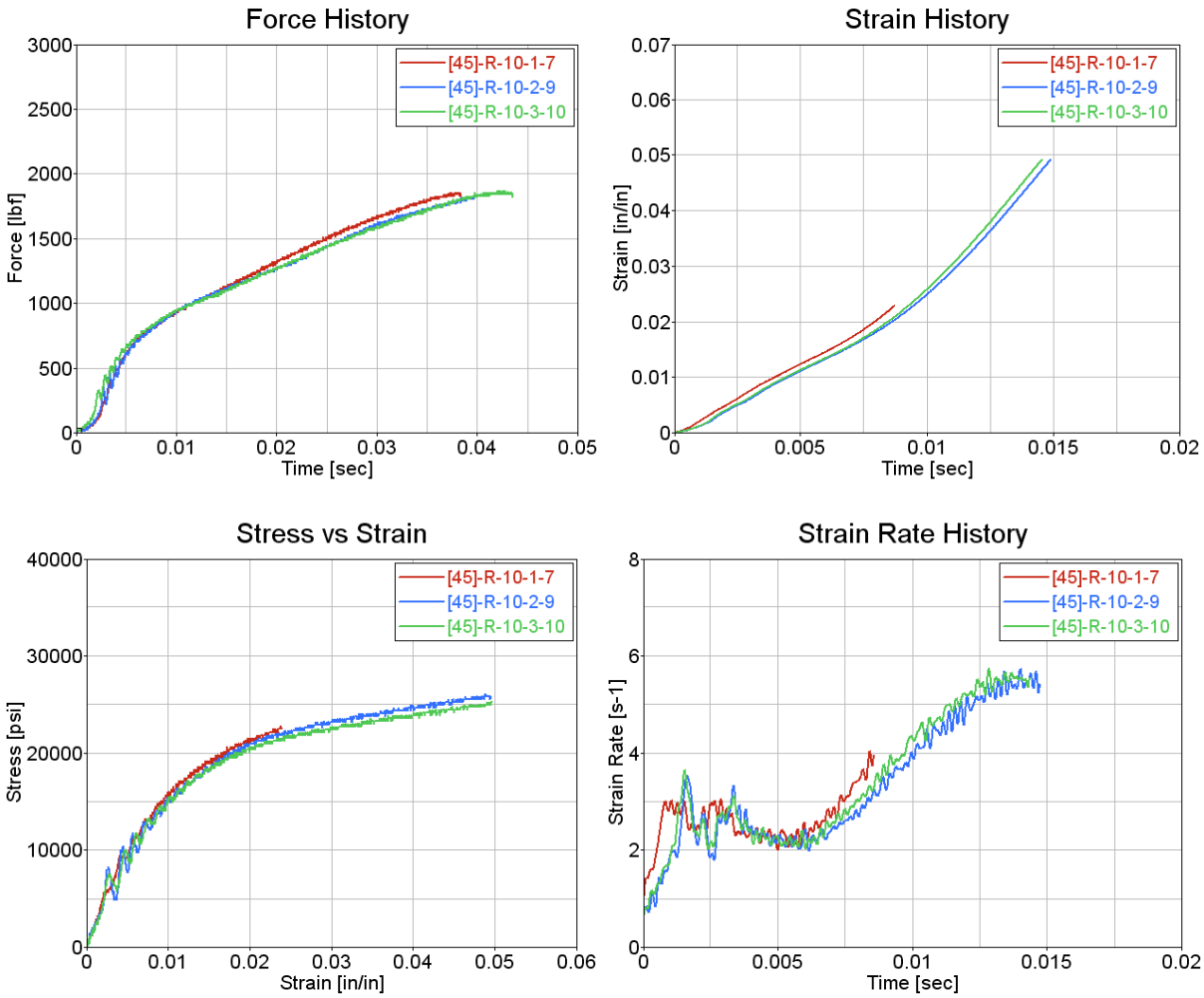

Figure B-30. Test results for fiberglass [45°/-45°]$_{2S}$ at a speed of 10 in/s

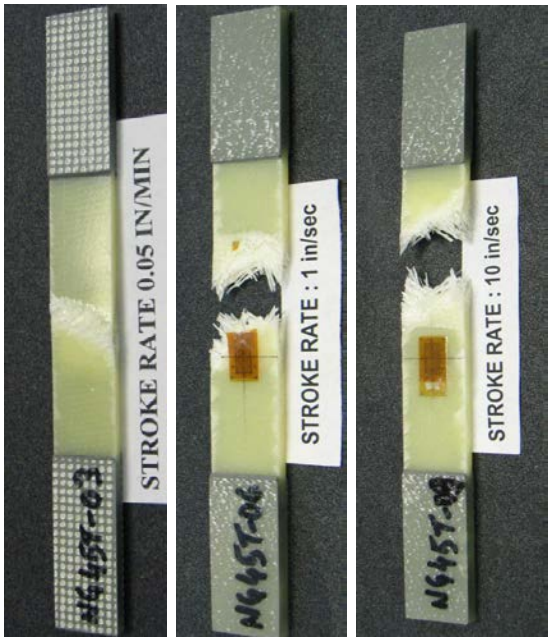

Figure B-31. Failure modes for fiberglass [45°/-45°]$_{2S}$: summary of all speeds

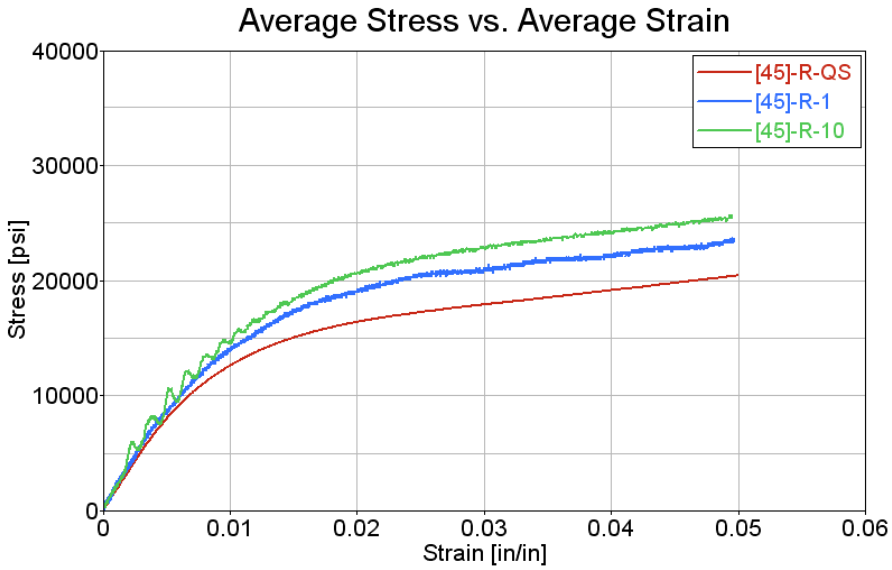

Figure B-32. Test results for fiberglass [45°/-45°]$_{2S}$: summary of all speeds

APPENDIX C—TORAY T800S/3900-2B UNITAPE TENSION TESTING RESULTS

C.1 CARBON UNITAPE $[0^{\circ}]_2$

Table C-1. Summary test results for carbon Unitape $[0^{\circ}]_2$ at a speed of 0.0008 in/s

Actuator Speed [in/s]	Specimen ID	Tensile Strength [psi]	Maximum Recorded Strain [in/in]	Young's Modulus [Msi]	Average Strain Rate [s^{-1}]
0.00083	[0]-R-QS-16	428,398	0.0210	16.23	0.000211
	[0]-R-QS-17	386,314	0.0178	19.11	0.000220
	[0]-R-QS-23	423,749	0.0194	18.78	0.000214
Average		412,820	0.0194	18.04	0.000215
Standard Deviation		23,072	0.0016	1.58	0.000005
Coefficient of Variation [%]		5.59	8.25	8.74	2.13

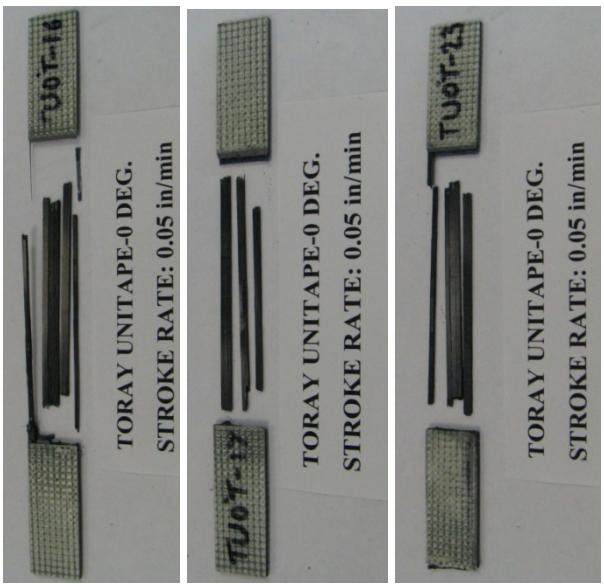

Figure C-1. Failure modes for carbon Unitape $[0^{\circ}]_2$ at a speed of 0.0008 in/s, in tension

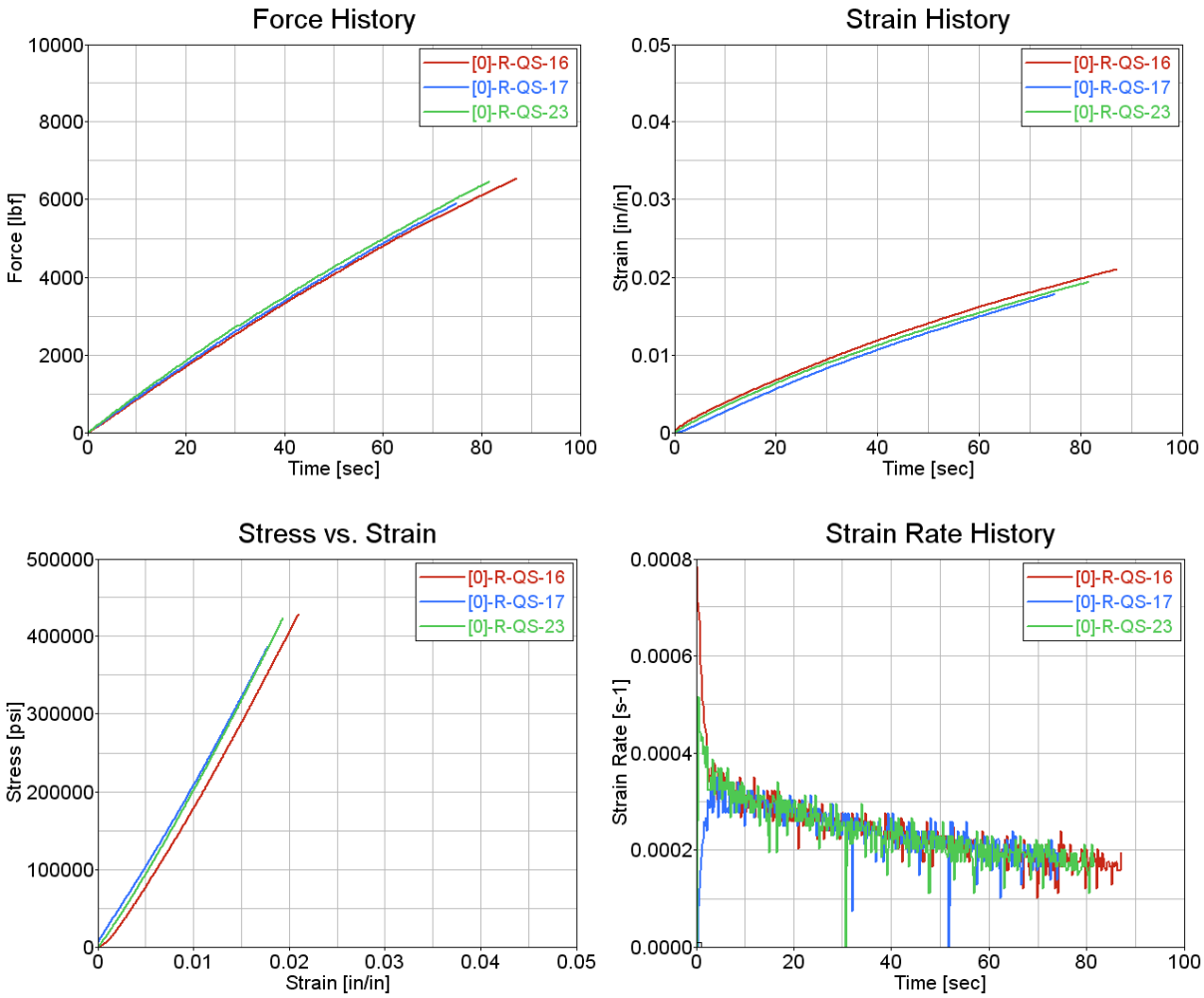

Figure C-2. Test results for carbon Unitape $[0^{\circ}]_2$ at a speed of 0.0008 in/s, in tension

Table C-2. Summary of test results for carbon Unitape $[0^{\circ}]_2$ at a speed of 1 in/s, in tension

Actuator Speed [in/s]	Specimen ID	Tensile Strength [psi]	Maximum Recorded Strain [in/in]	Young's Modulus [Msi]	Average Strain Rate [s^{-1}]
1	[0]-R-1-1-4	458,281	0.0181	23.87	0.1957
	[0]-R-1-2-5	398,305	0.0159	22.30	0.1988
	[0]-R-1-3-6	464,601	0.0170	24.46	0.1945
Average		440,396	0.0170	23.54	0.1963
Standard Deviation		36,588	0.0011	1.11	0.0022
Coefficient of Variation [%]		8.31	6.39	4.73	1.13

Figure C-3. Failure modes for carbon Unitape $[0^{\circ}]_2$ at a speed of 1 in/s, in tension

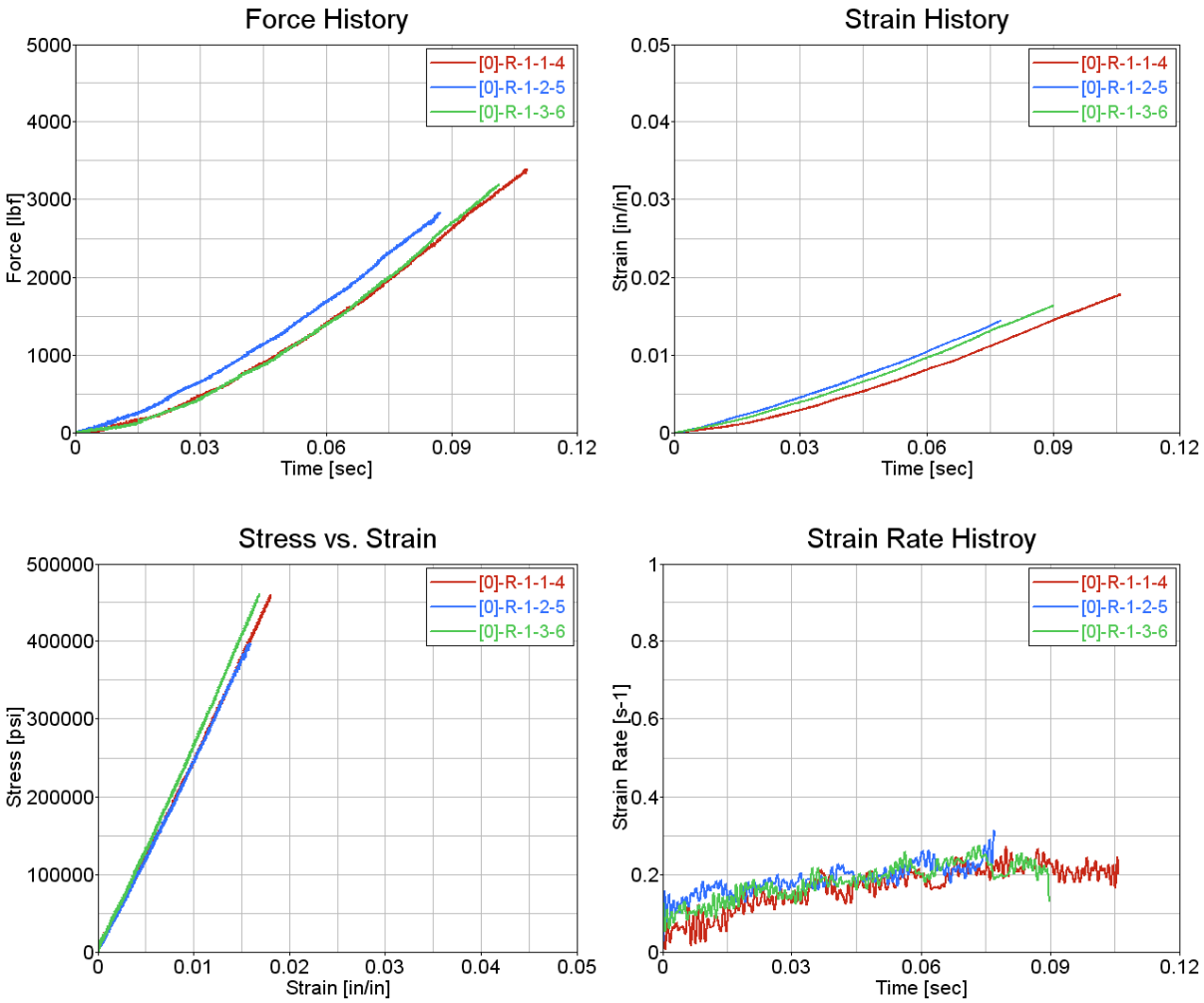

Figure C-4. Test results for carbon Unitape $[0^{\circ}]_2$ at a speed of 1 in/s, in tension

Table C-3. Summary test for results carbon Unitape $[0^{\circ}]_2$ at a speed of 10 in/s, in tension

Actuator Speed [in/s]	Specimen ID	Tensile Strength [psi]	Maximum Recorded Strain [in/in]	Young's Modulus [Msi]	Average Strain Rate [s^{-1}]
10	[0]-R-10-1-7	508,022	0.0179	26.19	1.0113
	[0]-R-10-2-8	527,199	0.0191	24.87	1.0437
	[0]-R-10-3-9	478,914	0.0172	25.17	1.0249
Average		504,711	0.0181	25.41	1.0266
Standard Deviation		24,312	0.0010	0.69	0.0163
Coefficient of Variation [%]		4.82	5.34	2.72	1.58

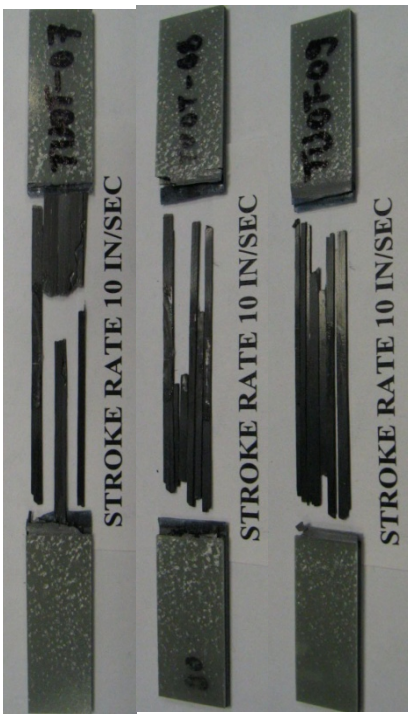

Figure C-5. Failure modes for carbon Unitape $[0^{\circ}]_2$ at a speed of 10 in/s, in tension

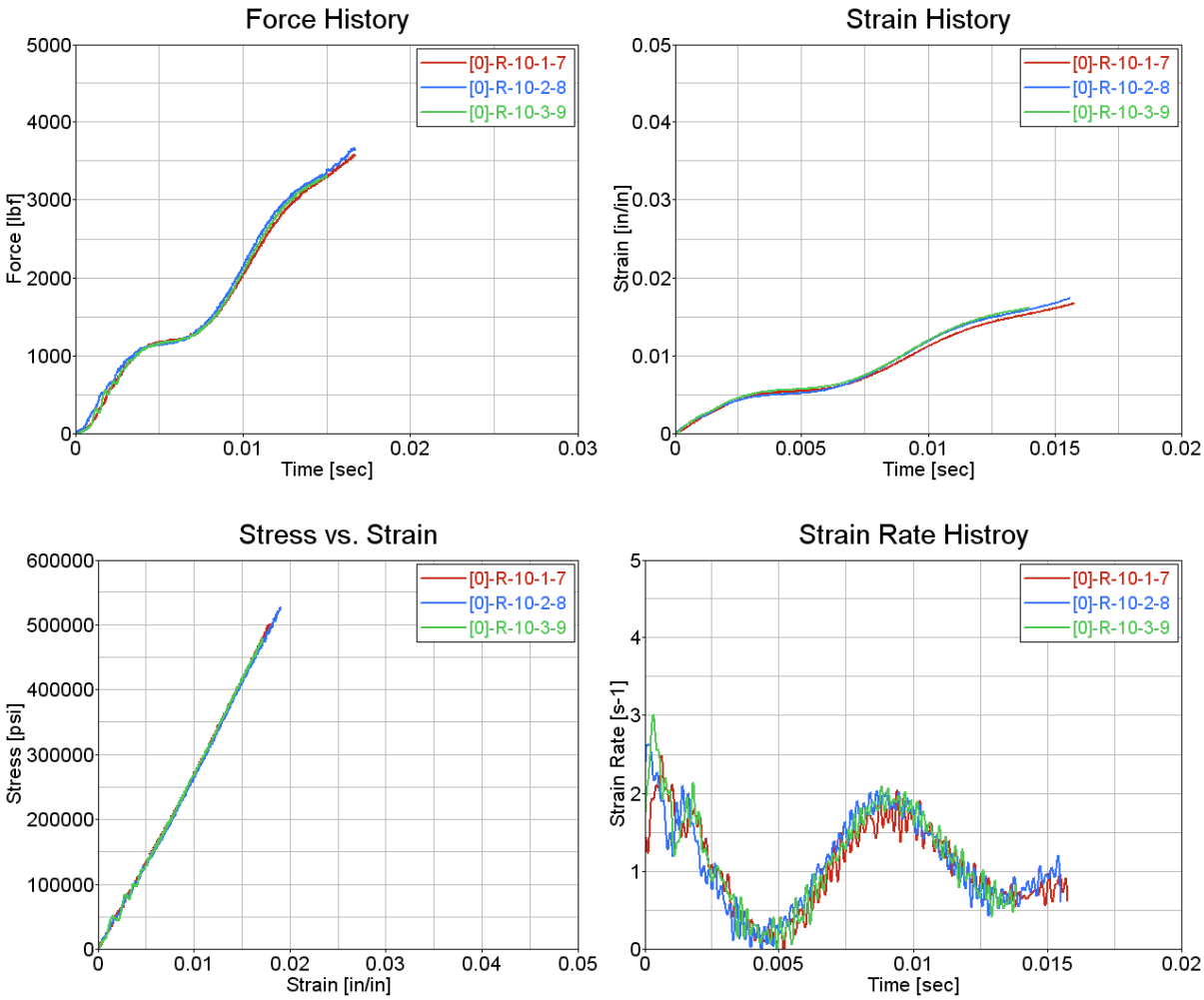

Figure C-6. Test results for carbon Unitape $[0^{\circ}]_2$ at a speed of 10 in/s, in tension

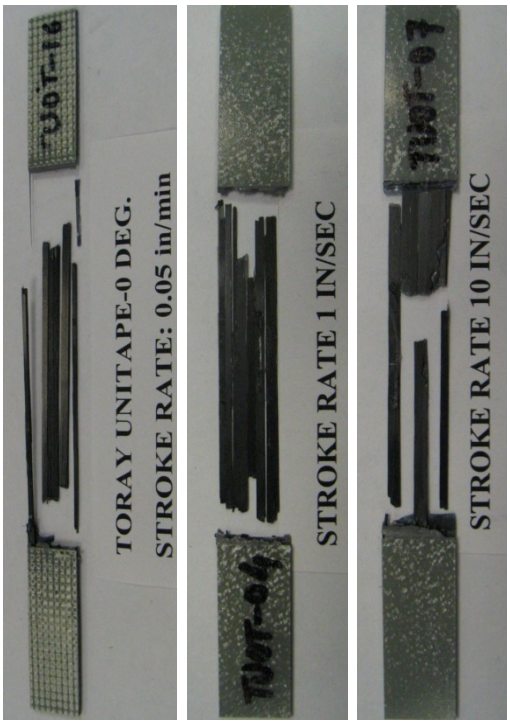

Figure C-7. Failure modes for carbon Unitape $[0^{\circ}]_2$: summary of all speeds, in tension

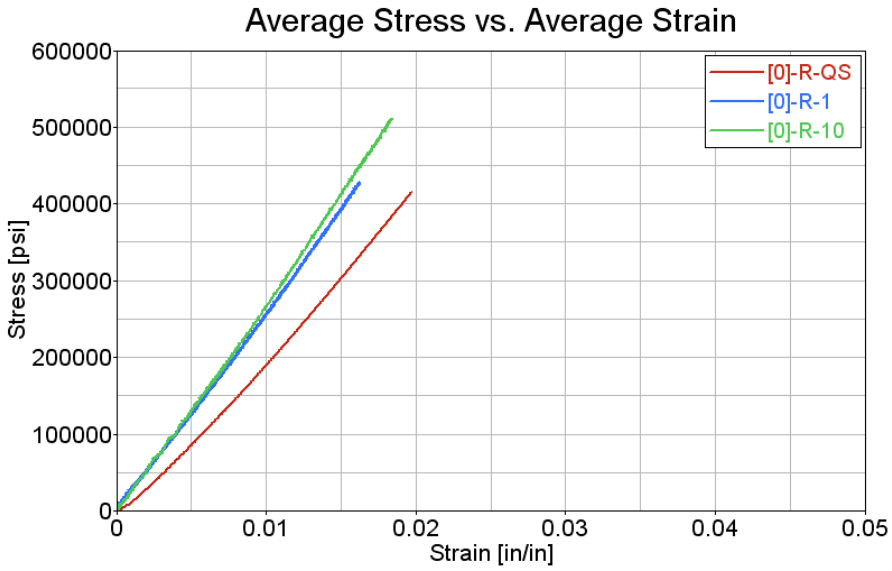

Figure C-8. Test results for carbon Unitape $[0^{\circ}]_2$: summary of all speeds, in tension

C.2 CARBON UNITAPE $[15^{\circ}/-15^{\circ}]_{2S}$

Table C-4. Summary of test results for carbon Unitape $[15^{\circ}/-15^{\circ}]_{2S}$ at a speed of 0.0008 in/s, in tension

Actuator Speed [in/s]	Specimen ID	Tensile Strength [psi]	Maximum Recorded Strain [in/in]	Young's Modulus [Msi]	Average Strain Rate [s^{-1}]
0.00083	[15]-R-QS-1	219,759	0.0147	14.90	0.000205
	[15]-R-QS-2	229,627	0.0152	15.16	0.000202
	[15]-R-QS-3	235,111	0.0155	15.05	0.000199
Average		228,166	0.0151	15.04	0.000202
Standard Deviation		7,779	0.0004	0.13	0.000003
Coefficient of Variation [%]		3.41	2.93	0.87	1.49

Figure C-9. Failure modes for carbon Unitape $[15^{\circ}/-15^{\circ}]_{2S}$ at a speed of 0.0008 in/s, in tension

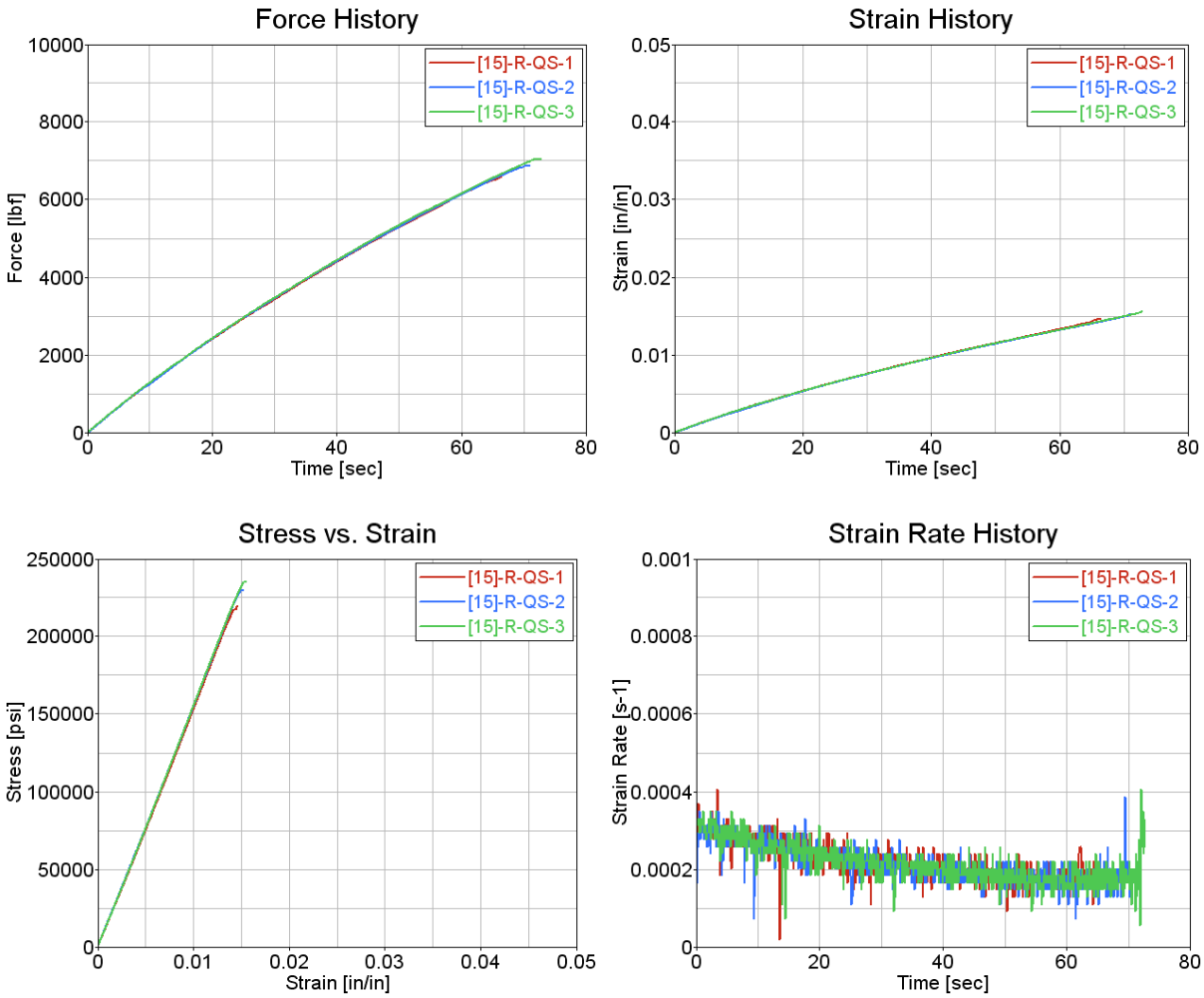

Figure C-10. Test results for carbon Unitape $[15^{\circ}/-15^{\circ}]_{2S}$ at a speed of 0.0008 in/s, in tension

Table C-5. Summary of test results for carbon Unitape [15°/-15°]$_{2S}$ at a speed of 1 in/s, in tension

Actuator Speed [in/s]	Specimen ID	Tensile Strength [psi]	Maximum Recorded Strain [in/in]	Young's Modulus [Msi]	Average Strain Rate [s^{-1}]
1	[15]-R-1-1-4	219,308	0.0126	17.60	0.1857
	[15]-R-1-2-5	226,661	0.0133	17.88	0.1839
	[15]-R-1-3-6	203,543	0.0109	18.60	0.1687
Average		216,504	0.0123	18.03	0.1794
Standard Deviation		11,811	0.0012	0.52	0.0093
Coefficient of Variation [%]		5.46	9.87	2.86	5.20

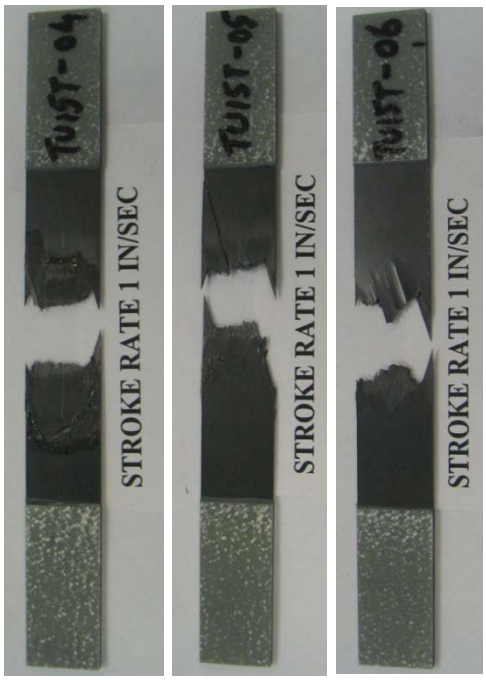

Figure C-11. Failure modes for carbon Unitape [15°/-15°]$_{2S}$ at a speed of 1 in/s, in tension

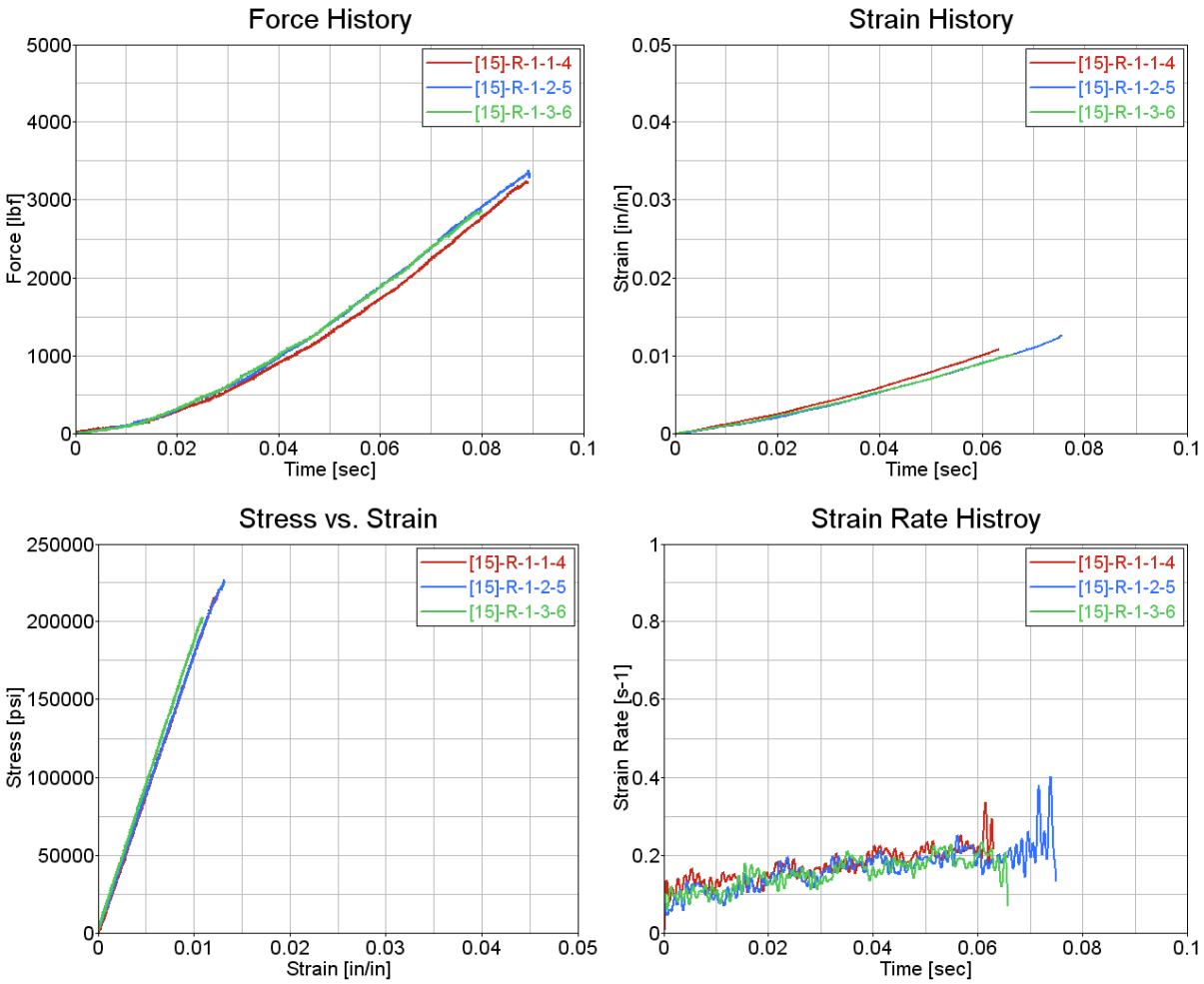

Figure C-12. Test results for carbon Unitape [15°/-15°]$_{2S}$ at a speed of 1 in/s, in tension

Table C-6. Summary of test results for carbon Unitape [15°/-15°]$_{2S}$ at a speed of 10 in/s, in tension

Actuator Speed [in/s]	Specimen ID	Tensile Strength [psi]	Maximum Recorded Strain [in/in]	Young's Modulus [Msi]	Average Strain Rate [s^{-1}]
10	[15]-R-10-1-7	229,602	0.0132	19.76	1.4561
	[15]-R-10-2-8	212,886	0.0121	19.08	1.3864
	[15]-R-10-3-9	218,119	0.0115	19.79	1.3218
Average		220,202	0.0122	19.54	1.3881
Standard Deviation		8,551	0.0009	0.40	0.0672
Coefficient of Variation [%]		3.88	7.05	2.04	4.84

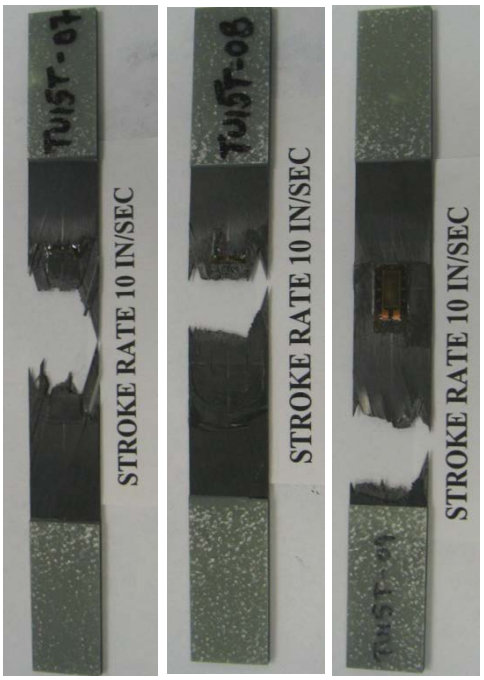

Figure C-13. Failure modes for carbon Unitape [15°/-15°]$_{2S}$ at a speed of 10 in/s, in tension

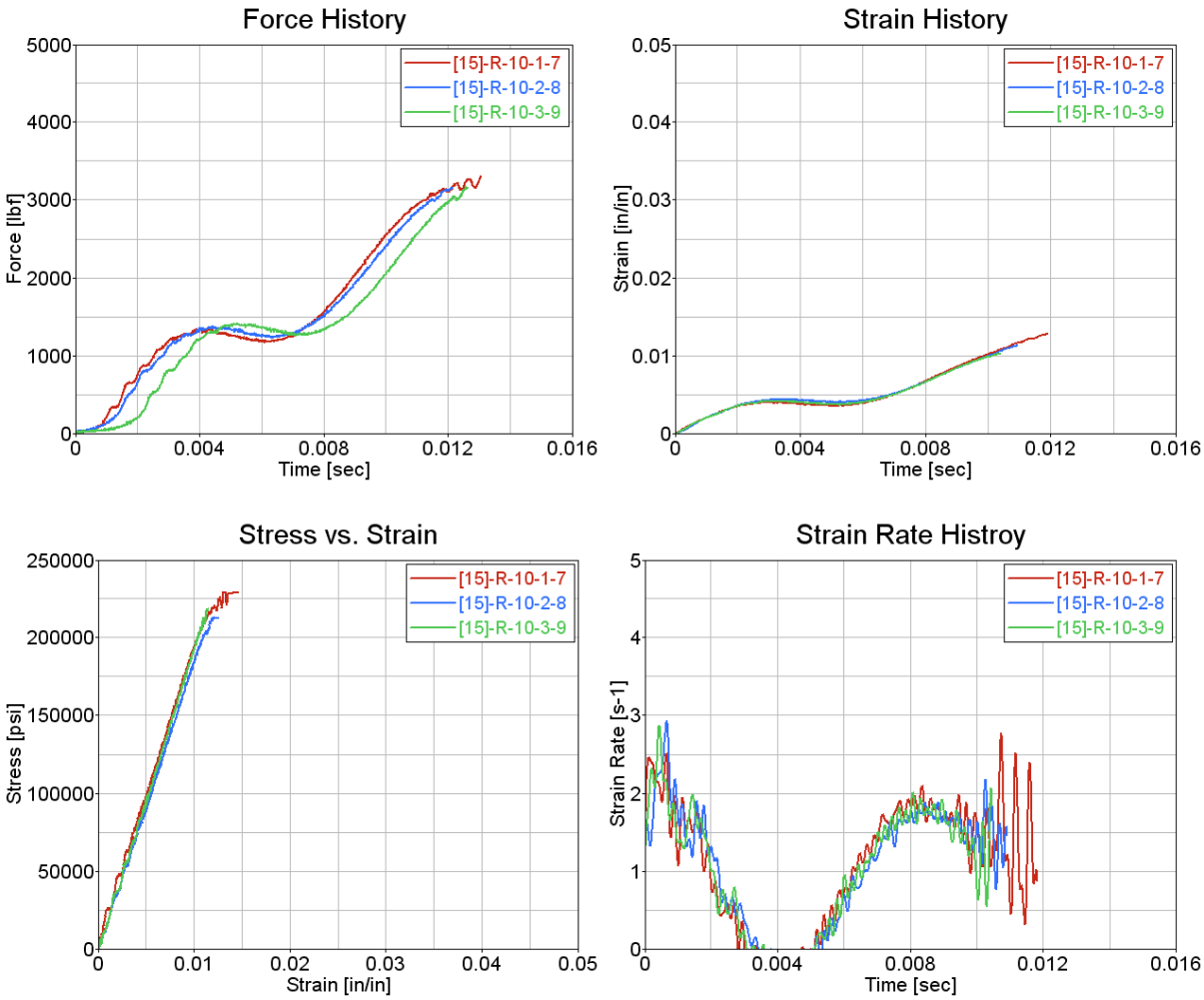

Figure C-14. Test results for carbon Unitape $[15^{\circ}/-15^{\circ}]_{2S}$ at a speed of 10 in/s, in tension

Figure C-15. Failure modes for carbon Unitape [15°/-15°]$_{2S}$: summary of all speeds, in tension

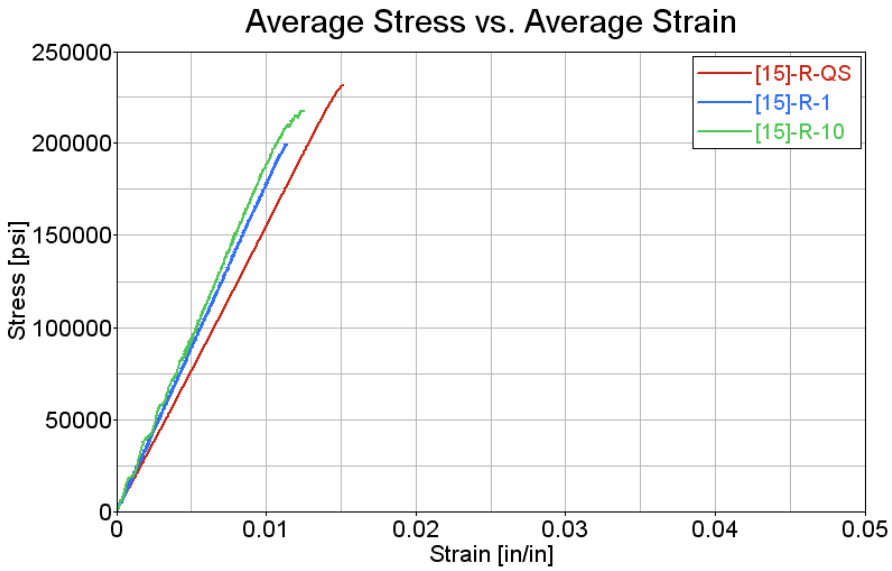

Figure C-16. Test results for carbon Unitape [15°/-15°]$_{2S}$: summary of all speeds, in tension

C.3 CARBON UNITAPE $[30^{\circ}/-30^{\circ}]_{2S}$

Table C-7. Summary of test results for carbon Unitape $[30^{\circ}/-30^{\circ}]_{2S}$ at a speed of 0.0008 in/s, in tension

Actuator Speed [in/s]	Specimen ID	Tensile Strength [psi]	Maximum Recorded Strain [in/in]	Young's Modulus [Msi]	Average Strain Rate [s^{-1}]
0.00083	[30]-R-QS-1	96,060	0.0325	5.27	0.000372
	[30]-R-QS-2	94,233	0.0342	5.33	0.000376
	[30]-R-QS-3	100,211	0.0332	5.59	0.000365
Average		96,835	0.0333	5.40	0.000371
Standard Deviation		3,063	0.0009	0.17	0.000006
Coefficient of Variation [%]		3.16	2.57	3.11	1.50

Figure C-17. Failure modes for carbon Unitape $[30^{\circ}/-30^{\circ}]_{2S}$ at a speed of 0.0008 in/s, in tension

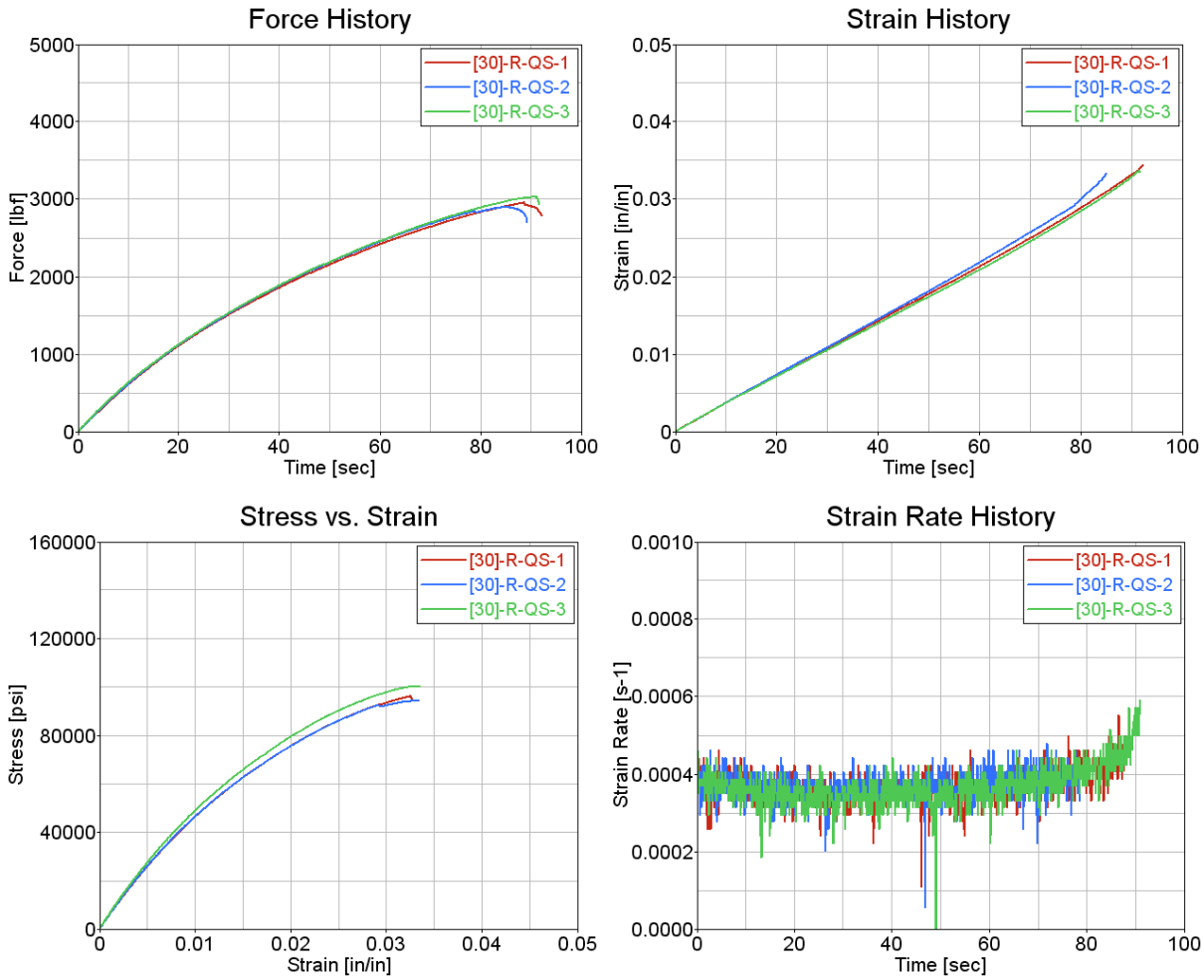

Figure C-18. Test results for carbon Unitape $[30^{\circ}/-30^{\circ}]_{2S}$ at a speed of 0.0008 in/s, in tension

Table C-8. Summary test results for carbon Unitape $[30^{\circ}/-30^{\circ}]_{2S}$ at a speed of 1 in/s, in tension

Actuator Speed [in/s]	Specimen ID	Tensile Strength [psi]	Maximum Recorded Strain [in/in]	Young's Modulus [Msi]	Average Strain Rate [s^{-1}]
1	[30]-R-1-1-4	117,530	0.0265	7.64	0.2635
	[30]-R-1-2-5	109,311	0.0243	7.73	0.2797
	[30]-R-1-3-6	114,884	0.0259	7.05	0.2535
Average		113,909	0.0255	7.47	0.2656
Standard Deviation		4,195	0.0011	0.37	0.0132
Coefficient of Variation [%]		3.68	4.35	4.94	4.98

Figure C-19. Failure modes for carbon Unitape $[30^{\circ}/-30^{\circ}]_{2S}$ at a speed of 1 in/s, in tension

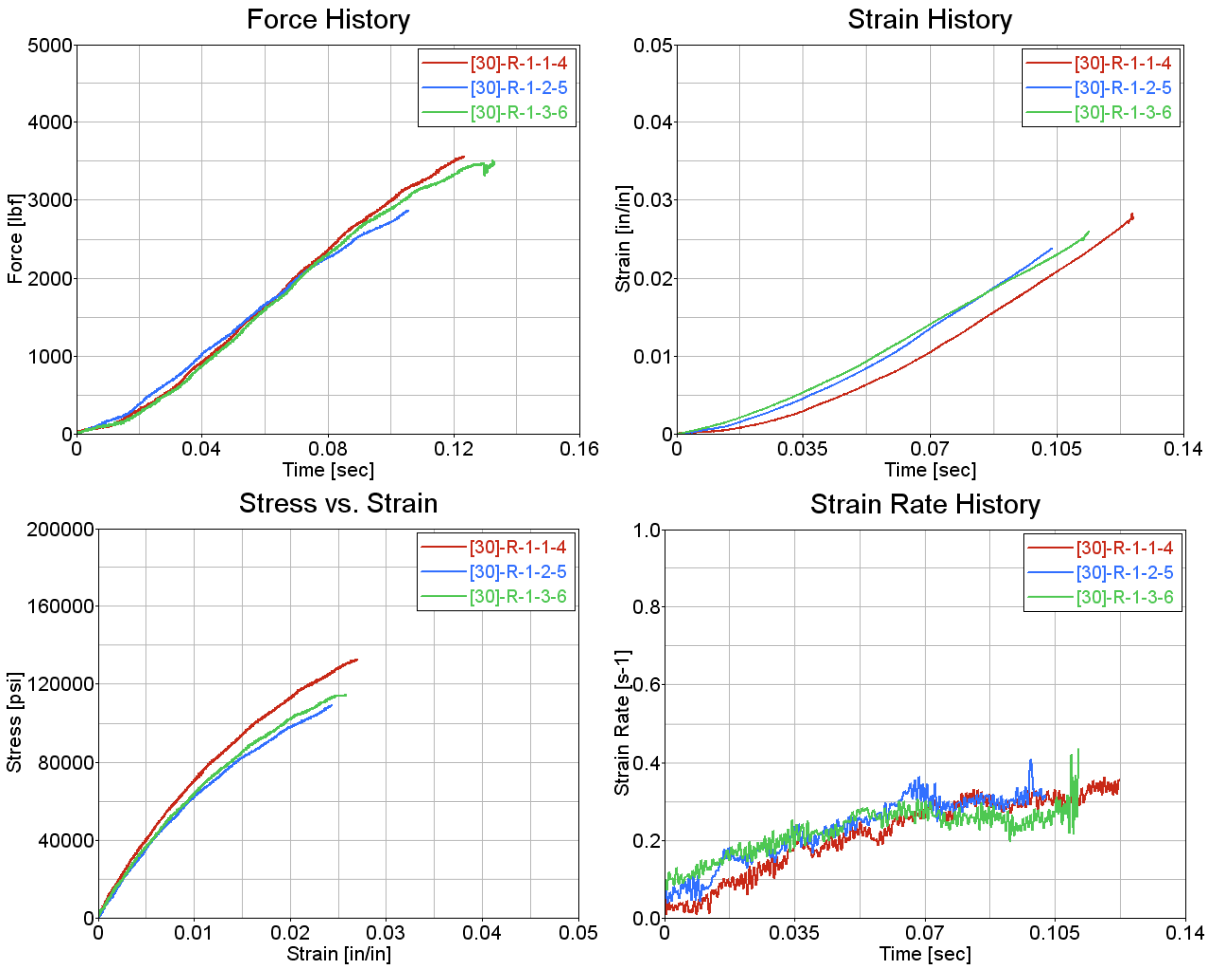

Figure C-20. Test results for carbon Unitape $[30^{\circ}/-30^{\circ}]_{2S}$ at a speed of 1 in/s, in tension

Table C-9. Summary of test results for carbon Unitape $[30^{\circ}/-30^{\circ}]_{2S}$ at a speed of 10 in/s, in tension

Actuator Speed [in/s]	Specimen ID	Tensile Strength [psi]	Maximum Recorded Strain [in/in]	Young's Modulus [Msi]	Average Strain Rate [s^{-1}]
10	[30]-R-10-1-7	124,488	0.0204	7.48	1.9123
	[30]-R-10-2-8	130,455	0.0172	8.13	1.9203
	[30]-R-10-3-9	126,204	0.0191	7.97	1.9624
Average		127,049	0.0189	7.86	1.9317
Standard Deviation		3,072	0.0016	0.34	0.0269
Coefficient of Variation [%]		2.42	8.53	4.29	1.39

Figure C-21. Failure modes for carbon Unitape $[30^{\circ}/-30^{\circ}]_{2S}$ at a speed of 10 in/s, in tension

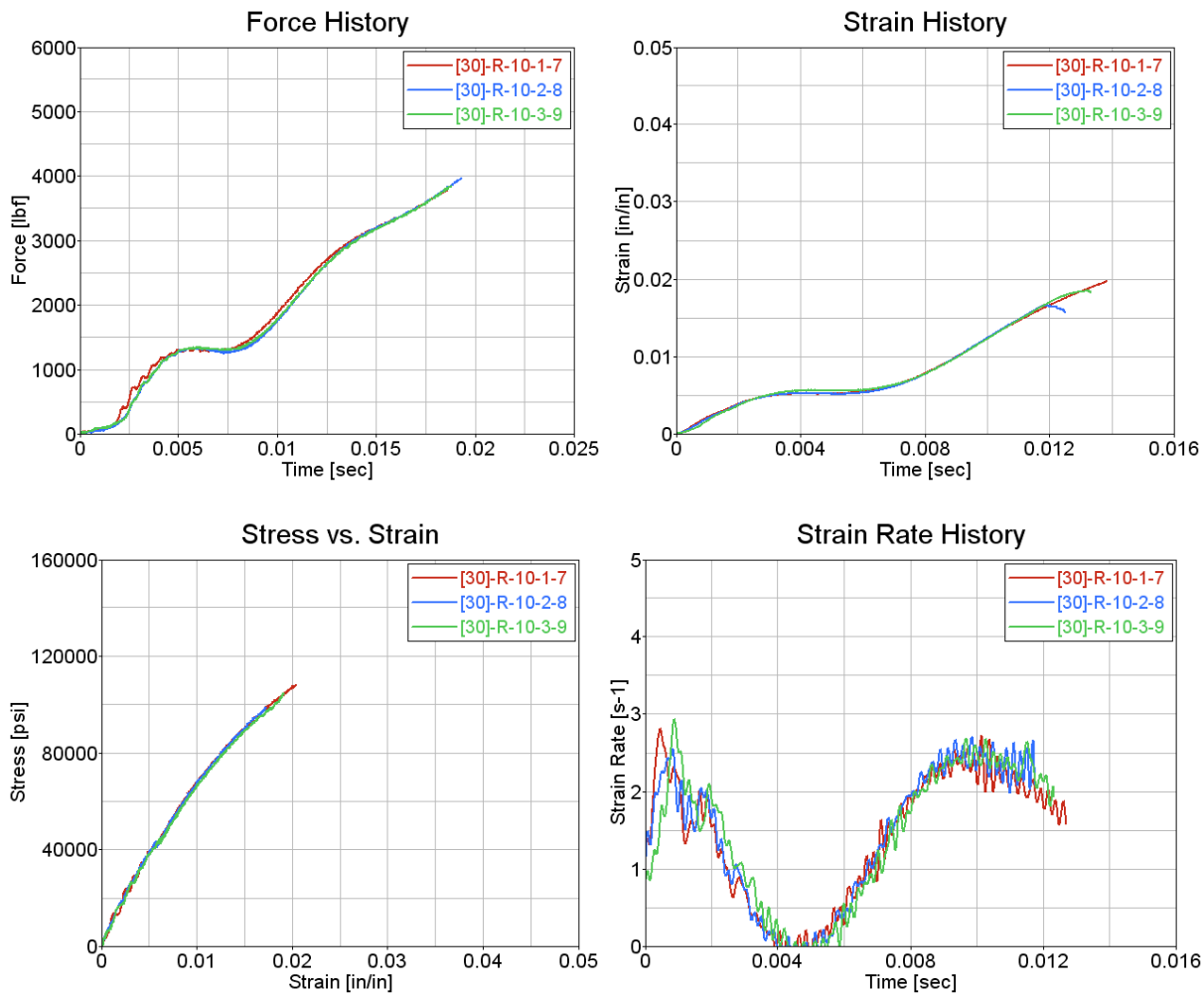

Figure C-22. Test results for carbon Unitape [30°/-30°]$_{2S}$ at a speed of 10 in/s, in tension

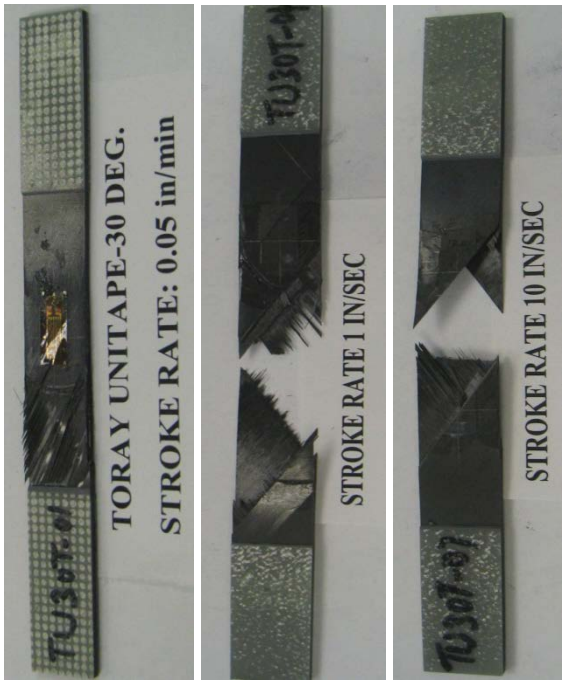

Figure C-23. Failure modes for carbon Unitape [30°/-30°]$_{2S}$: summary of all speeds, in tension

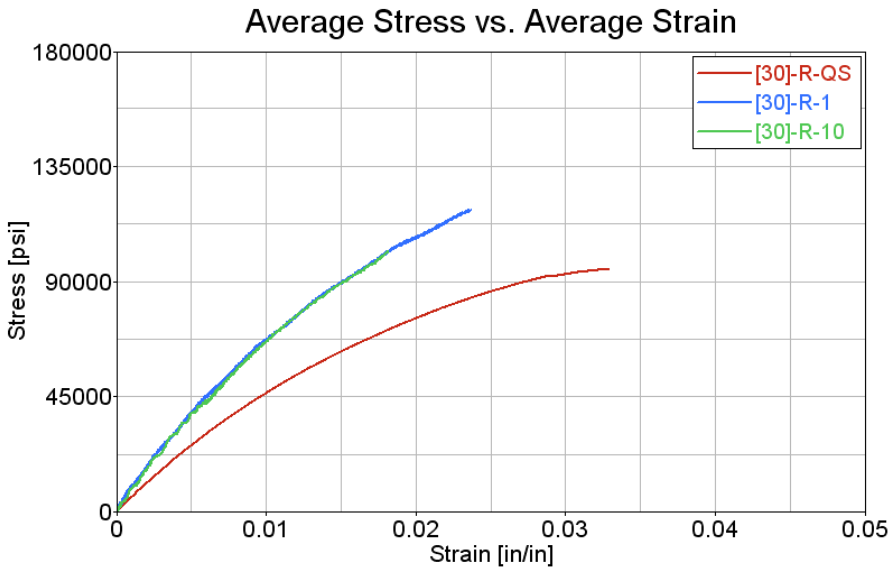

Figure C-24. Test results for carbon Unitape [30°/-30°]$_{2S}$: summary of all speeds, in tension

C.4 CARBON UNITAPE $[45^{\circ}/-45^{\circ}]_{2S}$

Table C-10. Summary of test results for carbon Unitape $[45^{\circ}/-45^{\circ}]_{2S}$ at a speed of 0.0008 in/s, in tension

Actuator Speed [in/s]	Specimen ID	Tensile Strength [psi]	Maximum Recorded Strain [in/in]	Young's Modulus [Msi]	Average Strain Rate [s^{-1}]
0.00083	[45]-R-QS-1	36,164	*	1.97	0.000440
	[45]-R-QS-2	34,265	*	2.07	0.000570
	[45]-R-QS-3	37,832	*	2.22	0.000386
Average		36,087	-	2.09	0.000465
Standard Deviation		1,785	-	0.13	0.000095
Coefficient of Variation [%]		4.95	-	6.26	20.33

*Exceeded strain gage capability of 0.05 in/in

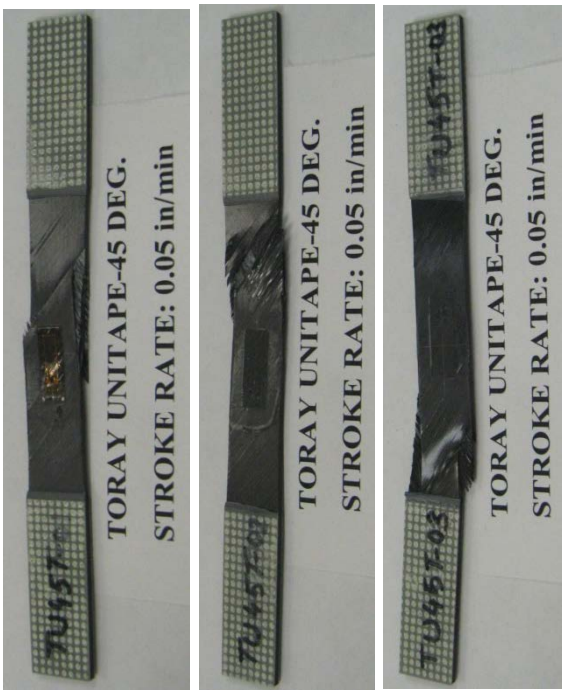

Figure C-25. Failure modes for carbon Unitape [45°/-45°]2S at a speed of 0.0008 in/s, in tension

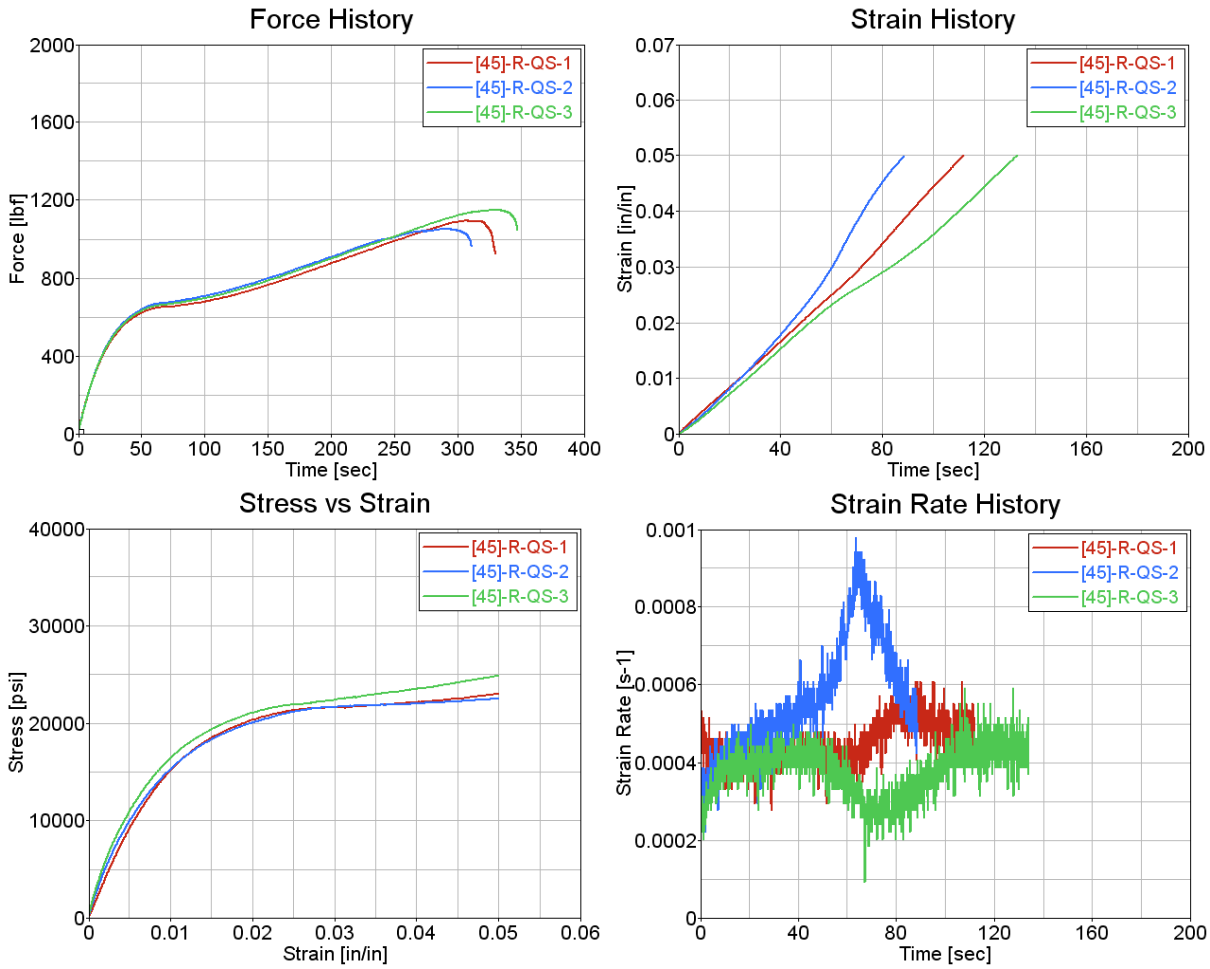

Figure C-26. Test results for carbon Unitape $[45^{\circ}/-45^{\circ}]_{2S}$ at a speed of 0.0008 in/s, in tension

Table C-11. Summary of test results for carbon Unitape [45°/-45°]$_{2S}$ at a speed of 1 in/s, in tension

Actuator Speed [in/s]	Specimen ID	Tensile Strength [psi]	Maximum Recorded Strain [in/in]	Young's Modulus [Msi]	Average Strain Rate [s^{-1}]
1	[45]-R-1-1-4	40,535	*	2.73	0.6200
	[45]-R-1-2-5	33,766	*	2.82	0.4840
	[45]-R-1-3-6	43,771	*	2.31	0.4650
Average		39,357	-	2.62	0.5230
Standard Deviation		5,105	-	0.28	0.0845
Coefficient of Variation [%]		12.97	-	10.51	16.16

*Exceeded strain gage capability of 0.05 in/in

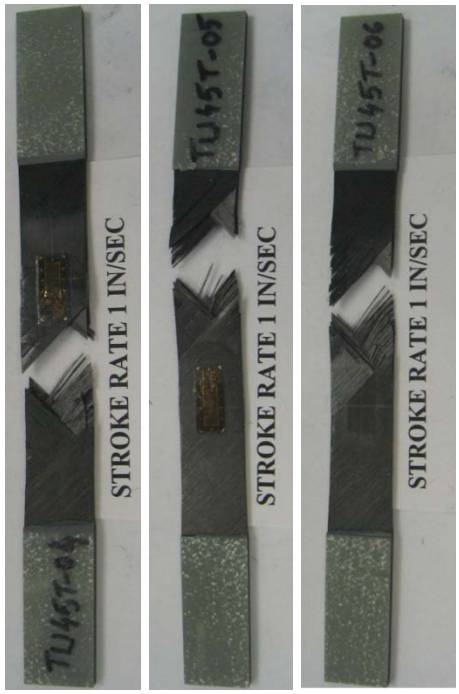

Figure C-27. Failure modes for carbon Unitape [45°/-45°]$_{2S}$ at a speed of 1 in/s, in tension

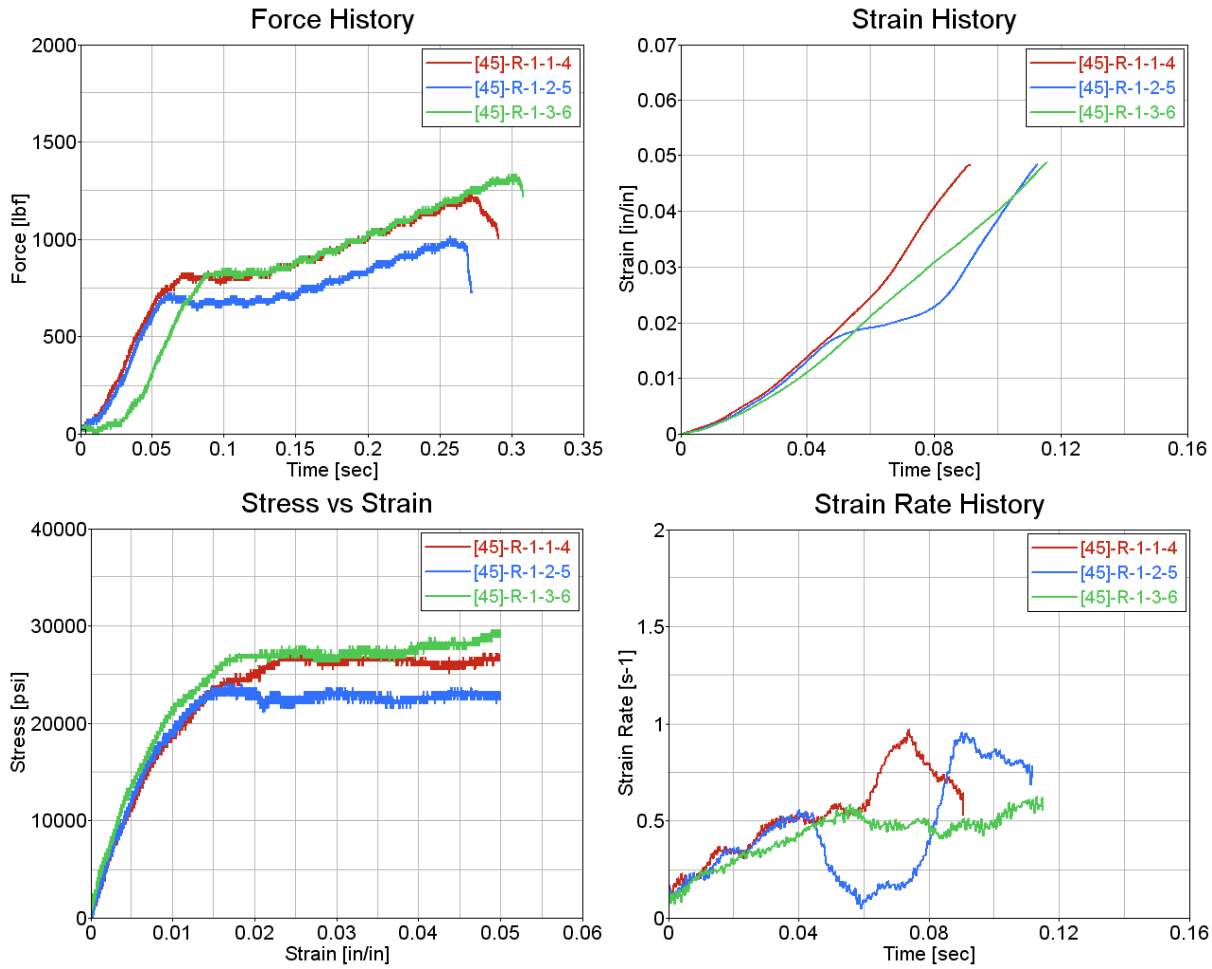

Figure C-28. Test results for carbon Unitape [45°/-45°]$_{2S}$ at a speed of 1 in/s, in tension

Table C-12. Summary of test results for carbon Unitape [45°/-45°]$_{2S}$ at a speed of 10 in/s, in tension

Actuator Speed [in/s]	Specimen ID	Tensile Strength [psi]	Maximum Recorded Strain [in/in]	Young's Modulus [Msi]	Average Strain Rate [s^{-1}]
10	[45]-R-10-1-7	42,220	**	2.98	2.8345
	[45]-R-10-1-8	47,005	*	3.15	2.6981
	[45]-R-10-1-9	40,483	*	3.88	2.8595
Average		43,236	-	3.34	2.7974
Standard Deviation		3,378	-	0.48	0.0869
Coefficient of Variation [%]		7.81	-	14.44	3.11

*Exceeded strain gage capability of 0.05 in/in
**Strain gage detached from testing specimen

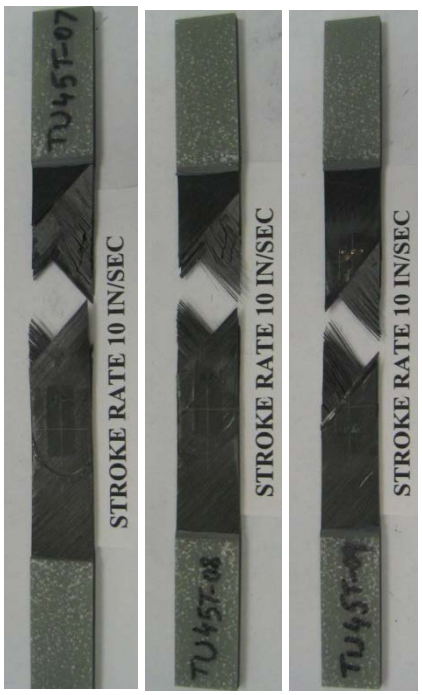

Figure C-29. Failure modes for carbon Unitape [45°/-45°]$_{2S}$ at a speed of 10 in/s, in tension

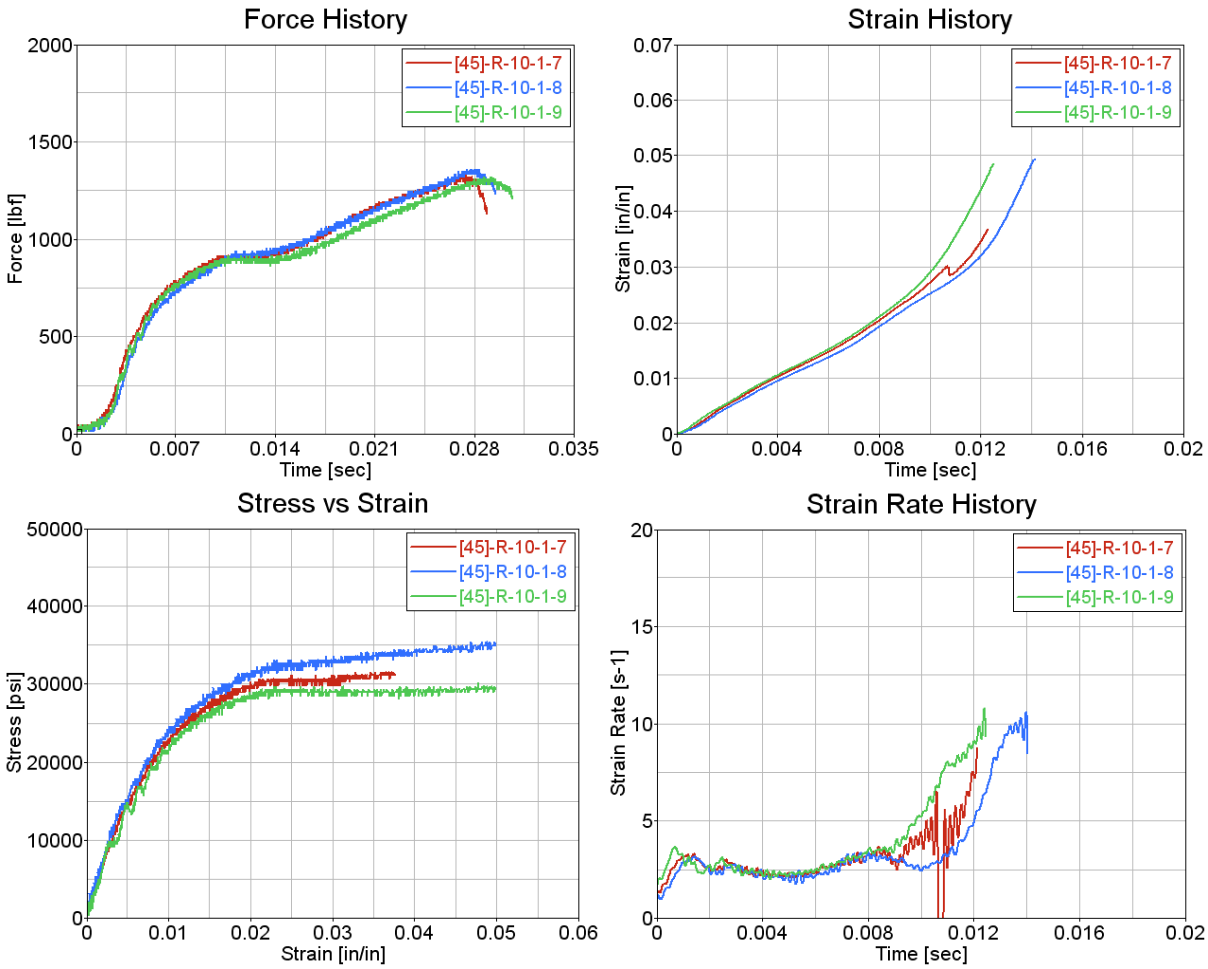

Figure C-30. Test results for carbon Unitape [45°/-45°]$_{2S}$ at a speed of 10 in/s, in tension

Figure C-31. Failure modes for carbon Unitape $[45^{\circ}/-45^{\circ}]_{2S}$: summary of all speeds, in tension

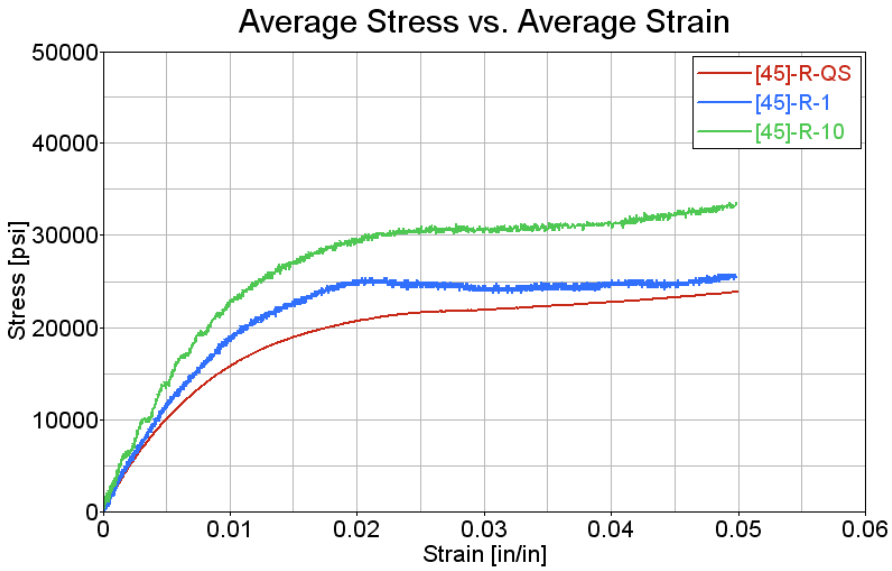

Figure C-32. Test results for carbon Unitape $[45^{\circ}/-45^{\circ}]_{2S}$: summary of all speeds, in tension

APPENDIX D—TORAY T700G-12K-PW/3900-2 CARBON FABRIC TENSION TESTING RESULTS

D.1 CARBON FABRIC $[0^{\circ}]_4$

Table D-1. Summary of test results for carbon fabric $[0^{\circ}]_4$ at a speed of 0.0008 in/s, in tension

Actuator Speed [in/s]	Specimen ID	Tensile Strength [psi]	Maximum Recorded Strain [in/in]	Young's Modulus [Msi]	Average Strain Rate [s^{-1}]
0.00083	[0]-R-QS-1	101,207	0.0129	7.13	0.000326
	[0]-R-QS-2	98,834	0.0134	6.69	0.000335
	[0]-R-QS-3	143,644	0.0165	7.63	0.000294
Average		114,562	0.0143	7.15	0.000318
Standard Deviation		25,214	0.0020	0.47	0.000022
Coefficient of Variation [%]		22.01	13.76	6.60	6.77

Figure D-1. Failure modes for carbon fabric $[0^{\circ}]_4$ at a speed of 0.0008 in/s, in tension

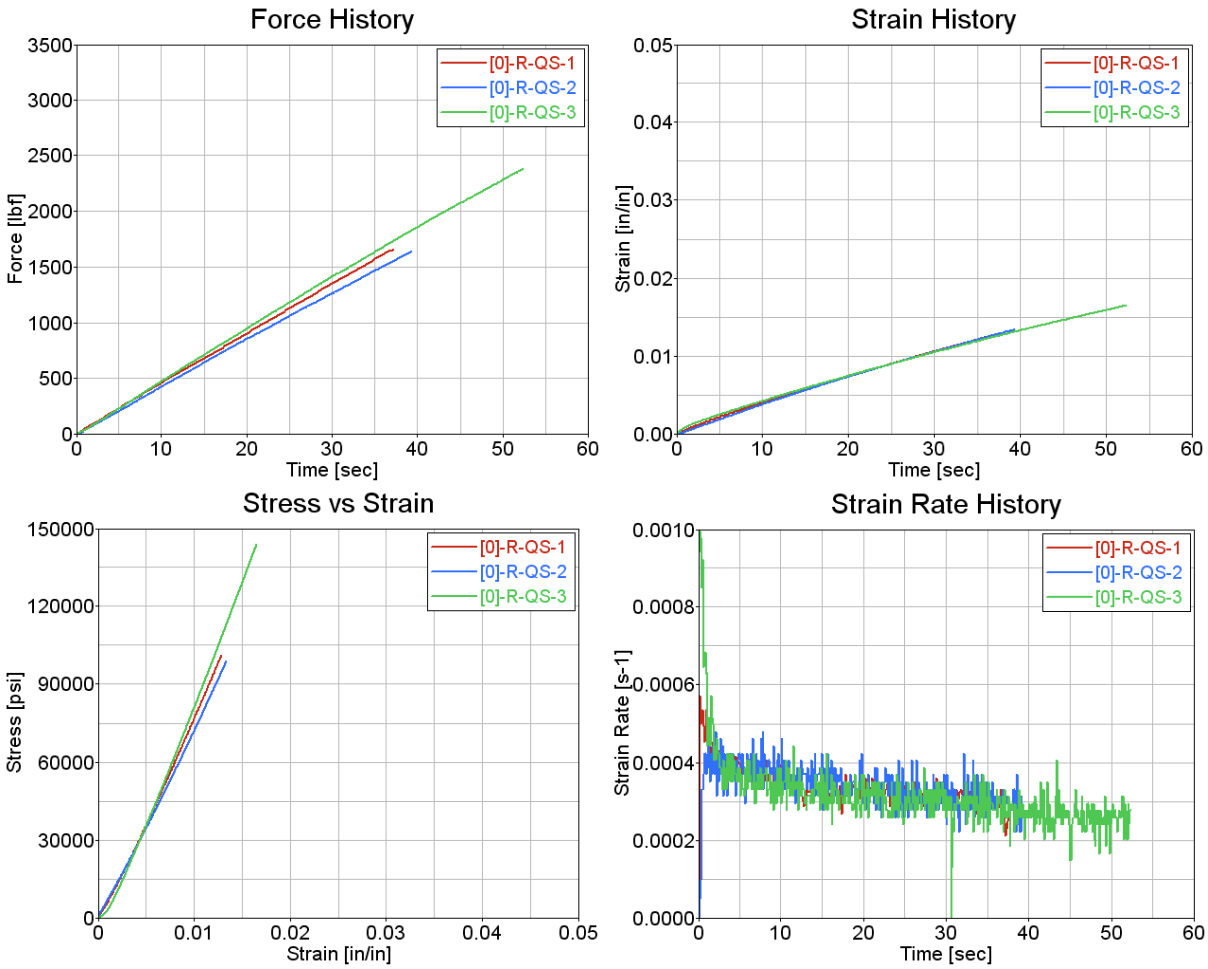

Figure D-2. Test results for carbon fabric $[0^{\circ}]_4$ at a speed of 0.0008 in/s, in tension

Table D-2. Summary of test results for carbon fabric $[0^{\circ}]_4$ at a speed of 1 in/s, in tension

Actuator Speed [in/s]	Specimen ID	Tensile Strength [psi]	Maximum Recorded Strain [in/in]	Young's Modulus [Msi]	Average Strain Rate [s^{-1}]
1	[0]-R-1-1-4	137,930	0.0120	11.31	0.1829
	[0]-R-1-2-5	90,927	0.0097	9.13	0.1829
	[0]-R-1-3-6	139,943	0.0124	10.24	0.1952
Average		122,934	0.0114	10.23	0.1870
Standard Deviation		27,736	0.0014	1.09	0.0071
Coefficient of Variation [%]		22.56	12.61	10.68	3.80

Figure D-3. Failure modes for carbon fabric $[0^{\circ}]_4$ at a speed of 1 in/s, in tension

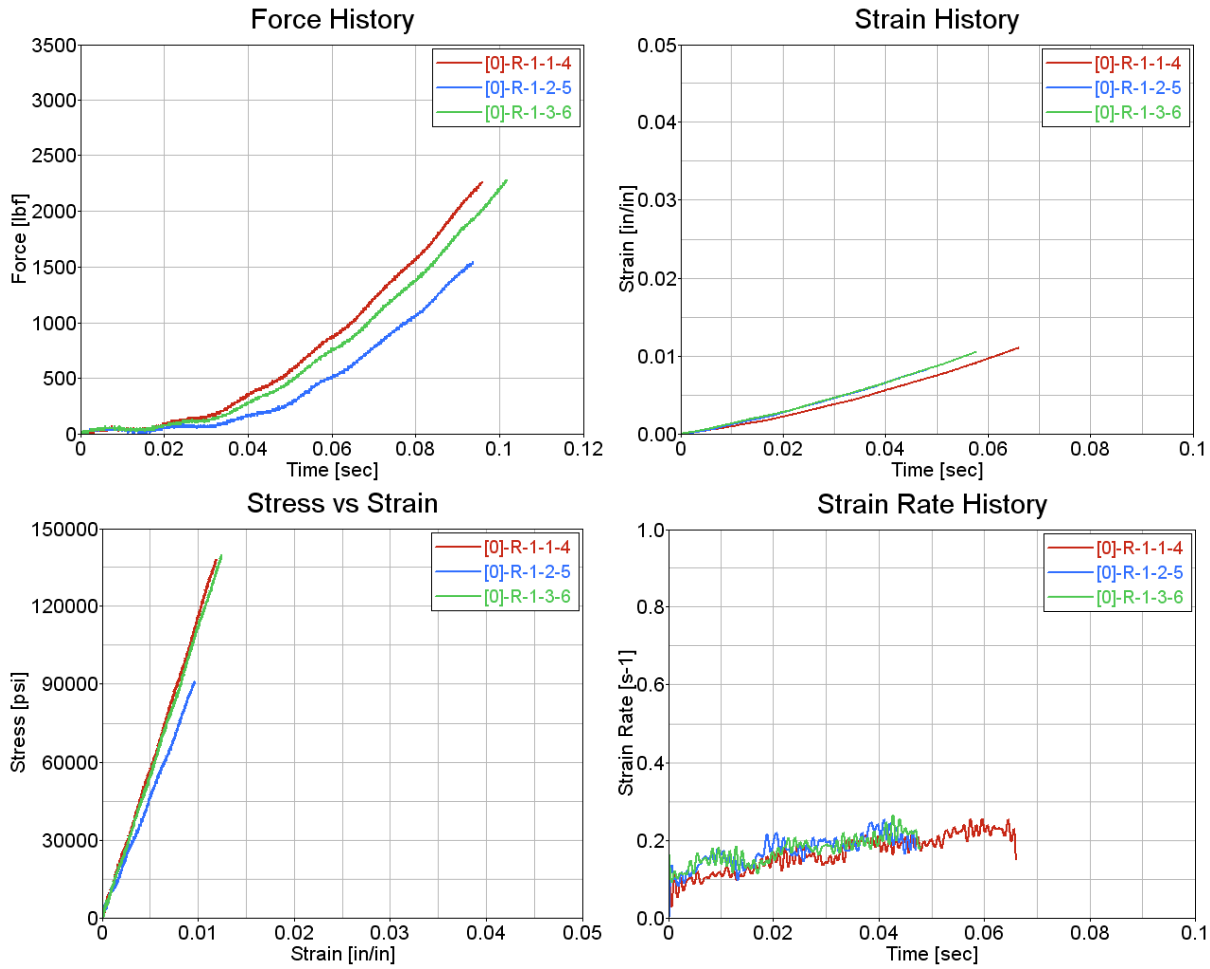

Figure D-4. Test results for carbon fabric $[0^{\circ}]_4$ at a speed of 1 in/s, in tension

Table D-3. Summary of test results for carbon fabric [0°]4 at a speed of 10 in/s, in tension

Actuator Speed [in/s]	Specimen ID	Tensile Strength [psi]	Maximum Recorded Strain [in/in]	Young's Modulus [Msi]	Average Strain Rate [s^{-1}]
10	[0]-R-10-1-8	134,818	0.0120	10.58	1.0000
	[0]-R-10-2-9	120,483	0.0121	9.40	1.1097
	[0]-R-10-3-10	96,103	0.0102	9.36	0.7924
Average		117,135	0.0114	9.78	0.9674
Standard Deviation		19,574	0.0011	0.69	0.1611
Coefficient of Variation [%]		16.71	9.33	7.10	16.66

Figure D-5. Failure modes for carbon fabric $[0^{\circ}]_4$ at a speed of 10 in/s, in tension

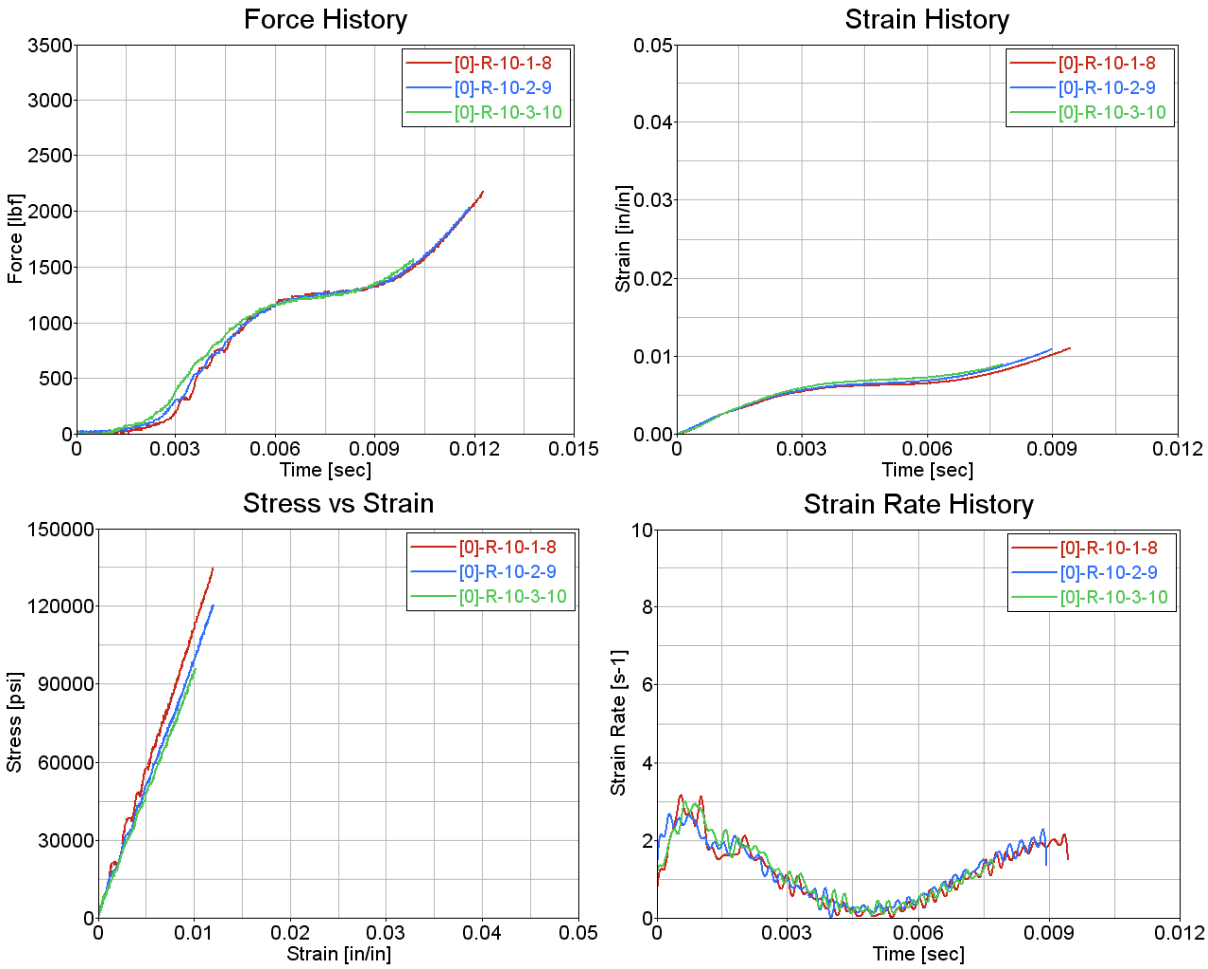

Figure D-6. Test results for carbon fabric $[0^{\circ}]_4$ at a speed of 10 in/s, in tension

Figure D-7. Failure modes for carbon fabric $[0^{\circ}]_4$: summary of all speeds, in tension

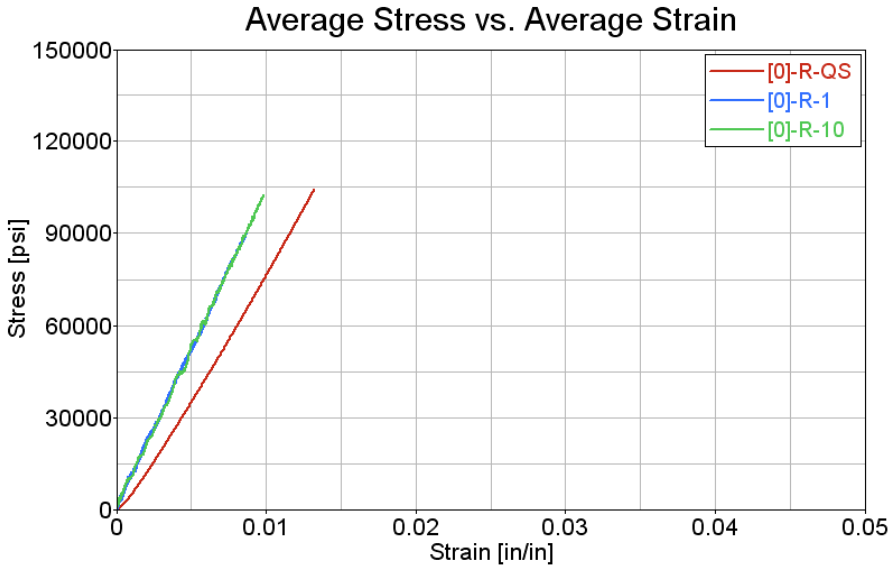

Figure D-8. Test results carbon fabric $[0^{\circ}]_4$: summary of all speeds, in tension

D.2 CARBON FABRIC $[15^{\circ}/-15^{\circ}]_{2S}$

Table D-4. Summary of test results for carbon fabric $[15^{\circ}/-15^{\circ}]_{2S}$ at a speed of 0.0008 in/s, in tension

Actuator Speed [in/s]	Specimen ID	Tensile Strength [psi]	Maximum Recorded Strain [in/in]	Young's Modulus [Msi]	Average Strain Rate [s^{-1}]
0.00083	[15]-R-QS-1	101,659	0.0154	6.44	0.000252
	[15]-R-QS-2	96,099	0.0154	6.00	0.000250
	[15]-R-QS-3	85,749	0.0130	6.24	0.000255
Average		94,502	0.0146	6.23	0.000252
Standard Deviation		8,074	0.0014	0.22	0.000003
Coefficient of Variation [%]		8.54	9.38	3.54	1.00

Figure D-9. Failure modes for carbon fabric $[15^{\circ}/-15^{\circ}]_{2S}$ at a speed of 0.0008 in/s, in tension

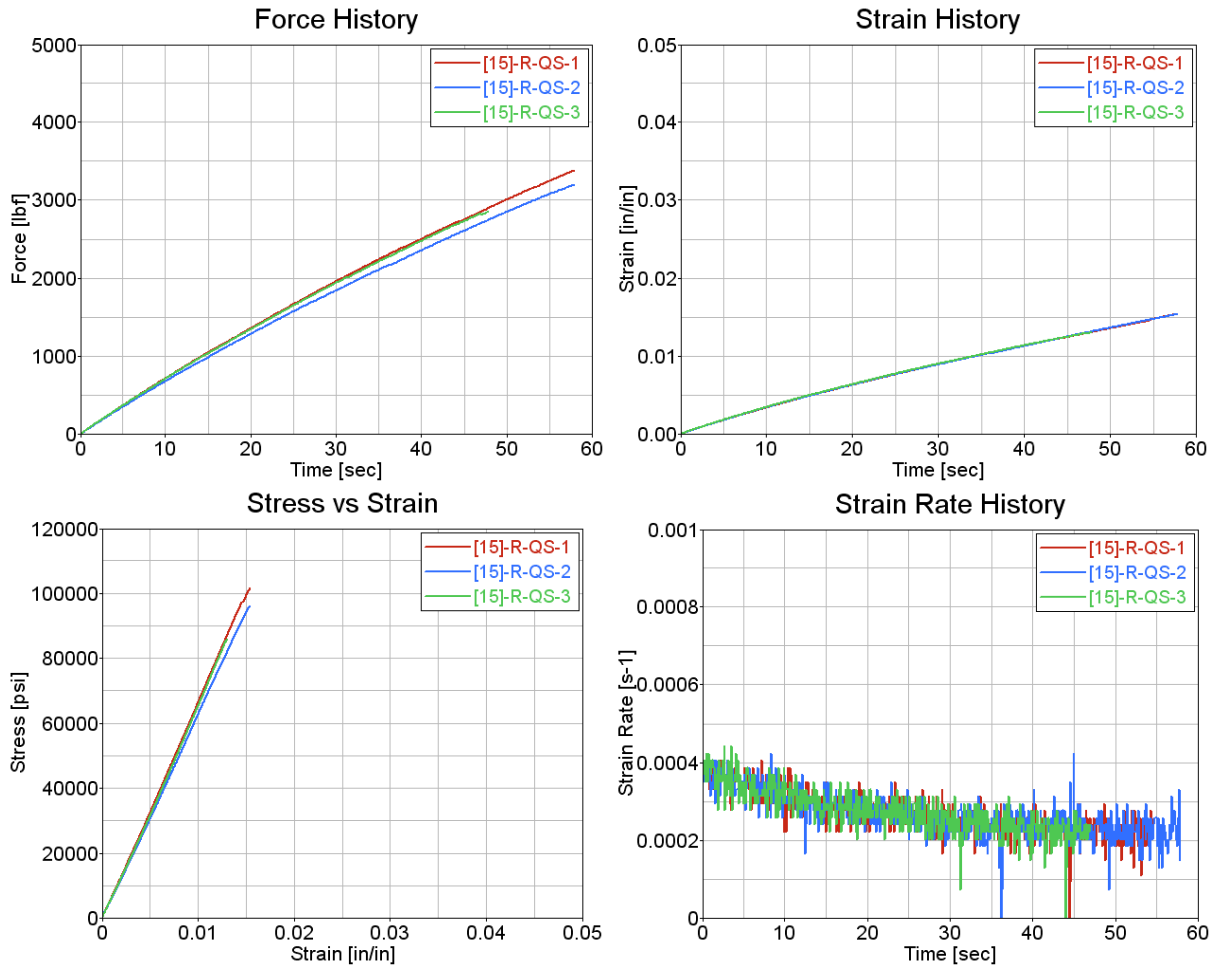

Figure D-10. Test results for carbon fabric $[15^{\circ}/-15^{\circ}]_{2S}$ at a speed of 0.0008 in/s, in tension

Table D-5. Summary of test results for carbon fabric $[15^{\circ}/-15^{\circ}]_{2S}$ at a speed of 1 in/s, in tension

Actuator Speed [in/s]	Specimen ID	Tensile Strength [psi]	Maximum Recorded Strain [in/in]	Young's Modulus [Msi]	Average Strain Rate [s^{-1}]
1	[15]-R-1-1-4	98,846	0.0124	7.48	0.1629
	[15]-R-1-2-5	104,454	0.0136	7.41	0.1656
	[15]-R-1-3-6	98,047	0.0123	8.17	0.1581
Average		100,449	0.0127	7.69	0.1622
Standard Deviation		3,491	0.0007	0.42	0.0038
Coefficient of Variation [%]		3.48	5.60	5.45	2.34

Figure D-11. Failure modes for carbon fabric $[15^{\circ}/-15^{\circ}]_{2S}$ at a speed of 1 in/s, in tension

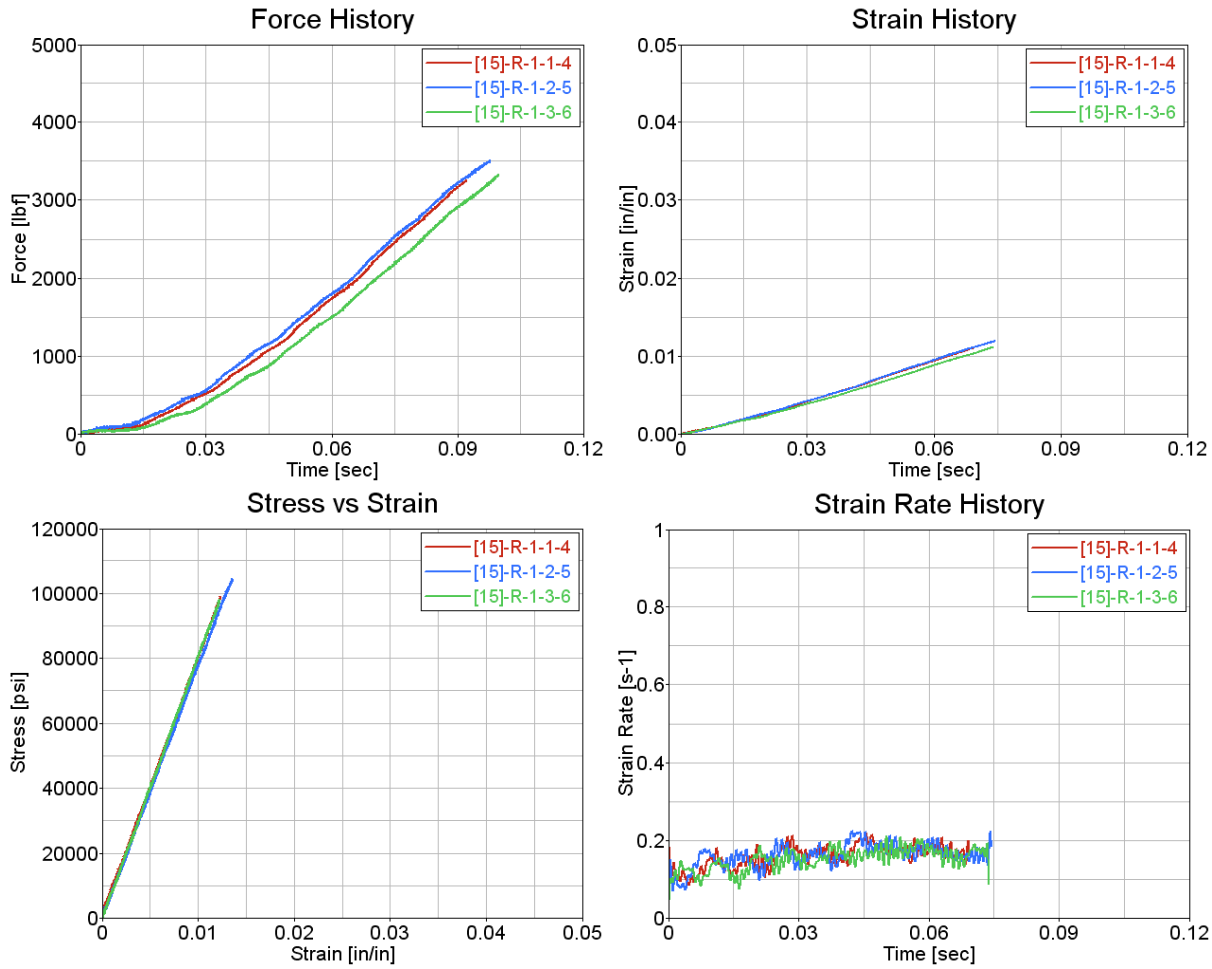

Figure D-12. Test results for carbon fabric $[15^{\circ}/-15^{\circ}]_{2S}$ at a speed of 1 in/s, in tension

Table D-6. Summary of test results for carbon fabric $[15^{\circ}/-15^{\circ}]_{2S}$ at a speed of 10 in/s, in tension

Actuator Speed [in/s]	Specimen ID	Tensile Strength [psi]	Maximum Recorded Strain [in/in]	Young's Modulus [Msi]	Average Strain Rate [s^{-1}]
10	[15]-R-10-1-7	101,816	0.0126	8.96	1.4734
	[15]-R-10-2-8	100,859	0.0130	7.79	1.5320
	[15]-R-10-3-9	101,846	0.01215	8.77	1.4229
Average		101,507	0.0122	8.51	1.4761
Standard Deviation		562	0.0004	0.63	0.0546
Coefficient of Variation [%]		0.55	3.23	7.38	3.70

Figure D-13. Failure modes for carbon fabric $[15^{\circ}/-15^{\circ}]_{2S}$ at a speed of 10 in/s, in tension

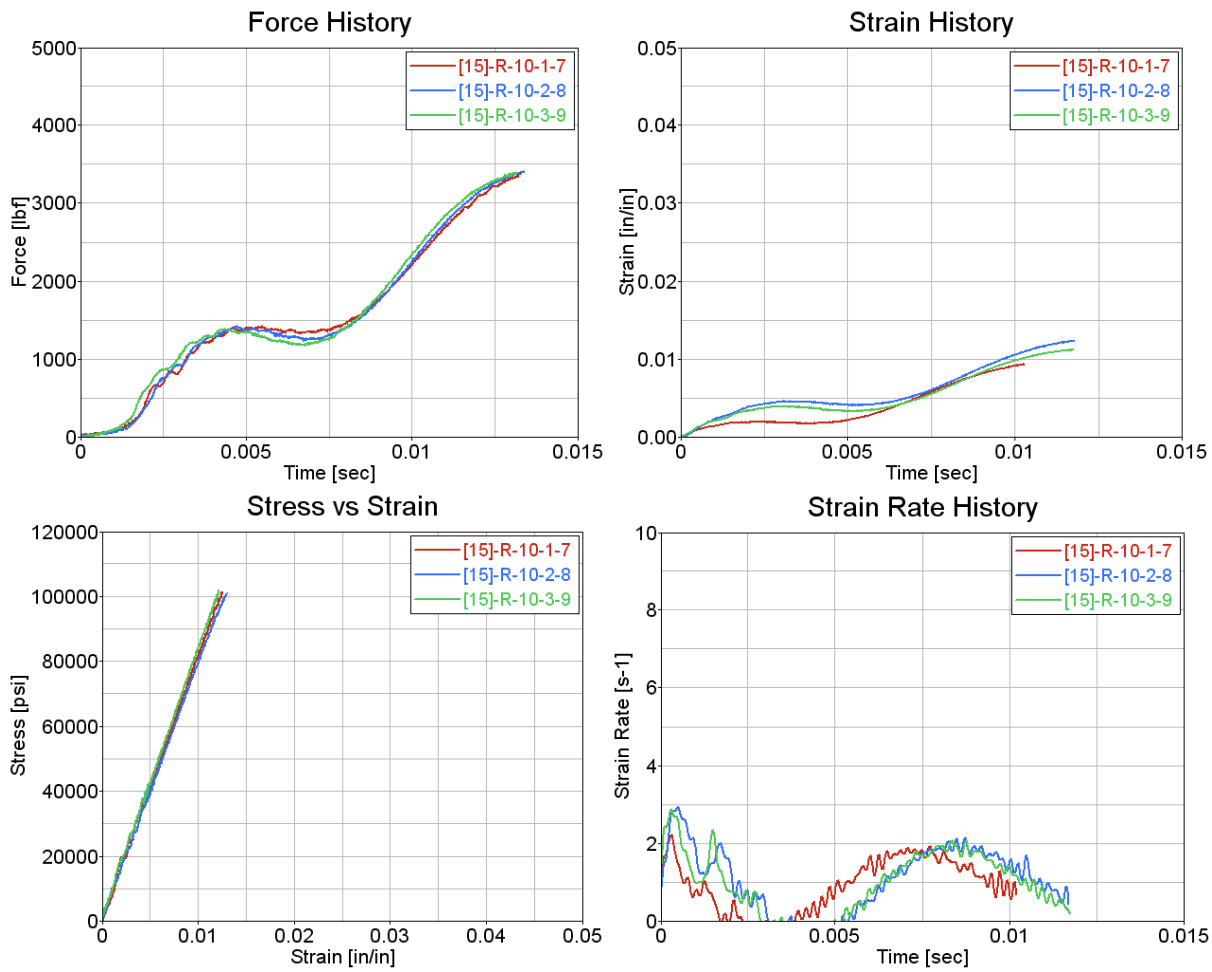

Figure D-14. Test results for carbon fabric [15°/-15°]$_{2S}$ at a speed of 10 in/s, in tension

Figure D-15. Failure modes for carbon fabric $[15^{\circ}/-15^{\circ}]_{2S}$: summary of all speed, in tension

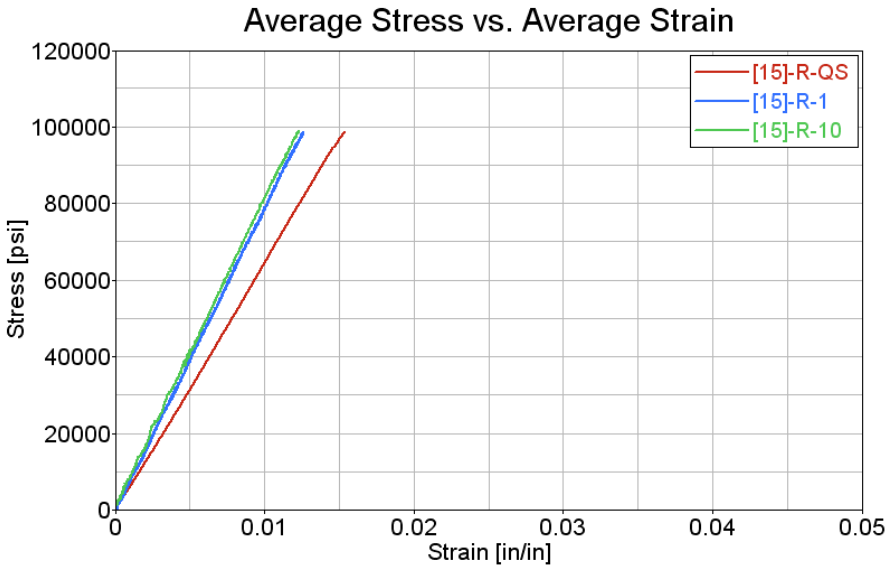

Figure D-16. Test results for carbon fabric $[15^{\circ}/-15^{\circ}]_{2S}$: summary of all speeds, in tension

D.3 CARBON FABRIC $[30^{\circ}/-30^{\circ}]_{2S}$

Table D-7. Summary test results carbon fabric $[30^{\circ}/-30^{\circ}]_{2S}$ at a speed of 0.0008 in/s, in tension

Actuator Speed [in/s]	Specimen ID	Tensile Strength [psi]	Maximum Recorded Strain [in/in]	Young's Modulus [Msi]	Average Strain Rate [s^{-1}]
0.00083	[30]-R-QS-1	62,367	0.0220	3.18	0.000346
	[30]-R-QS-2	66,894	0.0207	3.56	0.000310
	[30]-R-QS-3	65,855	0.0213	3.50	0.000320
Average		65,039	0.0213	3.41	0.000325
Standard Deviation		2,371	0.0006	0.21	0.000019
Coefficient of Variation [%]		3.65	2.94	6.07	5.71

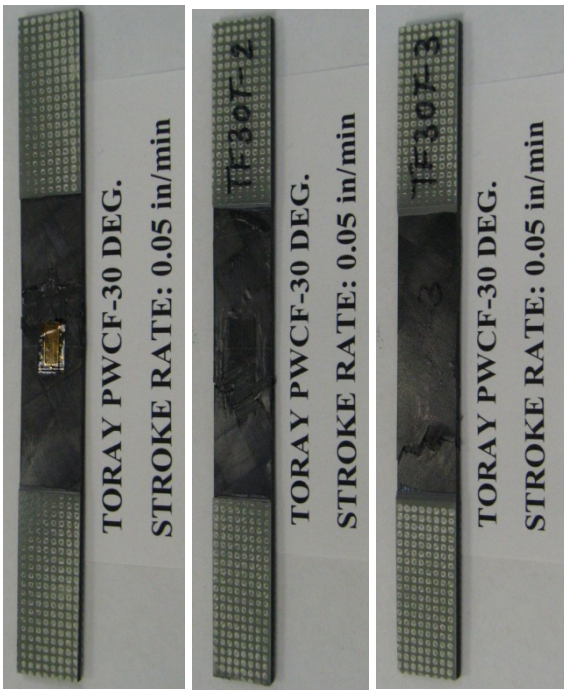

Figure D-17. Failure modes for carbon fabric $[30^{\circ}/-30^{\circ}]_{2S}$ at a speed of 0.0008 in/s, in tension

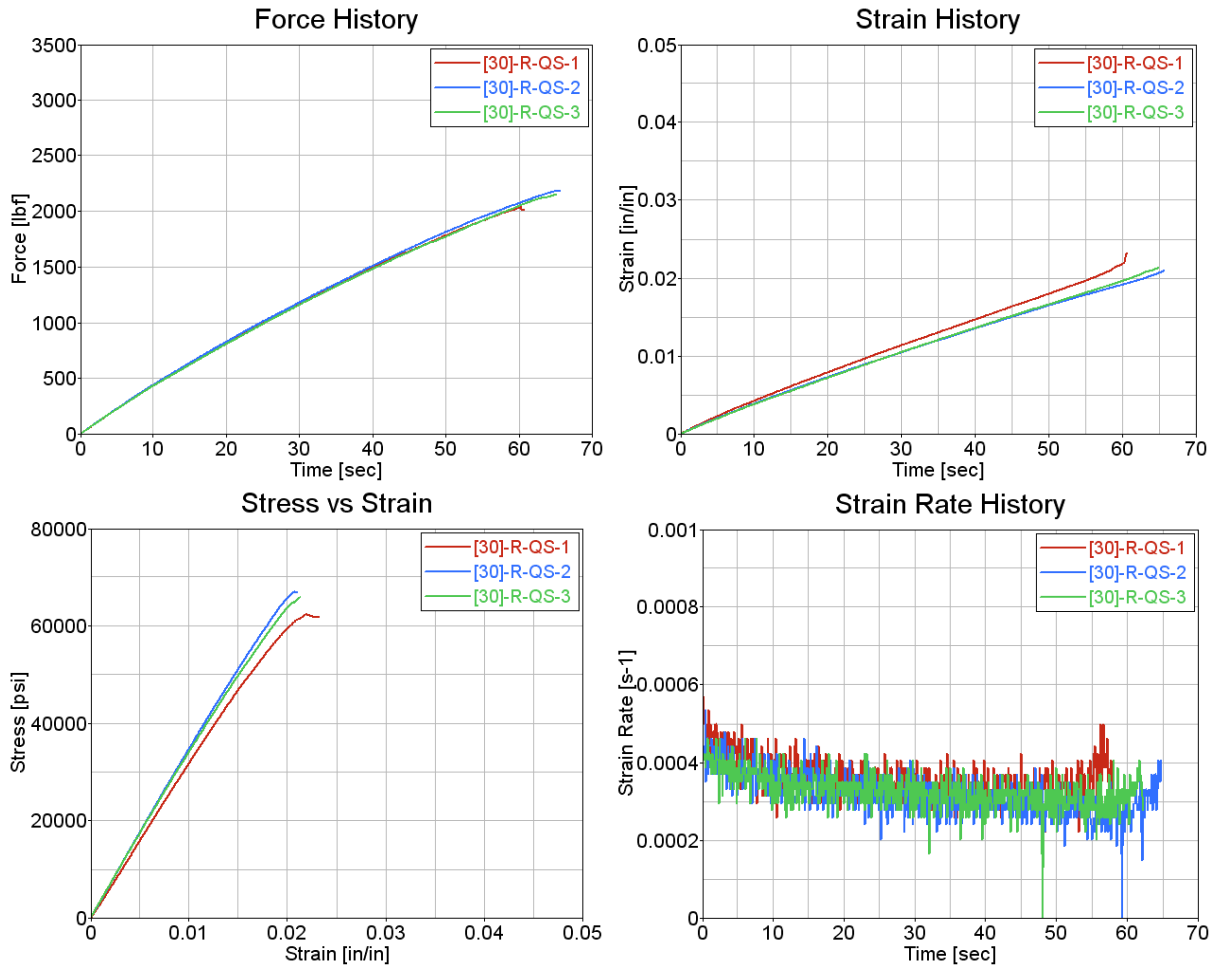

Figure D-18. Test results for carbon fabric [30°/-30°]$_{2S}$ at a speed of 0.0008 in/s, in tension

Table D-8. Summary of test results for carbon fabric $[30^{\circ}/-30^{\circ}]_{2S}$ at a speed of 1 in/s, in tension

Actuator Speed [in/s]	Specimen ID	Tensile Strength [psi]	Maximum Recorded Strain [in/in]	Young's Modulus [Msi]	Average Strain Rate [s^{-1}]
1	[30]-R-1-1-4	65,209	0.0163	4.04	0.2307
	[30]-R-1-2-6	69,042	0.0163	5.03	0.2221
	[30]-R-1-3-7	71,481	0.0175	4.30	0.2327
Average		68,577	0.0167	4.46	0.2285
Standard Deviation		3,162	0.0007	0.51	0.0056
Coefficient of Variation [%]		4.61	4.22	11.53	2.46

Figure D-19. Failure modes for carbon fabric $[30^{\circ}/-30^{\circ}]_{2S}$ at a speed of 1 in/s, in tension

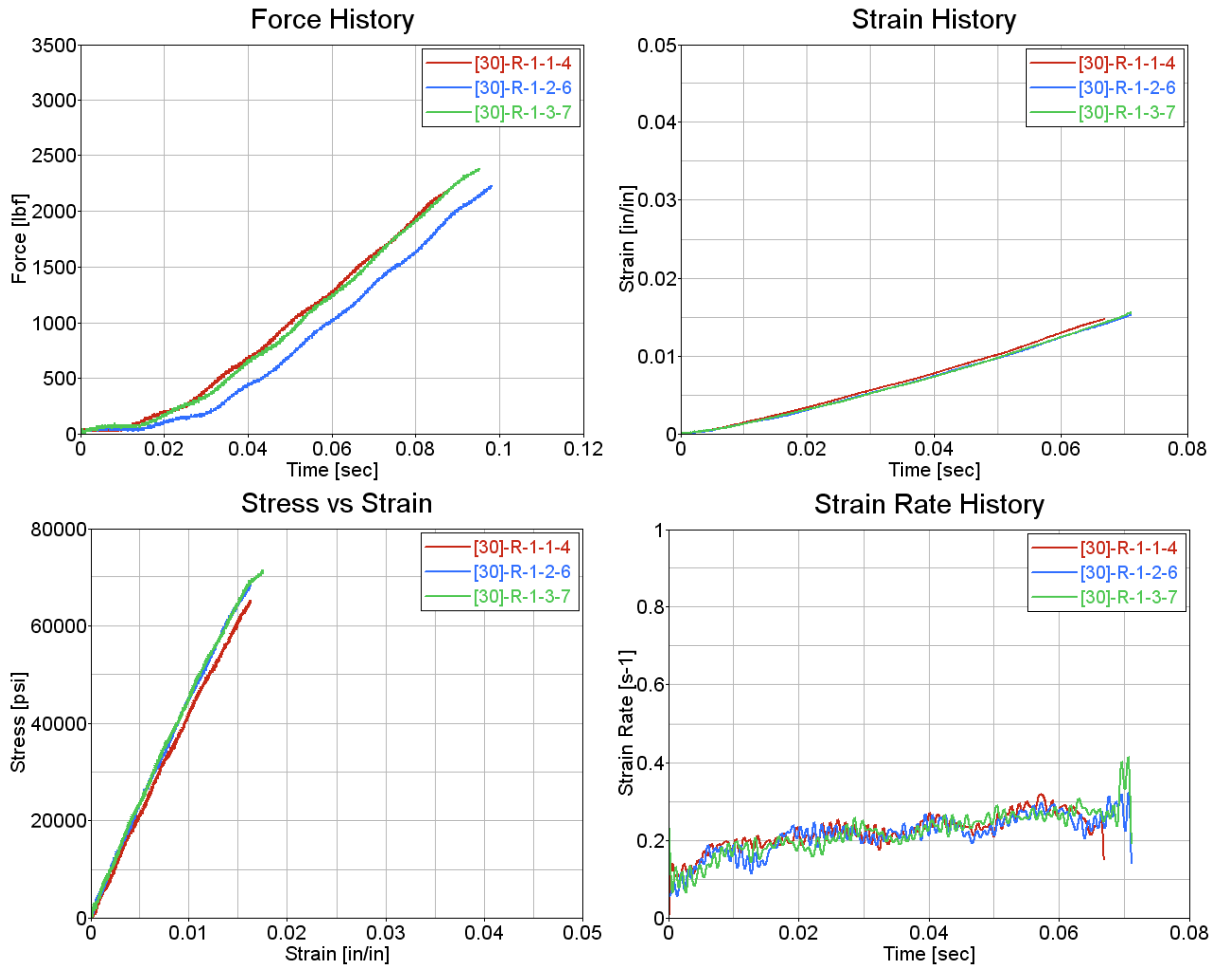

Figure D-20. Test results for carbon fabric $[30^{\circ}/-30^{\circ}]_{2S}$ at a speed of 1 in/s, in tension

Table D-9. Summary of test results for carbon fabric [30°/-30°]$_{2S}$ at a speed of 10 in/s, in tension

Actuator Speed [in/s]	Specimen ID	Tensile Strength [psi]	Maximum Recorded Strain [in/in]	Young's Modulus [Msi]	Average Strain Rate [s^{-1}]
10	[30]-R-10-1-8	70,034	0.0176	4.17	1.8572
	[30]-R-10-2-9	73,141	0.0195	4.02	1.9768
	[30]-R-10-3-10	74,097	0.0169	4.88	1.6969
Average		72,424	0.0180	4.36	1.8436
Standard Deviation		2,124	0.0013	0.46	0.1404
Coefficient of Variation [%]		2.93	7.30	10.54	7.62

Figure D-21. Failure modes for carbon fabric [30°/-30°]$_{2S}$ at a speed of 10 in/s, in tension

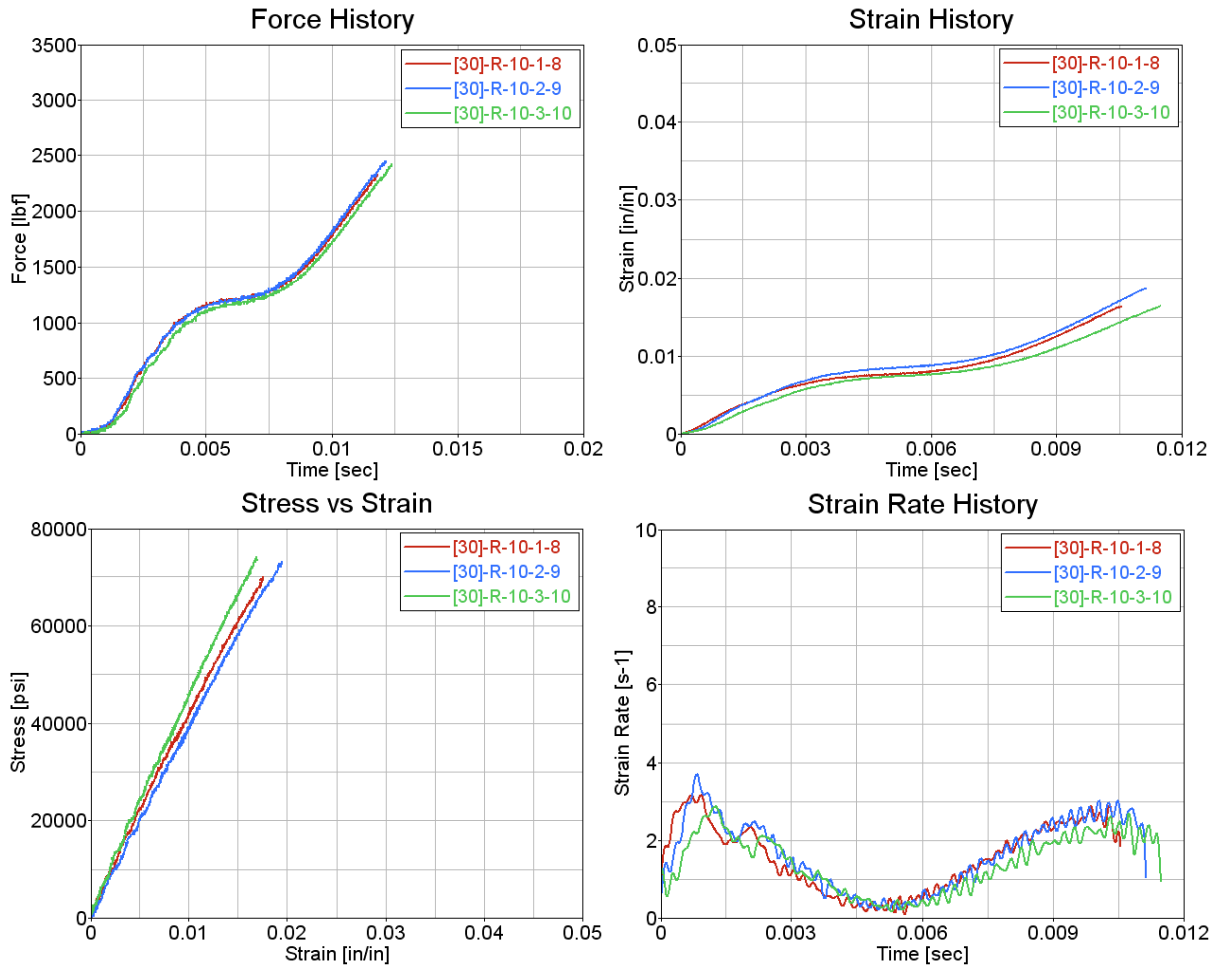

Figure D-22. Test results for carbon fabric [30°/-30°]$_{2S}$ at a speed of 10 in/s, in tension

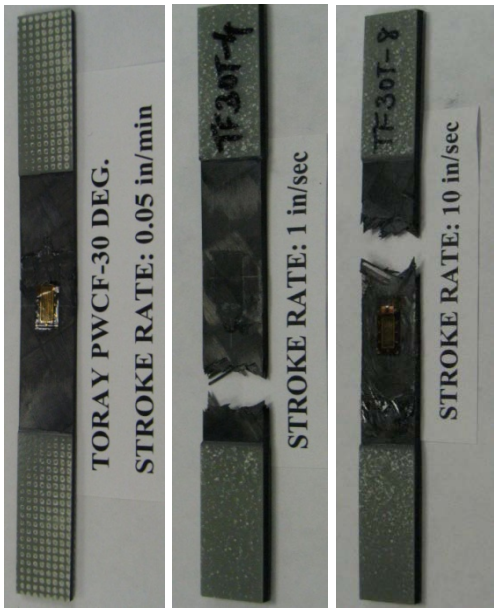

Figure D-23. Failure modes for carbon fabric [30°/-30°]$_{2S}$: summary of all speeds, in tension

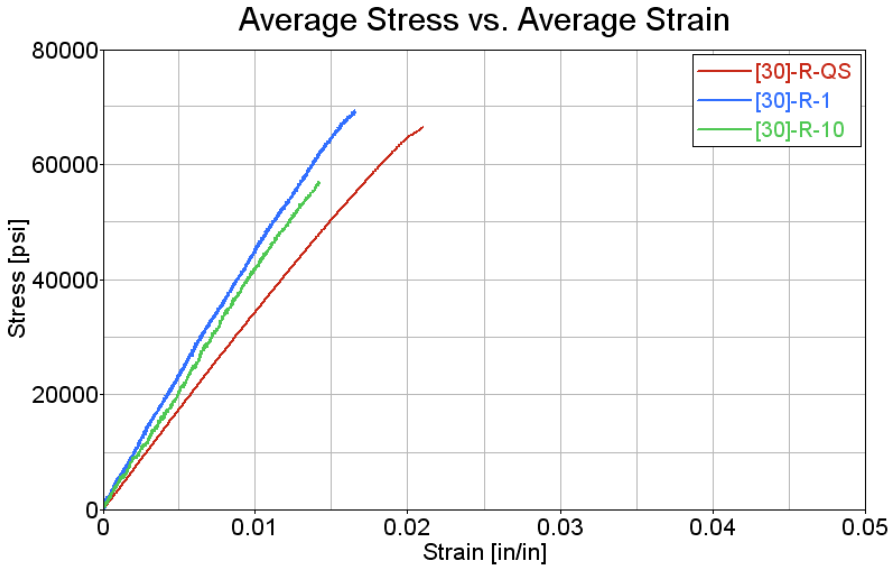

Figure D-24. Test results carbon fabric [30°/-30°]$_{2S}$: summary of all speeds, in tension

D.4 CARBON FABRIC $[45^{\circ}/-45^{\circ}]_{2S}$

Table D-10. Summary test results carbon fabric $[45^{\circ}/-45^{\circ}]_{2S}$ at a speed of 0.0008 in/s, in tension

Actuator Speed [in/s]	Specimen ID	Tensile Strength [psi]	Maximum Recorded Strain [in/in]	Young's Modulus [Msi]	Average Strain Rate [s^{-1}]
0.00083	[45]-R-QS-1	43,635	*	1.81	0.000378
	[45]-R-QS-2	34,544	**	1.89	0.000391
	[45]-R-QS-3	41,719	*	1.91	0.000370
Average		39,966	-	1.87	0.000380
Standard Deviation		4,792	-	0.05	0.000011
Coefficient of Variation [%]		11.99	-	2.78	2.79

*Exceeded strain gage capability of 0.05 in/in
**Strain gage detached from test specimen

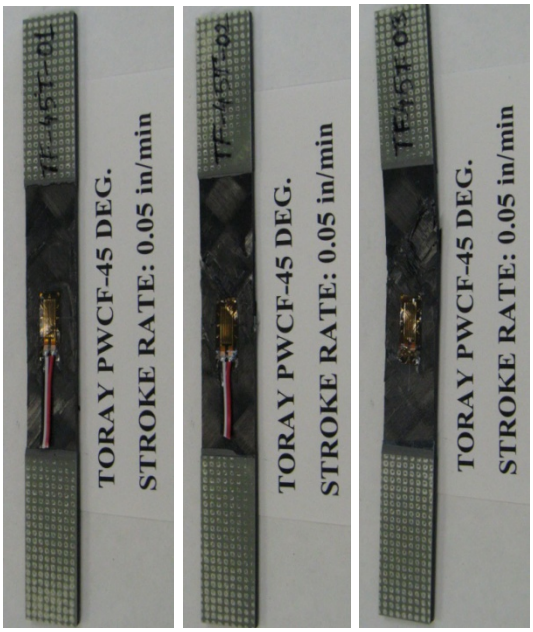

Figure D-25. Failure modes for carbon fabric $[45^{\circ}/-45^{\circ}]_{2S}$ at a speed of 0.0008 in/s, in tension

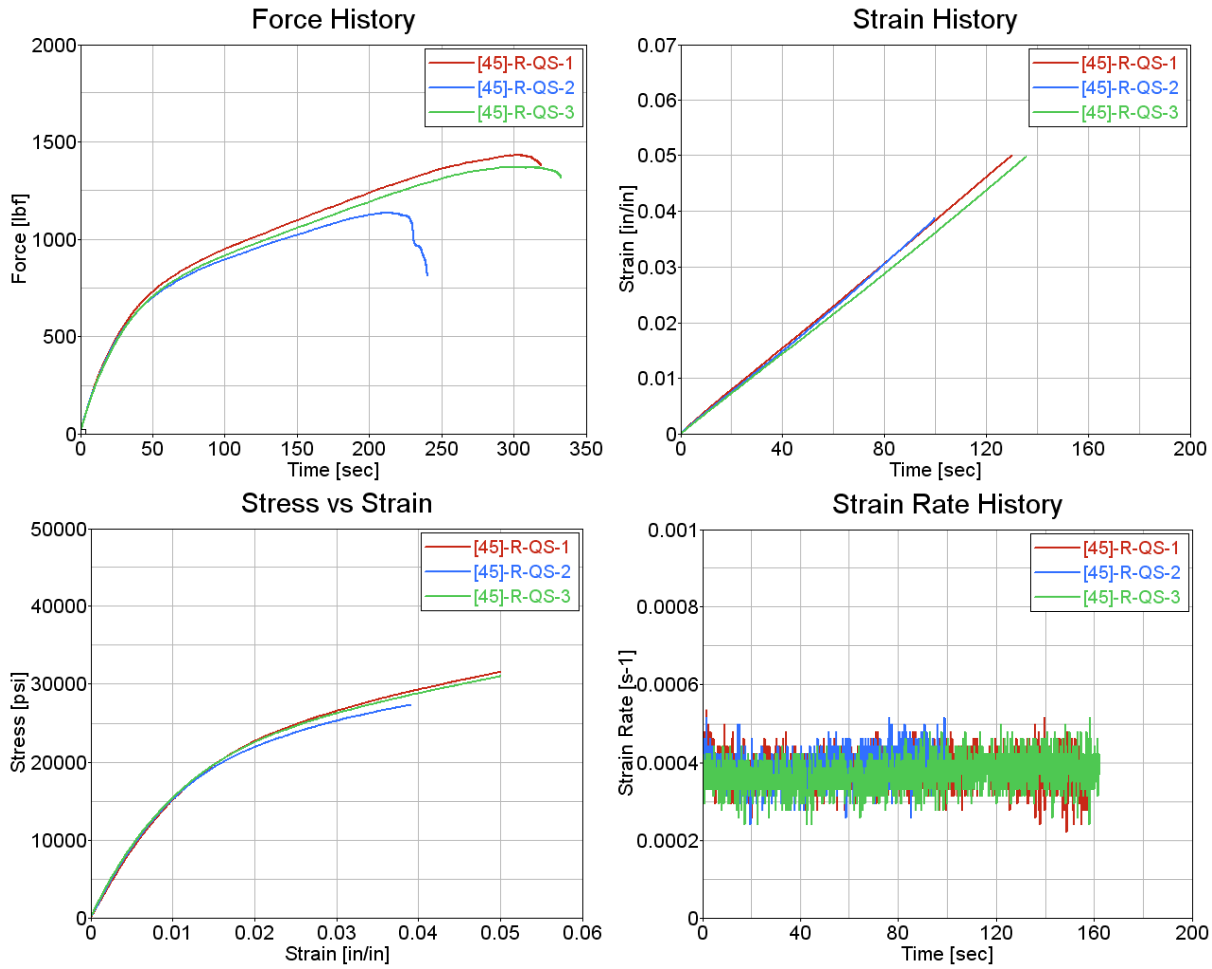

Figure D-26. Test results for carbon fabric [45°/-45°]$_{2S}$ at a speed of 0.0008 in/s, in tension

Table D-11. Summary of test results for carbon fabric [45°/-45°]$_{2S}$ at a speed of 1 in/s, in tension

Actuator Speed [in/s]	Specimen ID	Tensile Strength [psi]	Maximum Recorded Strain [in/in]	Young's Modulus [Msi]	Average Strain Rate [s^{-1}]
1	[45]-R-1-1-4	48,763	**	1.70	0.3484
	[45]-R-1-2-5	43,469	**	2.50	0.3724
	[45]-R-1-3-6	46,583	**	2.10	0.3118
Average		46,272	-	2.10	0.3442
Standard Deviation		2,661	-	0.40	0.0305
Coefficient of Variation [%]		5.75	-	18.96	8.87

**Strain gage detached from test specimen

Figure D-27. Failure modes for carbon fabric [45°/-45°]$_{2S}$ at a speed of 1 in/s, in tension

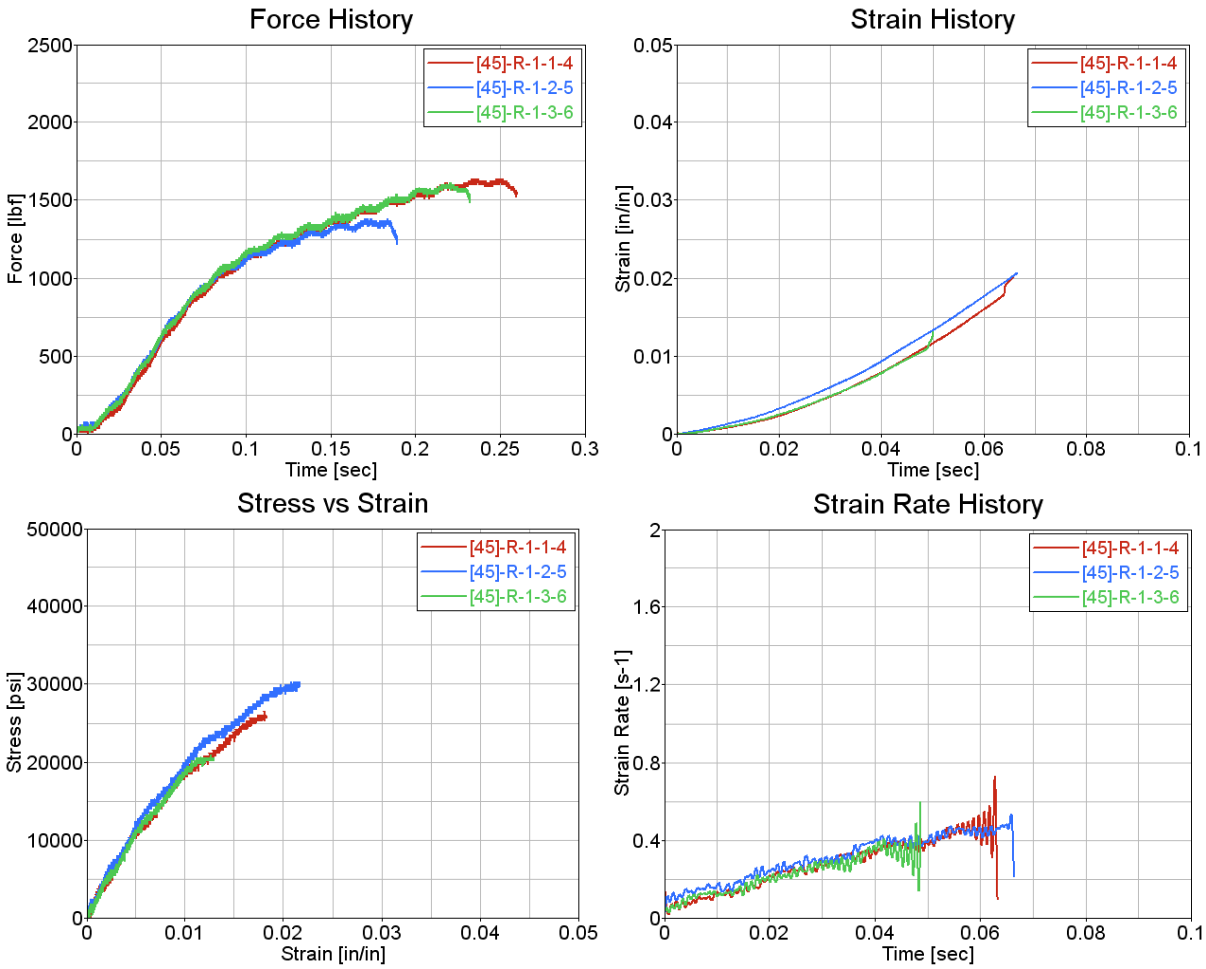

Figure D-28. Test results for carbon fabric [45°/-45°]$_{2S}$ at a speed of 1 in/s, in tension

Table D-12. Summary of test results for carbon fabric $[45^{\circ}/-45^{\circ}]_{2S}$ at a speed of 10 in/s, in tension

Actuator Speed [in/s]	Specimen ID	Tensile Strength [psi]	Maximum Recorded Strain [in/in]	Young's Modulus [Msi]	Average Strain Rate [s^{-1}]
10	[45]-R-10-1-7	53,116	**	3.26	2.5050
	[45]-R-10-2-8	49,957	**	2.84	2.4902
	[45]-R-10-3-9	51,067	**	2.21	2.4414
Average		51,380	-	2.77	2.4789
Standard Deviation		1,603	-	0.53	0.0333
Coefficient of Variation [%]		3.12	-	19.16	1.34

**Strain gage detached from test specimen

Figure D-29. Failure modes for carbon fabric $[45^{\circ}/-45^{\circ}]_{2S}$ at a speed of 10 in/s, in tension

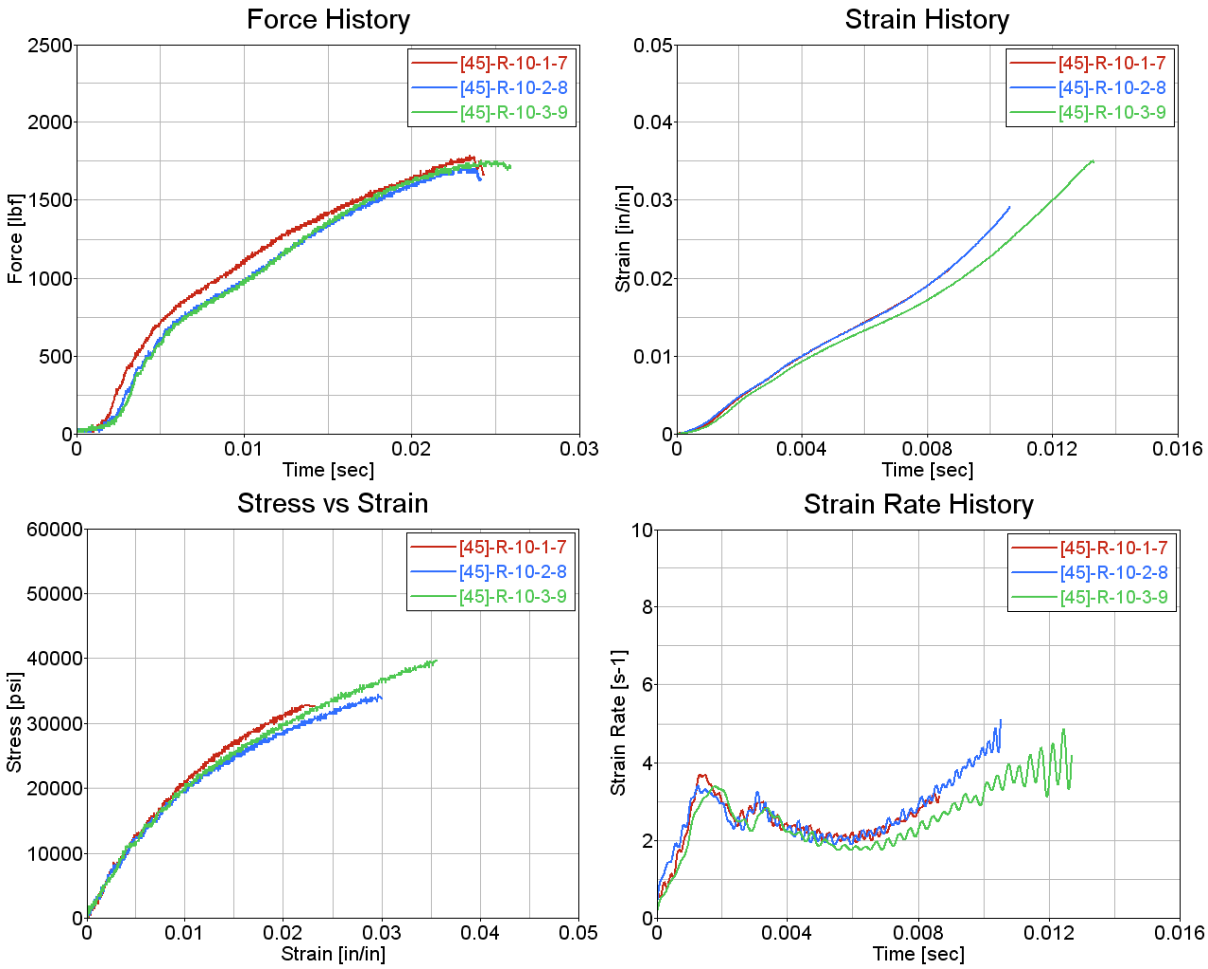

Figure D-30. Test results for carbon fabric $[45^{\circ}/-45^{\circ}]_{2S}$ at a speed of 10 in/s, in tension

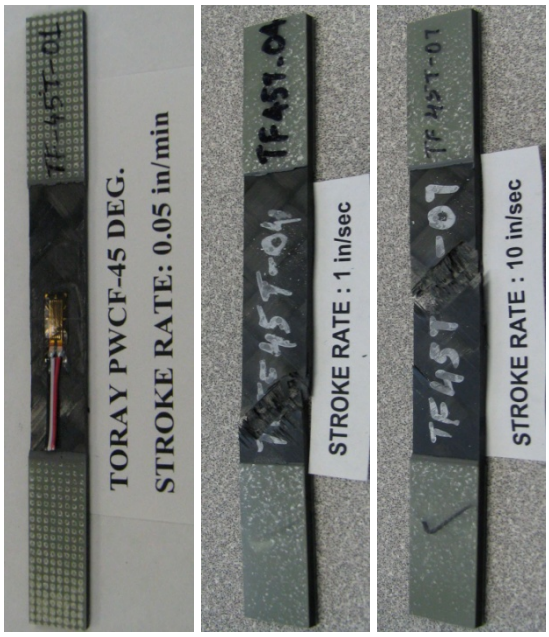

Figure D-31. Failure modes for carbon fabric [45°/-45°]$_{2S}$: summary of all speeds, in tension

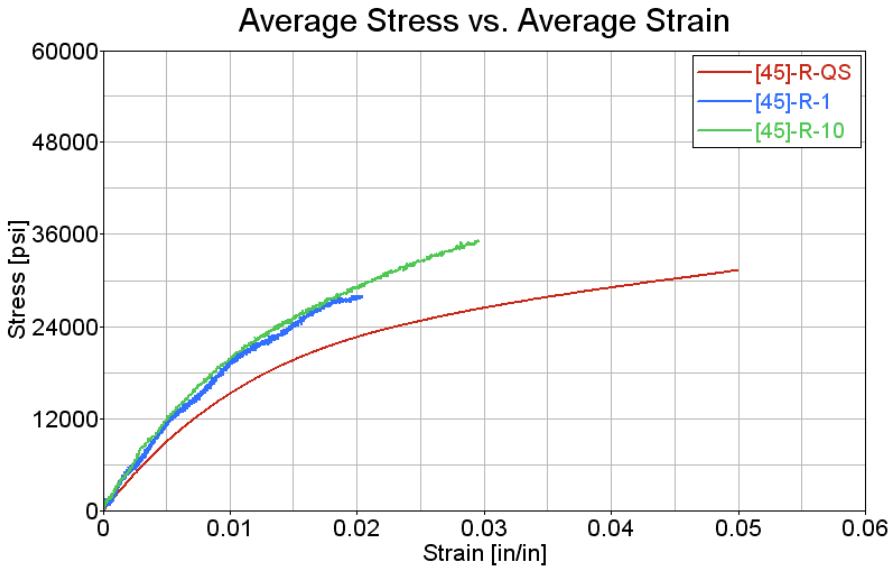

Figure D-32. Test results for carbon fabric [45°/-45°]$_{2S}$: summary of all speeds, in tension

APPENDIX E—NEWPORT E-GLASS FABRIC SHEAR TESTING RESULTS

E.1 FIBERGLASS $[0^{\circ}]_{12}$

Table E-1. Summary of test results for fiberglass $[0^{\circ}]_{12}$ at a speed of 0.0008 in/s, in shear

Actuator Speed [in/s]	Specimen ID	Shear Strength [psi]	Estimated Strain at Shear Strength [rad]	Shear Modulus [Msi]	Average Strain Rate [rad/s]
0.00083	R-QS-1	18,058	0.2031	0.59	0.001047
	R-QS-2	17,237	0.1771	0.57	0.001099
	R-QS-3	18,465	0.2054	0.58	0.001130
Average		17,920	0.1952	0.58	0.001092
Standard Deviation		626	0.0157	0.01	0.000042
Coefficient of Variation [%]		3.49	8.05	1.85	3.84

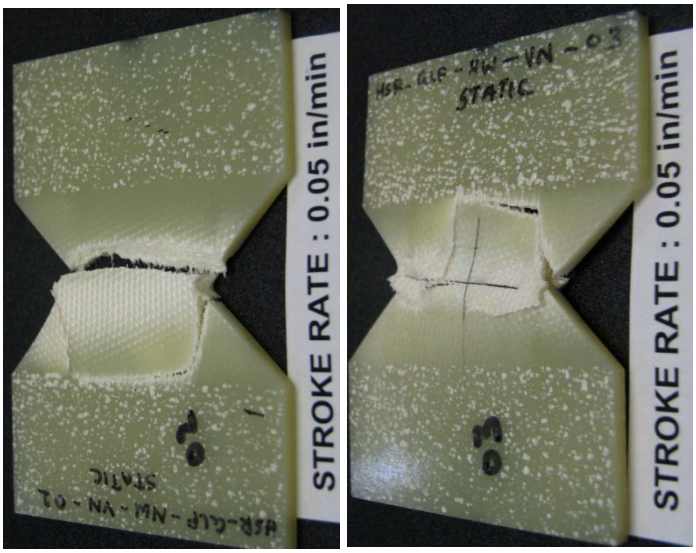

Figure E-1. Failure modes for fiberglass $[0^{\circ}]_{12}$ at a speed of 0.0008 in/s, in shear

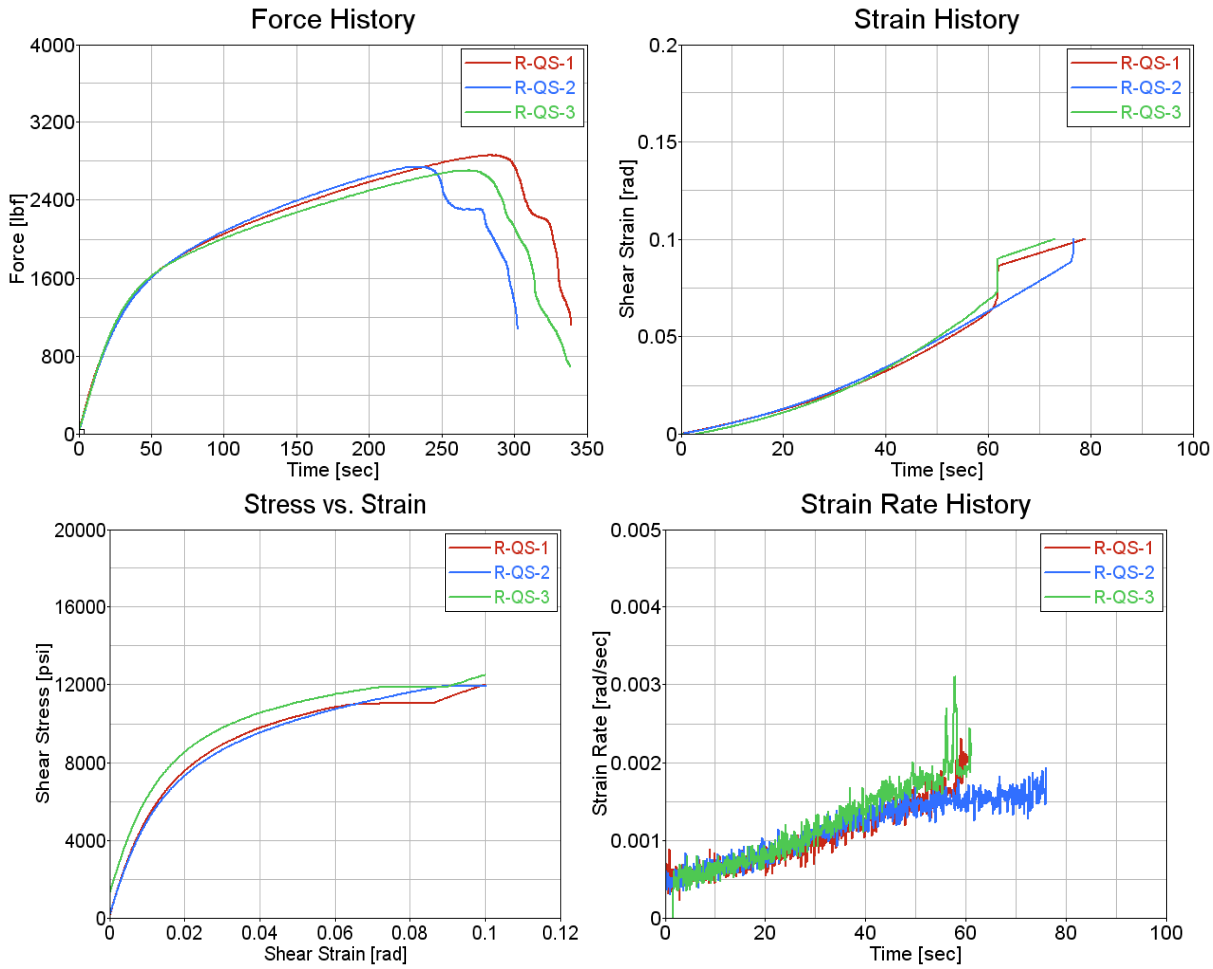

Figure E-2. Test results for fiberglass $[0^{\circ}]_{12}$ at a speed of 0.0008 in/s, in shear

Table E-2. Summary of test results for fiberglass $[0^{\circ}]_{12}$ at a speed of 1 in/s, in shear

Actuator Speed [in/s]	Specimen ID	Shear Strength [psi]	Estimated Strain at Shear Strength [rad]	Shear Modulus [Msi]	Average Strain Rate [rad/s]
1	R-1-1-4	19,699	0.1854	0.63	1.3836
	R-1-2-5	19,595	0.1786	0.63	1.4076
	R-1-3-6	20,081	0.2109	0.56	1.3777
Average		19,792	0.1916	0.61	1.3896
Standard Deviation		256	0.0170	0.04	0.0159
Coefficient of Variation [%]		1.29	8.89	6.07	1.14

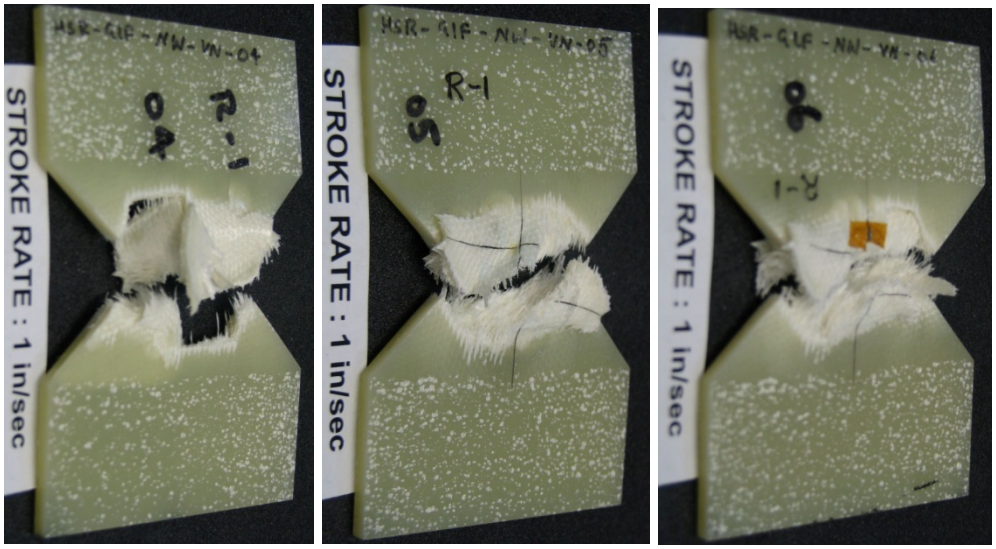

Figure E-3. Failure modes for fiberglass $[0^{\circ}]_{12}$ at a speed of 1 in/s, in shear

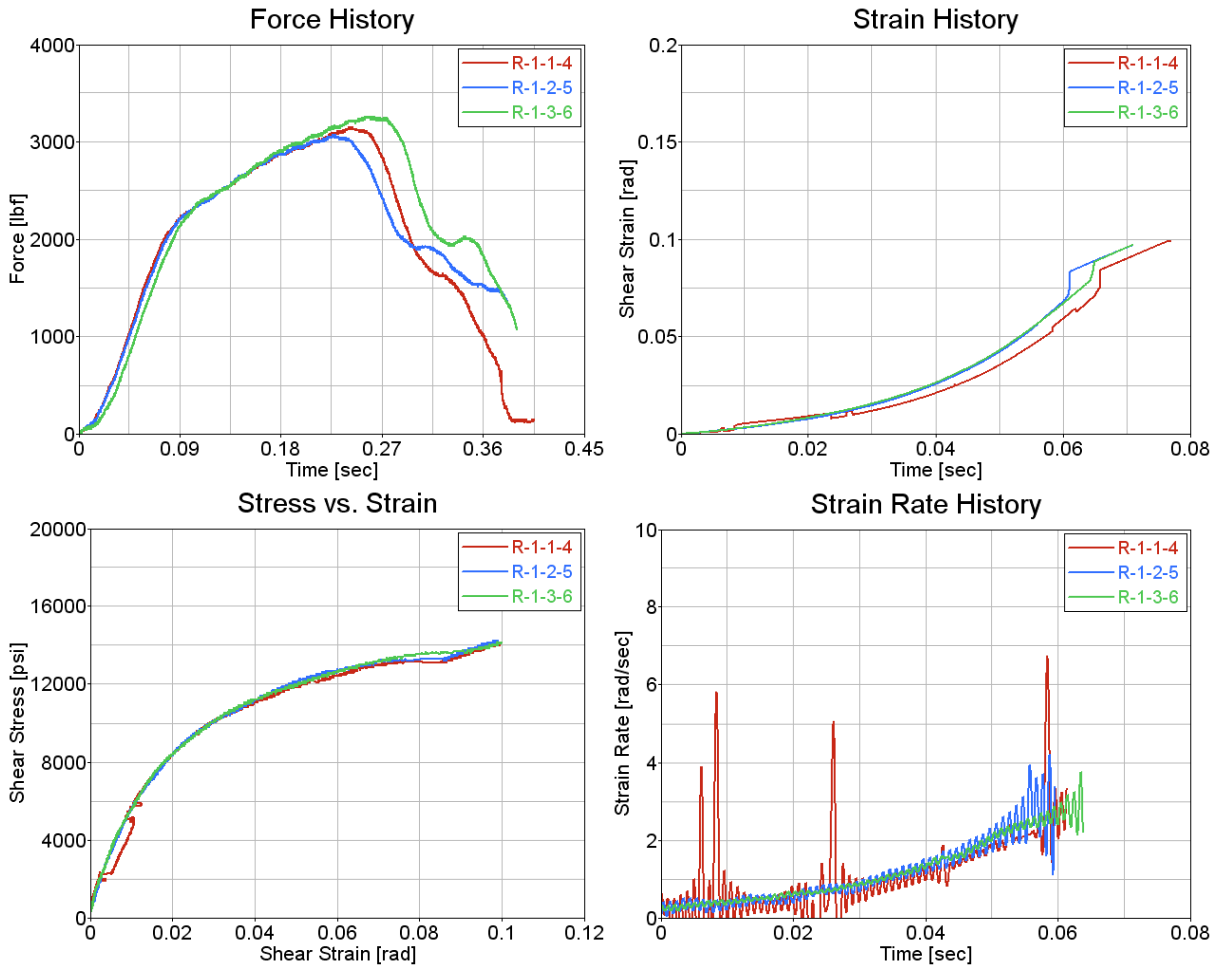

Figure E-4. Test results for fiberglass $[0^{\circ}]_{12}$ at a speed of 1 in/s, in shear

Table E-4. Summary of test results for fiberglass $[0^{\circ}]_{12}$ at a speed of 10 in/s, in shear

Actuator Speed [in/s]	Specimen ID	Shear Strength [psi]	Estimated Strain at Shear Strength [rad]	Shear Modulus [Msi]	Average Strain Rate [rad/s]
10	R-10-1-8	22,017	0.2640	0.64	10.3020
	R-10-2-9	21,329	0.2835	0.65	10.7051
	R-10-3-10	21,906	0.3820	0.64	10.2350
Average		21,750	0.3099	0.64	10.4140
Standard Deviation		369	0.0633	0.01	0.2543
Coefficient of Variation [%]		1.70	20.43	1.16	2.44

Figure E-5. Failure modes for fiberglass $[0^{\circ}]_{12}$ at a speed of 10 in/s, in shear

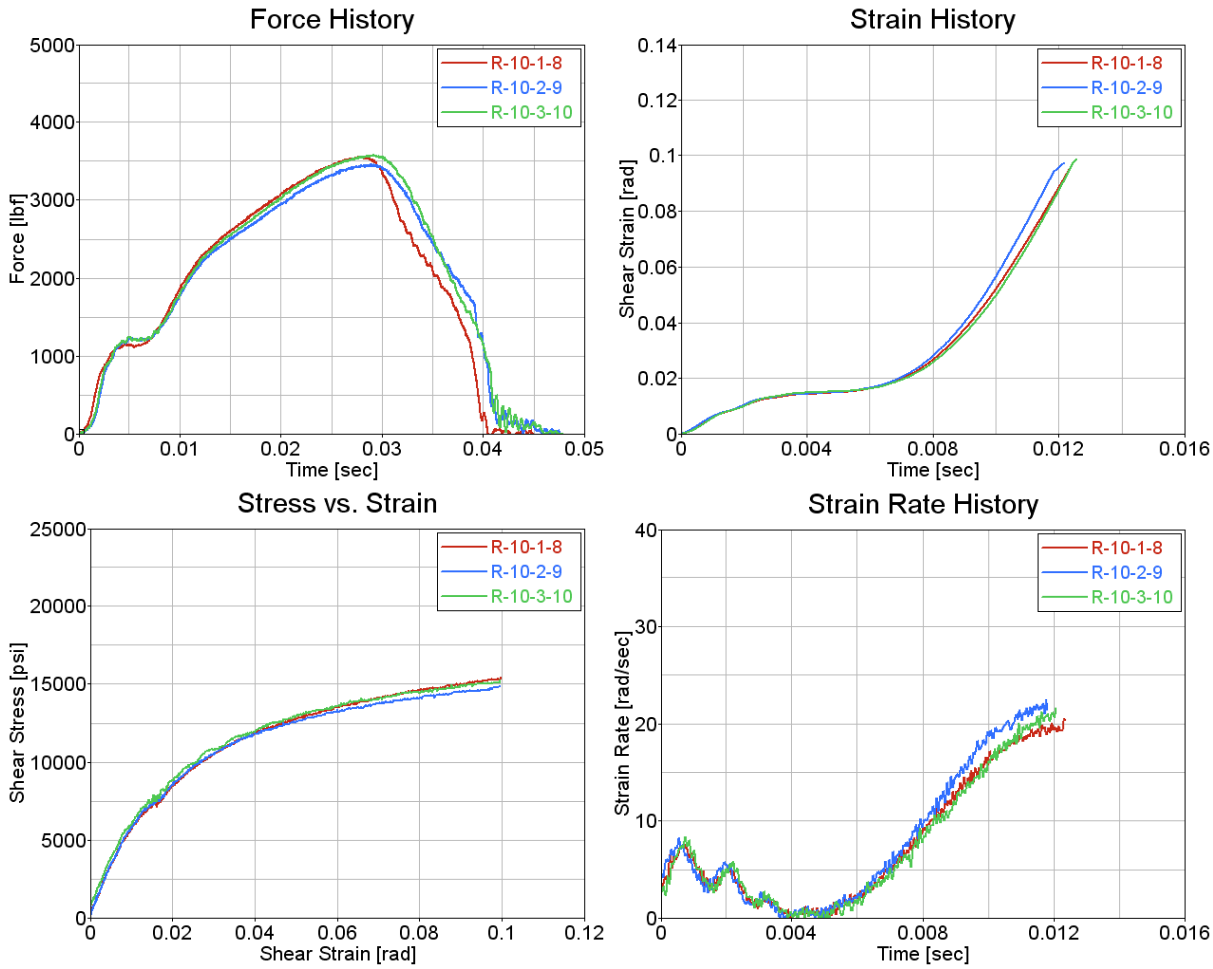

Figure E-6. Test results for fiberglass $[0^{\circ}]_{12}$ at a speed of 10 in/s, in shear

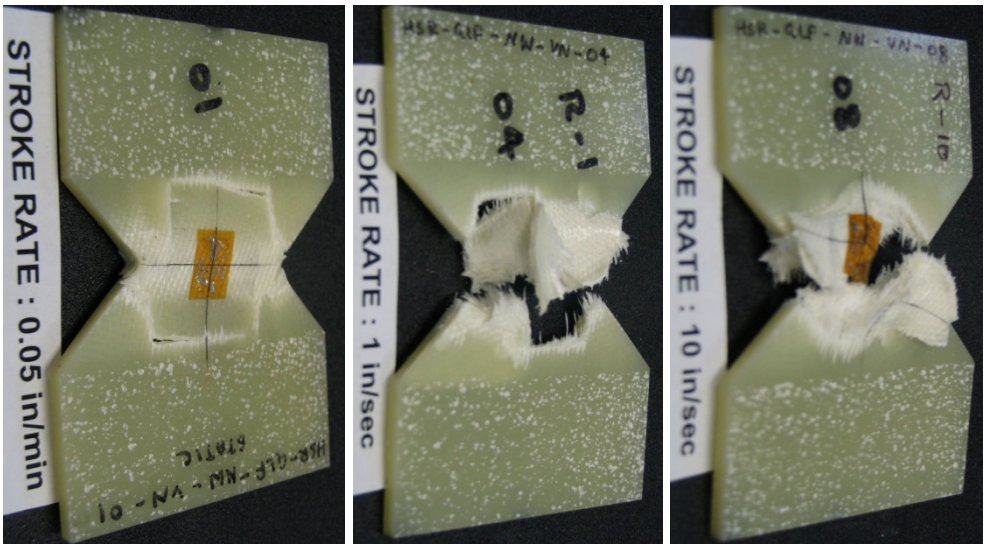

Figure E-7. Failure modes for fiberglass $[0^{\circ}]_{12}$: summary of all speeds, in shear

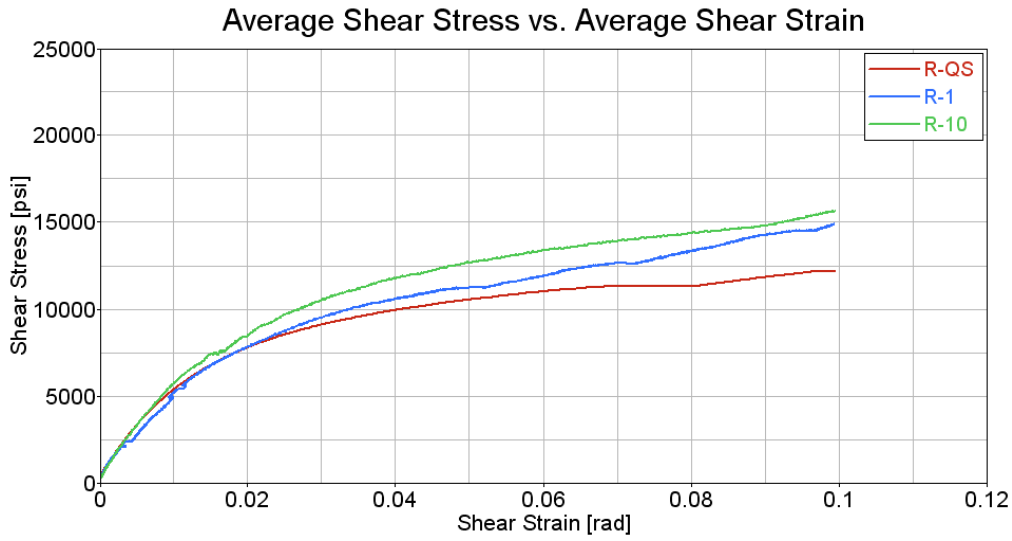

Figure E-8. Test results for fiberglass $[0^{\circ}]_{12}$: summary of all speeds, in shear

APPENDIX F—TORAY T800S/3900-2B UNITAPE SHEAR TESTING RESULTS

F.1 CARBON UNITAPE $[0^{\circ}]_{12}$

Table F-1. Summary of test results for carbon Unitape $[0^{\circ}]_{12}$ at a speed of 0.0008 in/s

Actuator Speed [in/s]	Specimen ID	Shear Strength [psi]	Estimated Strain at Shear Strength [rad]	Shear Modulus [Msi]	Average Strain Rate [rad/s]
0.00083	R-QS-1-17	18,625	0.3155	0.59	0.001300
	R-QS-2-18	16,827	0.3261	0.49	0.001318
	R-QS-3-19	16,378	0.3996	0.49	0.001312
Average		17,277	0.3471	0.52	0.001310
Standard Deviation		1,189	0.0458	0.06	0.000009
Coefficient of Variation [%]		6.88	13.19	11.34	0.70

Note: Pictures are not available for Toray Unitape quasi-static shear testing.

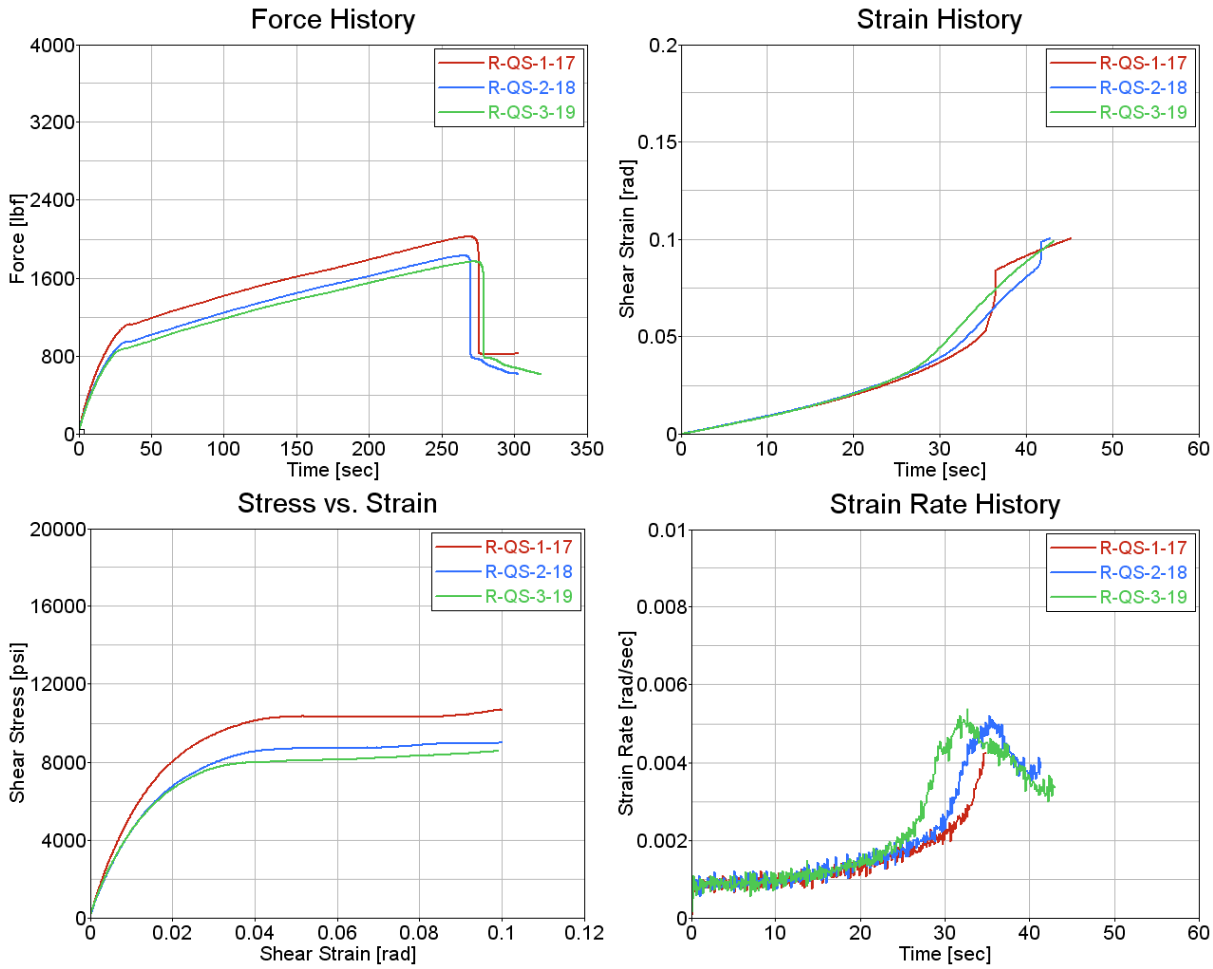

Figure F-1. Test results for carbon Unitape $[0^{\circ}]_{12}$ at a speed of 0.0008 in/s, in shear

Table F-2. Summary of test results carbon Unitape $[0^{\circ}]_{12}$ at a speed of 1 in/s

Actuator Speed [in/s]	Specimen ID	Shear Strength [psi]	Estimated Strain at Shear Strength [rad]	Shear Modulus [Msi]	Average Strain Rate [rad/s]
1	R-1-1	21,919	0.2895	0.73	0.9180
	R-1-2	22,026	0.4281	0.72	1.0518
	R-1-3	22,470	0.6783	0.72	0.9713
Average		22,138	0.4653	0.72	0.9804
Standard Deviation		292	0.1970	0.00	0.0674
Coefficient of Variation [%]		1.32	42.35	0.47	6.87

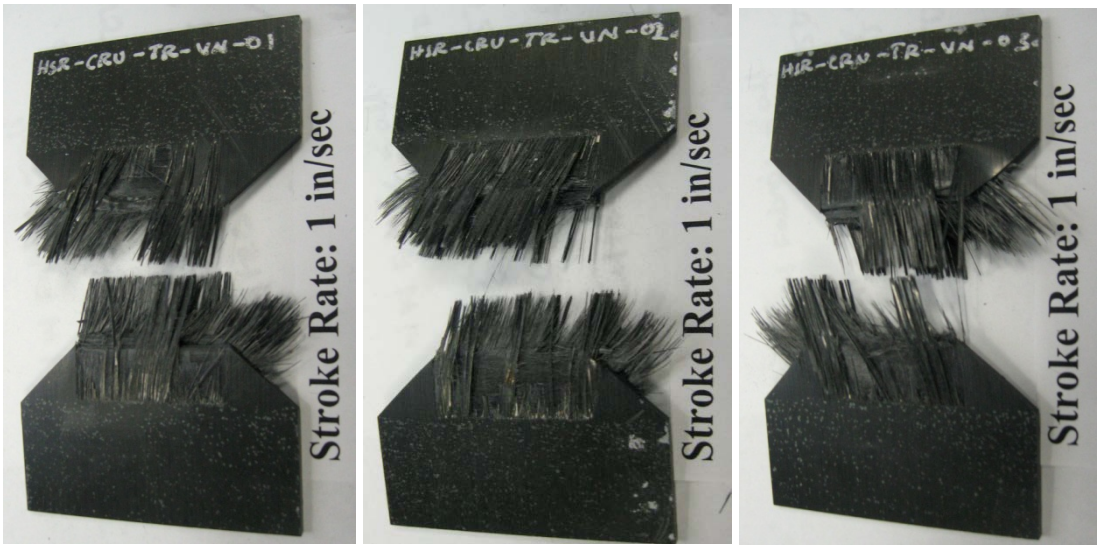

Figure F-2. Failure modes for carbon Unitape $[0^{\circ}]_{12}$ at a speed of 1 in/s, in shear

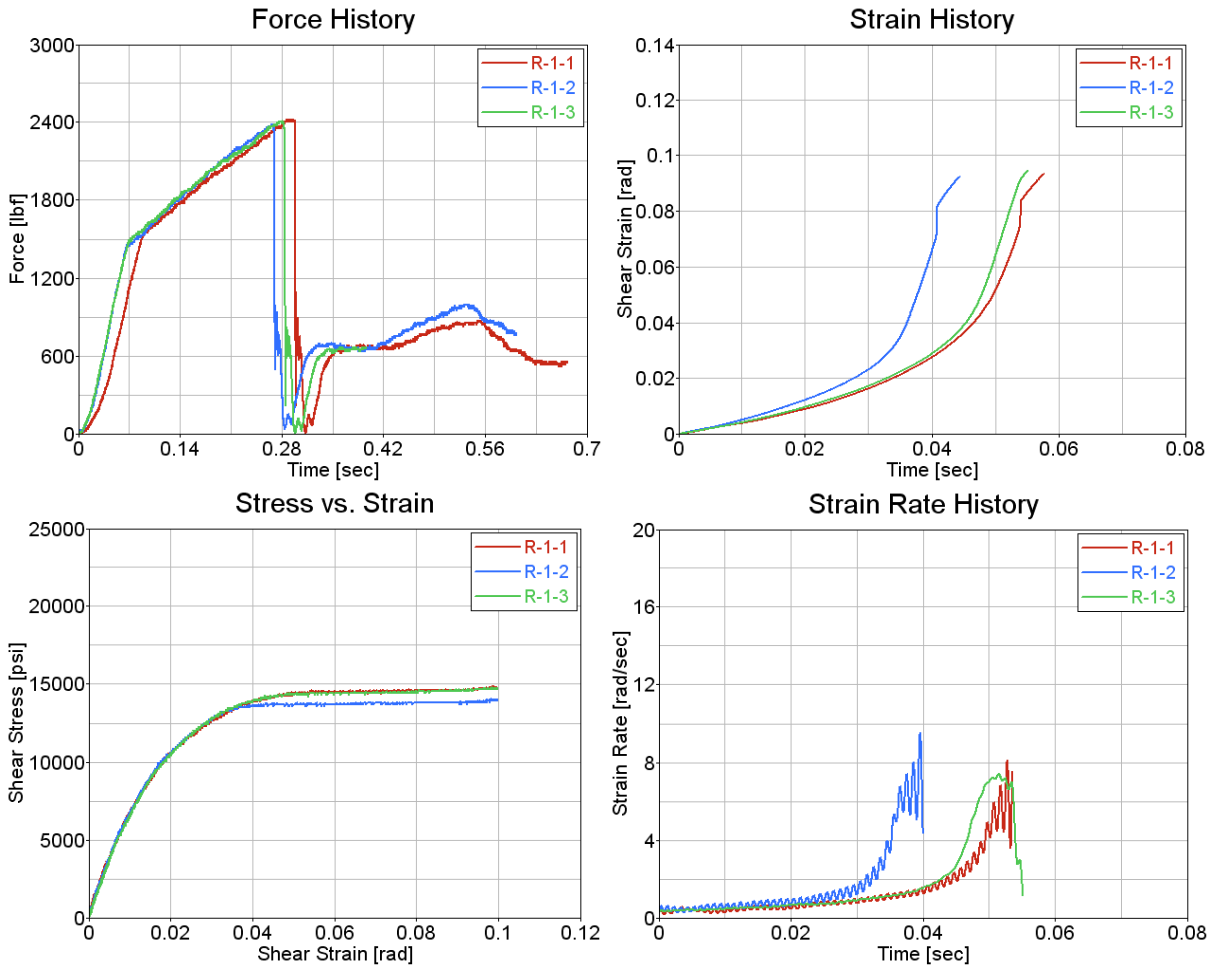

Figure F-3. Test results for carbon Unitape $[0^{\circ}]_{12}$ at a speed of 1 in/s, in shear

Table F-3. Summary of test results for carbon Unitape $[0^{\circ}]_{12}$ at a speed of 10 in/s

Actuator Speed [in/s]	Specimen ID	Shear Strength [psi]	Estimated Strain at Shear Strength [rad]	Shear Modulus [Msi]	Average Strain Rate [rad/s]
10	R-10-1-4	26,634	0.2851	0.80	4.4752
	R-10-2-5	23,710	0.3073	0.73	3.9184
	-	-	-	-	-
Average		25,172	0.2962	0.76	4.1968
Standard Deviation		2,068	0.0157	0.05	0.3939
Coefficient of Variation [%]		8.22	5.31	7.18	9.38

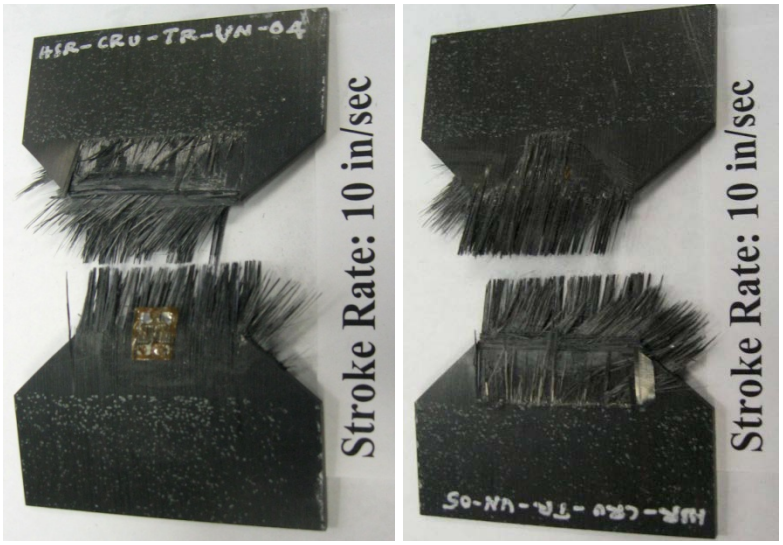

Figure F-4. Failure modes for carbon Unitape $[0^{\circ}]_{12}$ at a speed of 10 in/s, in shear

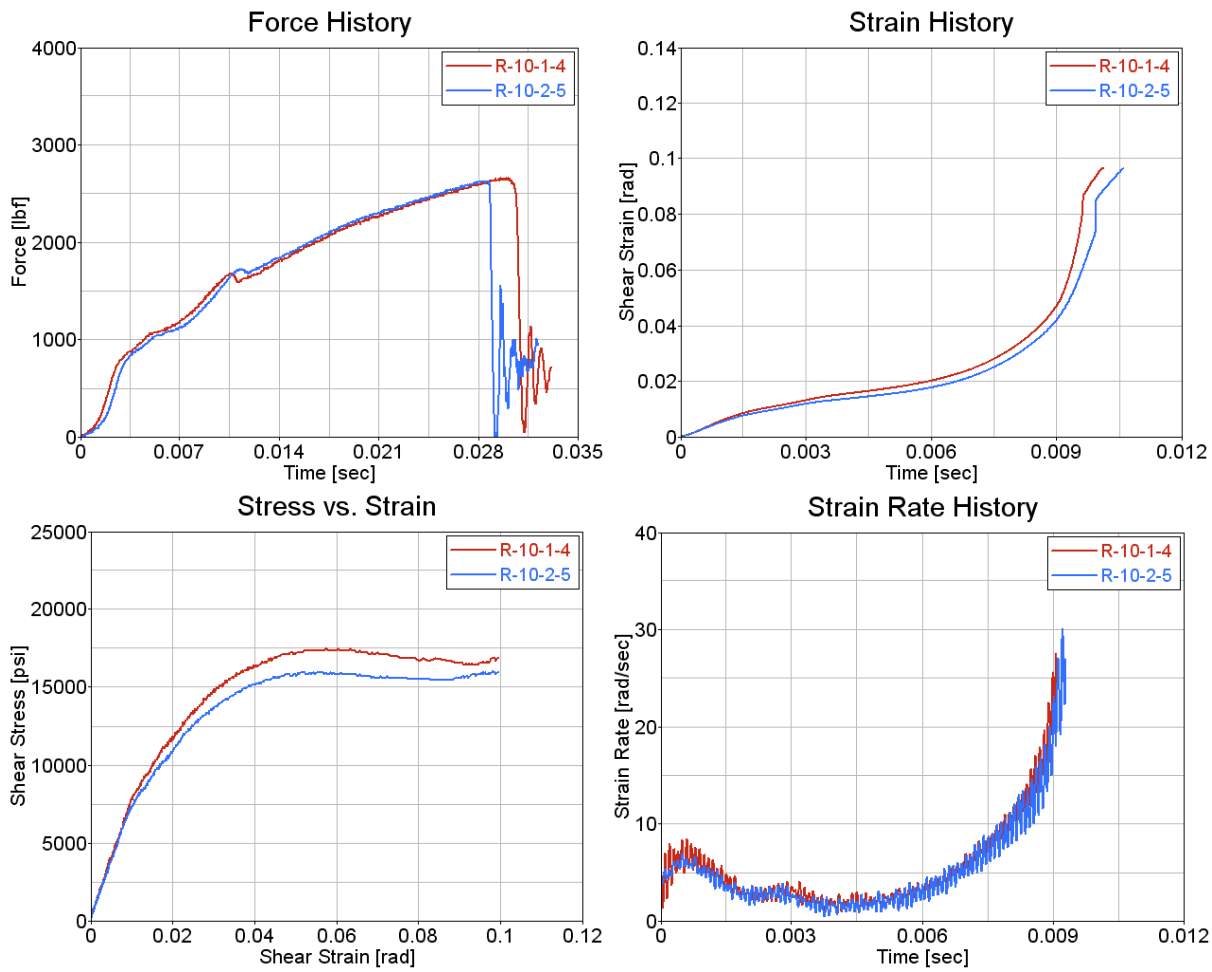

Figure F-5. Test results for carbon Unitape $[0^{\circ}]_{12}$ at a speed of 10 in/s, in shear

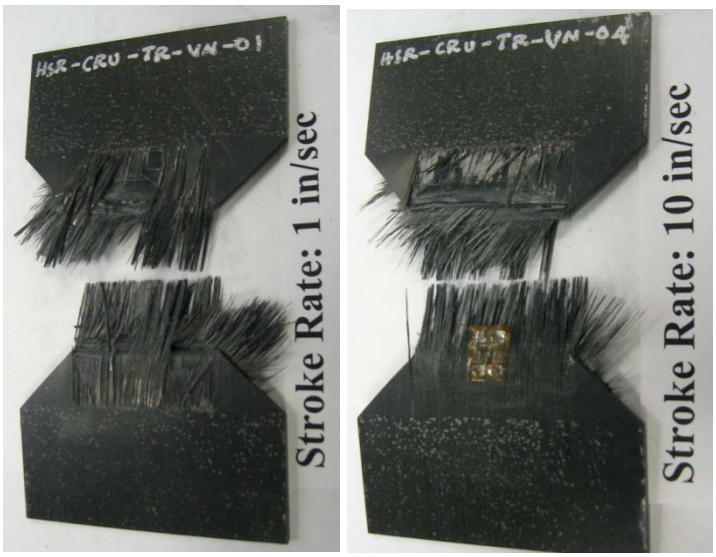

Figure F-6. Failure modes for carbon Unitape $[0^{\circ}]_{12}$: summary of all speeds, in shear

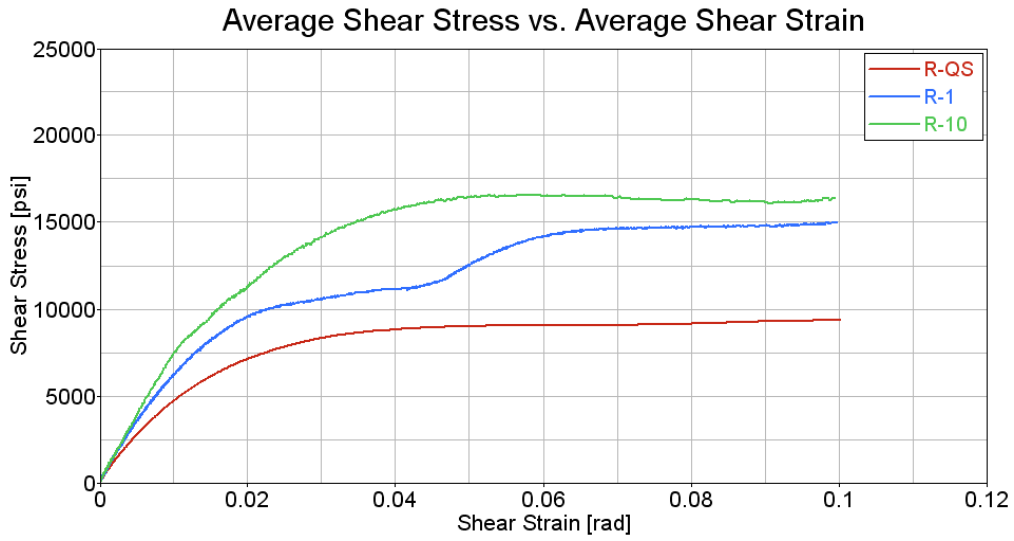

Figure F-7. Test results for carbon Unitape $[0^{\circ}]_{12}$: summary of all speeds, in shear

APPENDIX G—TORAY T700G-12K-PW/3900-2 CARBON FABRIC SHEAR TESTING RESULTS

G.1 CARBON FABRIC $[0^{\circ}]_{12}$

Table G-1. Summary of test results for carbon fabric $[0^{\circ}]_{12}$ at a speed of 0.0008 in/s, in shear

Actuator Speed [in/s]	Specimen ID	Shear Strength [psi]	Estimated Strain at Shear Strength [rad]	Shear Modulus [Msi]	Average Strain Rate [rad/s]
0.00083	R-QS-1-17	20,614	0.1814	0.51	0.001317
	-	-	-	-	-
	-	-	-	-	-
Average		20,614	0.1814	0.51	0.001317
Standard Deviation		-	-	-	-
Coefficient of Variation [%]		-	-	-	-

Note: Pictures are not available for Toray fabric quasi-static shear testing.

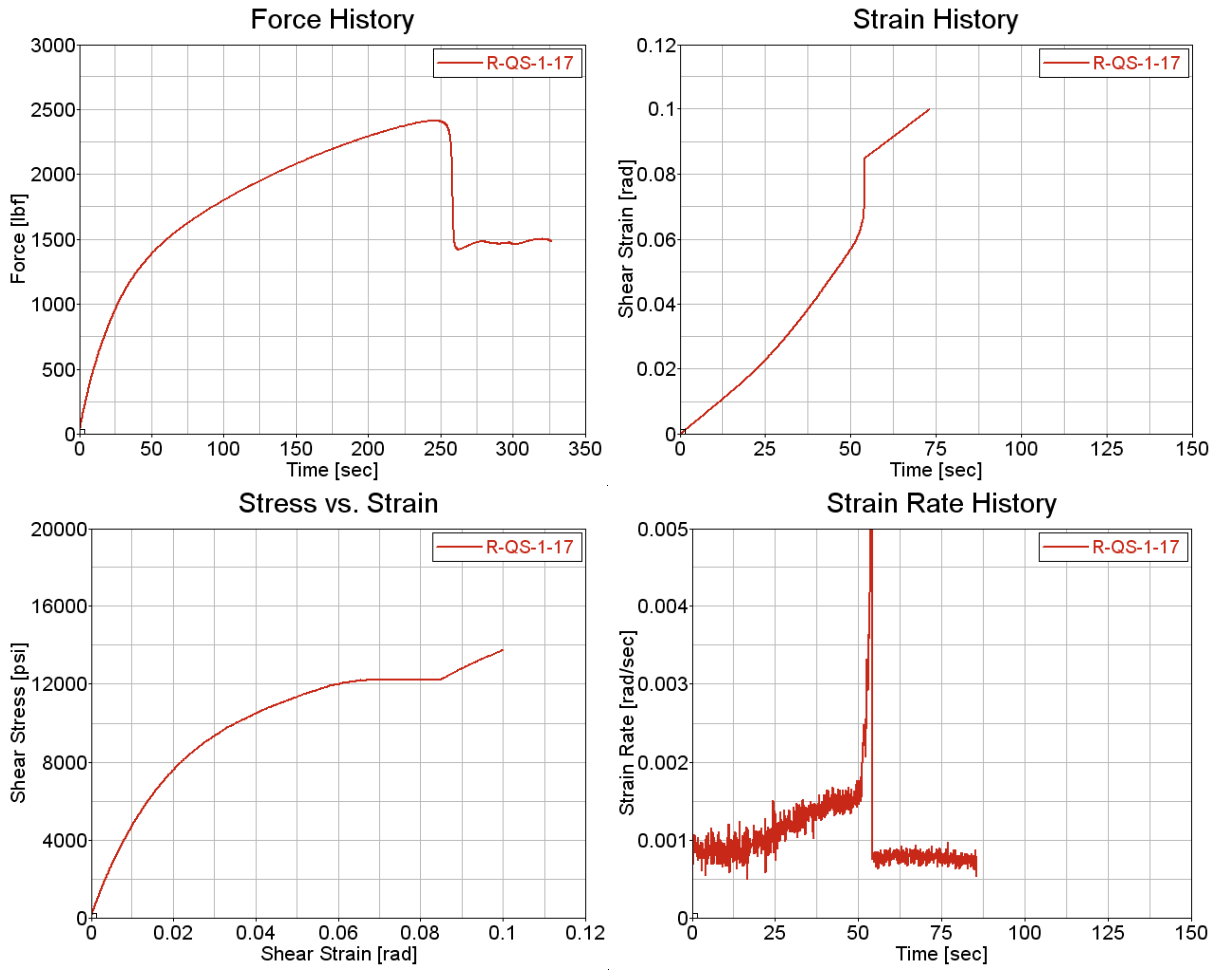

Figure G-1. Test results for carbon fabric $[0^{\circ}]_{12}$ at a speed of 0.0008 in/s, in shear

Table G-2. Summary of test results for carbon fabric $[0^{\circ}]_{12}$ at a speed of 1 in/s, in shear

Actuator Speed [in/s]	Specimen ID	Shear Strength [psi]	Estimated Strain at Shear Strength [rad]	Shear Modulus [Msi]	Average Strain Rate [rad/s]
1	R-1-1	25,024	0.1661	0.75	0.7392
	R-1-2	26,298	0.1627	0.73	0.6037
	R-1-3	25,754	0.1726	0.63	0.8228
Average		25,692	0.1671	0.70	0.7219
Standard Deviation		639	0.0050	0.06	0.1106
Coefficient of Variation [%]		2.49	2.99	8.82	15.32

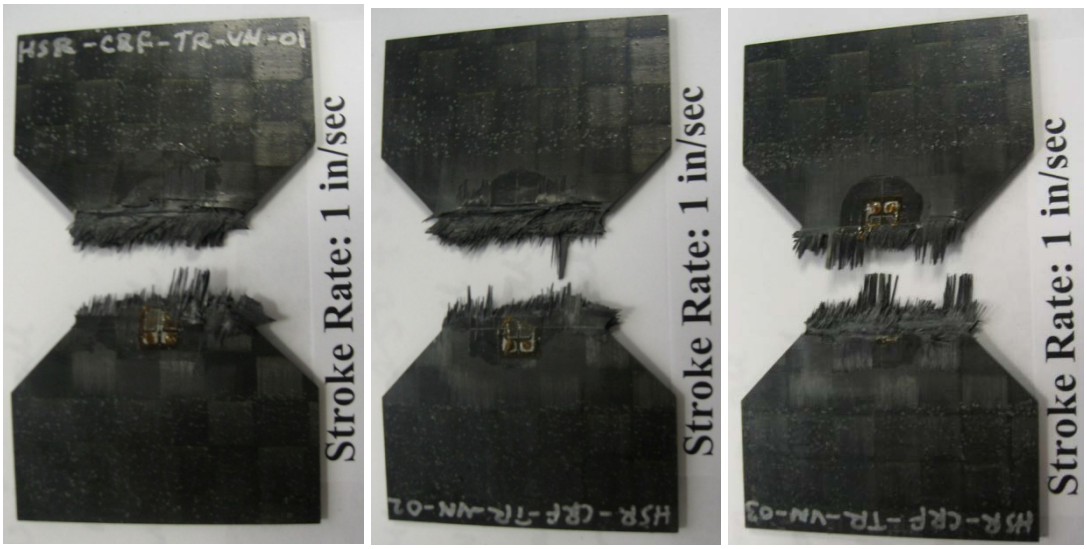

Figure G-2. Failure modes for carbon fabric $[0^{\circ}]_{12}$ at a speed of 1 in/s, in shear

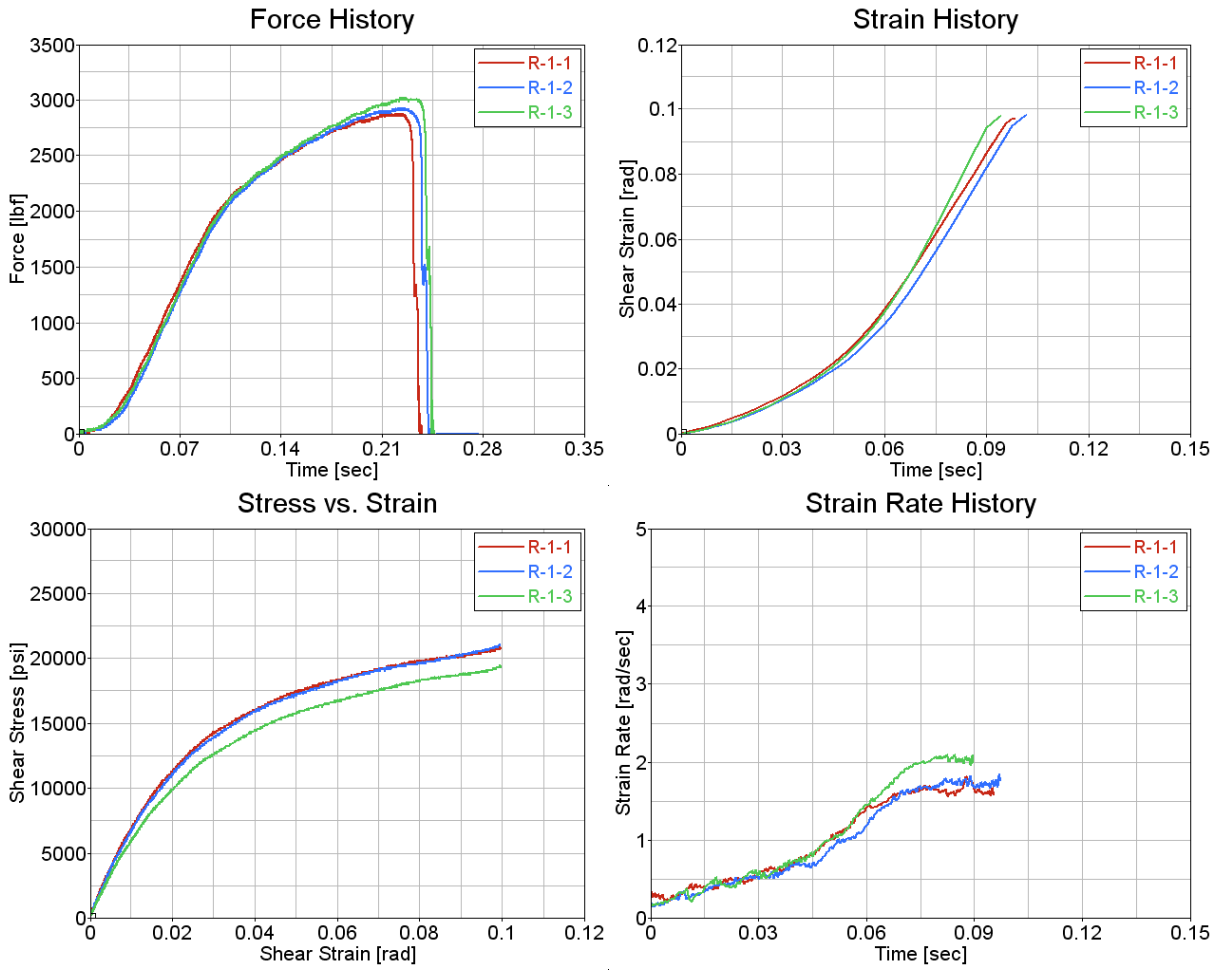

Figure G-3. Test results for carbon fabric $[0^{\circ}]_{12}$ at a speed of 1 in/s, in shear

Table G-3. Summary of test results for carbon fabric $[0^{\circ}]_{12}$ at a speed of 10 in/s, in shear

Actuator Speed [in/s]	Specimen ID	Shear Strength [psi]	Estimated Strain at Shear Strength [rad]	Shear Modulus [Msi]	Average Strain Rate [rad/s]
10	R-10-1-4	26,937	0.1446	0.74	6.3502
	R-10-2-5	26,409	0.1712	0.64	6.2536
	R-10-3-6	26,300	0.1754	0.65	6.3586
Average		26,549	0.1637	0.68	6.3208
Standard Deviation		341	0.0167	0.06	0.0584
Coefficient of Variation [%]		1.28	10.20	8.17	0.92

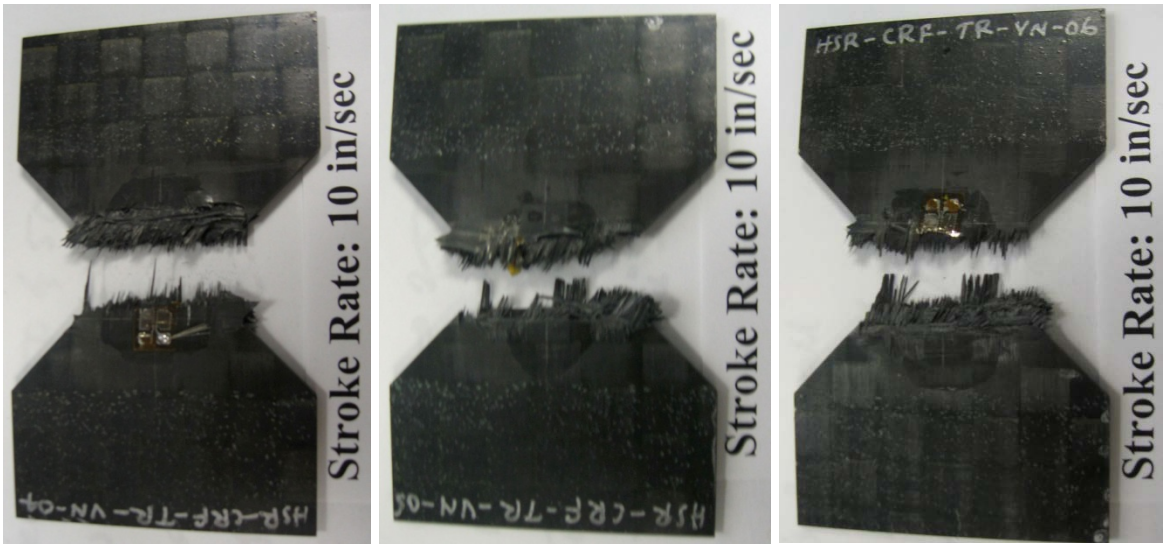

Figure G-4. Failure modes for carbon fabric $[0^{\circ}]_{12}$ at a speed of 10 in/s, in shear

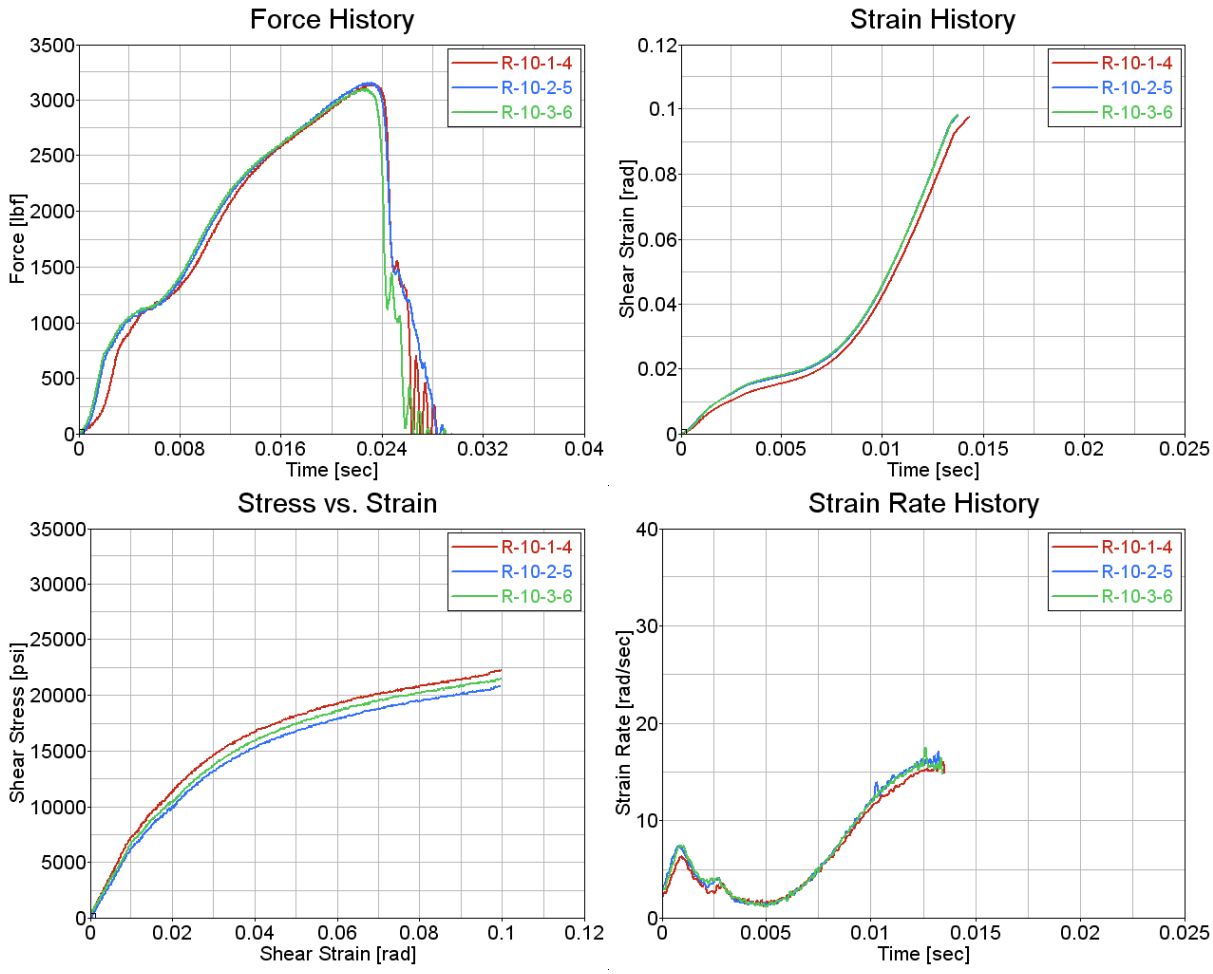

Figure G-5. Test results for carbon fabric $[0^{\circ}]_{12}$ at a speed of 10 in/s, in shear

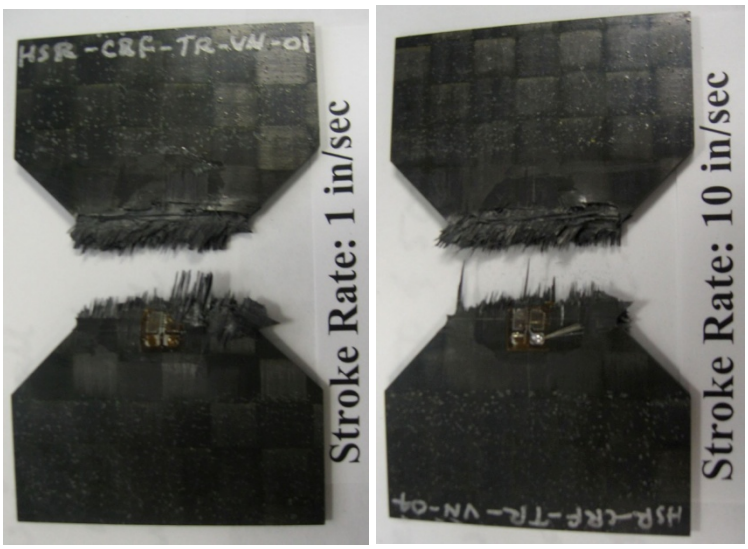

Figure G-6. Failure modes for carbon fabric $[0^{\circ}]_{12}$: summary of all speeds, in shear

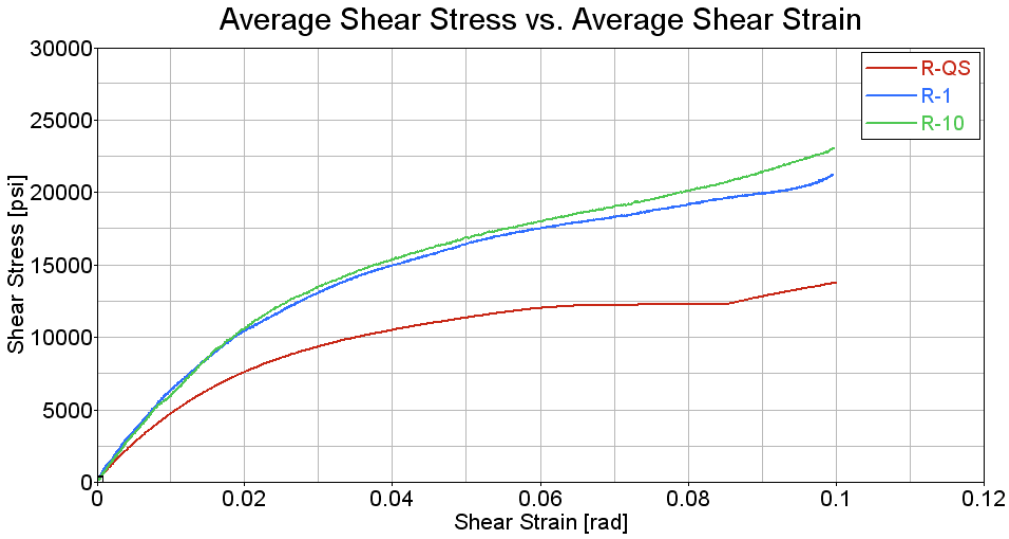

Figure G-7. Test results for carbon fabric $[0^{\circ}]_{12}$: summary of all speeds, in shear

APPENDIX H—FAILURE CRITERIA

H.1 Chang-Chang Failure Criteria

(a) Tensile fiber mode (fiber rupture), $\sigma_{aa} > 0$

$$e_f^2 = \left(\frac{\sigma_{aa}}{X_t}\right)^2 + \zeta\left(\frac{\sigma_{ab}}{S_c}\right) - 1 \begin{cases} \geq 0 \Rightarrow \textit{failed}, \\ < 0 \Rightarrow \textit{elastic}. \end{cases}$$

$0 < \zeta < 1 \rightarrow$ Weighting factor for shear term in tensile fiber mode

$E_a = E_b = G_{ab} = \upsilon_{ab} = \upsilon_{ba} = 0 \rightarrow$ After lamina failure by fiber rupture

(b) Compressive fiber mode (fiber buckling or kinking), $\sigma_{aa} < 0$

$$e_c^2 = \left(\frac{\sigma_{aa}}{X_c}\right)^2 - 1 \begin{cases} \geq 0 \Rightarrow \textit{failed}, \\ < 0 \Rightarrow \textit{elastic}. \end{cases}$$

$E_a = \upsilon_{ab} = \upsilon_{ab} = 0 \rightarrow$ After lamina failure by fiber buckling or kinking

(c) Tensile matrix mode (matrix cracking under transverse tension and in-plane shear), $\sigma_{bb} > 0$

$$e_m^2 = \left(\frac{\sigma_{bb}}{Y_t}\right)^2 + \zeta\left(\frac{\sigma_{ab}}{S_c}\right)^2 - 1 \begin{cases} \geq 0 \Rightarrow \textit{failed}, \\ < 0 \Rightarrow \textit{elastic}. \end{cases}$$

$E_b = \upsilon_{ab} = G_{ab} = 0 \rightarrow$ After lamina failure by matrix cracking

(d) Compressive matrix mode (matrix cracking under transverse compression and in-plane shear), $\sigma_{bb} < 0$

$$e_d^2 = \left(\frac{\sigma_{bb}}{2S_c}\right)^2 + \left[\left(\frac{Y_c}{2S_c}\right)^2 - 1\right]\frac{\sigma_{bb}}{Y_c} + \left(\frac{\sigma_{ab}}{S_c}\right)^2 - 1 \begin{cases} \geq 0 \Rightarrow \textit{failed}, \\ < 0 \Rightarrow \textit{elastic}. \end{cases}$$

$E_b = \upsilon_{ab} = \upsilon_{ba} = 0 \rightarrow G_{ab} = 0 \rightarrow$ After lamina failure by matrix cracking

Here,

$\sigma_{aa} \Rightarrow$ Stress in fiber direction

$\sigma_{bb} \Rightarrow$ Stress in transverse direction (normal to the fiber direction)

$\sigma_{ab} \Rightarrow$ Shear stress in lamina plane $aa-bb$

$X_t \Rightarrow$ Tensile strength in fiber direction

$X_c \Rightarrow$ Compressive strength in fiber direction

$S_c \Rightarrow$ Shear strength

$E_a \Rightarrow$ Young's modulus in longitudinal direction

$E_b \Rightarrow$ Young's modulus in transverse direction

H.2 Hashin Failure Criteria

(a) Tensile Fiber Mode, $\sigma_{11} > 0$

$$\left(\frac{\sigma_{11}}{T_{11}}\right)^2 + \frac{1}{S_{12}^2}\left(\sigma_{12}^2 + \sigma_{31}^2\right) \le 1$$

(b) Compressive Fiber Mode, $\sigma_{11} < 0$

$$\left(\frac{\sigma_{11}}{C_{11}}\right)^2 \le 1$$

(c) Tensile Matrix Mode, $\left(\sigma_{22} + \sigma_{33}\right) > 0$

$$\frac{1}{T_{22}^2}\left(\sigma_{22} + \sigma_{33}\right)^2 + \frac{1}{S_{23}^2}\left(\sigma_{23}^2 - \sigma_{22}\sigma_{33}\right) + \frac{1}{S_{12}^2}\left(\sigma_{12}^2 + \sigma_{31}^2\right) \le 1$$

(d) Compressive Matrix Mode, $\left(\sigma_{22} + \sigma_{33}\right) < 0$

$$\frac{1}{C_{22}}\left[\left(\frac{C_{22}}{2S_{23}}\right)^2 - 1\right]\left(\sigma_{22} + \sigma_{33}\right) + \frac{1}{4S_{23}^2}\left(\sigma_{22} + \sigma_{33}\right)^2 + \frac{1}{S_{23}^2}\left(\sigma_{23}^2 - \sigma_{22}\sigma_{33}\right) + \frac{1}{S_{12}^2}\left(\sigma_{12}^2 + \sigma_{31}^2\right) \le 1$$